université PARIS-SACLAY

NNT : 2019SACLX098

Thèse de doctorat

Differential measurement of the $\bar{\nu}_\mu$-CC0π cross sections on H_2O and CH and the H_2O / CH cross-section ratio with the WAGASCI experiment

Thèse de doctorat de l'Université Paris-Saclay
préparée à l'Ecole polytechnique

École doctorale n°576 Particules, Hadrons, Énergie, Noyau, Instrumentation, Imagerie, Cosmos et Simulation (PHENIICS)
Spécialité de doctorat : Physique des particules

Thèse présentée et soutenue à Palaiseau, le 2 décembre 2019, par

OLIVIER VOLCY

Composition du Jury :

David Lhuillier Professeur de Recherche, CEA (Saclay)	Rapporteur
Alessandra Tonazzo Professeur des Universités, APC (Paris)	Rapporteur
Jaime Dawson Chargée de Recherche, APC (Paris)	Examinateur
Yves Sirois Directeur de Recherche, LLR (Palaiseau)	Examinateur
Frédéric Yermia Maître de Conférence, Subatech (Nantes)	Examinateur
Thomas Mueller Chargé de Recherche, LLR (Palaiseau)	Directeur de thèse

Remerciements

À l'heure de finaliser mon manuscrit, je repense à ces trois années de thèse ainsi qu'à mon parcours préalable. La conclusion de ces années d'études a été possible grâce à la participation de nombre de gens que je peux remercier ici.

Tout d'abord je remercie Jean-Claude Brient, directeur du Laboratoire Leprince-Ringuet, pour m'avoir accueilli au sein de son laboratoire.

Dans un deuxième temps, je remercie Michel GONIN qui m'a accueilli dans le groupe neutrino du Laboratoire Leprince-Ringuet. Premièrement en stage de Laboratoire, puis en tant que doctorant. La gestion impeccable du groupe et l'organisation sans faille ont toujours permis aux thésards du groupe de se concentrer sur la physique.

Je remercie ensuite mon directeur de thèse, Thomas MUELLER pour son encadrement efficace et permanent. J'ai toujours pu me tourner vers lui lorsque j'étais coincé, et sa diligence à régler tous les problèmes qui sont survenus m'a offert un esprit tranquille et tous les outils pour mener à bien mon analyse. J'ai pu apprendre énormément sur la physique, mais aussi sur la programmation. Je me rappellerai toujours de sa volonté d'aller au delà de ses obligations de directeur de thèse.

Je remercie David LHUILLIER et Allessandra TONAZZO d'avoir accepté la responsabilité de rapporteurs de thèse et d'avoir été membres de mon jury. Je remercie d'ailleurs l'intégralité de mon jury de thèse, à savoir : Yves Sirois, Jaime Dawson et Frédéric Yermia. Pour leur temps et leur attention.

Je remercie Benjamin QUILAIN, sans qui cette thèse n'aurait probablement jamais été finalisée. Son aide immense au fil des années et son expertise incontestée m'ont tiré du pétrin bien des fois. Je remercie également Matthieu LICCIARDI, de la promotion précédant la mienne, pour son aide et sa passion contagieuse pour la physique. Son caractère égal et mesuré apportait une stabilité certaine qu groupe neutrino, qui s'est fait sentir après son départ.

Je remercie aussi le groupe neutrinos, en particulier Margherita BUIZZA et Stephen DOLAN qui ont suivi de près mon analyse et ont su me donner de grandes lignes lorsque j'étais perdu, ou encore m'aiguiller sur des aspects techniques. La bonne humeur de Olivier DRAPIER était une bonne représentation de l'atmosphère et de la cohésion régnant au sein du groupe.

Je remercie la collaboration T2K dans son ensemble, qui m'a offert une opportunité exceptionnelle de faire de la physique passionante, sur le sujet extrêmement vivant qu'est la physique des neutrinos. De m'avoir permis de passer de nombreux mois au Japon, ce qui m'a permis de découvrir ce merveilleux pays, en plus de mon travail académique. Mes remer-

ciements vont particulièrement au groupe WAGASCI, au professeur Akihiro MINAMINO, à mes pairs Japonais : Naruhiro CHIKUMA, Kenichi KIN et bien d'autres. Pour leur efficacité au travail et pour leurs corrections de mes nombreuses fautes de Japonais et leurs initiations aux soirées à la mode Japonaise. Je remercie le groups CC0π qui ont su critiquer mon analyse au cours de son développement et apporter des commentaires extrêmement utiles de la part d'experts du domaine.

Je remercie également mes collègues de bureau : Qinhua HUANG, Émilie MAURICE et Felipe Garcia, pour leur bonne humeur qui rendait le bureau très vivant.

Je remercie tous les membres du Laboratoire Leprince-Ringuet pour leur disponibilité et leur volonté d'aider. Les membres du service administratif : Marie-Thérèse THÉODORA, la récente retraitée Brigitte MAROQUESNE, Alimata BAGAYOKO. Mais aussi tous les membres des service techniques, en particulier Michel LASTES qui a su sauver mes données lorsque mon ordianteur a pris l'eau à deux mois de la remise de mon manuscrit. Je remercie aussi Jérôme NANNI, Hamid KHALED, Oscar Ferreira et Alain BONNEMAISON pour leur aide au cours de ces années.

Je remercie enfin mes parents, qui m'ont toujours laissé libre de choisir ma voie, et m'ont soutenu que ce soit en classes préparatoires, avant les concours aux grandes écoles, ou encore pendant ma thèse. Finalement, mes amis que je ne nommerai pas ici mais qui se reconnaîtront, pour m'avoir offert tous ces moments inoubliables hors de mon temps de travail, nécessaires à un rythme de vie équilibré.

Table of contents

List of figures

List of tables

Introduction

At the beginning of the 20^{th} century, when studying the β-decay where a neutron decayed into a proton and an electron [1], physicists were confused as to why the energy of the detected electrons showed a continuous spectrum and not a unique energy peak as expected from the conservation of the energy-momentum quadrivector.

During the early 1930s, Wolfgang Pauli postulated the existence of an electrically neutral particle [2], whose mass was much smaller than the proton, which would be involved in the β-decay but not detectable.

$$n \mapsto pe^{-}\nu \tag{1}$$

Soon after Enrico Fermi formulated the theory of β-decay [3], now known as the Fermi theory, in analogy with quantum electrodynamics. In 1933, the name neutrino was adopted by all as the name of this new particle. At first everyone thought that this particle was a mathematical device that could never be detected as stated by Pauli in 1930: "I have done a terrible thing, I have postulated a particle that cannot be detected". However, the neutrino would eventually be detected. First the electronic flavour in 1956, by Frederick Reines and Clyde Cowan [4] using the intense flux of the Savannah River power plant. Then the muon neutrino would be detected in the American laboratory of Brookhaven in 1960 [5]. Finally the tau neutrino would be detected in the American complex Fermilab, by the DONUT experiment [6].

During the 20^{th} century, while the Standard Model of particle physics was progressively standardized, the neutrino continued to be shrouded in mystery. It is to this day unknown whether it is a Dirac or a Majorana particle (*i.e.* whether it is its own antiparticle or if the conjugation operator transform the neutrino field into a different field). This rather strange hypothesis was first proposed by Ettore Majorana in 1937 [7]. It was also unknown for a long time whether neutrinos had a mass. The only thing certain was the existence of three flavour states, the states of the electroweak interaction, at the low energy scales at which we are able to perform experiments.

The concept of neutrino oscillation was first proposed in 1957 by Bruno Pontecorvo [8] in analogy with $K^0 \rightleftarrows \bar{K}^0$. But the only possible explanation was $\nu \rightleftarrows \bar{\nu}$ for Majorana neutrinos. A more realistic case of oscillations was then proposed in 1967 by the Japanese physicists Jiro Maki, Masami Nakagawa and Shoichi Sakata were ν_e and ν_μ are mixed states of two mass eigenstates [9]. They developed the mathematical formalism of the oscillation phenomenon and introduced the PMNS matrix which coefficients cannot be predicted but have to be measured by various experiments.

But before that, the solar neutrino deficit had already corroborated this theory: the Standard Solar Model prediction was overestimating the ν_e flux measured by the Homestake experiment [10]. However, it was not yet a proof since the deficit was compatible with the oscillation model but not necessarily caused by it.

It is only in 1998 that the Super-Kamiokande experiment would show, in a model-independent way, the oscillation of atmospheric neutrinos [11]. Super-Kamiokande showed that the ν_μ rate on Earth was dependent of the zenith angle that is to say dependent on the distance crossed by the neutrinos through the Earth. The oscillation mechanism was confirmed in 2002 by the SNO experiment [12] using solar neutrinos. Both works were awarded the Nobel Prize in Physics in 2015 "for the discovery of neutrino oscillations, which shows that neutrinos have mass".

By 2010, most of the parameters of the PMNS matrix had been measured. Two remaining parameters were the mixing angle θ_{13} and the CP violation phase δ_{CP}. In order to measure those parameters, two kinds of experiments where carried by: reactor $\bar{\nu}_e$ disappearance to measure θ_{13} and accelerator $\nu_e/\bar{\nu}_e$ appearance to measure both θ_{13} and δ_{CP} in a degenerated way. In 2012, Daya Bay [13], Double Chooz [14] and RENO [15] experiments provided the 1$^{\mathrm{st}}$ evidence of $\bar{\nu}_e$ disappearance and measured the smallest mixing angle θ_{13}. T2K evidence of ν_e appearance happened in 2013 [16]. By using reactor experiment results, T2K is nowadays able to shed light on the value of the CP violation phase but the precision is limited by the systematics.

As all modern accelerator-based oscillation experiments, T2K measurements depend on a set of detectors near the beam production site to be able to predict the neutrino flux at the far detector, namely Super-Kamiokande. Neutrino interaction model is used to extrapolate the near detector spectra to the (oscillated) far detector spectra in a few significant ways. First the T2K off-axis near detector angular acceptance is much more limited than the far detector. Second, the near detector event rate also includes significant interactions on materials other than the far detector (water) target. Finally, the interaction model is tuned at the near detector to predict the far detector energy spectra and this parametrization can be incomplete.

The WAGASCI (WAter Grid And SCIntillator) experiment has for goal to improve the knowledge on the neutrino cross-sections through a measurement of those cross-section on water, on plastic as well as their ratio. The measurement will be done with a very large acceptance thanks to an innovative grid structure as well as the use of Side Muon Range Detectors (side-MRDs). The detectors include both water and plastic targets, which allows to measure the ratio of the two cross-sections with the same neutrino flux. The flux being the main source of systematics errors, the precision of the measurement will be greatly improved in the ratio measurement since most of the systematics will cancel out.

In this thesis we will first present the theoretical framework of neutrino oscillation and neutrino interactions with matter (Chapter 1). In Chapter 2 we will discuss both T2K and WAGASCI experimental setups and highlight the intermediate setup that has been used for our measurement. We will then describe our Monte-Carlo simulation and CC0π event selection in Chapter 3. Especially we will present the particle identification algorithm used in this selection. We will explain the method we chose to extract the cross-section (the Bayesian unfolding) in Chapter 4 and the determination of a convergence criterion based on both the Monte-Carlo and the data (Chapter 6). In between we will carefully describe in Chapter 5 both statistical and systematic errors and how we evaluated them as well as their impact on the cross-section measurement. Finally, Chapter 7 will present our experimental results on the measurement of σ_{H2O}, σ_{CH} as well as their ratio.

Because the configuration used in this thesis is not the final one, we cannot yet work with

high-angle events. Side-MRDs were not yet installed at the time when the data were taken. Furthermore, the muon detector used could not stop high-momentum muons because of a limited depth. However, our intermediate setup will be enough to conduct a comprehensive analysis with sufficient statistics.

Chapter 1

The neutrinos in the Standard Model and beyond

In this chapter we will describe the neutrinos and their description in the Standard Model. We will also see how we can explain that they have a mass, as proved by the oscillation phenomenon, while they should not have one in the theory. We will also go over an explanation of why the neutrino masses are so small compared to the other fermions.

1.1 The Standard Model

In modern physics, particle interactions are described by a quantum field theory known as the Standard Model. Product of decades of research, theories and experiments, the Standard Model is a parametric renormalizable gauge theory based on the symmetry group $SU(3)_C \times SU(2)_L \times U(1)_Y$ that needs experiments to measure the different parameters describing three of the four fundamental interactions:

- The electromagnetic interaction.
- The strong interaction.
- The weak interaction.

It also classifies all the known elementary particles. The finalized formulation was given in the 1970s after most of the predicted particles were experimentally discovered. However a few of them would need more years to be detected, for instance the Higgs boson who was only discovered in 2012. The popularity of the theory is based on its consistency in the description of the different phenomena as well as its strong predictive power. The existence of the three families of quarks were all measured by experimental results. Furthermore, the structure of the families was validated shortly after a particle in a new generation was discovered. Still quite a few phenomena are unable to be explained by the theory such as:

- The gravitational force. The theory collapses at the Planck scale when trying to incorporate general relativity.
- Dark matter. There is no candidate among the elementary particles for matter only sensitive to gravity.
- Matter-antimatter asymmetry.
- The neutrinos are predicted to have no mass and therefore should not oscillate. However it has been experimentally proved that they do.

A lot of theories extended from the Standard Model tried to fill these blanks but so far the work is either incomplete or the theory has been discarded by experiment:

- The string theories to merge the Standard Model and General Relativity: Too many different parameters and no way to decide on the right one at the moment.
- Supersymmetry could provide candidates for dark matter but the latest runs at LHC failed to detect the supermassive particles predicted by the theory.

1.1.1 The particles of the Standard Model: bosons and fermions

The Standard Model describes two types of particles:

- Fermions: the elementary bricks that are used to build matter.
- Bosons: the vectors that carry the three fundamental interactions.

Whether a particle is a fermion or a boson can be decided by the way they respond to the Pauli exclusion principle. Two identical fermions within a quantum system cannot be in the same quantum state, meaning they cannot have the exact same set of quantum numbers. Conversely, several identical bosons can occupy the same quantum state and actually tend to do so statistically speaking: bosons are gregarious particles.

Fermions have half-integer spins while bosons have integer spins. The breakdown of all the known elementary matter particles can be found in Table 1.1. The breakdown of all the bosons is detailed in Table 1.2.

Fermions are split in three families, or generations, that are identical between one another, except for their masses that are at different scales.

- The first family regroups the quarks up (u) and down (d), the leptons electron (e) and electron neutrino (ν_e).
- The second family regroups the quarks charm (c) and strange (s), the leptons muon (μ) and muon neutrino (ν_μ).
- The third family regroups the quarks top (t) and bottom (b), the leptons tau (τ) and tau neutrino (ν_τ).

Furthermore if the matter fermions were presented in Table 1.1, there are also an anti-matter partners for every fermion.

Particle	Family			Strong interaction	Hig gs coupling	Electric charge	Electromagnetic interaction	Weak interaction
	1	2	3					
Quarks	u d	c s	t b	yes	yes	$2/3$ $-1/3$	yes	yes
Leptons	e ν_e	μ ν_μ	τ ν_τ	no	yes no	0 0	yes no	yes

Table 1.1 – The fermions of the Standard Model.

The particles are all described by fields of nature depending on the spin of the particle:

- Scalar field for the Higgs field (spin 0).

Role	Boson	Spin	Strong interaction	Electromagnetic interaction	Weak interaction
Strong interaction vector	8 gluons g	1	yes	no	no
Electromagnetic interaction vector	Photon γ	1	no	yes	no
Weak interaction vector	W^+ W^- Z^0	1	no	yes yes no	yes
Mass generation scalar field	Higgs boson H^0	0	no	no	no

Table 1.2 – The bosons of the Standard Model.

- Spinor fields for the fermion fields (spin 1/2).
- Vector fields for the gauge fields (spin 1).

One of the big unknowns of the Standard Model is the nature of the neutrinos. Since only the left-handed component (eigenstate for the chirality operator) of the neutrino spinor field is coupled to a bosonic field, we do not know whether or not the conjugation operator conserves the neutrino field and only transform the left-handed component into the right-handed one or if there is actually a right-handed component different from the left-handed component, like all the other fermions in the Standard Model, that would be coupled to no gauge field.

In the former case the neutrinos fields would be Majorana spinors while in the latter case they would be Dirac spinor. We often choose to represent neutrinos with Dirac spinors because the mass generation is easier this way, but we will see later on alternative choices and the perks they present.

Every field can be written as

$$\phi(x) = \int \frac{d^3\overrightarrow{p}}{(2\pi)^3 2\sqrt{\overrightarrow{p}^2 + m^2}} [u_p e^{-ip.x} + v_p^* e^{ip.x}] \tag{1.1}$$

where $p.x = p_\mu x^\mu = E.t - \overrightarrow{p}.\overrightarrow{x}$ and p is the quadri-momentum and x a position quadri-vector in the Minkowski metric.

u_p and v_p are the solution at the momentum p of the Equation the field satisfies. Dirac fermions satisfy the Dirac equation, Majorana fermions satisfy the Majorana equation, scalars and gauge bosons satisfy the Klein-Gordon Equation as scalar (spin 0) or as vectors (spin 1).

u_p and u_p^* are the annihilation and creation operators for a fermion of momentum p described by the field. v_p and v_p^* are the annihilation and creation operators for a antifermion of momentum p described by the field.

1.1.2 The Lagrangian and the gauge symmetry

The Standard Model is a theory described by a Lagrangian. This Lagrangian originally derived from the Hamiltonian describing the propagation of a particle has been completed by different gauge theories and ended up describing the interactions between the different

fermionic and bosonic fields to provide the theory we know today.

A gauge theory stems from the belief that if a system preserves a symmetry, then the Lagrangian describing said theory must be left invariant by any transformation from the gauge symmetry group. We will go over the different gauge symmetries involved in the Standard Model and in the way they shaped the Lagrangian into the canonical form we know. But first let's take a look at what the free Lagrangian, without any regard for symmetries, would look like.

For a field theory like the Standard Model, we actually consider the Lagrangian density $\mathcal{L}$ such as the Lagrangian L is

$$L = \int \mathcal{L} d^4x \tag{1.2}$$

For each one of the Dirac fermion f, their contribution to the free Lagrangian is

$$\mathcal{L}_{D,f} = \overline{\psi_f}(i\partial\!\!\!/ - m_f)\psi_f \tag{1.3}$$

where $\partial\!\!\!/ = \partial_\mu \gamma^\mu$ and γ^μ are the Dirac matrices

$$\gamma^0 = \begin{pmatrix} \mathbf{1} & \mathbf{0} \\ \mathbf{0} & \mathbf{-1} \end{pmatrix} , \gamma^k = \begin{pmatrix} \mathbf{0} & \sigma^k \\ -\sigma_k & \mathbf{0} \end{pmatrix} \tag{1.4}$$

where $\mathbf{0}$ and $\mathbf{1}$ are the 2×2 zero and unity matrices and the Pauli matrices are

$$\sigma_1 = \begin{pmatrix} 0 & 1 \\ 1 & 0 \end{pmatrix} , \sigma_2 = \begin{pmatrix} 0 & -i \\ i & 0 \end{pmatrix} , \sigma_3 = \begin{pmatrix} 1 & 0 \\ 0 & -1 \end{pmatrix}$$

and m_f is the mass of the particle f. The free Lagrangian $\mathcal{L}_D$ describing the free propagation of fermions is the sum of all the contribution from each one of the fermions.

The QED component of the Lagrangian

The electromagnetic field is described by the quadrivector potential A^μ. We can define the electromagnetic tensor as

$$F^{\mu\nu} = \partial^\mu A^\nu - \partial^\nu A^\mu \tag{1.5}$$

The free Lagrangian describing the propagation of photons is

$$\mathcal{L}_\gamma = -\frac{1}{4} F_{\mu\nu} F^{\mu\nu} \tag{1.6}$$

When choosing the quadrivector field A, we actually have a degree of liberty in the choice. Meaning that we can choose an arbitrary scalar field χ (we call χ a gauge) and take $A^\mu + \partial^\mu \chi$ instead of A^μ and we will obtain the same electromagnetic tensor $F^{\mu\nu}$.
Hence, $\mathcal{L}_\gamma$ is preserved by the gauge symmetry group of scalar functions.

We want a Lagrangian describing the propagation of fermions and photons and who is als left invariant by this gauge symmetry. We then try to infer said Lagrangian from the $\mathcal{L}_D + \mathcal{L}_\gamma$.

We saw earlier that transforming the gauge of the electromagnetic potential $A^\mu \mapsto A^\mu + \partial^\mu \chi$ where $x \mapsto \chi(x)$ left $\mathcal{L}_\gamma$ unchanged.
Each fermionic field is affected by this gauge transformation as

$$\psi \mapsto e^{-iq\chi}\psi \tag{1.7}$$

This means that the charge-current associated to the particle f $j^\mu(f) = \overline{\psi}_f \gamma^\mu Q \psi_f$ is also left invariant by this gauge transformation (Q is the charge operator whose value is the electrical charge of the field).
The gauge transformation transforms the free Lagrangian as

$$\mathcal{L}_D + \mathcal{L}_\gamma \mapsto \mathcal{L}_D + \mathcal{L}_\gamma + e \sum_f j^\mu(f) \partial_\mu \chi \tag{1.8}$$

In order to have an invariant Lagrangian, we define the Quantum ElectroDynamic (QED) Lagrangian by adding a coupling between the fermionic fields and the gauge fields

$$\mathcal{L}_{QED} = \mathcal{L}_D + \mathcal{L}_\gamma - \underbrace{e \sum_f j^\mu(f) A_\mu}_{\text{coupling fermions/photon}} \tag{1.9}$$

left invariant by gauge transformation.

Additionally, this new invariant Lagrangian makes appear a coupling between the fermionic fields for the particle f and the bosonic field for the photons:

$$- e \overline{\psi}_f \gamma^\mu Q \psi_f A_\mu \tag{1.10}$$

This coupling allows us to compute the amplitude of an interaction between fermions, antifermions and photons (Figure 1.1)

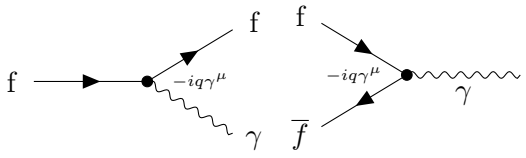

Figure 1.1 – Interaction between charged fermions and photons. Scattering (left) and anihilation of a fermion/antifermion pair (right)

We proceed in the same way for all of the symmetries in order to obtain a Lagrangian invariant by all the gauge transformation and therefore derive the couplings between all the different fields.

Extension to the electroweak interaction component of the Lagrangian

The weak interaction is an interaction that only ever involves the left-handed component of matter fields. We have a set of doublets and a set of singlets summarized in Table 1.3.

	doublets	singlets
leptons	$\begin{pmatrix}\nu_e \\ e\end{pmatrix}_L, \begin{pmatrix}\nu_\mu \\ \mu\end{pmatrix}_L, \begin{pmatrix}\nu_\tau \\ \tau\end{pmatrix}_L$	e_R , μ_R , τ_R , ν_{eR} , $\nu_{\mu R}$, $\nu_{\tau R}$
quarks	$\begin{pmatrix}u \\ d'\end{pmatrix}_L, \begin{pmatrix}c \\ s'\end{pmatrix}_L, \begin{pmatrix}t \\ b'\end{pmatrix}_L$	u_R , c_R , t_R , d'_R , s'_R , b'_R

Table 1.3 – Doublets of left-handed particles and singlets of right-handed matter fields, eigenstates of the weak interaction

We know that the chirality projectors P_L (left-handed) and P_R (right-handed) have the relation $P_L P_R = 0$ and that all matter field ψ can be decomposed as $\psi = P_L\psi + P_R\psi =$

$\psi_L + \psi_R$.
This means that the free Lagrangian for the matter field can be written as:

$$\begin{aligned}\sum_{i=1}^{3}\Bigg[& \overline{\begin{pmatrix}\nu_{e^i}\\ e^i\end{pmatrix}_L} i\partial\!\!\!/ \begin{pmatrix}\nu_{e^i}\\ e^i\end{pmatrix}_L + \overline{\begin{pmatrix}u^i\\ d'^i\end{pmatrix}_L} i\partial\!\!\!/ \begin{pmatrix}u^i\\ d'^i\end{pmatrix}_L \\ & + \overline{e^i_R} i\partial\!\!\!/ e^i_R + \overline{\nu_{e^i R}} i\partial\!\!\!/ \nu_{e^i R} + \overline{u^i_R} i\partial\!\!\!/ u^i_R + \overline{d'^i_R} i\partial\!\!\!/ d'^i_R \\ & + \text{mass terms}\Bigg]\end{aligned} \tag{1.11}$$

where

$$e^{i=1,2,3} = e, \mu, \tau \text{ and } u^{i=1,2,3} = u, c, t \text{ and } d'^{i=1,2,3} = d', s', b' \tag{1.12}$$

In the future, we will note the weak isodoublets and weak isosinglets

$$L = \begin{pmatrix}\psi_L\\ \psi'_L\end{pmatrix} \text{ , } \psi_R \text{ , } \psi'_R \text{ with: } \begin{pmatrix}\psi\\ \psi'\end{pmatrix} = \begin{pmatrix}\nu_{e^i}\\ e^i\end{pmatrix} \ i = 1,2,3 \text{ and } \begin{pmatrix}\psi\\ \psi'\end{pmatrix} = \begin{pmatrix}u^i\\ d'^i\end{pmatrix} \ i = 1,2,3 \tag{1.13}$$

So the Lagrangian becomes

$$\mathcal{L} = \sum_f \left[\overline{L} i\partial\!\!\!/ L + \overline{\psi_R} i\partial\!\!\!/ \psi_R + \overline{\psi'_R} i\partial\!\!\!/ \psi'_R + \text{mass terms}\right] \tag{1.14}$$

The gauge transformation for the electroweak gauge group is $\mathrm{SU}(2)_L \times \mathrm{U}(1)_Y$. There are the three generators of $\mathrm{SU}(2)_L$ defined with the Pauli matrices and the generator of $\mathrm{U}(1)_Y$

$$T_i = \frac{1}{2}\sigma_i \text{ and } Y \text{ with: } \sigma_1 = \begin{pmatrix}0 & 1\\ 1 & 0\end{pmatrix} \text{ , } \sigma_2 = \begin{pmatrix}0 & -i\\ i & 0\end{pmatrix} \text{ , } \sigma_3 = \begin{pmatrix}1 & 0\\ 0 & -1\end{pmatrix} \tag{1.15}$$

As well as four fields associated to each generator: W^a_μ associated to T_a and B_μ associated to Y.

The electromagnetic field is a linear combination of these four fields:

$$A_\mu = \cos(\theta_W) B_\mu + \sin(\theta_W) W^3_\mu \tag{1.16}$$

where θ_W is the Weinberg angle.

A gauge transformation transforms:

- the weak bosonic fields as $W^a_\mu \mapsto W^a_\mu + \partial_\mu \alpha^a(x) + g_w \alpha^b \epsilon_{abc} W^c_\mu$ with g_w the coupling constant for the weak interaction and ϵ_{abc} the antisymetric tensor.
- the hypercharge bosonic field as $B_\mu \mapsto B_\mu + \partial_\mu \beta(x)$
- the matter fields weak isodoublets as $L \mapsto e^{-i\overrightarrow{\alpha}(x).\frac{\overrightarrow{\sigma}}{2} - i\beta(x)\frac{Y}{2}} L$
- the matter fields weak isosinglets as $\psi_R \mapsto e^{-i\beta(x)\frac{Y}{2}} \psi_R$

Just as we did with the QED Lagrangian analysis, we can make the free Lagrangian **without the mass terms** invariant under the electroweak interaction

$$\mathcal{L}_{EW} - \text{ mass terms} = \sum_f \left[\overline{L} i\not{D} L + \overline{\psi_R} i\not{D} \psi_R + \overline{\psi'_R} i\not{D} \psi'_R\right] \tag{1.17}$$

where

$$\begin{aligned} \text{For weak isodoublets: } D_\mu &= \partial_\mu + ig_w \sum_{a=1}^{3} \frac{\sigma_a}{2} W_\mu^a + ig\frac{Y}{2} B_\mu \\ \text{For weak isosinglets: } D_\mu &= \partial_\mu + ig\frac{Y}{2} B_\mu \end{aligned} \tag{1.18}$$

with g_w and g the coupling constants for the weak interaction and the hypercharge interaction. However, the mass terms are not invariant by the electroweak gauge transformations. We will need another mechanism for the particle mass generation: the Higgs mechanism. this mechanism will be detailed in Section 1.1.3

The four bosons of the weak interactions are

- $W_\mu^\pm = \frac{1}{\sqrt{2}} \left(W_\mu^1 - \mp i W_\mu^2 \right)$
- $\begin{pmatrix} A_\mu \\ Z_\mu \end{pmatrix} = \begin{pmatrix} \cos(\theta_W) & \sin(\theta_W) \\ -\sin(\theta_W) & \cos(\theta_W) \end{pmatrix} \begin{pmatrix} B_\mu \\ W_\mu^3 \end{pmatrix}$

The weak currents respectively coupled to these bosons are

- $-\frac{g_w}{\sqrt{2}} W_\mu^+ j_{\mathrm{CC}_+}^\mu$ with $j_{cc+}^\mu = \overline{\psi}_L \gamma^\mu \psi'_L$
- $-\frac{g_w}{\sqrt{2}} W_\mu^- j_{\mathrm{CC}_-}^\mu$ with $j_{cc-}^\mu = \overline{\psi}'_L \gamma^\mu \psi_L$
- $-eA_\mu j_{em}^\mu$ with $j_{em}^\mu = \overline{\psi} \gamma^\mu Q \psi + \overline{\psi}' \gamma^\mu Q \psi'$
- $-\frac{g_w}{\cos\theta_W} Z_\mu j_{\mathrm{NC}}^\mu$ with $j_{\mathrm{NC}}^\mu = \frac{1}{2} \left(\overline{\psi}_L \gamma^\mu \psi_L - \overline{\psi}'_L \gamma^\mu \psi'_L \right) - \sin^2 \theta_W j_{em}^\mu$

So the weak interaction bosons ($W^\pm$ and Z bosons) are coupled to the weak isodoublets while the electromagnetic boson (photon γ) are coupled to the charged fermionic fields (Figure 1.2 and Figure 1.3)

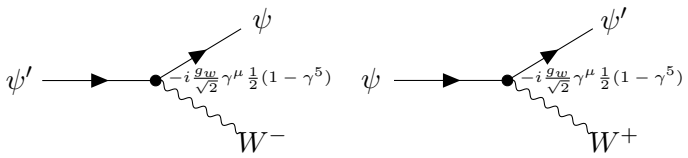

Figure 1.2 – Interaction between fermions and W bosons. W^- (left) and W^+ (right)

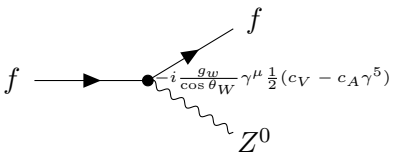

Figure 1.3 – Interaction between fermions and Z bosons. c_V and c_A are coefficients who depends on the fermion involved in the interaction. They are respectively the vector and axial part of the current who express the chirality of the electroweak interaction.

The strong interaction

We proceed just as for the electroweak interaction. The gauge group for the strong interaction is $SU(3)_C$ which possesses 8 generators

$T_a = \frac{\lambda_a}{2}$ with:

$$\lambda_1 = \begin{pmatrix} 0 & 1 & 0 \\ 1 & 0 & 0 \\ 0 & 0 & 0 \end{pmatrix} \quad \lambda_2 = \begin{pmatrix} 0 & -i & 0 \\ i & 0 & 0 \\ 0 & 0 & 0 \end{pmatrix} \quad \lambda_3 = \begin{pmatrix} 1 & 0 & 0 \\ 0 & -1 & 0 \\ 0 & 0 & 0 \end{pmatrix} \quad \lambda_4 = \begin{pmatrix} 0 & 0 & 1 \\ 0 & 0 & 0 \\ 1 & 0 & 0 \end{pmatrix}$$
$$\lambda_5 = \begin{pmatrix} 0 & 0 & -i \\ 0 & 0 & 0 \\ i & 0 & 0 \end{pmatrix} \quad \lambda_6 = \begin{pmatrix} 0 & 0 & 0 \\ 0 & 0 & 1 \\ 0 & 1 & 0 \end{pmatrix} \quad \lambda_7 = \begin{pmatrix} 0 & 0 & 0 \\ 0 & 0 & -i \\ 0 & i & 0 \end{pmatrix} \quad \lambda_8 = \begin{pmatrix} \frac{1}{\sqrt{3}} & 0 & 0 \\ 0 & \frac{1}{\sqrt{3}} & 0 \\ 0 & 0 & \frac{-2}{\sqrt{3}} \end{pmatrix} \tag{1.19}$$

where λ_a are the Gell-Mann matrices.

This sets the existence of 8 gluon fields G^a_μ, a=1,...,8

So for each of the quarks, we have three colours for this quark gathered in a strong isotriplet that will be influenced by the strong gauge transformation

$$q_f = \begin{pmatrix} u^i_1 \\ u^i_2 \\ u^i_3 \end{pmatrix} \text{ or } q_f = \begin{pmatrix} d^i_1 \\ d^i_2 \\ d^i_3 \end{pmatrix} \text{ i=1,2,3} \tag{1.20}$$

And the covariant derivative for the quarks of the three generations in this representation is modified

$$D_\mu = \partial_\mu + ig\frac{Y}{2}B_\mu + ig_s\sum_{a=1}^{8}\frac{\lambda_a}{2}G^a_\mu \tag{1.21}$$

So the Lagrangian for the electroweak and strong interactions is

$$\begin{aligned} \mathcal{L} = & \sum_{f=u,d,c,s,t,b}\left[\overline{q_f}(i\partial\!\!\!/ - m)q_f\right] \\ & -\frac{1}{4}\sum_{a=1}^{8}G^a_{\mu\nu}G^{\mu\nu}_a \\ & -g_s\sum_{f=u,d,c,s,t,b}\left[\sum_{a=1}^{8}\overline{q_f}\gamma^\mu\frac{\lambda_a}{2}q_fG^a_\mu\right] \\ & +\sum_f\left[\overline{L}i\partial\!\!\!/L + \overline{\psi_R}i\partial\!\!\!/\psi_R + \overline{\psi'_R}i\partial\!\!\!/\psi'_R + \text{mass terms}\right] \\ & -\frac{1}{4}\sum_{a=1}^{3}F^a_{\mu\nu}F^{\mu\nu}_a - \frac{1}{4}B_{\mu\nu}B^{\mu\nu} \\ & -\sum_f\left[g_w\sum_{a=1}^{3}\overline{L}\gamma^\mu\frac{\sigma_a}{2}LW^a_\mu + g\overline{L}\gamma^\mu\frac{Y}{2}LB_\mu + g\overline{\psi_{fR}}\gamma^\mu\frac{Y}{2}\psi_{fR}B_\mu + g\overline{\psi'_{fR}}\gamma^\mu\frac{Y}{2}\psi'_{fR}B_\mu\right] \end{aligned} \tag{1.22}$$

where

- $G^a_{\mu\nu} = \partial_\mu G^a_\nu - \partial_\nu G^a_\mu - g_s f_{abc}G^b_\mu G^c_\nu$
- $F^a_{\mu\nu} = \partial_\mu F^a_\nu$

- $B_{\mu\nu} = \partial_\mu B_\nu - \partial_\nu B_\mu - \partial_\nu F^a_\mu - g_w \epsilon_{abc} W^b_\mu W^c_\nu$

This Lagrangian can be decomposed in several parts which each have a physical meaning and describe a certain part of the theory. The breakdown is as follows:

- The first line is the free Lagrangian for the quark fields in the QCD representation.
- The second line is the part of the strong interaction Lagrangian describing the free propagation of the gluons in the QCD representation.
- The third line is the part of the strong interaction Lagrangian describing the interaction between gluons and quarks in the QCD representation.
- The fourth line is the free Lagrangian for the fermionic fields in the EW representation.
- The fifth line is the part of the electroweak interaction Lagrangian describing the free propagation of the electroweak bosons in the EW representation.
- The sixth line is the part of the electroweak interaction Lagrangian describing the interaction between electroweak bosons and fermionic fields in the EW representation.

From the second line of the Lagrangian we can deduce the amplitude of the interactions between quarks and gluons (Figure 1.4)

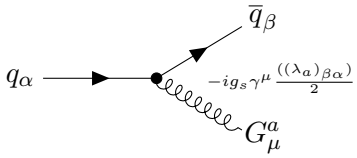

Figure 1.4 – Interaction between fermions and Z bosons

As stated earlier, removing the mass terms from the free Lagrangian makes $\mathcal{L}$ invariant by strong and electroweak gauge transformation. The problem comes from the weak interaction. Only the left-handed fields are transformed by gauge transformation while the right-handed fields are left untouched. At the same time the mass terms couple right-handed and left-handed fields: $m\overline{\psi}\psi = m(\overline{\psi_R}\psi_L + \overline{\psi_L}\psi_R)$

The fermions mass generation must be described by a gauge-covariant mechanism that will ensure the invariance of the total Lagrangian $\mathcal{L}$.

1.1.3 Generation of the mass of the particles

In the Standard Model, the Dirac fermionic fields would have their left-handed and right-handed components coupled by a trivial mass term $m\bar{\psi}\psi = m(\bar{\psi}_L\psi_R + \bar{\psi}_R\psi_L)$. This term breaks is not invariant under the electroweak gauge symmetry $\mathrm{SU}(2)_L$.
In order to cirumvent this problem, we use the Higgs mechanism which generates the masses of the W and Z bosons as well as the fermions'. We will describe the process in this section.

The Higgs field

The generation is obtained by coupling the fields to a scalar field electroweak isodoublet called the Higgs field:

$$\phi = \begin{pmatrix} \phi^+ \\ \phi^0 \end{pmatrix} \tag{1.23}$$

This doublet has an isospin $I = \frac{1}{2}$ and an hypercharge $Y = 1$. ϕ^+ has a charge $q = 1$ and a third component $I_3 = \frac{1}{2}$ while ϕ^0 has a charge $q = 0$ and a third component $I_3 = -\frac{1}{2}$ This new field adds an additional term to the Lagrangian

$$\mathcal{L}^{EW}_{Higgs} = (D_\mu \phi)^\dagger D^\mu \phi - (\mu^2 \phi^\dagger \phi + \lambda(\phi^\dagger \phi)^2) \tag{1.24}$$

with: $\mu^2 < 0$, $\lambda > 0$, $D_\mu = \partial_\mu + i g_w \frac{\sigma_i}{2} W^i_\mu + i g \frac{Y}{2} B_\mu$

Trying to find a minimum to the Higgs potential $V(\phi) = \mu^2 \phi^\dagger \phi + \lambda(\phi^\dagger \phi)^2$, we find that the minimum is attained for $|\phi| = \sqrt{\frac{-\mu^2}{2\lambda}}$ Since the vacuum is a potential minimum and that the fields are perturbations of the vacuum, we want a field centered around a minimum of the potential. It means that the vacuum expected value is non zero. Taking into account the neutrality of the vacuum, we choose the Higgs doublet:

$$\phi = \begin{pmatrix} 0 \\ \frac{1}{\sqrt{2}}(v + h(x)) \end{pmatrix} \tag{1.25}$$

This doublet is not invariant by $SU(2)_L \times U(1)_Y$ but is invariant by $U(1)_{em}$: this is called the electroweak symmetry breaking.
The vacuum expected value (v.e.v) of this Higgs field is non-zero

$$< 0|\phi^* \phi|0 >= \frac{v^2}{2} = \frac{-\mu^2}{2\lambda} \tag{1.26}$$

However it must be understood that the Lagrangian is still invariant under the $SU(2)_L \times U(1)_Y$ even if the Higgs field "chooses" a value that no longer respects said symmetry (Figure 1.5)

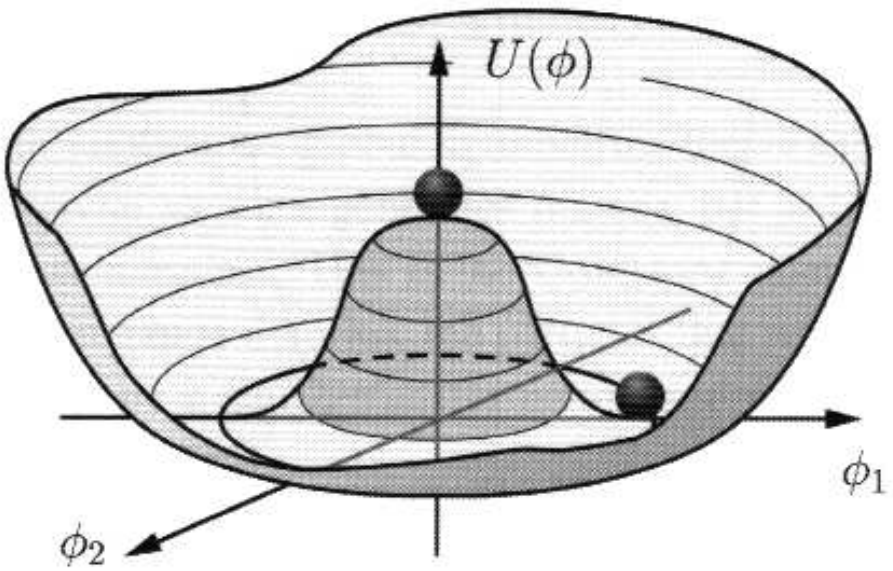

Figure 1.5 – Spontaneous symmetry breaking of the Higgs field $\phi^0 = \phi_1 + i\phi_2$

The bosons mass generation

The electroweak interaction has 4 bosonic fields: W^a_μ, a=1,2,3 and B_μ

When combining the electroweak free propagation Lagrangian with $\mathcal{L}^{EW}_{Higgs}$ we obtain the following Lagrangian for each bosonic field:

- $-\frac{1}{4}(W^+_{\mu\nu})^* W^{+\mu\nu} + \frac{1}{2}(\frac{g_w v}{2})^2 (W^+_\mu)^* W^{+\mu}$
- $-\frac{1}{4}(W^-_{\mu\nu})^* W^{-\mu\nu} + \frac{1}{2}(\frac{g_w v}{2})^2 (W^-_\mu)^* W^{-\mu}$
- $-\frac{1}{4}(Z_{\mu\nu})^* Z^{\mu\nu} + \frac{1}{2}(\frac{g_w v}{2\cos(\theta_W)})^2 (Z_\mu)^* Z^\mu$
- $-\frac{1}{4} A_{\mu\nu} A^{\mu\nu}$

This combines with the Euler-Lagrange Equation shows that the W bosons and Z boson fields propagate as massive fields of mass $m_W = \frac{g_w v}{2}$ and $m_Z = \frac{g_w v}{2\cos(\theta_W)}$.
The photon still propagates as a massless field.

The fermions mass generation

In the free propagation Lagrangian for the fermions, we replace all the mass terms

$$\sum_f [-m\overline{\psi}\psi - m'\overline{\psi'}\psi'] \mapsto \mathcal{L}^{EW}_{yuk} = \sum_f \Big[-\frac{m}{v}(\overline{L}\phi^c\psi_R + \overline{\psi_R}\phi^{c*}L) - \frac{m'}{v}(\overline{L}\phi\psi'_R + \overline{\psi'_R}\phi^* L)\Big] \quad (1.27)$$

with $\begin{pmatrix}\psi\\ \psi'\end{pmatrix} = \begin{pmatrix}u^i\\ d'^i\end{pmatrix}$ or $\begin{pmatrix}\psi\\ \psi'\end{pmatrix} = \begin{pmatrix}\nu_{e^i}\\ e^i\end{pmatrix}$ with i=1,2,3
This Lagrangian, called the Yukawa Lagrangian, is left invariant by gauge transformations. After the spontaneous symmetry breaking of the Higgs field, we recover the usual mass terms and an additional coupling to the Higgs field

$$\mathcal{L}^{EW}_{yuk} \mapsto \sum_f \Big[-m\overline{\psi}\psi - \frac{m}{v}\overline{\psi}\psi h - m'\overline{\psi'}\psi' - \frac{m'}{v}\overline{\psi'}\psi' h\Big] \quad (1.28)$$

However we didn't take into account the mixing of the fermions. If we do then the Yukawa Lagrangian for quarks OR for leptons becomes

$$\mathcal{L}^{EW}_{yuk} = \sum_{j,k=1}^{3} \Big[-\frac{m_{jk}}{v}\overline{L_j}\phi^c\psi_{kR} - \frac{m'_{jk}}{v}\overline{L_j}\phi\psi'_{kR}\Big] + h.c. \quad (1.29)$$

where the ψ_j j=1,2,3 are 3 generations of up-type fermions and ψ'_j j=1,2,3 are the 3 generations of down-type fermions (quarks type or lepton type depending on the Lagrangian)

After the spontaneous symmetry breaking, the Yukawa Lagrangian for quarks OR for leptons becomes

$$\mathcal{L}^{EW}_{yuk} \mapsto -\overline{\Psi_L} M \Psi_R (1 + \frac{h}{v}) - \overline{\Psi'_L} M' \psi'_R (1 + \frac{h}{v}) + h.c. \quad (1.30)$$

where $\Psi = \begin{pmatrix}\psi_1\\ \psi_2\\ \psi_3\end{pmatrix}$ and $\Psi' = \begin{pmatrix}\psi'_1\\ \psi'_2\\ \psi'_3\end{pmatrix}$ and $M = \begin{pmatrix}m_{11} & m_{12} & m_{13}\\ m_{21} & m_{22} & m_{23}\\ m_{31} & m_{32} & m_{33}\end{pmatrix}$ and $M' = \begin{pmatrix}m'_{11} & m'_{12} & m'_{13}\\ m'_{21} & m'_{22} & m'_{23}\\ m'_{31} & m'_{32} & m'_{33}\end{pmatrix}$
It must be said that we assumed neutrinos where Dirac fields when generating their masses through the Yukawa coupling. for all we know.

1.1.4 The Majorana neutrinos

We assumed up to now that neutrinos are Dirac fermions in the Standard Model. However there is another option which is also completely consistent with the observations.

In the Standard Model, all fermions besides neutrinos are electrically charged. Because of this they must be different from their antiparticles since the charge conjugation flips the electrical charge.

However neutrinos are electrically neutral, so the charge conjugation doesn't change the neutrino as obviously. Furthermore the right-handed Dirac neutrinos are not coupled with the gauge bosons of the theory, which means that they only propagate and are not detectable. A Standard Model theory without them would still be able to accurately describe the exact same couplings and interactions between fermions and bosons.

The charge conjugation is the transformation

$$\psi \mapsto \psi^C \equiv \mathcal{C}\psi^* \tag{1.31}$$

where $\mathcal{C} = i\gamma^2$

While Dirac fermionic fields are different from their conjugated fields, Majorana fermionic fields are left invariant by the charge conjugation. They satisfy the following relation

$$\psi^C = \psi \tag{1.32}$$

When decomposing $\psi = \psi_L + \psi_R$, this condition implies that

$$\psi_L^C + \psi_R^C = \psi_L + \psi_R \tag{1.33}$$

but we have

$$\begin{aligned} P_R(\psi_L^C) &= \frac{1}{2}(1+\gamma^5)(i\gamma^2\left(\frac{1}{2}(1-\gamma^5)\psi\right)^*) \\ &= \frac{1}{2}(1+\gamma^5)i\gamma^2\frac{1}{2}(1-\gamma^5)\psi^* \\ &= i\gamma^2\frac{1}{2}(1-\gamma^5)\frac{1}{2}(1-\gamma^5)\psi^* \\ &= i\gamma^2 P_L P_L(\psi^*) \\ &= i\gamma^2 P_L(\psi^*) \\ &= i\gamma^2(\psi_L^*) \\ &= \psi_L^C \end{aligned} \tag{1.34}$$

so ψ_L^C is a right-handed field. Similarly ψ_R^C is a left-handed field.

But the chirality states are eigenstates of projectors so each field can be decomposed in an unique way as the sum of a left-handed and a right-handed field. Combining Equation 1.33 and Equation 1.34, we can identify the component, and we obtain

$$\psi_L^C = \psi_R \text{ as well as } \psi_R^C = \psi_L \tag{1.35}$$

The consequence is that a Majorana field can be written as

$$\psi = \psi_L + \psi_L^C \text{ and also as } \psi = \psi_R + \psi_R^C \tag{1.36}$$

While a Dirac field is of dimension 4, a Majorana field is of dimension 2 since there is a coupling between the right-handed and left-handed spinors (Equation 1.35).

While the Dirac mass term of the Lagrangian is written as $-m(\overline{\psi_L}\psi_R + \overline{\psi_R}\psi_L)$, we can define a Majorana mass term as

$$-\frac{1}{2}m(\overline{\psi_L}\psi_L^C + \overline{\psi_L^C}\psi_L) \tag{1.37}$$

We can say already that this mass term is not invariant by the electroweak gauge symmetry. Indeed, left-handed fermions are part of a weak isodoublet and a rotation of this doublet would change the value of the mass term.

Another consequence of such a mass term , in the case where neutrinos are Majorana fermions ν_M, would be the violation of the leptonic number with interaction such as Figure 1.6 made possible.

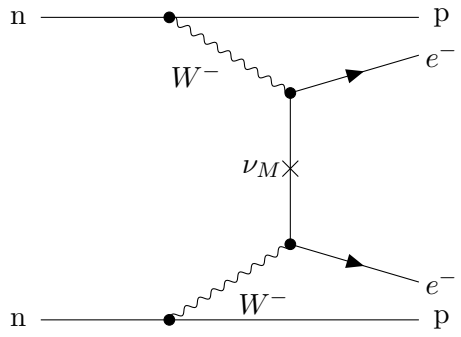

Figure 1.6 – Leptonic number violation with a Majorana neutrino

Let us now assume that there are two neutrino fields

- a neutrino sensitive to the electroweak interaction: $\nu = \nu_L + \nu_L^C$, with an hypercharge $Y = -1$ and an isospin $I_3 = \frac{1}{2}$
- a sterile neutrino $N = N_R + N_R^C$ sensitive to no interaction , with an hypercharge $Y = 0$ and an isospin $I_3 = 0$

We can write the mass term of the Lagrangian as the sum one Dirac mass term and two Majorana mass terms:

$$\begin{aligned}\mathcal{L}_m &= \mathcal{L}_m^D + \mathcal{L}_m^L + \mathcal{L}_m^R \\ &= -\tfrac{1}{2}m_D(\overline{N}\nu + \overline{\nu}N) - \tfrac{1}{2}m_L\overline{\nu}\nu - \tfrac{1}{2}m_R\overline{N}N \\ &= -m_D(\overline{N_R}\nu_L + \overline{\nu_L}N_R) - \tfrac{1}{2}m_L(\overline{\nu_L^C}\nu_L + \overline{\nu_L}\nu_L^C) - \tfrac{1}{2}m_R(\overline{N_R^C}N_R + \overline{N_R}N_R^C)\end{aligned} \tag{1.38}$$

So we have

$$\mathcal{L}_m = -\frac{1}{2}\overline{\mathbf{V}}\cdot\mathbf{M}\cdot\mathbf{V} \text{ where } \mathbf{V} \equiv \begin{pmatrix}\nu \\ N\end{pmatrix} \text{ and } \mathbf{M} \equiv \begin{pmatrix}m_L & m_D \\ m_D & m_R\end{pmatrix} \tag{1.39}$$

The Dirac mass term can be written as a Yukawa coupling with a Higgs doublet, while the Majorana mass term for the sterile neutrino has zero quantum numbers. These two terms are thus invariant under $SU(2) \times U(1)$. However the Majorana mass term associated to the active neutrino is not invariant under the symmetry and cannot be expressed as the result of a Yukawa coupling to the Higgs doublet.

The See-saw mechanism

One can easily be surprised by the difference of scale between the masses of the neutrinos which are so small compared to the other fermions of the Standard Model (Figure 1.7). We will present here a specific case which provides an elegant justification to these oddity.

We assume that $m_L, m_D \ll m_R$.

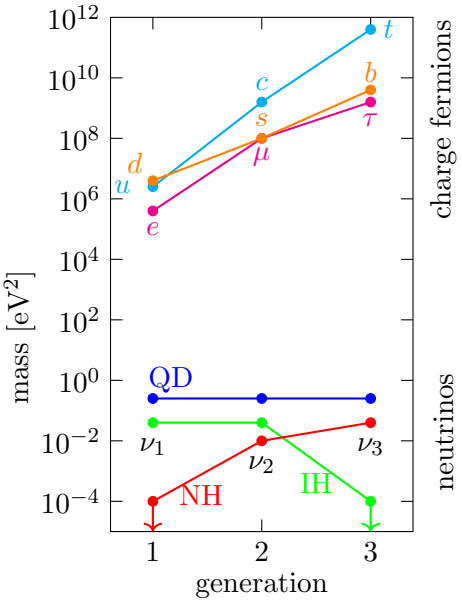

Figure 1.7 – Masses of the fermions in the Standard Model

With m_D the Yukawa coupling at the same order of magnitude as the other fermions'. m_L can even be taken as zero, which has the advantage of making the mass term invariant under $\mathrm{SU}(2)_L \times \mathrm{U}(1)_Y$. But with a concern of generality, we will keep it unspecified in this study since the results still apply.

To find the massive eigenstates and eigenvalues we need to diagonalize $\mathbf{M}$. So we want to solve the equation

$$\mathbf{M} \cdot \begin{pmatrix} x \\ y \end{pmatrix} = \lambda \begin{pmatrix} x \\ y \end{pmatrix} \text{ where } x \text{ , } y \text{ and } \lambda \text{ are unknown variables}$$

This translates as

$$\begin{cases} m_L x + m_D y &= \lambda x \\ m_D x + m_R y &= \lambda y \end{cases}$$

$$\iff \begin{cases} m_D y &= (\lambda - m_L) x \\ m_D x &= (\lambda - m_R) y \end{cases}$$

$$\iff \begin{cases} y &= \frac{\lambda - m_L}{m_D} x \\ m_D x &= (\lambda - m_R) y \end{cases}$$

$$\iff \begin{cases} y &= \frac{\lambda - m_L}{m_D} x \\ m_D x &= (\lambda - m_R) \frac{\lambda - m_L}{m_D} x \end{cases}$$

$$\iff \begin{cases} y & = \frac{\lambda - m_L}{m_D} x \\ m_D^2 & = (\lambda - m_R)(\lambda - m_L) \text{ ou } x = 0 \end{cases}$$

$$\iff \begin{cases} y = \frac{\lambda - m_L}{m_D} x \\ \lambda^2 - (m_R + m_L)\lambda + (m_L m_R - m_D^2) = 0 \text{ (eigenvector must be non-zero)} \end{cases}$$

The eigenvalues are obtained by solving the Equation on λ. The two values are

$$\lambda = \frac{m_L + m_R \pm \sqrt{(m_L + m_R)^2 + 4(m_D^2 - m_L m_R)}}{2} \tag{1.40}$$

We have $m_L + m_R \approx m_R$ and $(m_L + m_R)^2 + 4(m_D^2 - m_L m_R) \approx m_R^2 + 4(m_D^2 - m_L m_R) \approx m_R^2$

So we have

$$\sqrt{(m_L + m_R)^2 + 4(m_D^2 - m_L m_R)} \approx (m_L + m_R)(1 + \frac{2(m_D^2 - m_L m_R)}{(m_L + m_R)^2})$$

The eigenvalues are thus

$$\lambda_1 \approx \frac{m_R m_L - m_D^2}{m_R} \approx -\frac{m_D^2}{m_R} \text{ associated to the eigenstate } \widetilde{\nu}_1$$
$$\lambda_2 \approx m_R \text{ associated to the eigenstate } \widetilde{\nu}_2$$

And we have

$$\begin{pmatrix} \nu \\ N \end{pmatrix} = \mathcal{O} \begin{pmatrix} \widetilde{\nu}_1 \\ \widetilde{\nu}_2 \end{pmatrix} \text{ and } \mathcal{O}^T \mathbf{M} \mathcal{O} = \begin{pmatrix} \lambda_1 & 0 \\ 0 & \lambda_2 \end{pmatrix} \text{ with } \mathcal{O} = \begin{pmatrix} \cos(\theta_{ss}) & \sin(\theta_{ss}) \\ -\sin(\theta_{ss}) & \cos(\theta_{ss}) \end{pmatrix} \tag{1.41}$$

We define

$$\begin{pmatrix} \nu_1 \\ \nu_2 \end{pmatrix} \equiv \begin{pmatrix} i\widetilde{\nu}_1 \\ \widetilde{\nu}_2 \end{pmatrix}$$

And the result is:

$$\begin{pmatrix} \nu \\ N \end{pmatrix} = U \begin{pmatrix} \nu_1 \\ \nu_2 \end{pmatrix} \text{ and } U^T \mathbf{M} U = \begin{pmatrix} -\lambda_1 & 0 \\ 0 & \lambda_2 \end{pmatrix} \text{ with } U \equiv \begin{pmatrix} i & 0 \\ 0 & 1 \end{pmatrix} \mathcal{O} = \begin{pmatrix} -i\cos(\theta_{ss}) & \sin(\theta_{ss}) \\ i\sin(\theta_{ss}) & \cos(\theta_{ss}) \end{pmatrix} \tag{1.42}$$

However, because of the Majorana fields property $\psi^C = \psi$, we have

$$\begin{aligned} \overline{\psi} &= \overline{\psi^C} \\ &= \overline{i\gamma^2 \psi^*} \\ &= \left(i\gamma^2 \psi^*\right)^{*T} \gamma^0 \\ &= \left(i\gamma^2 \psi\right)^{T} \gamma^0 \\ &= \psi^T i(\gamma^2)^T \gamma^0 \\ &= \psi^T i\gamma^2 \gamma^0 \end{aligned}$$

So

$$\overline{\mathbf{V}} = \mathbf{V}^T i\gamma^2\gamma^0 \text{ and } \overline{\mathbf{V}'} = \mathbf{V}'^T i\gamma^2\gamma^0 \text{ where } \mathbf{V}' \equiv \begin{pmatrix}\nu_1\\ \nu_2\end{pmatrix}$$

And the mass term in the Lagrangian is

$$\begin{aligned}
\mathcal{L}_m &= -\frac{1}{2}\mathbf{V}^T i\gamma^2\gamma^0\mathbf{M}\cdot\mathbf{V} \\
&= -\frac{1}{2}\mathbf{V}'^T U^T i\gamma^2\gamma^0\mathbf{M}\cdot U\cdot\mathbf{V}' \\
&= -\frac{1}{2}\mathbf{V}'^T i\gamma^2\gamma^0 U^T\mathbf{M}\cdot U\cdot\mathbf{V}' \\
&= -\frac{1}{2}\mathbf{V}'^T i\gamma^2\gamma^0\begin{pmatrix}-\lambda_1 & 0\\ 0 & \lambda_2\end{pmatrix}\cdot\mathbf{V}' \\
&= -\frac{1}{2}\overline{\mathbf{V}'}\begin{pmatrix}-\lambda_1 & 0\\ 0 & \lambda_2\end{pmatrix}\cdot\mathbf{V}'
\end{aligned}$$

So ν_1 and ν_2 are massive neutrino fields of masses $m_1 \equiv |\lambda_1|$ and $m_2 \equiv \lambda_2$.

Hence we can go to the active/sterile neutrinos from the massive neutrinos with the relation

$$\begin{pmatrix}\nu\\ N\end{pmatrix} = \begin{pmatrix}-i\cos(\theta_{ss}) & \sin(\theta_{ss})\\ i\sin(\theta_{ss}) & \cos(\theta_{ss})\end{pmatrix}\cdot\begin{pmatrix}\nu_1\\ \nu_2\end{pmatrix} \tag{1.43}$$

where the massive neutrinos ν_1 and ν_2 have the masses $m_1 \approx \left|\frac{m_D^2}{m_R}\right|$ and $m_2 \approx m_R$. The mixing angle is

$$tan(2\theta_{ss}) \approx \frac{2m_D}{m_R} \tag{1.44}$$

This means that the active neutrino ν is mainly constituted from the light neutrino ν_1 while the sterile neutrino N is mainly constituted from the very heavy neutrino ν_2. The seesaw mechanism allows us to explain the light mass of the observable neutrinos.

1.2 The oscillation of neutrinos

1.2.1 In the vacuum

The neutrino flavour states ν_α, $\alpha = e, \mu, \tau$ are involved in the weak interaction while the mass eigenstates neutrinos ν_k, $k = 1, 2, 3$ are involved in the propagation of the neutrinos.

The PMNS matrix allows to go from one basis to the other

$$\begin{pmatrix}\nu_e\\ \nu_\mu\\ \nu_\tau\end{pmatrix} = U^\dagger_{PMNS}\begin{pmatrix}\nu_1\\ \nu_2\\ \nu_3\end{pmatrix} = \begin{pmatrix}U^*_{e1} & U^*_{e2} & U^*_{e3}\\ U^*_{\mu1} & U^*_{\mu2} & U^*_{\mu3}\\ U^*_{\tau1} & U^*_{\tau2} & U^*_{\tau3}\end{pmatrix}\begin{pmatrix}\nu_1\\ \nu_2\\ \nu_3\end{pmatrix} \tag{1.45}$$

When neutrinos are produced via the weak interaction, they are produced in one of the flavour states ν_α, $\alpha = e, \mu, \tau$. Each flavour state is a combination of massive states with the coefficients given by the PMNS matrix

So that we have

$$|\nu_\alpha\rangle = \sum_{k=1}^{3} U^*_{\alpha k}\,|\nu_k\rangle \tag{1.46}$$

We assume that the massive neutrinos propagate as plane waves. So that if a massive neutrino ν_k is created with an energy $E_k^2 = |\overrightarrow{p}|^2 + m_k^2$ at $(0, \overrightarrow{0})$ the propagation is

$$|\nu_k(t, \overrightarrow{x})\rangle = e^{-i(E_k t - \overrightarrow{p}.\overrightarrow{x})} |\nu_k\rangle \tag{1.47}$$

We assume that the neutrinos are ultra-relativistic, which means $|p|^2 c^2 \gg m^2 c^4$.
This implies that we can take the time of propagation equal to the distance between the production and detection points $t = |\overrightarrow{x}| = L$.
We also assume that all the neutrinos are produced in the same direction with the same momentum of norm p.

So the produced neutrino after propagation becomes

$$\begin{aligned}
|\nu_\alpha(t, \overrightarrow{x})\rangle &= \sum_{k=1}^{3} U_{\alpha k}^* e^{-i(E_k t - \overrightarrow{p}.\overrightarrow{x})} |\nu_k\rangle \\
&= \sum_{k=1}^{3} U_{\alpha k}^* e^{-i(E_k t - \overrightarrow{p}.\overrightarrow{x})} \sum_{\beta} U_{\beta k} |\nu_\beta\rangle \\
&= \sum_{k=1}^{3} \sum_{\beta} U_{\alpha k}^* e^{-i(E_k t - pL)} U_{\beta k} |\nu_\beta\rangle
\end{aligned}$$

Hence the probability of transition $P_{\nu_\alpha \mapsto \nu_\beta}$ is

$$\begin{aligned}
P_{\nu_\alpha \mapsto \nu_\beta}(E, L) &= \left| \langle \nu_\beta | \sum_{k=1}^{3} \sum_{\beta} U_{\alpha k} e^{-i(E_k t - pL)} U_{\beta k}^* |\nu_\beta\rangle \right|^2 \\
&= \sum_{k,j} U_{\alpha k} U_{\beta k}^* U_{\alpha j}^* U_{\beta j} e^{-i(E_k t - pL)} e^{i(E_j t - pL)}
\end{aligned}$$

We have $E_k \approx E_j = E \approx p$

$$\begin{aligned}
E_k t - pL &= (E_k - p)L \\
&= \frac{E_k^2 - p^2}{E_k + p} L \\
&= \frac{m_k^2}{E_k + p} L \\
&= \frac{m_k^2}{2E} L
\end{aligned}$$

This simplifies the oscillation formula into

$$P_{\nu_\alpha \mapsto \nu_\beta}(E, L) = \sum_{k,j} U_{\alpha k} U_{\beta k}^* U_{\alpha j}^* U_{\beta j} e^{-i \frac{\Delta m_{kj}^2}{2E} L} \text{ with } \Delta m_{kj}^2 = m_k^2 - m_j^2 \tag{1.48}$$

By defining the oscillation length as

$$L_{kj}^{osc} = \frac{4\pi E}{\Delta m_{kj}^2} \tag{1.49}$$

We can then separate the constant terms from the oscillating ones to write the probability as

$$P_{\nu_\alpha \mapsto \nu_\beta}(L) = \sum_{k} |U_{\alpha k}|^2 |U_{\beta k}|^2 + 2Re \sum_{k>j} U_{\alpha k} U_{\beta k}^* U_{\alpha j}^* U_{\beta j} \exp\left(-2\pi i \frac{L}{L_{kj}^{osc}}\right) \tag{1.50}$$

We first assumed that the neutrinos propagated as plane waves. Actually, this is inaccurate because it does not express the fact that the different massive neutrinos have different kinematics and that after a certain time, the coherence will be lost and the oscillation will disappear. A correct treatment of the problem would be to consider the beam as wave packets. It results in the formula [17]

$$\begin{aligned} P_{\nu_\alpha \mapsto \nu_\beta}(E,L) = \; & \textstyle\sum_k |U_{\alpha k}|^2 |U_{\beta k}|^2 \\ & + 2Re \textstyle\sum_{k>j} U_{\alpha k} U^*_{\beta k} U^*_{\alpha j} U_{\beta j} \exp\left(-2\pi i \frac{L}{L^{osc}_{kj}} - \left(\frac{L}{L^{coh}_{kj}}\right)^2 - 2\pi^2 \kappa \left(\frac{\sigma_x}{L^{osc}_{kj}}\right)^2 \right) \end{aligned} \tag{1.51}$$

where the coherence length is

$$L^{coh}_{kj} = \frac{4\sqrt{2\omega}E^2}{\Delta m^2_{kj}} \sigma_x$$

The different quantities are defined as follow

- $\sigma_x^2 = \sigma_{xP}^2 + \sigma_{xD}^2$ the total spatial coherence length where σ_{xP} is the production coherence length and σ_{xD} is the detection coherence length
- ω (κ) depends on the production (detection) process. The order of magnitude of both these factors is around 1

We still have the oscillation term, but now when L is large before the coherence length L^{coh}_{kj} we have a decoherence of the massive neutrinos. The reason is that the speeds of the different massive neutrinos is not the same. So after a certain distance, the wave packets are no longer superposed and we only have the constant term of the probability formula. L^{coh}_{kj} represents the scale of this decoherence process.

We also have decoherence if the location of the production and detection points is known with less precision than the oscillation length. If we have $L \ll L^{coh}_{kj}$ and $\sigma_x \ll L^{osc}_{kj}$, we can use the formula given by the plane wave formalism in the Equation 1.50.

In the Chapter 2 we will describe the T2K experiment which is a long baseline accelerator neutrinos experiment measuring the disappearance of muon neutrinos as well as the appearance of electron neutrinos in a beam of muon neutrinos. The muon neutrinos are produced inside a 100 m long decay tunnel and a muon neutrino beam with an energy spectrum peaked at 600 MeV travels 295 km until Super-Kamiokande. In this water-based Cerenkov detector, the detection of the neutrinos has a spatial error around 1 m.
Let us estimate the values for the T2K experiment

- $L^{osc}_{ij} = 2.48 \frac{E[\mathrm{MeV}]}{\Delta m^2_{ij}[\mathrm{eV}^2/\mathrm{c}^4]} \mathrm{m}$
- $L^{coh}_{ij} = 5.66 \frac{E^2[\mathrm{MeV}^2]\sigma_x[\mathrm{mm}]}{\Delta m^2_{ij}[\mathrm{eV}^2/\mathrm{c}^4]} \mathrm{km}$
- $\Delta m^2_{21} \sim 7.39 \times 10^{-5}\,\mathrm{eV}^2$ $|\Delta m^2_{32}| \sim 2.45 \times 10^{-3}\,\mathrm{eV}^2$
- $\sigma_{xP} \sim 100\,\mathrm{m}$ the length of the decay tunnel
- $\sigma_{xD} \sim 1\,\mathrm{m}$ the precision of the vertex in Super Kamiokande
- $E \sim 600\,\mathrm{MeV}$

So for the T2K experiment we have

- $L_{21}^{osc} \sim 20000\,\text{km}$
- $L_{32}^{osc} \sim 600\,\text{km}$
- $L_{21}^{coh} \sim 10^{15}\,\text{km}$
- $L_{32}^{coh} \sim 10^{14}\,\text{km}$

So $L \ll L_{kj}^{coh}$ and $\sigma_x \ll L_{ij}^{osc}$ and the two attenuation factors are negligible at the distance considered. We recover the expression from Equation 1.50

We have

$$\begin{aligned}\sum_{k,j} U_{\alpha k} U_{\beta k}^* U_{\alpha j}^* U_{\beta j} &= \sum_k U_{\alpha k} U_{\beta k}^* \times \sum_j U_{\alpha j}^* U_{\beta j} \\ &= \delta_{\alpha\beta} \times \delta_{\alpha\beta} \\ &= \delta_{\alpha\beta}\end{aligned}$$

But we also have

$$\sum_{k,j} U_{\alpha k} U_{\beta k}^* U_{\alpha j}^* U_{\beta j} = \sum_k |U_{\alpha k}|^2 |U_{\beta k}|^2 + 2Re \sum_{k>j} U_{\alpha k} U_{\beta k}^* U_{\alpha j}^* U_{\beta j}$$

So by combining the two we get

$$\sum_k |U_{\alpha k}|^2 |U_{\beta k}|^2 = \delta_{\alpha\beta} - 2Re \sum_{k>j} U_{\alpha k} U_{\beta k}^* U_{\alpha j}^* U_{\beta j}$$

We inject this relation in Equation 1.50 to obtain

$$P_{\nu_\alpha \mapsto \nu_\beta}(E, L) = \delta_{\alpha\beta} - 2Re \left[\sum_{k>j} U_{\alpha k} U_{\beta k}^* U_{\alpha j}^* U_{\beta j} (1 - \exp\left(-2\pi i \frac{L}{L_{kj}^{osc}}\right)) \right]$$

The right term can be rewritten as

$$\begin{aligned}2Re \left[\sum_{k>j} U_{\alpha k} U_{\beta k}^* U_{\alpha j}^* U_{\beta j} \exp\left(-2\pi i \frac{L}{L_{kj}^{osc}}\right)) \right] =& 2Re \sum_{k>j} U_{\alpha k} U_{\beta k}^* U_{\alpha j}^* U_{\beta j} \cos\left(-2\pi \frac{L}{L_{kj}^{osc}}\right) \\ & - 2Im \sum_{k>j} U_{\alpha k} U_{\beta k}^* U_{\alpha j}^* U_{\beta j} \sin\left(-2\pi \frac{L}{L_{kj}^{osc}}\right)\end{aligned}$$

Which gives us

$$\begin{aligned}P_{\nu_\alpha \mapsto \nu_\beta}(E, L) =& \delta_{\alpha\beta} - 2Re \sum_{k>j} U_{\alpha k} U_{\beta k}^* U_{\alpha j}^* U_{\beta j} \left(1 - \cos\left(2\pi \frac{L}{L_{kj}^{osc}}\right)\right) \\ & 2Im \sum_{k>j} U_{\alpha k} U_{\beta k}^* U_{\alpha j}^* U_{\beta j} \sin\left(2\pi \frac{L}{L_{kj}^{osc}}\right))\end{aligned}$$

In the end we can produce the formula for the oscillation of neutrinos

$$P_{\nu_\alpha \mapsto \nu_\beta}(E, L) = \delta_{\alpha\beta} - 4Re \sum_{k>j} U_{\alpha k} U_{\beta k}^* U_{\alpha j}^* U_{\beta j} \sin^2\left(\pi \frac{L}{L_{kj}^{osc}}\right) \tag{1.52}$$

$$2Im \sum_{k>j} U_{\alpha k} U_{\beta k}^* U_{\alpha j}^* U_{\beta j} \sin\left(2\pi \frac{L}{L_{kj}^{osc}}\right) \tag{1.53}$$

Thanks to the $\mathcal{CPT}$ symmetry that gives the relation $P_{\nu_\alpha \mapsto \nu_\beta} = P_{\bar{\nu}_\beta \mapsto \bar{\nu}_\alpha}$ we can infer the oscillation formula for antineutrinos

$$P_{\bar{\nu}_\alpha \mapsto \bar{\nu}_\beta}(E, L) = \delta_{\alpha\beta} - 4Re \sum_{k>j} U_{\alpha k} U^*_{\beta k} U^*_{\alpha j} U_{\beta j} \sin^2 \left(-\pi \frac{L}{L^{osc}_{kj}} \right) \tag{1.54}$$

$$- 2Im \sum_{k>j} U_{\alpha k} U^*_{\beta k} U^*_{\alpha j} U_{\beta j} \sin \left(2\pi i \frac{L}{L^{osc}_{kj}} \right) \tag{1.55}$$

Two flavours oscillation

If we assume that there is only oscillation between two flavour eigenstates and two massive eigenstates, and that the mixing matrix is real, we can make a change of parameters to simplify the formula. We will take $\theta = \theta_{12}$ and $\Delta m^2 = \Delta m^2_{21}$ to treat the solar case where the oscillations are between ν_e and ν_μ and between ν_1 and ν_2 but what follows can be applied to any pair of eigenstates.
The mixing matrix becomes

$$\mathbf{U} = \begin{pmatrix} \cos(\theta) & \sin(\theta) \\ -\sin(\theta) & \cos(\theta) \end{pmatrix} \tag{1.56}$$

The transition probability is written as

$$P_{\nu_e \mapsto \nu_\mu} = \sin^2(2\theta) \sin^2 \left(\frac{\Delta m^2 L}{4E} \right)$$

which is equivalent to

$$P_{\nu_e \mapsto \nu_\mu} = \frac{1}{2} \sin^2(2\theta) \left(1 - \cos \left(\frac{\Delta m^2 L}{2E} \right) \right)$$

The evolution of this probability is displayed by the black dotted curve in Figure 1.8

However, the energy and the crossed distance of the neutrinos detected in Super Kamiokande are only known with an uncertainty, because it is impossible to know E and L with infinite precision. Hence, $\frac{L}{E}$ is a random variable X. We need to average the probability computed earlier over $\frac{L}{E}$. We will study the case where X has a reasonable Gaussian probability density function. $\phi(x) = \frac{1}{\sigma_{\frac{L}{E}} \sqrt{2\pi}} \exp \left(-\frac{(x - \langle \frac{L}{E} \rangle)^2}{2\sigma^2_{\frac{L}{E}}} \right)$

The real probability is

$$P_{\nu_e \mapsto \nu_\mu} = \frac{1}{2} \sin^2(2\theta) \left(1 - \mathbb{E} \left[\cos \left(\frac{\Delta m^2}{2} \frac{L}{E} \right) \right] \right)$$

We consider the characteristic function of the random variable X

$$\varphi(t) \equiv \mathbb{E} \left[e^{itX} \right] = \sum e^{itx} \phi(x) dx$$

We have

$$P_{\nu_e \mapsto \nu_\mu} = \frac{1}{2} \sin^2(2\theta) \left(1 - \mathfrak{Re} \left[\varphi \left(\frac{\Delta m^2}{2} \right) \right] \right)$$

We can show that φ satisfy a differential equation

$$\begin{aligned}
\varphi'(t) &= \int i\mathrm{x}\ \mathrm{e}^{itx}\phi(x)dx \\
&= i\left\langle\frac{L}{E}\right\rangle\int \mathrm{e}^{itx}\phi(x)dx - i\sigma^2_{\frac{L}{E}}\int\left(\frac{-\left(x-\left\langle\frac{L}{E}\right\rangle\right)}{\sigma^2_{\frac{L}{E}}}\right)\mathrm{e}^{itx}\phi(x)dx \\
&= i\left\langle\frac{L}{E}\right\rangle\varphi(t) - i\sigma^2_{\frac{L}{E}}\int \mathrm{e}^{itx}\left(\frac{d}{dx}\phi\right)(x)dx \\
&= i\left\langle\frac{L}{E}\right\rangle\varphi(t) - i\sigma^2_{\frac{L}{E}}\left(\left[\mathrm{e}^{itx}\phi(x)\right]_{x=-\infty}^{x=\infty} - \int it\mathrm{e}^{itx}\phi(x)dx\right) \\
&= i\left\langle\frac{L}{E}\right\rangle\varphi(t) - i\sigma^2_{\frac{L}{E}}(-it)\int \mathrm{e}^{itx}\phi(x)dx \\
&= i\left\langle\frac{L}{E}\right\rangle\varphi(t) - \sigma^2_{\frac{L}{E}}t\varphi(t) \\
&= \left(i\left\langle\frac{L}{E}\right\rangle - \sigma^2_{\frac{L}{E}}t\right)\varphi(t)
\end{aligned}$$

Solving this differential equation gives an analytical expression for the characteristic function

$$\varphi(t) = \exp\left(i\left\langle\frac{L}{E}\right\rangle t - \frac{t^2}{2}\sigma^2_{\frac{L}{E}}\right)$$

Using this expression with the formula for the transition probability gives the averaged transition formula

$$P_{\nu_e\mapsto\nu_\mu} = \frac{1}{2}\sin^2(2\theta)\left(1-\cos\left(\frac{\Delta m^2}{2}\left\langle\frac{L}{E}\right\rangle\right)\exp\left(-\frac{1}{2}\left(\frac{\Delta m^2}{2}\sigma_{\frac{L}{E}}\right)^2\right)\right) \tag{1.57}$$

We assume that we the uncertainty $\sigma_{\frac{L}{E}}$ is proportional to $\left\langle\frac{L}{E}\right\rangle$

$$\sigma_{\frac{L}{E}} = \alpha\left\langle\frac{L}{E}\right\rangle \tag{1.58}$$

We then have

$$P_{\nu_e\mapsto\nu_\mu} = \frac{1}{2}\sin^2(2\theta)\left(1-\cos\left(\frac{\Delta m^2}{2}\left\langle\frac{L}{E}\right\rangle\right)\exp\left(-\alpha^2\frac{1}{2}\left(\frac{\Delta m^2}{2}\left\langle\frac{L}{E}\right\rangle\right)^2\right)\right) \tag{1.59}$$

This averaging of the transition probability causes an attenuation of the oscillations when L increases (Figure 1.8)

1.2.2 In matter

In the vacuum, the Hamiltonian is the same for all three massive neutrinos. However, when propagating in matter, the neutrinos are submitted to an additional potential due to the presence of electrons and nucleons.
The neutrinos interactions (Figure 1.9) and antineutrinos interactions (Figure 1.10) can be described by Feynman diagrams and the amplitudes matrices factor can be computed thanks to spinor arithmetic.

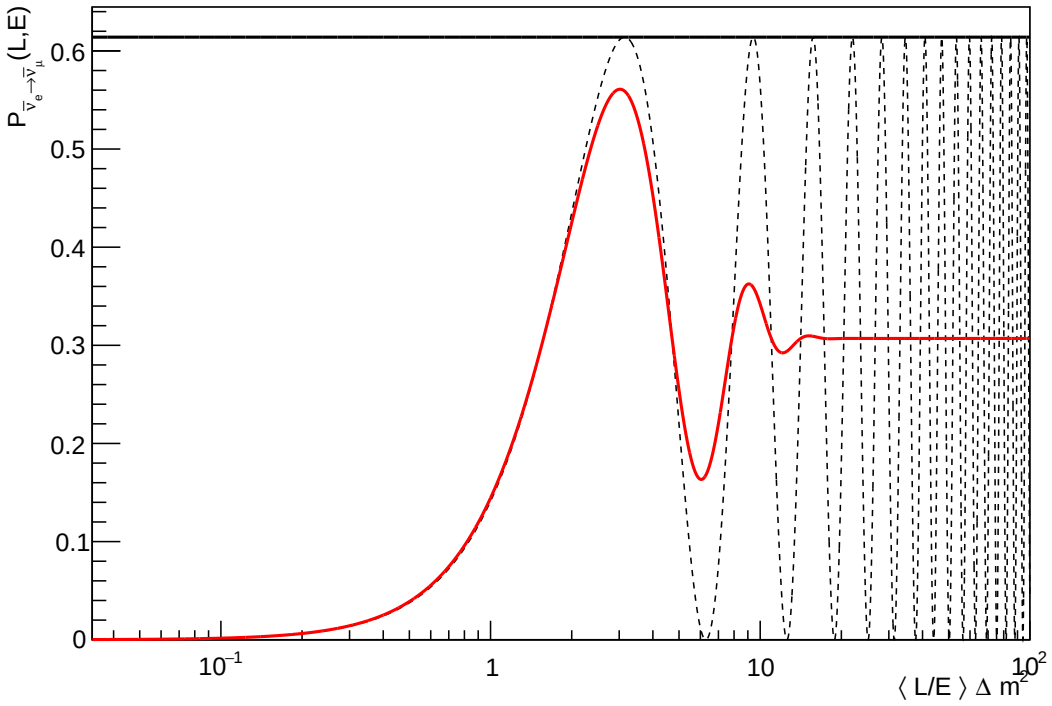

Figure 1.8 – Transition probability in the two flavours case. Dotted line represent the oscillation without attenuation while the red line represents the averaged oscillations. We took $\alpha = 0.2$ here.

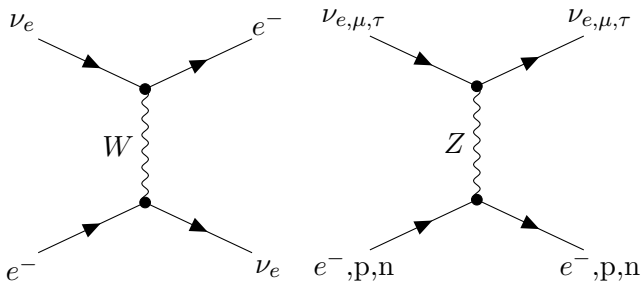

Figure 1.9 – Interaction of neutrinos with matter

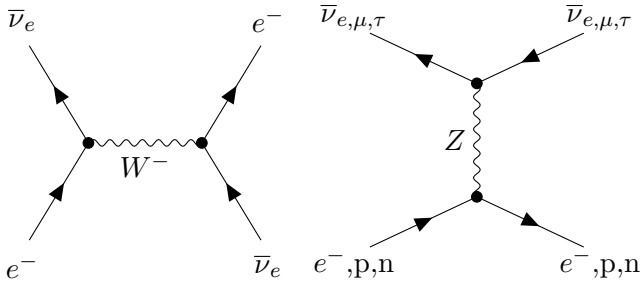

Figure 1.10 – Interaction of antineutrinos with matter

While the interactions via neutral weak current are identical for all three flavour states, resulting in a simple additional constant phase on the whole state, the charged weak current is only sensitive to electron neutrinos and antineutrinos.
The result of these computations gives the interaction Hamiltonian for the neutrinos in matter

$$\mathcal{H}_I = \epsilon \sum_\alpha \mathcal{V}_\alpha \left|\nu_\alpha\right\rangle \left\langle\nu_\alpha\right| = \epsilon \sum_\alpha (V_{CC}\delta_{\alpha e} + V_{NC}) \left|\nu_\alpha\right\rangle \left\langle\nu_\alpha\right| \tag{1.60}$$

where

$$\begin{cases} V_{CC} &= \sqrt{2} G_F N_e(x) \\ V_{NC} &= \sum\limits_{f=e,n,p} \sqrt{2} G_F c_V^f N_f(x) \\ \epsilon &= +1 \text{ for neutrinos and -1 for antineutrinos} \end{cases} \tag{1.61}$$

Hence we can consider the Schrödinger equation

$$i\frac{d}{dt}\left|\nu_\alpha(x,t)\right\rangle = (\mathcal{H}_0 + \mathcal{H}_I)\left|\nu_\alpha(x,t)\right\rangle \tag{1.62}$$

where $\mathcal{H}_0$ is the free propagation Hamiltonian used in the vacuum and computed earlier as

$$\begin{cases} \mathcal{H}_0 &= \sum\limits_\alpha \left(\sum\limits_k \sum\limits_\eta U_{\alpha k} E_k U_{\eta k}^* \left|\nu_\eta(x,t)\right\rangle \right) \left\langle\nu_\alpha(x,t)\right| \\ \mathcal{H}_I &= \sum_\eta \mathcal{V}_\eta \left|\nu_\eta\right\rangle \left\langle\nu_\eta\right| \end{cases} \tag{1.63}$$

Hence we have

$$i\left\langle \nu_\beta | \frac{d}{dt}\nu_\alpha(x,t) \right\rangle = \sum_k \sum_\eta U_{\alpha k} E_k U_{\eta k}^* \left\langle\nu_\beta|\nu_\eta(x,t)\right\rangle + \sum_\eta \delta_{\beta\eta}\mathcal{V}_\eta \left\langle\nu_\eta|\nu_\alpha(x,t)\right\rangle$$

Which gives us

$$i\frac{d}{dt}\left\langle\nu_\beta|\nu_\alpha(x,t)\right\rangle = \sum_\eta \left(\sum_k U_{\alpha k} E_k U_{\eta k}^* + \delta_{\beta\eta}\mathcal{V}_\beta \right) \left\langle\nu_\eta|\nu_\alpha(x,t)\right\rangle \tag{1.64}$$

However we have $E_k \approx E + \frac{m_k^2}{2E}$, $p \approx E$, $t \approx x$ for these ultra-relativistic neutrinos.
We also have $\mathcal{V}_\beta = V_{NC} + \delta_{e\beta} V_{CC}$
So we can write

$$\begin{array}{rc} \frac{d}{dt}\left\langle\nu_\beta|\nu_\alpha(x,t)\right\rangle = & \sum_\eta \left(p + \frac{m_1^2}{2E} + V_{NC} \right) \left\langle\nu_\beta|\nu_\alpha(x,t)\right\rangle \\ & + \sum_\eta \left(\sum_k U_{\alpha k} \frac{m_{k1}^2}{2E} U_{\eta k}^* + \delta_{\beta\eta}\delta_{e\beta} V_{CC} \right) \left\langle\nu_\eta|\nu_\alpha(x,t)\right\rangle \end{array} \tag{1.65}$$

We can then observe that the neutral current only creates a global phase shift while the charged current creates a phase shift only for the electron neutrino component of a wave packet, equivalent to the action of a potential

$$V(x) = \epsilon\sqrt{2} G_F N_e(x) \tag{1.66}$$

where G_F is the Fermi constant and N_e is the density of electrons in the matter where the neutrinos are propagating.

For the electron antineutrinos, the potential is the same, but epsilon is negative. An approximation at the first order tells us that the types of potentials encountered on Earth or

on the Sun gives oscillation formulas similar to the one for the oscillation in the vacuum, as long as we modify the values of $i\theta = \theta_{12}$ and $\Delta m^2 = \Delta m^2_{12}$ with

$$\begin{cases} \Delta m^2_M(x) &= \sqrt{(\Delta m^2 \cos(2\theta) - 2EV(x))^2 + (\Delta m^2 \sin(2\theta))^2} \\ tan(2\theta_M(x)) &= \frac{\Delta m^2 \sin(2\theta)}{\Delta m^2 \cos(2\theta) - 2EV(x)} \end{cases} \tag{1.67}$$

where the sign of V depends on whether we work with neutrinos or antineutrinos.

We can rewrite these parameters as

$$\begin{cases} \Delta m^2_M(x) &= \sqrt{(\Delta m^2_{21})^2 + a(x)^2 - 2a(x)\Delta m^2_{21} \cos(2\theta_{12})} \\ tan(2\theta_M(x)) &= \frac{\Delta m^2_{21} \sin(2\theta)}{\Delta m^2_{21} \cos(2\theta) - a(x)} \end{cases} \quad \text{with } a(x) \equiv 2EV(x) \tag{1.68}$$

we also have

$$\begin{aligned} \sin(2\theta_M(x)) &= \frac{\Delta m^2 \sin(2\theta)}{\sqrt{(\Delta m^2_{21})^2 + a(x)^2 - 2a(x)\Delta m^2_{21} \cos(2\theta_{12})}} \\ \cos(2\theta_M(x)) &= \frac{\Delta m^2 \cos(2\theta) - a(x)}{\sqrt{(\Delta m^2_{21})^2 + a(x)^2 - 2a(x)\Delta m^2_{21} \cos(2\theta_{12})}} \end{aligned} \tag{1.69}$$

When the potential is constant we can look at the way these apparent parameters behave.

The evolution of θ_M in the case the potential is constant and we work with antineutrinos is given in Figure 1.11.

- When $2EV \ll \Delta m^2 \cos(2\theta)$, the mixing angle θ_M and the squared mass difference Δm^2_M are close to the ones for the vacuum oscillation
- When $2EV \approx \Delta m^2 \cos(2\theta)$, We are at the resonance energy $E_{res} = \cos(2\theta)$ where the mixing angle $\theta_M = \frac{\pi}{4}$ and the squared mass difference is minimal at $\Delta m^2_M = \Delta m^2 |\sin(2\theta)|$
  Moreover, the mixing is maximal, which means $|\nu_e\rangle = \frac{1}{2}(|\nu_1\rangle - |\nu_2\rangle)$ and $|\nu_\mu\rangle = \frac{1}{2}(|\nu_1\rangle + |\nu_2\rangle)$. This is the MSW effect.
- When $2EV \gg \Delta m^2 \cos(2\theta)$, the mixing angle $\theta_M = \frac{\pi}{2}$ and the squared mass difference Δm^2_M is infinite.
  There is no mixing in this case with $|\nu_e\rangle \approx |\nu_2\rangle$ and $|\nu_\mu\rangle \approx |\nu_1\rangle$.
  There is also no oscillation since flavour states and massive states are basically the same.

We can see that neutrinos and anti-neutrinos are not subject to the MSW effect at the same time. Indeed, for neutrinos, EV is positive while it is negative for antineutrinos. Hence, the MSW is possible for neutrinos only if $\theta < \frac{\pi}{4}$ while it is possible for antineutrinos only if $\theta > \frac{\pi}{4}$.

Two flavours oscillation

The mixing matrix and the mass matrix are now 2×2 matrices

$$U_M(x) = \begin{pmatrix} \cos(\theta_M(x)) & \sin(\theta_M(x)) \\ -\sin(\theta_M(x)) & \cos(\theta_M(x)) \end{pmatrix} \text{ and } M_M(x) = \begin{pmatrix} 0 & 0 \\ 0 & \Delta m^2_M(x)) \end{pmatrix} \tag{1.70}$$

And the treatment is the same as the oscillations in the vacuum.

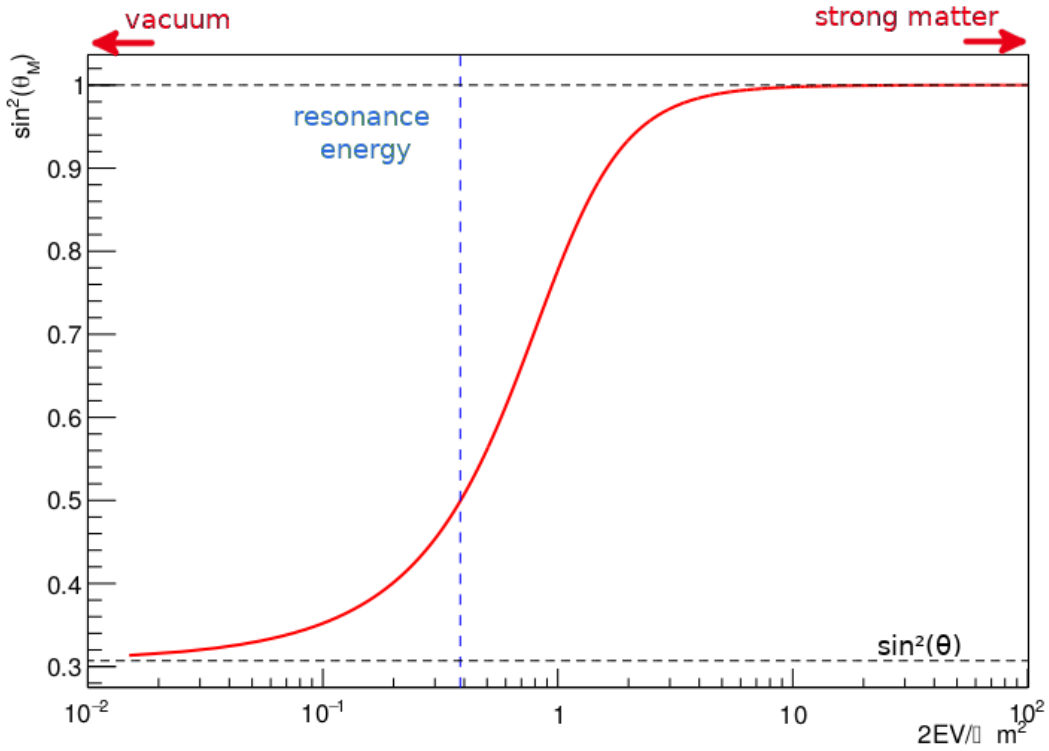

Figure 1.11 – Evolution of the matter mixing angle θ_M with the neutrino energy (constant potential)

1.2.3 Measurement of the oscillation parameters

The squared mass differences $\Delta m^2_{21}, \Delta m^2_{31}$ and the mixing angles $\theta_{12}, \theta_{13}, \theta_{23}$ and the CP violation phase δ_{CP} are free parameters of the Standard Model and have to be measured by experiments. They have all been measured by several experiments and the values are recorded in Table 1.4

- $\sin^2(\theta_{12})$ and Δm^2_{21} have been measured by studying the transition from electron neutrinos to muon neutrinos. The solar neutrinos experiments are sensitive to these parameters: Super-Kamiokande [18], SNO [19]. The long baseline reactor neutrino experiment KamLAND [20] is also sensitive to these parameters.

- $\sin^2(\theta_{23})$ and Δm^2_{32} have been measured by studying the disappearance of muon (anti)neutrinos. Accelerator neutrinos and atmoshperic neutrinos experiments provide this. T2K [21], MINOS [22], NOνA [23], Super-Kamiokande [18] and IceCube [24].

- $\sin^2(\theta_{13})$ has been measured by studying the transition from muon (anti)neutrinos to electron (anti)neutrinos with the T2K experiment and NOνA as well as short baseline reactor neutrinos experiments: Daya Bay [25], Double Chooz [26]. RENO [27] has also measured this parameter through the $\bar{\nu}_e$ disappearance.

We notice that out of the squared mass difference, only the sign of Δm^2_{21} has been determined. The reason is that there is a MSW effect in the oscillation of neutrinos traveling through the Sun. As we said earlier, this is only possible for $\frac{2EV}{\Delta m^2_{21}} = \cos(2\theta_{12})$. Since $\cos(2\theta_{12}) > 0$ and $V > 0$ (neutrino potential), it means that Δm^2_{21} is positive too.
Depending on the sign of Δm^2_{32} we can have two different mass repartitions for the neutrinos

parameter	value
$\sin^2(\theta_{12})$	0.310 ± 0.013
$\sin^2(\theta_{13})$	0.022 ± 0.001
$\sin^2(\theta_{23})$	0.558 ± 0.033
Δm^2_{21}	$7.39 \times 10^{-5}\,\mathrm{eV}^2 \pm 0.21 \times 10^{-5}\,\mathrm{eV}^2$
$\lvert\Delta m^2_{31}\rvert$	$2.52 \times 10^{-3}\,\mathrm{eV}^2 \pm 0.04 \times 10^{-3}\,\mathrm{eV}^2$
δ_{CP}	$222^\circ \pm 38^\circ$

Table 1.4 – Values of the oscillation parameters for the normal hierarchy. Taken from [28]

(Figure 1.12)

If $\Delta m^2_{31} > 0$ we talk of normal mass hierarchy. Else we talk of inverted mass hierarchy. in the first case we have ν_3 heavier than the other two massive states ν_1, ν_2 In the second case, we ν_1 and ν_2 of similar masses and heavier than ν_3.

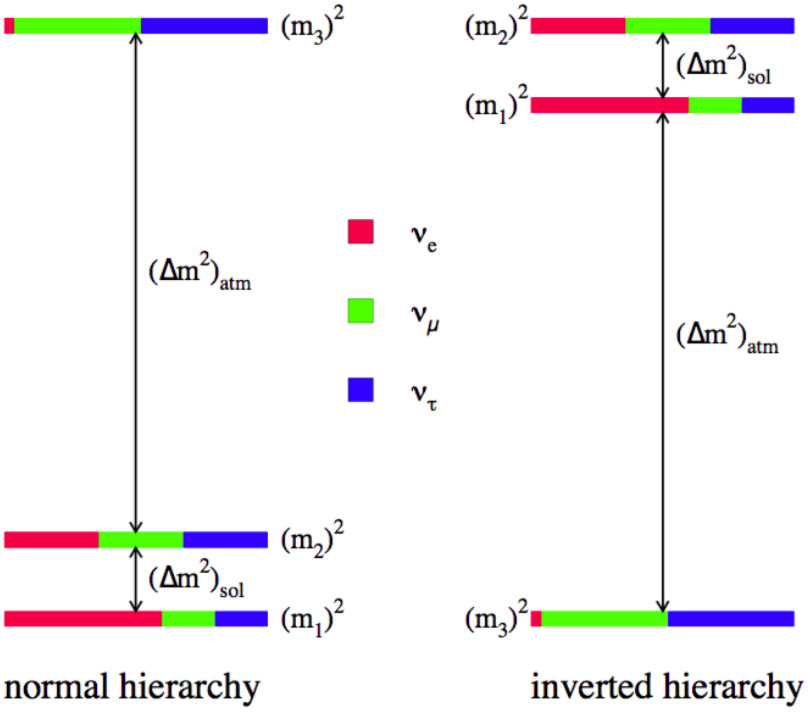

Figure 1.12 – neutrinos mass hierarchy

If the matter has a density ρ and a proton fraction $\frac{Z}{A}$ then we have a density of electrons $N_e = \frac{\rho}{m_p} \times \frac{Z}{A}$ where m_p is the proton mass, Z is the number of protons of the matter and A the number of nucleons.

Moreover we have

$$\sqrt{2}G_F \approx 7.63 \times 10^{-14} \frac{\mathrm{eVcm}^3}{\mathcal{N}_A}$$

so we have

$$2EV = 1.515 \times 10^{-4}\,\mathrm{eV}^2 \times \rho[g \cdot cm^{-3}] \times E[\mathrm{GeV}] \times \frac{Z}{A}$$

We will talk at length about the T2K experiment in Chapter 2, but we can already estimate the impact the matter effect will have on the measurement. The neutrinos have to

travel through the Earth from the beam production to the Super-Kamiokande detector. This creates matter effect for the neutrino oscillation. Precise measurement on the composition of the crust gives an average $\left\langle \frac{Z}{A} \right\rangle = 0.495$ coupled to the average density $\langle \rho \rangle = 2.6\,\mathrm{g}\cdot\mathrm{cm}^{-3}$ on the path the neutrinos go through [29] gives us the matter effect

$$a \equiv 2EV = 1.17 \cdot 10^{-4}\,\mathrm{eV}^2 \tag{1.71}$$

We see that $a \ll \Delta m^2_{31}, \Delta m^2_{32}$ the matter effect is small before the oscillation associated to these two mass differences. Let us see how it effects the total transition probability.

We can write the PMNS matrix as

$$U_{PMNS} = \begin{pmatrix} 1 & 0 & 0 \\ 0 & c_{23} & s_{23} \\ 0 & -s_{23} & c_{23} \end{pmatrix} \times \begin{pmatrix} c_{13} & 0 & s_{13}e^{-i\delta} \\ 0 & 1 & 0 \\ -s_{13}e^{i\delta} & 0 & c_{13} \end{pmatrix} \times \begin{pmatrix} c_{12} & s_{12} & 0 \\ -s_{12} & c_{12} & 0 \\ 0 & 0 & 1 \end{pmatrix} \tag{1.72}$$

where $c_{ij} = \cos(\theta_{ij})$ and $s_{ij} = \sin(\theta_{ij})$.

By writing $\Delta_{ij} = \frac{\Delta m^2_{ij} L}{4E}$, the transition probability in the vacuum is

$$\begin{aligned} P^0_{\nu_\mu \mapsto \nu_e} = \; & 4c^2_{13}s^2_{13}s^2_{23}\sin^2\Delta_{31} \\ & +4c^2_{13}s^2_{12}(c^2_{12}c^2_{23} + s^2_{12}s^2_{13}s^2_{23} - 2c_{12}c_{23}s_{12}s_{13}s_{23}\cos\delta)\sin^2\Delta_{21} \\ & +8c^2_{13}s_{12}s_{13}s_{23}(c_{12}c_{23}\cos\delta - s_{12}s_{13}s_{23})\sin\Delta_{31}\sin\Delta_{21}\cos\Delta_{32} \\ & -8c^2_{13}c_{12}c_{23}s_{12}s_{13}s_{23}\sin\delta\sin\Delta_{31}\sin\Delta_{21}\sin\Delta_{32} \end{aligned} \tag{1.73}$$

while the transition probability taking into account the matter effects is

$$\begin{aligned} P^M_{\nu_\mu \mapsto \nu_e} = \; & \boxed{4c^2_{13}s^2_{13}s^2_{23}\sin^2\Delta_{31}} \\ & +4s^2_{12}c^2_{13}(c^2_{12}c^2_{23} + s^2_{12}s^2_{23}s^2_{13} - 2c_{12}c_{23}s_{12}s_{13}s_{23}\cos\delta)\sin^2\Delta_{21} \\ & +8c^2_{13}s_{12}s_{13}s_{23}(c_{12}c_{23}\cos\delta - s_{12}s_{13}s_{23})\sin\Delta_{31}\sin\Delta_{21}\cos\Delta_{32} \\ & -8c^2_{13}c_{12}c_{23}s_{12}s_{13}s_{23}\sin\delta\sin\Delta_{31}\sin\Delta_{21}\sin\Delta_{32} \\ & -8c^2_{13}s^2_{12}s^2_{23}\tfrac{aL}{4E}(1-2s^2_{13})\cos\Delta_{32}\sin\Delta_{31} + 8c^2_{13}s^2_{13}s^2_{23}\tfrac{a}{\Delta m^2_{31}}(1-2s^2_{13})\sin^2\Delta_{31} \end{aligned} \tag{1.74}$$

But the distance $L = 295\,\mathrm{km}$ and the energy $E = 600\,\mathrm{MeV}$ have been chosen so that $\Delta_{31} \approx \Delta_{32} \approx \frac{\pi}{2}$. We also have $\Delta_{21} \ll \Delta_{31}$

So the term proportional to $\cos\Delta_{32}$ (third line) vanishes while the terms proportional to $\sin\Delta_{21}$ (second and fourth) are very small in front of the term on the first line.

Hence, the apparition term for electron neutrinos in the vacuum is given mainly by the first line

$$P^M_{\nu_\mu \mapsto \nu_e} \approx 4c^2_{13}s^2_{13}s^2_{23}\sin^2\Delta_{31} \tag{1.75}$$

When taking into account the matter effects (fourth line), we obtain a shift of the peak values and of the position where the peak is attained (cf Figure 1.13). This modification is different for normal and inverted mass hierarchies. However in T2K we cannot disentangle the matter effects from the mass hierarchy effects because the baseline is not long enough.

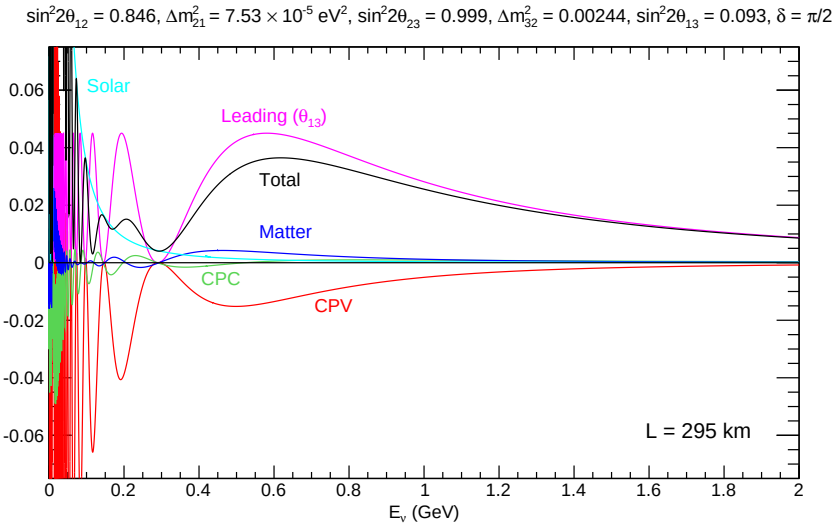

Figure 1.13 – T2K ν_e appearance probability as a function of the neutrino energy split up into its different contributions.

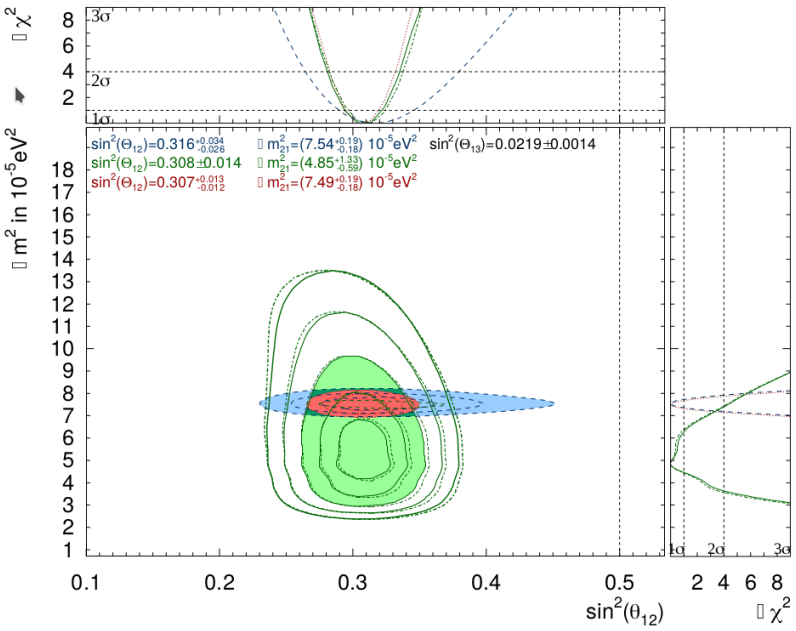

Figure 1.14 – Measurement on Δm^2_{21} and $\sin^2(\theta_{12})$ for the normal mass hierachy. Taken from [18]

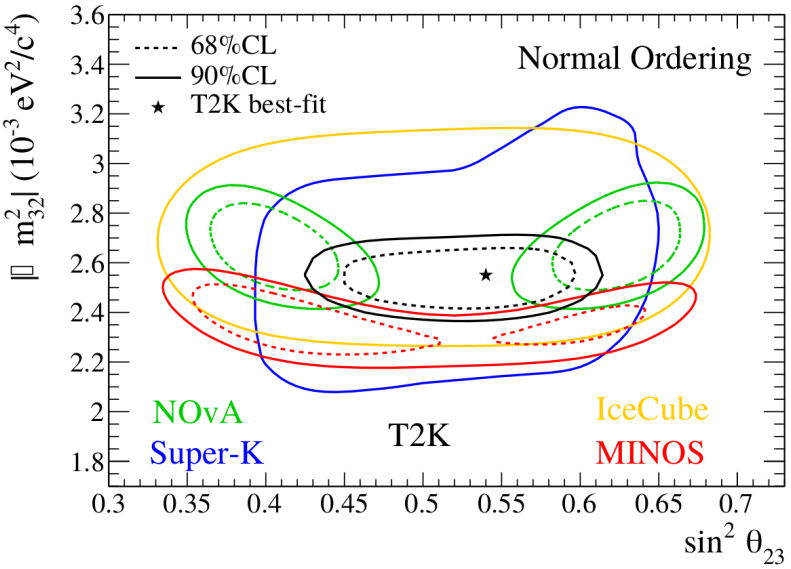

Figure 1.15 – Measurement on Δm^2_{32} and $\sin^2(\theta_{23})$ for the normal mass hierachy. Taken from [30]

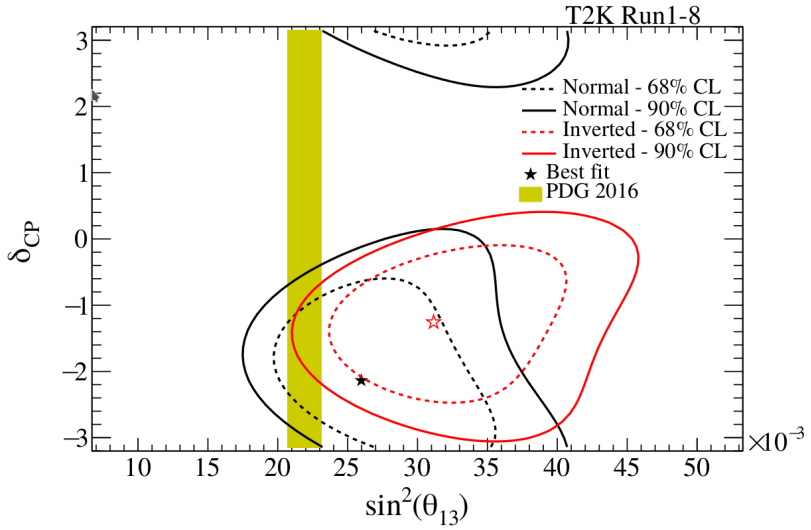

Figure 1.16 – Measurement on δ^2_{CP} and $\sin^2(\theta_{13})$ for the the two mass hierachies. Taken from [31]

1.3 Interactions between neutrinos and nuclei

(Anti)Neutrinos can interact with matter via the weak interaction. The interaction can be done either by neutral current (Z boson) or by charged current (W^+ boson for neutrinos and W^- boson for antineutrinos).

In the T2K experiment, and in neutrino experiments generally, the neutral current interactions are difficult to detect while the charged current interactions produce a charged lepton and are easier to detect. This is the reason why we focus on detecting charged current interactions of the form

$$\nu + A \mapsto \sum_X X \text{ or } \bar{\nu} + A \mapsto \sum_X X \tag{1.76}$$

for neutrinos

where A is the target of the (anti)neutrino and where the set X are particles or hadrons products of the interaction. The threshold for that interaction to be possible is passed if the following inequality is satisfied

$$(\underline{P}_\nu + \underline{P}_A)^2 \geq (\sum_X m_X)^2 \tag{1.77}$$

Where $\underline{P}_\nu$ is the momentum quadrivector of the (anti)neutrino This quantities are Lorentz invariant so we can compute them in the laboratory frame, where $\underline{P}_\nu = (E_\nu, \mathbf{p}_\nu)$ and $\underline{P}_A = (m_A, \mathbf{0})$

Neglecting the (anti)neutrino mass, the condition becomes

$$m_A^2 + 2E_\nu m_A \geq (\sum_X m_X)^2$$

So the condition for the reaction to be possible is

$$E_\nu \geq E_\nu^{thres} \equiv \frac{(\sum_X m_X)^2}{2m_A} - \frac{m_A}{2} \tag{1.78}$$

Table 1.5 summarize the masses of the particles most often encountered in the scatterings we will consider.

particle	mass (MeV)	spin
muon μ	105.66	1/2
proton p	938.272	1/2
neutron n	939.565	1/2
baryon Δ	1232	3/2
pion π^0	134.977	0
pion π^-	139.570	0
pion π^+	139.570	0

Table 1.5 – Mass of different particles

1.3.1 Quasi Elastic Charged Current scattering (CCQE)

The Quasi Elastic scattering by charged current (CCQE) of a neutrino on a nucleon (Figure 1.18) is the scattering which involves the least number of product particles and also is the

first threshold in energy for Charged current interactions

$$\begin{array}{ll} \nu_\mu(p) + n(k) \mapsto \mu^-(p') + p(k') & \text{for neutrinos} \\ \bar{\nu}_\mu(p) + p(k) \mapsto \mu^+(p') + n(k') & \text{for antineutrinos} \end{array} \tag{1.79}$$

The condition becomes $E_\nu^{thres} = 110\,\text{MeV}$

Before considering the scattering on a nucleon we can compute a simpler process which is treatable in the scope of the Standard Model: the scattering of a (anti)neutrino on a free quark (Figure 1.17)

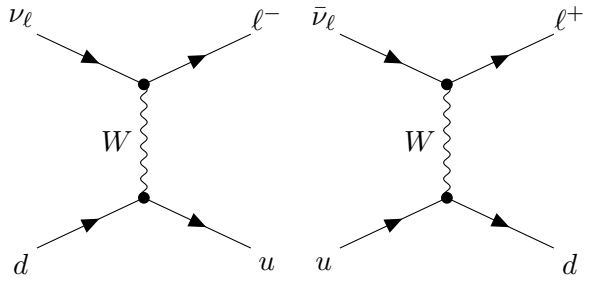

Figure 1.17 – Quasi Elastic (QE) scattering of a (anti)neutrino and a free quark by charged curent

$$\begin{array}{ll} \nu_\mu(p) + d(k) \mapsto \mu^-(p') + u(k') & \text{for neutrinos} \\ \bar{\nu}_\mu(p) + u(k) \mapsto \mu^+(p') + d(k') & \text{for antineutrinos} \end{array} \tag{1.80}$$

We can compute the amplitude for the neutrino scattering

$$\begin{aligned} i\mathcal{M}_{\nu_\mu d \mapsto \mu^- u} &= -i\tfrac{g_w}{\sqrt{2}} V_{ud} \left(\bar{u}_u(k') \gamma^\rho \tfrac{1}{2}(1-\gamma^5) u_d(k) \right) \\ &\times - \tfrac{g_{\rho\kappa} - q_\rho q_\kappa / M_w^2}{q^2 - M_w^2} \\ &\times - i\tfrac{g_w}{\sqrt{2}} \left(\bar{u}_{\mu^-}(p') \gamma^\kappa \tfrac{1}{2}(1-\gamma^5) u_{\nu_\mu}(p) \right) \end{aligned}$$

When we have $q^2 \ll M_w^2$ we can simplify the relation to

$$\mathcal{M}_{\nu_\mu d \mapsto \mu^- u} = -i\frac{G_F}{\sqrt{2}} V_{ud} \times \underbrace{\left(\bar{u}_u(k') \gamma_\rho \frac{1}{2}(1-\gamma^5) u_d(k) \right)}_{\text{quark part}} \times \underbrace{\left(\bar{u}_{\mu^-}(p') \gamma^\rho \frac{1}{2}(1-\gamma^5) u_{\nu_\mu}(p) \right)}_{\text{leptonic part}} \tag{1.81}$$

where $\frac{G_F}{\sqrt{2}} = \frac{g_w^2}{8 M_w^2}$

Similarly the antineutrino scattering when $q^2 \ll M_w^2$ is

$$\mathcal{M}_{\bar{\nu}_\mu u \mapsto \mu^+ d} = -i\frac{G_F}{\sqrt{2}} V_{ud}^* \times \underbrace{\left(\bar{u}_d(k') \gamma_\rho \frac{1}{2}(1-\gamma^5) u_u(k) \right)}_{\text{quark part}} \times \underbrace{\left(\bar{v}_{\mu^+}(p') \gamma^\rho \frac{1}{2}(1-\gamma^5) v_{\bar{\nu}_\mu}(p) \right)}_{\text{leptonic part}} \tag{1.82}$$

We can then use these matrices amplitudes to compute the cross sections of the scattering with nucleons.

However there are no free quarks at the energy scales we consider. They are confined within nucleons which are themselves packed into atomic nuclei. Hence we need to compute the scattering of (anti)neutrinos with nucleons (Figure 1.18).

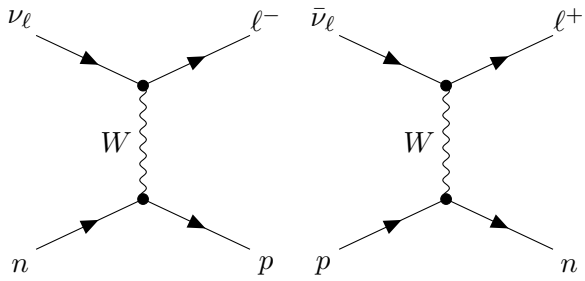

Figure 1.18 – Quasi Elastic (QE) scattering of a (anti)neutrino and a nucleon by charged curent

The Standard Model doesn't allow an analytical description of the interaction of a (anti)neutrino with quarks bound into a nucleon. We usually choose a phenomenological approach and use the form factors formalism.

We can start from the amplitudes for the scattering on free quarks (equations 1.81 and 1.82) and work a new amplitude for the nucleons from there. The vertices implying the leptons in the Feynman diagrams describing the scattering remains unchanged when going from scattering on u, d quarks to scattering on p, n nucleons. So does the propagator. However, we have to modify the "quark part" of the amplitude and turn it into an "hadronic part" which describe the behavior of nucleons.

The vector-axial (V-A) current is a formalism adapted to treat the chirality of the weak interaction. for two members of a weak isodoublet $\begin{pmatrix} a \\ b \end{pmatrix}$, we express the weak charged current as

$$\begin{aligned} j^\rho_{cc+} &= \bar{a}(\mathbf{v}^\rho_+ - \mathbf{a}^\rho_+)b \\ j^\rho_{cc-} &= \bar{b}(\mathbf{v}^\rho_- - \mathbf{a}^\rho_-)a \end{aligned}$$

where the $\mathbf{a}^\rho$ are factors depending on γ^5 called "axial components" and $\mathbf{v}^\rho$ are factors not containing γ^5 called "vector component".

For the free quarks $\begin{pmatrix} u \\ d \end{pmatrix}$, the factors are $(\mathbf{v}^\rho_+, \mathbf{a}^\rho_+) = \left(\frac{V_{ud}}{2}\gamma^\rho, \frac{V_{ud}}{2}\gamma^\rho\gamma^5\right)$ and $(\mathbf{v}^\rho_-, \mathbf{a}^\rho_-) = \left(\frac{V^*_{ud}}{2}\gamma^\rho, \frac{V_{ud}}{2}\gamma^\rho\gamma^5\right)$.

Neglecting the mass mixing of the quarks, we can consider $\begin{pmatrix} p \\ n \end{pmatrix}$ as an isospin doublet and thus define charged currents as well as vector and axial currents. We can use the following factors [32]

$$\begin{cases} \mathbf{v}^\rho_+ = \gamma^\rho F_1(Q^2) + \frac{i}{2m_N}\sigma^{\rho\eta}q_\eta F_2(Q^2) \\ \mathbf{a}^\rho_+ = (\gamma^\rho G_A(Q^2) + \frac{q^\rho}{m_N}G_P(Q^2))\gamma^5 \end{cases}$$

$$\begin{cases} \mathbf{v}^\rho_- = \gamma^\rho F_1(Q^2) + \frac{i}{2m_N}\sigma^{\rho\eta}q_\eta F_2(Q^2) \\ \mathbf{a}^\rho_- = (\gamma^\rho G_A(Q^2) - \frac{q^\rho}{m_N}G_P(Q^2))\gamma^5 \end{cases}$$

where $Q^2 \equiv -q^2$ and $\sigma^{\rho\eta} = \frac{1}{2}\left(\gamma^\rho\gamma^\eta - \gamma^\eta\gamma^\rho\right)$. We obtain the negative charged current factors from the positive charged current factors by using the fact that $j^\rho_{cc-} = j^{\rho\dagger}_{cc+}$ and that the form factors are real [33] and the anti-commutation rules of the Clifford algebra $\gamma^{\rho\dagger} = \gamma^0\gamma^\rho\gamma^0$ and $\gamma^5\gamma^\rho = -\gamma^\rho\gamma^5$.

So the quark terms in the formulas 1.81 and 1.82 are replaced by the hadronic terms

$$\begin{array}{ll} \langle p(k')|j^\rho_{cc+}|n(k)\rangle & \text{for neutrinos} \\ \langle n(k')|j^\rho_{cc-}|p(k)\rangle & \text{for antineutrinos} \end{array} \tag{1.83}$$

So the terms for the hadronic vertices are

$$\begin{array}{ll}\bar{u}_p(k')\left[\gamma^\rho F_1(Q^2)+\frac{i}{2m_N}\sigma^{\rho\eta}q_\eta F_2(Q^2)-(\gamma^\rho G_A(Q^2)+\frac{q^\rho}{m_N}G_P(Q^2))\gamma^5\right]u_n(k) & \text{for neutrinos}\\ \bar{u}_n(k')\left[\gamma^\rho F_1(Q^2)+\frac{i}{2m_N}\sigma^{\rho\eta}q_\eta F_2(Q^2)-(\gamma^\rho G_A(Q^2)-\frac{q^\rho}{m_N}G_P(Q^2))\gamma^5\right]u_p(k) & \text{for antineutrinos}\end{array} \tag{1.84}$$

Hence the matrix amplitudes are

$$\begin{aligned}\mathcal{M}_{\nu_\mu n\mapsto\mu^- p} &= -i\tfrac{G_F}{\sqrt{2}}V_{ud}\\ &\times\underbrace{\left(\bar{u}_{\mu^-}(p')\gamma_\rho\frac{1}{2}(1-\gamma^5)u_{\nu_\mu}(p)\right)}_{\text{leptonic part}}\\ &\times\underbrace{\bar{u}_p(k')\left[\gamma^\rho F_1(Q^2)+\frac{i}{2m_N}\sigma^{\rho\eta}q_\eta F_2(Q^2)-(\gamma^\rho G_A(Q^2)+\frac{q^\rho}{m_N}G_P(Q^2))\gamma^5\right]u_n(k)}_{\text{hadronic part}}\end{aligned} \tag{1.85}$$

$$\begin{aligned}\mathcal{M}_{\bar{\nu}_\mu p\mapsto\mu^+ n} &= -i\tfrac{G_F}{\sqrt{2}}V_{ud}^*\\ &\times\underbrace{\left(\bar{v}_{\mu^+}(p')\gamma_\rho\frac{1}{2}(1-\gamma^5)v_{\bar{\nu}_\mu}(p)\right)}_{\text{leptonic part}}\\ &\times\underbrace{\bar{u}_n(k')\left[\gamma^\rho F_1(Q^2)+\frac{i}{2m_N}\sigma^{\rho\eta}q_\eta F_2(Q^2)-(\gamma^\rho G_A(Q^2)-\frac{q^\rho}{m_N}G_P(Q^2))\gamma^5\right]u_p(k)}_{\text{hadronic part}}\end{aligned} \tag{1.86}$$

From then we can express the differential cross-section using the matrix amplitudes.

Now let's see what the form factors look like.

Let's note

$$Q=\begin{pmatrix}u\\d\end{pmatrix}\text{ and }N=\begin{pmatrix}p\\n\end{pmatrix}\text{ and }\widehat{\mathbf{v}}_+^\rho=\bar{p}\cdot\mathbf{v}_+^\rho\cdot n \tag{1.87}$$

Since we assumed no mass mixing, the isospin symmetry is conserved. We can also identify the vector operator $\widehat{v}_+^\rho$ with the charge raising operator $\gamma^\rho\sigma^+\equiv\gamma^\rho\left(\sigma^1/2+i\sigma^2/2\right)$

$$\langle Q|\widehat{v}_+^\rho|Q\rangle=\left\langle Q|\gamma^\rho\sigma^+|Q\right\rangle$$

We also have $\left[\gamma^\rho\sigma^3/2,\sigma^+\right]=\gamma^\rho\sigma^+$
so we can write

$$\left\langle p(k')|\left[\gamma^\rho\sigma^3/2,\sigma^+\right]|n(k)\right\rangle=\left\langle p(k')|\gamma^\rho\sigma^+|n(k)\right\rangle=\langle p(k')|\widehat{\mathbf{v}}_+^\rho|n(k)\rangle \tag{1.88}$$

But we also have

$$\begin{aligned}\langle p(k')|\left[\gamma^\rho\sigma^3/2,\sigma^+\right]|n(k)\rangle &= \left\langle p(k')|\gamma^\rho\tfrac{\sigma^3}{2}\sigma^+|n(k)\right\rangle-\left\langle p(k')|\sigma^+\gamma^\rho\tfrac{\sigma^3}{2}|n(k)\right\rangle\\ &= \left\langle p(k')|\gamma^\rho\tfrac{\sigma^3}{2}|p(k)\right\rangle-\left\langle n(k')|\gamma^\rho\tfrac{\sigma^3}{2}|n(k)\right\rangle\end{aligned} \tag{1.89}$$

We then use the Gell-Mann-Nishijima relation [34] $Q=I_3^{strong}+\frac{Y^{strong}}{2}$
Since proton and neutron have the same weak hypercharge and $\gamma^\rho\frac{\sigma^3}{2}$ is the operator for the

strong isospin charge , the hypercharge values cancel each other in the second line of the relation 1.89 and we obtain

$$\left\langle p(k')\right| \left[\gamma^\rho \sigma^3/2, \sigma^+\right] \left|n(k)\right\rangle = \langle p(k')|\widehat{\mathbf{v}}^{em\rho}|p(k)\rangle - \langle n(k')|\widehat{\mathbf{v}}^{em\rho}|n(k)\rangle$$

So combining the two relations gives

$$\langle p(k')|\widehat{\mathbf{v}}^{\rho}_{+}|n(k)\rangle = \langle p(k')|\widehat{\mathbf{v}}^{\mathrm{em}\rho}|p(k)\rangle - \langle n(k')|\widehat{\mathbf{v}}^{\mathrm{em}\rho}|n(k)\rangle \tag{1.90}$$

Identifying the form factors of the two operators $\widehat{\mathbf{v}}^{\rho}_{+}$ and $\widehat{\mathbf{v}}^{\mathrm{em}\rho}$ gives the relation

$$F_k(Q^2) = F^p_{k,em}(Q^2) - F^n_{k,em}(Q^2) \tag{1.91}$$

The electromagnetic form factors $F_{1,em}$ and $F_{2,em}$ are obtained by electromagnetic elastic scattering of electrons on protons and neutrons [32]

We usually choose to parametrize G_A as

$$G_A(Q^2) = \frac{g_A}{(1 + Q^2/M_A^2)^2} \tag{1.92}$$

where $g_A \approx 1.26$ is given by the Goldberger-Treiman relation [35] a constant and where M_A the axial mass is measured by cross-section measurements

Form factors are convenient and provide a phenomenological description of the phenomenon we study. However, they need to be refined by experiments in order to guarantee that the modeling is accurate and that we properly understand their limitations.

1.3.2 Resonant Charged Current scattering (CCRes)

This channel is actually the result of two successive reactions as depicted in Figure 1.19

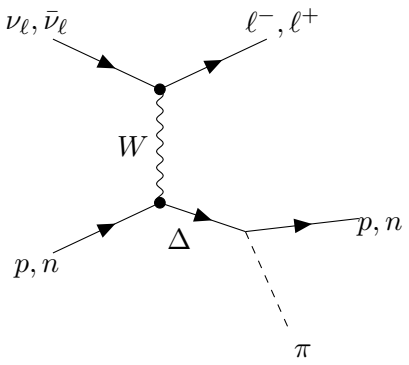

Figure 1.19 – Resonant scattering of a (anti)neutrino and a nucleon by charged current

First the neutrino interacts with a nucleon and produces a baryon $\mathcal{R}$ which is often a Δ. Then the baryon decays into a nucleon an a pion

$$\begin{aligned} \nu_\mu(p) + N(k) \mapsto \mu^-(p') + \quad & \mathcal{R}(k') \\ & \hookrightarrow A'(k_1) + \pi(k_2) \end{aligned} \tag{1.93}$$

$$\begin{aligned} \bar{\nu}_\mu(p) + A(k) \mapsto \mu^+(p') + \quad & \mathcal{R}(k') \\ & \hookrightarrow A'(k_1) + \pi(k_2) \end{aligned} \tag{1.94}$$

The computation of the matrix amplitudes is much more complex than what we did the CCQE. But the core idea remains the same. We replace the "quark part" of the amplitudes

in 1.81 and 1.82 by a "baryonic part" given with a phenomenological $\widehat{\mathbf{j}}^{\rho}$ which respects the chirality of the weak interaction.

$$\left\langle \mathcal{R}(k')|\widehat{\mathbf{j}}^{\rho}|A(k)\right\rangle \tag{1.95}$$

And obtain the amplitude $\mathcal{M}_{\nu_\mu A\mapsto\mu^-\mathcal{R}}$ which describes the first part of the interaction. Then we multiply the resulting amplitude by another amplitude $\mathcal{M}_{\mathcal{R}\mapsto A'\pi}$ describing the decay and obtain the amplitude of the total interaction

$$\mathcal{M}_{\nu_\mu A\mapsto\mu^- A'\pi} = \mathcal{M}_{\nu_\mu A\mapsto\mu^-\mathcal{R}} \times \mathcal{M}_{\mathcal{R}\mapsto A'\pi} \tag{1.96}$$

As for the energetic threshold of such a reaction, we can compute it with the relation 1.78 and the mass values given in Table 1.5. We find

$$E_\nu^{thres} \approx 320\,\text{MeV} \tag{1.97}$$

when taking $m_\Delta - \Gamma_\Delta$ as the mass of the Delta,
with $\Gamma_\Delta = 117\,\text{MeV}$ the decay width of the Δ. For reminder, we can detect the mass of a particle X with an error Γ_X, where Γ_X is its decay width.

1.3.3 Deep Inelastic Charged Current scattering (CCDIS)

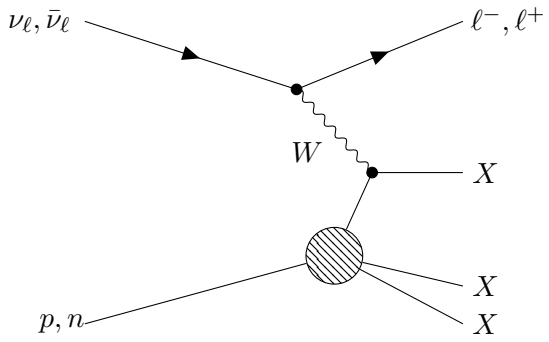

Figure 1.20 – Deep Inelastic scattering of a (anti)neutrino and a nucleus by charged curent

The energy threshold is usually above 2 or 3 GeV. In the T2K oscillation experiment the neutrinos are at energies around 600 MeV. This means that this channel has a negligible contribution to the interactions.

1.3.4 Interaction of (anti)neutrinos with a nucleus: nuclear effects

Up until now we considered the interaction of a neutrino directly on a nucleon (proton or neutron) at rest in the laboratory frame.
However this formalism is inaccurate for two reasons:

- It neglects the interactions between nucleons which are bonded by the strong interaction.
- Nucleons are fermions which means they are bonded by the Pauli principle which forbids same particles in one quantum system from being in the same quantum state.

As we said, the nucleons of a nucleus are bound by the Pauli principle which means they cannot all be all at rest. To properly discuss the kinematics of the nucleons we use the Fermi sphere formalism ; considering the neutrons and the protons of the nucleus as two Fermi gases.

In a cubic space of side length L, the quantum states have an energy

$$E_{\mathbf{n}} = m + \frac{\pi^2}{2mL^2}|\mathbf{n}|^2$$

where $\mathbf{n} = (n_x, n_y, n_z)$ is the vector of quantum numbers for the energies in each dimension.

Keeping in mind that each energy is accessible by two particles (spin $\frac{1}{2}$ and spin $-\frac{1}{2}$), the number of states with an energy smaller than $m + E_F = \frac{\pi^2}{2mL^2}n_F^2$ is

$$N = 2 \times \frac{1}{8} \times \frac{4}{3}\pi n_F^2$$

The factor 2 is for the degree of freedom from the spin. The factor $\frac{1}{8}$ is because only on eigth of the sphere has exclusively positive coordinates.

So $n_F = \left(\frac{3N}{\pi}\right)^{1/3}$.
And we have

$$E_F = \frac{\pi^2}{2mL^2}\left(\frac{3N}{\pi}\right)^{2/3}$$

But we also have $L^2 = V^{2/3}$. So we find

$$E_F = \frac{1}{2m}\left(\frac{3\pi^2 N}{V}\right)^{2/3} = \frac{1}{2m}\left(3\pi^2\rho\right)^{2/3} \tag{1.98}$$

where ρ is the density of nucleons in the space.

We also have

$$m + E_F = \sqrt{m^2 + p_F^2} \approx m + \frac{1}{2}\frac{p_F^2}{m}$$

where p_F is called the fermi momentum.
so we find the relation between the nucleon density and the fermi momentum.

$$p_F = (3\pi^2\rho)^{1/3} \tag{1.99}$$

Now we can use this to go from the cross-section σ_0 of the quasi elastic scattering $\nu_\mu(p) + n(k) \mapsto \mu^-(p') + p(k')$ studied earlier to the cross-section $\sigma_{\mathcal{N}}$ of the scattering of a neutrino with the nucleus $\nu_\mu(p) + \mathcal{N}(k) \mapsto \mu^-(p') + \mathcal{N}'(k')$: $d\sigma_{\mathcal{N}} = R(q^0) \times d\sigma_0$ [36] where

$$R(q^0) = \int d^3\mathbf{k}\frac{m_n^2}{E_p E_n}\mathcal{P}(\mathbf{k}) \times \delta(q^0 + E_{\mathcal{N}} - E_{\mathcal{N}'} - E_b) \times \theta(p_F - |\mathbf{k}|) \times \theta(|\mathbf{k}'| - p_F) \tag{1.100}$$

- $\int \mathcal{P}(\mathbf{k})d^3\mathbf{k} = 1$ where $\mathcal{P}(\mathbf{k})$ is the probability that the initial momentum of the target nucleon is $\mathbf{k}$.
- $\delta(q^0 + E_{\mathcal{N}} - E_{\mathcal{N}'} - E_b)$ is for the conservation of enrgy, minus the bounding energy E_b of the nucleus that is necessary to eject the nucleon.
- $\theta(p_F - |\mathbf{k}|)$ and $\theta(|\mathbf{k}'| - p_F)$ represent the fact that the target nucleon $\mathcal{N}$ must have a momentum smaller than the fermi momentum in order to be bound to the nucleus while the product nucleon $\mathcal{N}'$ must have a momentum greater than the fermi momentum to escape the nucleus.

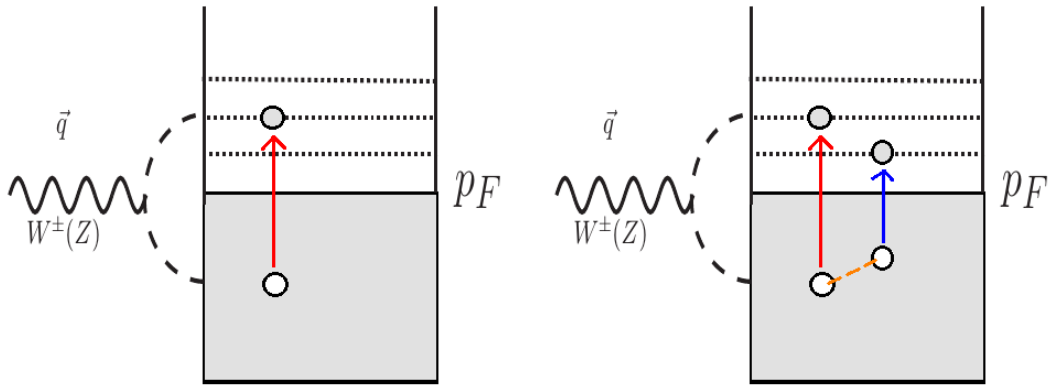

Figure 1.21 – Interaction of a neutrino with a nucleus. (left) 1 particle - 1 hole (1p-1h) interaction where only one nucleon is ejected. (right) 2 particle - 2 hole (2p-2h) interaction where a pair of interacting nucleon is ejected

We just treated the case of 1p-1h interaction, pictured in the Figure 1.21.

Now we also need to discuss the strong interaction between the nucleons of a nucleus. The mediators of this interaction between nucleons are virtual scalars, the pions π.

The incoming W boson can interact with a nucleon interacting with another nucleon (Figure 1.22) and both of them will be ejected of the nucleus. This is the 2p-2h pictured in Figure 1.21.

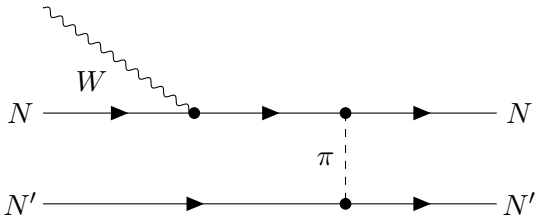

Figure 1.22 – Example of a W boson interacting with a nucleon pair interacting via strong interaction. The two nucleons will be ejected (2p-2h)

Coherent interactions

When the energy of the mediator boson W is too weak to probe the internal structure of the nucleus, then the whole nucleus can eject a meson and remain unchanged (same amount of proton and neutrons). We talk in these cases of "coherent interaction". In the case of carbon ^{12}C or oxygen ^{16}O nuclei (the one involved in the WAGASCI experiment), these interactions are relevant below an energy of about 400 MeV.

1.3.5 Total cross-section

We sum the cross sections from all these **different** scattering channels and obtain the cross-section models for neutrinos and antineutrinos (Figure 1.23)

1.3.6 Final State Interactions (FSI)

The particles produced by the weak interaction of the (anti)neutrino and the nucleon are not necessarily those who will be found going out of the nucleus. Indeed, there can and will be secondary interactions between the product particles and the nucleons of the nucleus (cf Figure 1.24).

For instance, if a pion is produced by the initial interaction, the pion can be absorbed by another nucleon, or have its charge/momentum changed, another pion can be produced. The bottom line is the final state we observed is with difficulty relatable to the type of interaction described up to now.

This is the reason why in this thesis we will mainly work with the Final State of the interaction, meaning the particles exiting the nucleus that we are actually able to detect (Table 1.6).

Final state	muons	charged pions $\pi^{\pm}$	neutral pions π^0	protons	neutrons	excited baryons (Δ, Ξ, etc)
CC0π	1	0	0	*	*	0
CC1π	1	1	0	*	*	0
CCnπ	1	n	0	*	*	0
CCπ^0	1	0	1	*	*	0
CCother	1	*	*	*	*	*
NC	0	*	*	*	*	*

Table 1.6 – List of the possible final states in terms of their particle contents. The "*" means that any number is possible.

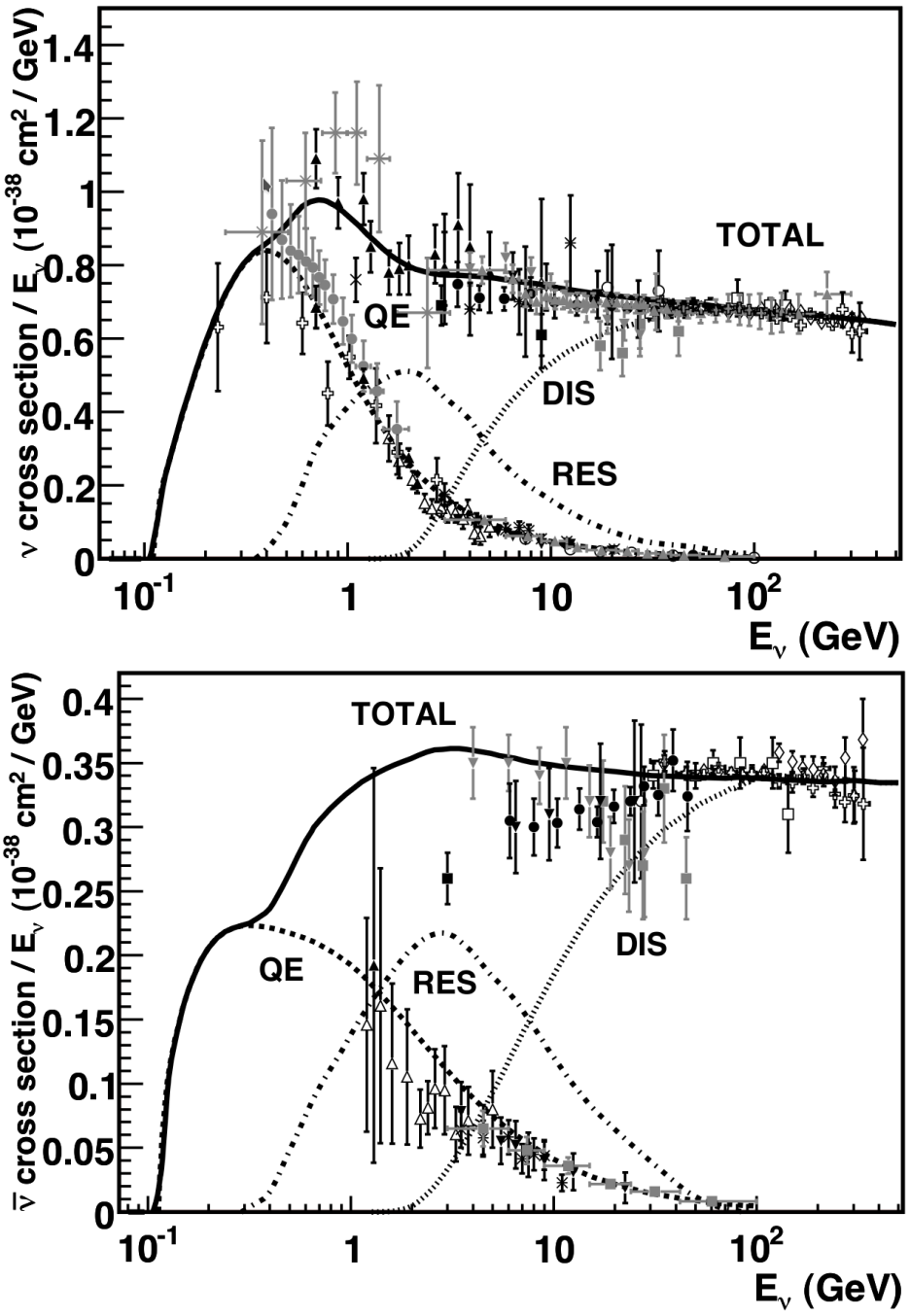

Figure 1.23 – Total neutrino and antineutrino per nucleon CC cross sections (for an isoscalar target) divided by neutrino energy and plotted as a function of energy. Note that the quasi-elastic scattering data and predictions have been averaged over neutron and proton targets and hence have been divided by a factor of two for the purposes of this plot. Taken from [37]

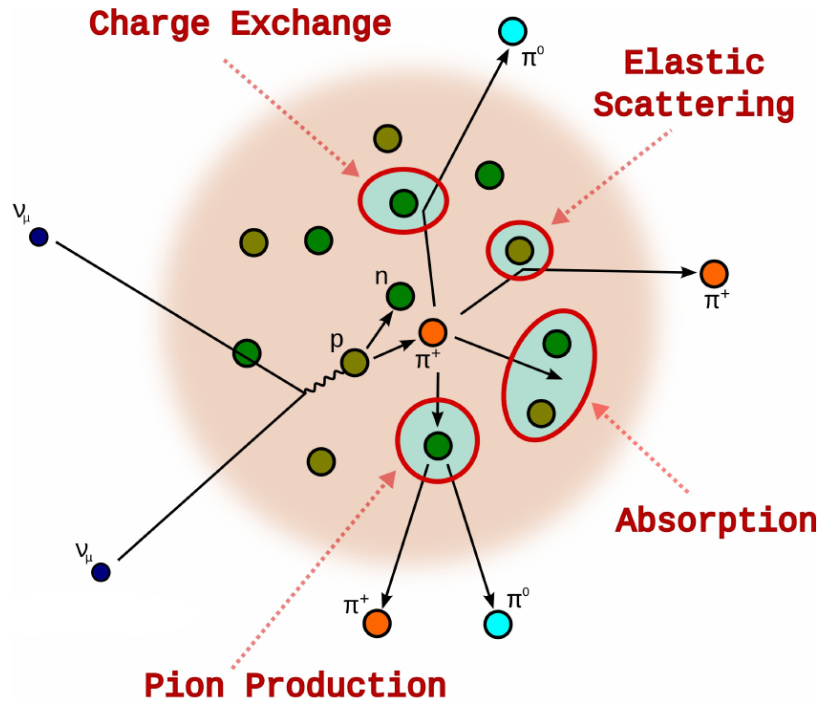

Figure 1.24 – Agents of the Final State Interactions. Taken from [38]

Chapter 2

The T2K and the WAGASCI experiments

2.1 The T2K (Tokai To Kamioka) experiment

The Tokai To Kamioka (T2K) experiment is a long baseline neutrino oscillation experiment that measure some coefficients of the PMNS matrix coefficients,

The experiment uses a muon neutrino (or antineutrino) beam produced at the JPARC(Japan Proton Accelerator Research Complex) facility in Tokai, Japan by colliding an accelerated proton beam on a carbon target. The beam propagates for 295 km and until Kamioka where it is detected by the Super-Kamiokande (SK) detector (figure 2.1).

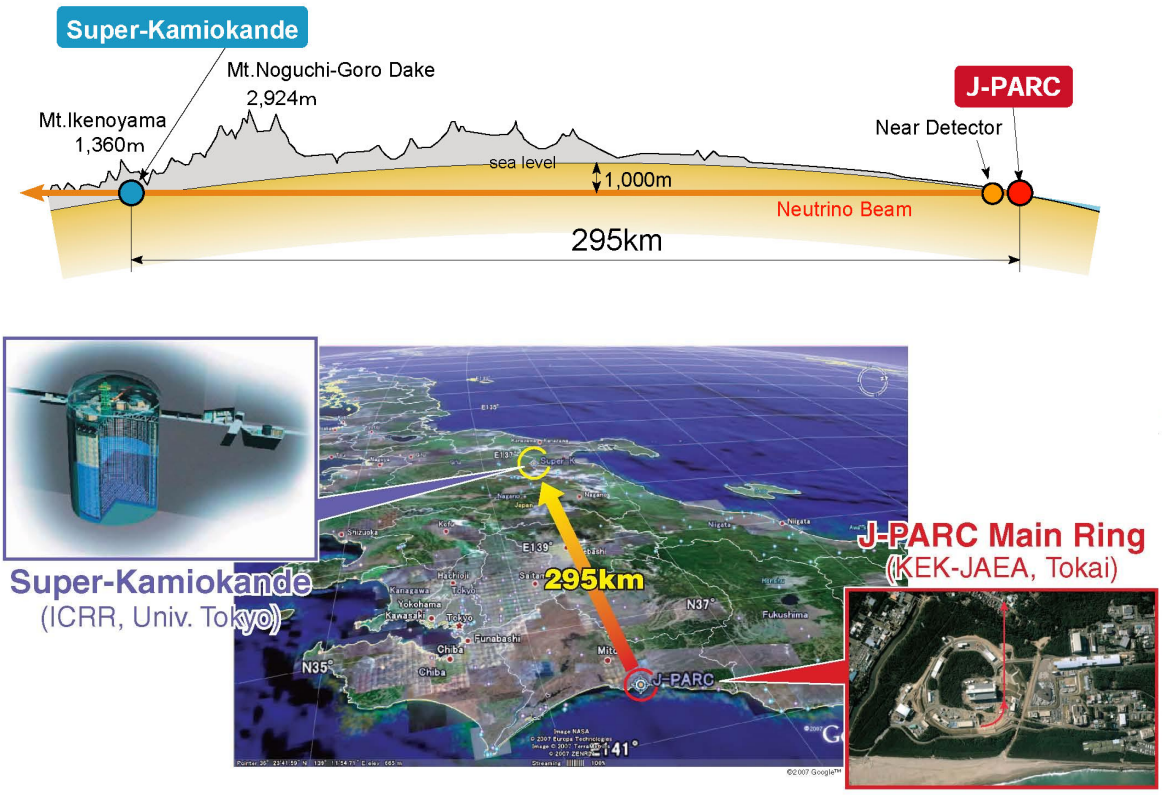

Figure 2.1 – Top: sectional view of the T2K experiment. Bottom: location of the J-PARC (Tokai) and of the Super-Kamiokande detector. The baseline of 295 km is represented by the orange arrow

The neutrino oscillation phenomenon that is presented in Section 1.2 means that the flavour composition of this beam will change with the traveled distance. In order to maximize the oscillation probability (**??**) one has to tune the L/E ratio so that the phase of the sinusoidal function is close to $\pi/2$. The baseline of 295 km is fixed by the location of J-PARC and Super-Kamiokande. This corresponds to an optimal energy of about 600 MeV. However, as shown in Figure 2.2 the on-axis neutrino energy distribution is peaked around 1 GeV and is relatively broad. One could have changed the energy of the proton beam but other experiments were using it so this wasn't very realistic. This lead the choice of the T2K experiment to use the off-axis technique: the neutrino beam is not directed towards Super-Kamiokande but there is an angle of 2.5 ° between the beam axis and the SK detector. With this choice, the energy of the neutrinos reaching SK is adjusted to 600 MeV. Furthermore, this technique has another advantage - it produces a much narrower band energy beam - that will be detailed in the next section.

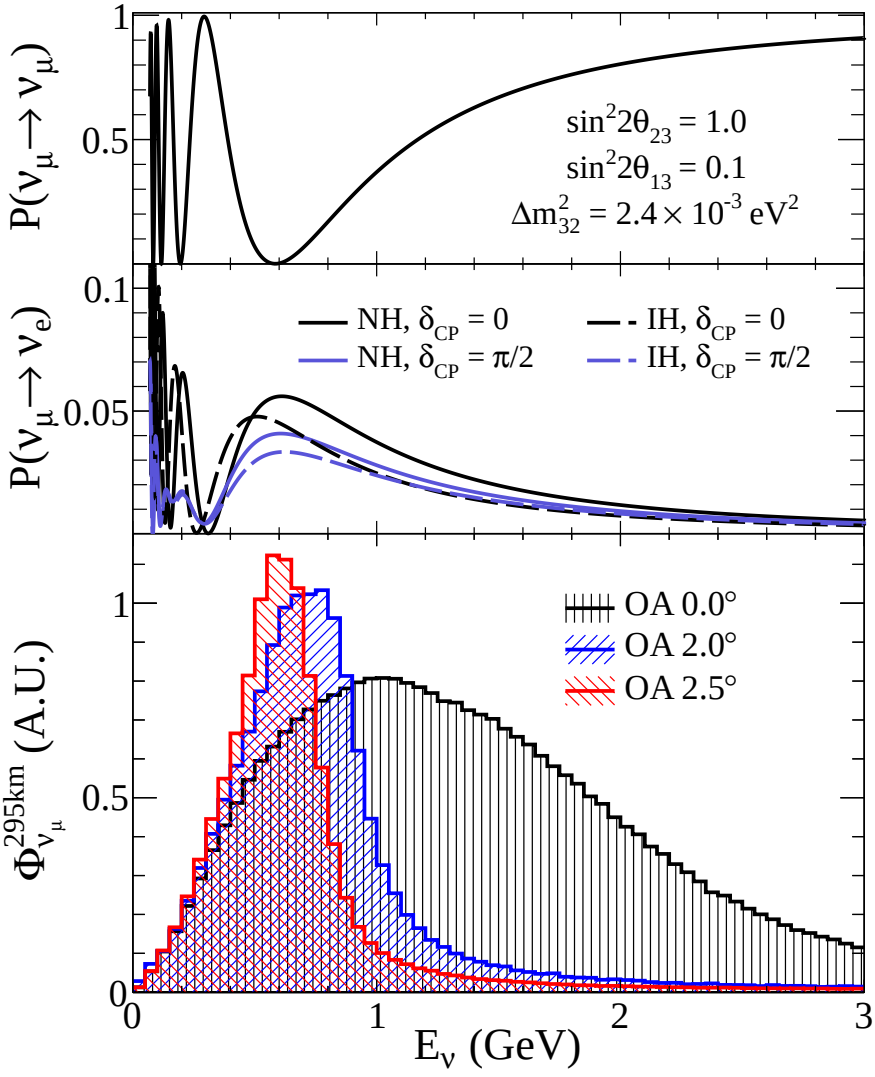

Figure 2.2 – Top: ν_μ survival probability as a function of the neutrino energy. Middle: ν_e appearance probability as a function of the neutrino energy for different values of δ_{CP}. Bottom: ν_μ flux for three different off-axis angles. The relative normalization of those fluxes is arbitrary. Both ν_μ disappearance and ν_e appearance are maximal at 600 MeV which is the peak of the flux at 2.5°.

The appearance of electron (anti)neutrinos ($\nu_\mu \mapsto \nu_e$ or $\bar{\nu}_\mu \mapsto \bar{\nu}_e$) gives us a measurement on the mixing angle θ_{13} and the CP violation phase δ_{CP} while the disappearance of muon

(anti)neutrinos ($\nu_\mu \mapsto \nu_\mu$ or $\bar{\nu}_\mu \mapsto \bar{\nu}_\mu$) gives us a measurement on θ_{23} as well as the squared mass difference Δm^2_{32}.

2.1.1 The beam production

The JPARC facility hosts a synchrotron, a circular particle accelerator that accelerates protons up to 30 GeV (figure 2.3). Once they have been accelerated to the required energy, these protons are sent by bunches towards a carbon target, whith each bunch being separated by 2.48 ns. This corresponds to a power of 475 kW.

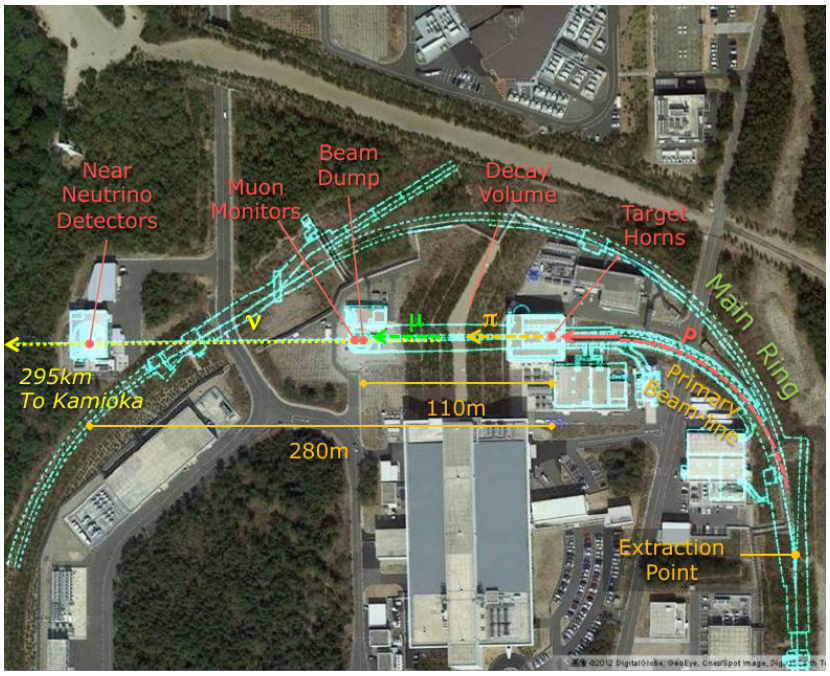

Figure 2.3 – Aerial picture of the neutrino beamline at the J-PARC facility.

The carbon target is a cylinder of 91.4 cm in length with a radius of 2.6 cm and is placed inside a titanium container of 0.3 cm as shown in Figure 2.4. Around this titanium container and after it are a set of three electromagnetic horns (Figure 2.5).

Figure 2.4 – Scheme of the carbon target installed in the beamline.

These horns are ran through by a 250kA electric current of positive or negative sign, depending on whether we run in Forward Horn Current (FHC) mode to produce muon neutrinos or in Reverse Horn Current (RHC) mode to produce muon antineutrinos. This creates a solenoidal magnetic field inside the horns whose direction depends on the sign of the elec-

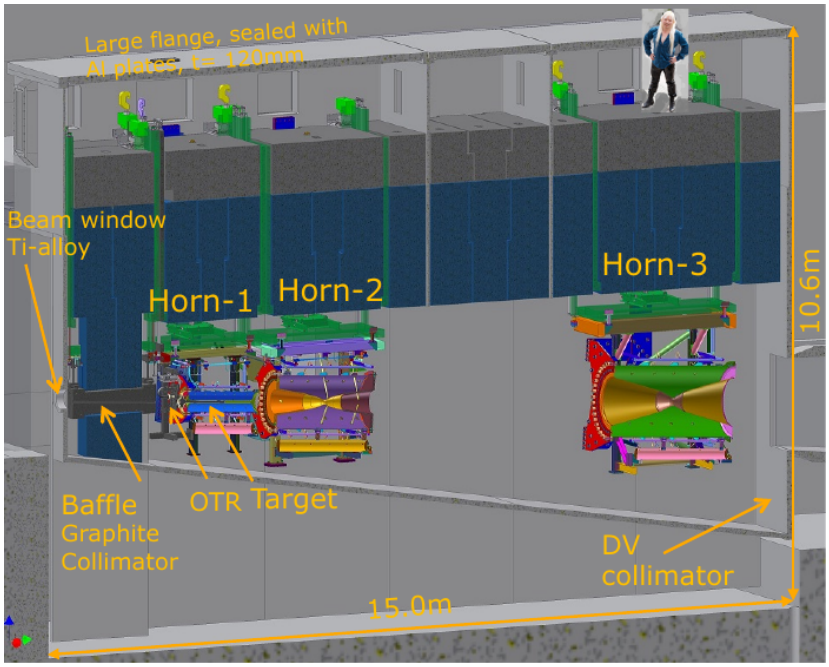

Figure 2.5 – Scheme of the target station. The protons redirected from the synchrotron collide with the carbon target and create all kinds of charged mesons that are focused by the magnetic fields of the horns.

trical current (figure 2.6).

The collisions between the accelerated protons and the target carbon atoms create several hadrons. These hadrons are mainly charged pions $\pi^{\pm}$. The second most common hadrons are kaons $K^{\pm}, K^0_L$. Depending on the sign of the current running through the horns and thus the direction of the magnetic field, positively charged or negatively charged particles will be focused in the direction of the beam. The particles of opposite sign will conversely be deflected away from the beam direction by the same magnetic field. After the target station, all the particles with a small enough angle will enter the decay tunnel, about 100 m long and filled in helium. In this tunnel, the hadrons will decay, possibly several times until neutrinos are created. The list of the decays producing neutrinos can be found in Table 2.1.

At the end of the decay tunnel is a "beam dump", a block of concrete that will stop the non-neutrino products of the decays, namely the muons, electrons and the hadrons. But the neutrino beam will freely go through it. However some high energy muons will still go through the dump and arrive at the Muon Monitor (MuMon) that has for purpose to monitor the intensity of the flux, as well as to determine the position of the center of the beam. This information is very important in order to be sure we are working at the correct angles. The hadrons will not go through the beam dump however, as their cross sections with matter are much more important than those of the muons.

Then, all the particles go through the ground before arriving to the detectors pit, 280 m further. This causes all the muons to stop while the ground is not opaque to the neutrinos.

In the FHC mode, the final neutrino beam is mainly composed by muon neutrinos, with a small contamination of muon antineutrinos, electron neutrinos and electron antineutrinos. In the RHC mode, the final antineutrino beam has mainly muon antineutrinos, with a contami-

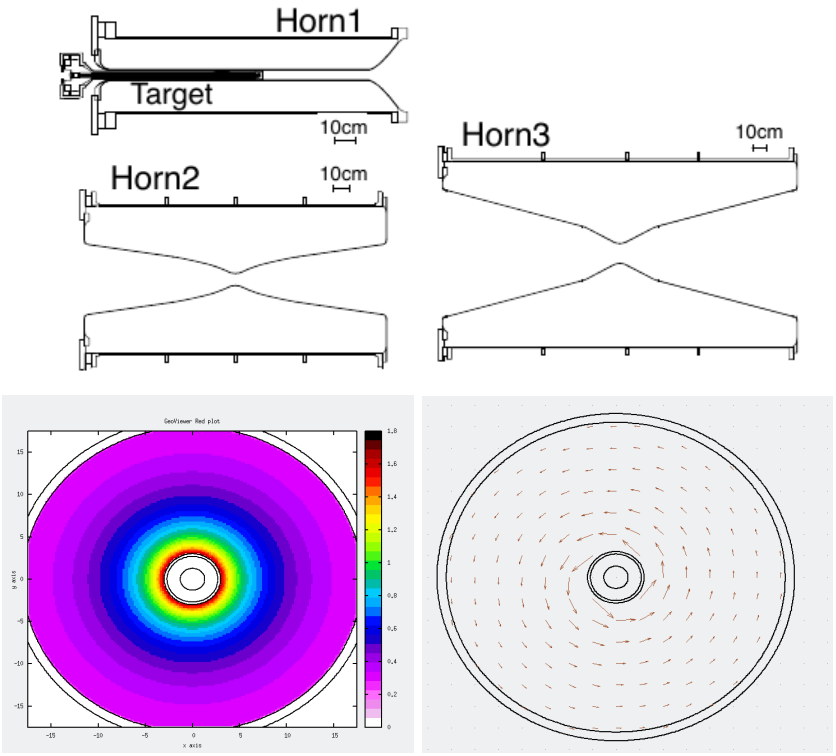

Figure 2.6 – Scheme of the three electromagnetic horns in the target station (top). Magnetic field intensity in Tesla (bottom left) and direction (bottom right) inside the first horn of the target station.

Channel		branching ratio (%)
$\pi^+ \mapsto$	$\mu^+ + \nu_\mu$	99.99
	$e^+ + \nu_e$	00.01
$\pi^- \mapsto$	$\mu^- + \bar{\nu}_\mu$	99.99
	$e^- + \bar{\nu}_e$	00.01
$K^+ \mapsto$	$\mu^+ + \nu_\mu(+\pi^0)$	66.9
	$e^+ + \nu_e + \pi^0$	5.1
	$\pi^+ + \pi^0, \pi^+\pi^0 + \pi^0, \pi^+\pi^+ + \pi^-$	28.0
$K^- \mapsto$	$\mu^- + \bar{\nu}_\mu(+\pi^0)$	66.9
	$e^- + \bar{\nu}_e + \pi^0$	5.1
	$\pi^- + \pi^0, \pi^- + \pi^0 + \pi^0, \pi^+ + \pi^- + \pi^-$	28.0
$K^0_L \mapsto$	$\pi^+ + \mu^- + \bar{\nu}_\mu, \pi^- + \mu^+ + \bar{\nu}_\mu$	27.0
	$\pi^+ + e^- + \bar{\nu}_e(+\gamma), \pi^- + e^+ + \bar{\nu}_\mu(+\gamma)$	40.9
	$\pi^- + \pi^+ + \pi^0$	12.5

Table 2.1 – Main decay channels of the hadrons products of the proton-carbon collisions and branching ratio Taken from [39]

nation of muon neutrinos, electron neutrinos and electron antineutrinos. This contamination is higher in the RHC mode because of the initial beam is made of protons which are positively charged particles thus producing more positively charged hadrons.

The detailed prediction of all those hadronic processes is extremely difficult. For this reason a dedicated experiment NA61/SHINE [40] has been conducted in order to measure the production of hadrons using a replica target of the T2K experiment. The composition of the flux and the makeup of the parents hadrons decaying into the neutrinos measured by this experiment is shown in Figure 2.7.

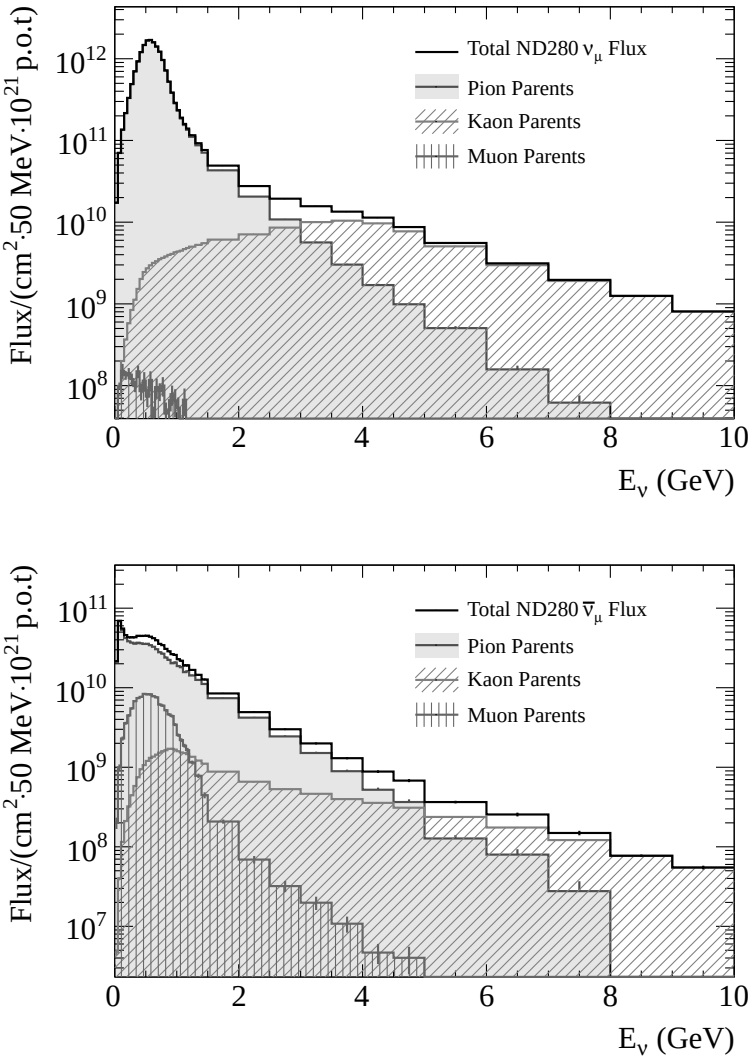

Figure 2.7 – Neutrino flux prediction in FHC mode at the ND280 detector complex using the measurements of the NA61/SHINE experiment. Those fluxes are broken down by their different parent hadrons contributions. Top panel displays the ν_μ flux and bottom panel the $\bar{\nu}_\mu$ flux. Taken from [39].

Now we can study the kinematics of the neutrinos production to see another advantage of working with the off-axis technique. When considering the decay of pions (cf Figure 2.8)

$$\pi^+ \mapsto \mu^+ + \nu_\mu \tag{2.1}$$

the conservation of the quadrimomentum gives

$$\underline{P}_\pi = \underline{P}_\mu + \underline{P}_\nu \tag{2.2}$$

where $P_\pi = (E_\pi, \vec{p}_\pi)$, $P_\mu = (E_\mu, \vec{p}_\mu)$, $P_\nu = (E_\nu, \vec{p}_\nu)$ where $E_\nu \approx p_\nu$ and the angle between $\vec{p_\pi}$ and $\vec{p_\nu}$ is θ.

So we can write

$$\underline{P}_\mu = \underline{P}_\pi - \underline{P}_\nu$$

Squaring the terms gives

$$\underline{P}_\mu^2 = (\underline{P}_\pi - \underline{P}_\nu)^2$$

The left term can be developed as

$$\underline{P}_\mu^2 = m_\mu^2$$

while the right term can be developed as

$$\begin{aligned}(\underline{P}_\pi - \underline{P}_\nu)^2 &= \underline{P}_\pi^2 + \underline{P}_\nu^2 - 2\underline{P}_\pi \cdot \underline{P}_\nu \\ &= m_\pi^2 - 2\left(E_\pi E_\nu - \vec{p}_\pi \cdot \vec{p}_\nu\right) \\ &= m_\pi^2 - 2\left(E_\pi E_\nu - p_\pi E_\nu cos(\theta)\right)\end{aligned}$$

Combining the two terms we obtain

$$m_\mu^2 = m_\pi^2 - 2\left(E_\pi E_\nu - p_\pi E_\nu cos(\theta)\right)$$

$$m_\pi^2 - m_\mu^2 = 2E_\nu\left(E_\pi - p_\pi cos(\theta)\right)$$

And so

$$E_\nu = \frac{m_\pi^2 - m_\mu^2}{2\left(E_\pi - p_\pi cos(\theta)\right)} \tag{2.3}$$

On axis the energy distribution of the neutrinos tends to be spread out and is directly related to the parent pion. But off-axis the neutrino energy is distributed more narrowly because of the consequences of the Equation 2.3, as depicted in Figure 2.9. This is the additional reason why off-axis beams are advantageous, despite the loss in beam intensity.
Indeed we know that the oscillation formula varies in $\frac{L}{E}$, and the baseline Length L is fixed, so when averaging the probability of oscillation over the distribution of E, a narrower energy peak is very favourable to an accurate measurement of the parameters.

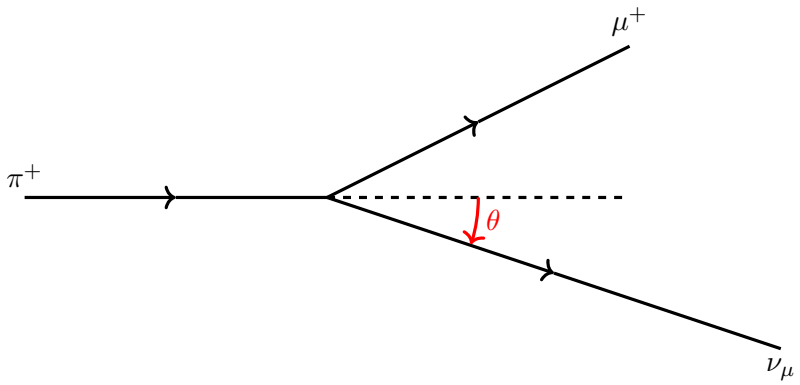

Figure 2.8 – Decay of a pion into a muon and a muon neutrino

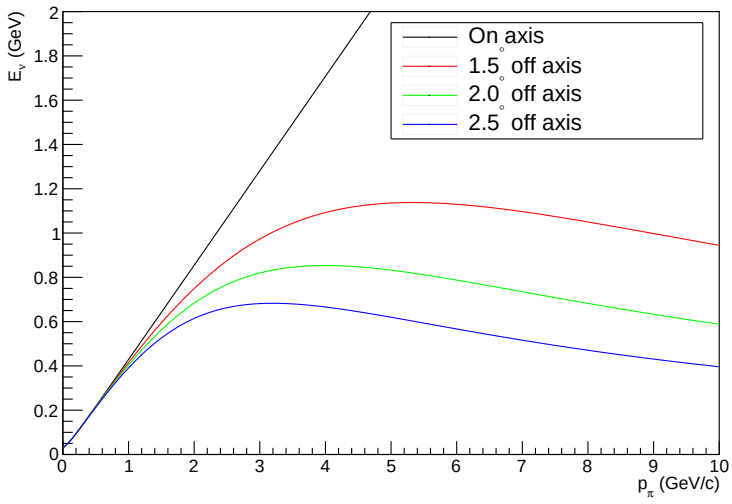

Figure 2.9 – Neutrino energy in function of the pion parent momentum on-axis and for three different off-axis angles.

2.1.2 The near detectors

The T2K neutrino beam flux can only be predicted with a 10% uncertainty. In order to observe the subdominant $\nu_\mu \rightarrow \nu_e$ oscillation one has to be able to measure the neutrino energy spectrum, flavour content, and interaction rates of the unoscillated beam to be able to correctly predict the neutrino interaction rate at Super-Kamiokande. This is the purpose behind the installation of the near detectors in the J-PARC complex.

The near detectors are all gathered 280 m after the carbon target, in a pit. Some of them are aligned with the axis of the neutrino beam, while the other are at the same off-axis angle than Super-Kamiokande. The peak of the neutrino energy spectrum depends on the angle between the beam axis and the direction between the target and the detector. The higher the angle, the lower the energy peak (Figure 2.2)

The on axis detectors: INGRID and Proton Module

The INGRID (Interactive Neutrino GRID) detector is centered on the neutrino beam axis and has been design to monitor directly the neutrino beam direction and intensity on a daily timescale. The detector consists of 14 modules arranged as a cross of 7 horizontal and 7 vertical modules, as shown in Figure 2.10. Two additional modules have been temporarily used at off-axis directions outside the main cross to check the transverse profile of the beam. An INGRID module (see Figure 2.26) is made of 9 iron plates which serve as neutrino target interleaved by 11 tracking planes made of plastic scintillators. A more thorough description of a module can be found in Section 2.3.3 describing the WAGASCI experiment. The measurement of INGRID and the information provided by the Muon Monitor (MuMon) are used to estimate the intensity of the flux.

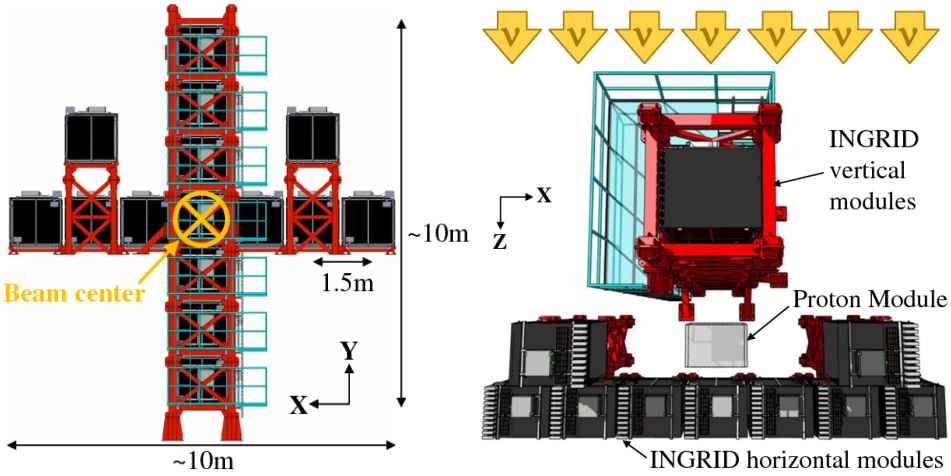

Figure 2.10 – The INGRID on-axis detector (left) cross centered on the beam axis. The position of the Proton Module is displayed on the right panel.

The beam width is about 10 m at the distance of the near detectors (280 m from the target station). The width of the INGRID cross (10.3 m) has been chosen with this in mind.

An extra module, called the Proton Module, different from the 16 INGRID modules, has been added in order to detect with good efficiency the muons together with the protons produced by the neutrino beam in INGRID. The goal of this Proton Module is to identify the

quasi-elastic channel for comparison with Monte Carlo simulations of beamline and neutrino interactions. It consists of scintillator planes without any iron plate. A detailed description of the Proton Module

The off-axis detector: ND280

The main goal of the ND280 detector is to characterize the neutrino flux produce by the accelerator by measuring both its flavour composition and its energy spectrum. For this reason it is magnetized in order to distinguish the charge of the lepton produced by CC interactions.

The ND280 detector is constituted of several major parts pictured in Figure 2.11. All of them are placed inside the old CERN UA1/NOMAD magnet providing a magnetic field of 0.2 T, to measure momenta with good resolution and determine the sign of charged particles produced by neutrino interactions.

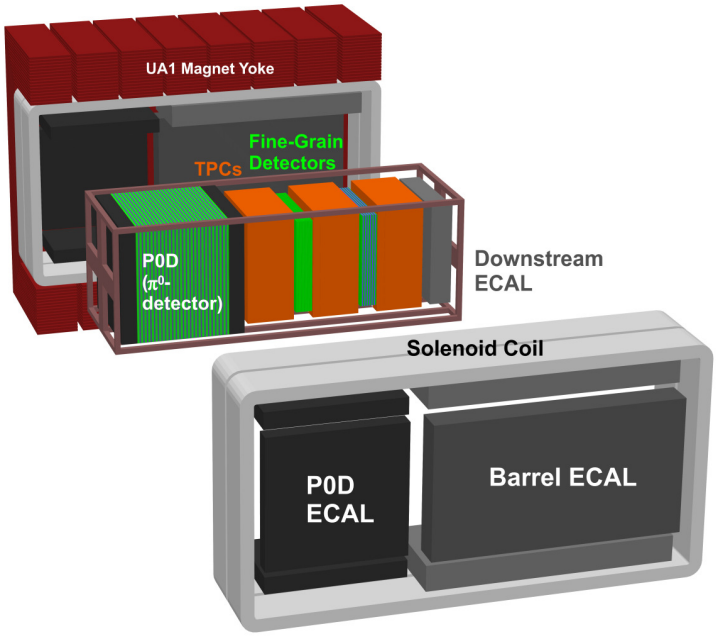

Figure 2.11 – Scheme of the ND280 detector.

The first upstream detector is the π^0 Detector (P0D). It has the role to detect the π^0 that can be created by the Neutral Current interaction NCπ^0 where an incoming neutrino interacts with a nucleus to create a neutral pion π^0. NCπ^0 interactions are the second main source of background in the search for ν_e appearance at SK. The reason behind is that π^0 mainly decay into two photon. In SK, a photon will create an electromagnetic showers which is similar to an electron signal. If one of those produced photons is missed, a NCπ^0 event will completely mimic the ν_eCC signal searched at SK. For this reason, it is very important that we be able to estimate the cross section of this interaction mode on water. The P0D is made of a central module in between two electromagnetic calorimeters. The central module has twenty-five pairs of horizontal and vertical scintillator planes interleaved with twenty-five 3 cm-thick water target planes and twenty-five 1.6 mm-thick brass planes. The two electromagnetic calorimeters each have seven pairs of horizontal and vertical scintillator planes interleaved with 4 mm-thick lead planes.

Downstream of the P0D, the tracker, comprises three Time Projection Chambers (TPCs) and two Fine Grained Detectors (FGDs). The upstream FGD has thirty pairs of horizontal and vertical scintillator planes. The downstream FGD has the same structure but the planes are interleaved with seven 3 cm-thick water planes. Each FGD weighs about 1 ton. The first FGD is a hydrocarbon target while the second FGD is a both a hydrocarbon and water target. The TPCs are argon-based. They have excellent imaging capabilities in three-dimensions, are able to measure the momenta of charged particles thanks to being operated in a magnetic field and possess an excellent e/μ particle identification.

The three TPCs and the two FGDs are surrounded by a barrel electromagnetic calorimeter (ECAL). In addition a downstream ECAL is places after the most downstream TPC. The barrel ECAL is made of thirty-two scintillator planes interleaved with thirty-one 1.75 mm-thick lead planes. The downstream ECAL is made of thirty-five scintillator planes interleaved with thirty-four 1.75 mm-thick lead planes. The ECALs' function is to measure the energy of the particles tracked by the TPCs and the FGDs (Figure 2.12) and moreover to detect the γ-rays that do not convert in the inner detectors.

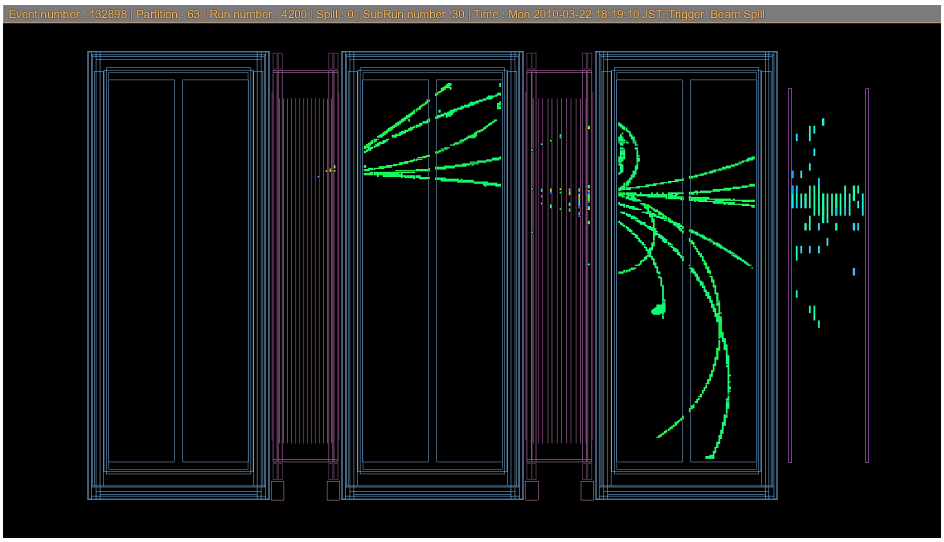

Figure 2.12 – Tracking of an event by the FGDs, TPCs and downstream ECAL of ND280.

2.1.3 The far detector: Super-Kamiokande

295 km down the beamline, at the Kamioka prefecture stands the Super-Kamiokande detector. This is the detector that detects the neutrino beam after the disappearance of muon neutrinos and the appearance of electron neutrinos. But it actually precedes the T2K experiment by about a decade since it has been operating since 1996, and first gave evidence of neutrino oscillations by detecting atmospheric neutrinos. It still does to this day and is an actor in the measurement of the parameters θ_{23} and Δm^2_{32}.

The Super-Kamiokande detector is a tank full of 50 kton of water (cf Figure 2.13), based on the Cerenkov effect that will be detailed further down. It appears as a cylinder of 39 m wide and 41 m high. This tank is placed 1 km under a local mountain, inside a pit. This suppresses a large amount of cosmic background

The detector is optically separated into two regions, the Outer Detector (OD) and the Inner Detector (ID) by a stainless steel structure covered by plastic sheets. The OD walls are

covered by highly reflective Tyvek sheets. The stainless steel structure holds 1885 outward-facing 8 inches Photo-Multiplier Tubes (PMTs). Though sparsely instrumented, the OD acts as an active veto of cosmic ray muons and other backgrounds and rule out the events in which a particle has been created outside the detector. The ID is well instrumented, with 11129 inward-facing 20 inches PMTs. The distance between two adjacent PMTs is around 70 cm which in the end represents 40% PMT coverage. The wall facing into the ID is lined with a black sheet of plastic meant to absorb light and minimize the number of photons which either scatter off of the ID wall back into the ID volume, or pass through from the ID to the OD. In order to remove edge effects, the fiducial volume is usually defined as a cylinder 2 meters away from the walls of the ID. The fiducial mass of Super-Kamiokande is therefore of 22.5 kton of water.

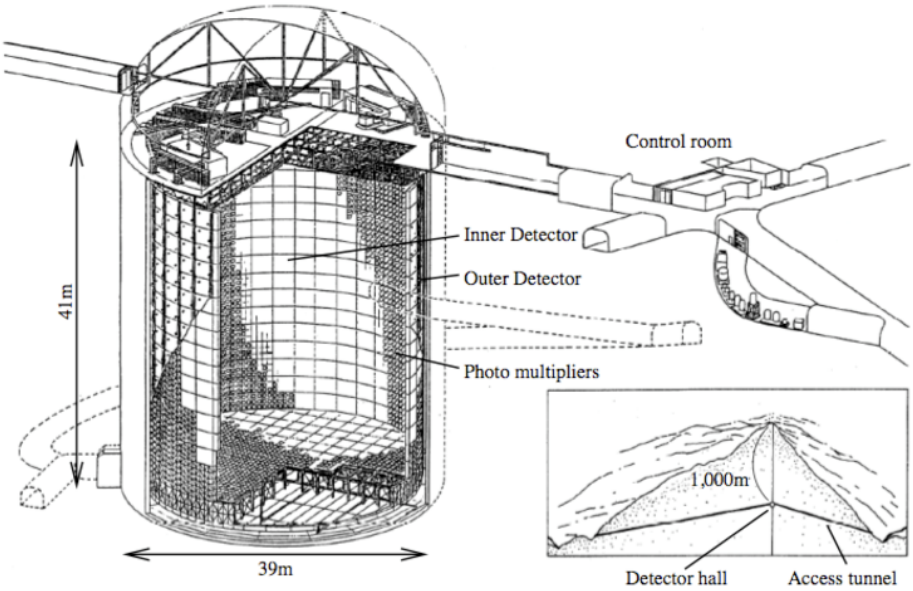

Figure 2.13 – Scheme of the Super-Kamiokande detector [41].

Super-Kamiokande is a Cerenkov effect based detector. The neutrino detection channels are CC interactions with nucleons from the water. The associated charged lepton produce in the interaction will propagate in the water and excite the surrounding atoms and emit light. Because of the energies involved in T2K, the leptons propagate faster than light in the water of the detector (light speed is ≈ 200000 km/s in water). The light is coherently emitted and intense enough for detection only if the particle propagates faster than light. However the loss of energy of a particle in matter is more important the slower the particle. Hence we can assume that the angle of emission of the light is more or less constant while the particle is still traveling faster than light and that the light emission stops when the particle is slowed down under the light speed. Because of this the light will be collected by the PMTs on the wall and form a light ring if the particle stops in the detector and a light disk if the particle exits the detector still traveling faster than light.

The flavour of the produced lepton (and therefore of the initial neutrino) affect the appearance of the light ring. Because of their weight, muons are almost not affected while traveling in matter. However, electrons being much lighter encounter much more scattering processes during their propagation, causing the light to be emitted in different directions. As a result, muon-like rings are clear and well-defined while electron-like rings are fuzzier. This is the basis of the Particle IDentification (PID) in SK. The comparison of a muon-like ring

and an electron-like ring is displayed on Figure 2.14. In the T2K experiment, τ lepton cannot almost be produced with a mean neutrino energy of 600 MeV. Few τ could be produced from the very end tail of the neutrino energy spectrum but even so, the τ would decay immediately in the detector leaving no observable Cerenkov ring (note however that some searches of ν_τ are done at SK through the observation of their decay products). This is the reason why only the disappearance of muon neutrinos and the appearance of electron neutrinos are studied at SK.

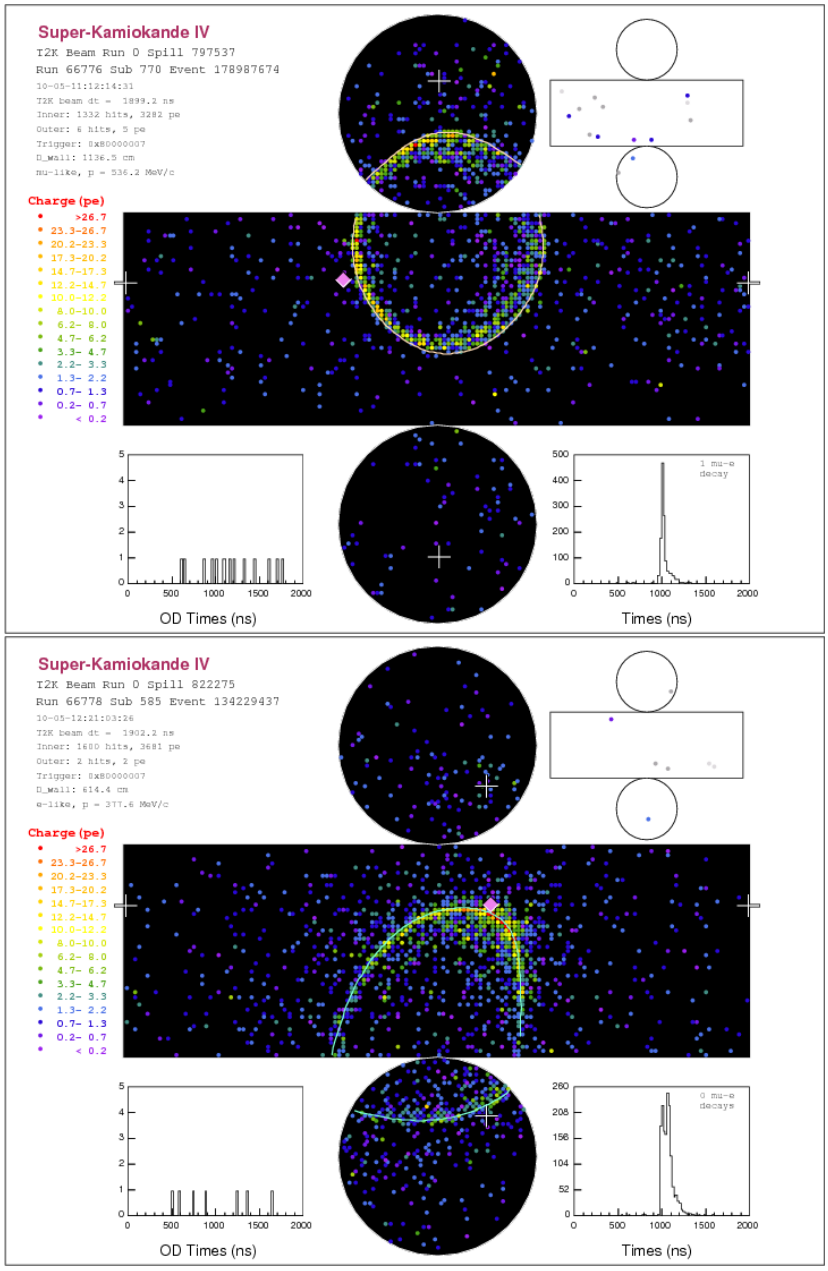

Figure 2.14 – Muon event (top) and electron event (bottom) produced by the interaction of a neutrino in Super-Kamiokande. The muon ring appears much sharper than Cerenkov ring produced by the electron [42].

2.1.4 Results

The T2K experiment has successfully observed the muon neutrino and antineutrino disappearance and is currently the world leading experiment concerning the measurement of the parameters θ_{23} and Δm^2_{32} (see Figure 1.15). T2K has also observed the appearance of electron (anti)neutrino the initial muon (anti)neutrino beam. This lead to a degenerate measurement of both θ_{13} and δ_{CP} (Figure 1.16). Thanks to the independent measurement provided by reactor experiment, T2K is currently accumulating data in order to determine the value of δ_{CP}.

2.2 The WAGASCI experiment

Thanks to the combination of its near and far detectors, the T2K experiment has observed the oscillation of neutrinos and derived some measurements on the oscillation parameters θ_{23}, θ_{13}, Δm^2_{32} and δ_{CP}. But when analyzing the results, we extract the measurements with uncertainties. There are the statistical uncertainty that are related to the number of events we detect, but there are also the systematic errors that are related to the structure and the operation of the detectors. The list of the systematic errors on the number of detected events at Super-Kamiokande is shown on Table 2.2.

As one can one of the main source of systematic error concerns both the prediction of the flux and of the interaction rate (cross-section) at Super-Kamiokande. Even with the constraints from ND280 measurements, this error is of the order of 3% (without ND280, this error would be of about 12%). One of the reasons why this error is still relatively high is that the measurement of the flux and cross-section at ND280 and SK are structurally different:

- The SK detector is a water based detector while the ND280 detectors are carbon-based detector, with only a small water volume. Even though the cross-section on water can be obtained from P0D and second FGD, the small amount of water prevents from obtaining a precise measurement.
- The SK detector has a 4π angular acceptance (isotropic detection) while the near detectors have a forward angular acceptance (an event in a FGD has to reach its downstream TPC). ND280 detectors are unable to constrain neutrino cross-sections at high angle.
- The ND280 doesn't measure neither the flux nor the cross-section but the product of the two quantities. For this reason, in order to measure the cross-section one needs

2016 analysis error table	$\delta N_{SK}/N_{SK}$				
	1-Ring μ		1-Ring e		
Error type	ν mode	$\bar{\nu}$ mode	ν mode	$\bar{\nu}$ mode	$\nu/\bar{\nu}$
SK detector	3.9	3.3	2.5	3.1	1.6
SK Final State & Secondary Interactions	1.5	2.1	2.5	2.5	3.5
ND280 Constrained Flux & Cross-section	2.8	3.3	3.0	3.3	2.2
$\sigma_{\nu_e}/\sigma_{\nu_\mu}$,$\sigma_{\bar{\nu}_e}/\sigma_{\bar{\nu}_\mu}$	0.0	0.0	2.6	1.5	3.1
NC 1γ Cross-section	0.0	0.0	1.5	3.0	1.5
NC Other Cross-section	0.8	0.8	0.2	0.3	0.2
Total Systematic Error	5.1	5.2	5.5	6.8	5.9
External Constraint on θ_{12}, θ_{13}, Δm^2_{21}	0.0	0.0	4.1	4.0	0.8

Table 2.2 – Systematic errors on the number of detected events at Super Kamiokande. The column "1-ring μ" lists the errors on the $\nu_\mu/\bar{\nu}_\mu$ disappearance and the column "1-ring e" the errors on the $\nu_e/\bar{\nu}_e$ appearance. The line labeled "ND280 constrained flux & cross-section" is the one addressed by the WAGASCI experiment. Taken from [43][44].

a measurement at several off-axis angles. This is partly done using INGRID and the Proton Module [45] [46].

Because of these differences, the constraint is not as efficient as it would be if the near detector as the same characteristics as the far detector.

In order to solve these issues, the WAGASCI detector has been designed. The objective is to provide a solution to each of the three issues we mentioned earlier: providing a wider angular coverage, a larger water target, and a single off-axis angle.
The WAGASCI detector (cf Figure 2.15)has three target modules. The proton module (described further down), a set of plastic scintillator planes. This is the carbon target as well as a tracking device. Downstream of this module are two successive water modules (described further down). The water modules are a succession of plastic scintillator planes intertwined with plastic scintillator grids. These structures are placed inside stainless steel tanks filled with water. These are the water and carbon targets ($\sim$ 80% water/20% carbon).
A downstream magnetized calorimeter (babyMIND, [47]) serves to measure the momentum and the charge of the charged leptons produced in the targets by charged current interactions between the incident neutrinos and the nuclei of the target. It is mainly made of interleaved magnetized iron and plastic scintillator planes. Finally, two side calorimeters (Side Muon Range Detectors, sMRD) placed on the right and left of the targets provide a high angle coverage for the charged leptons produced in the targets. Their working principle is the same than Baby-MIND but the iron is not magnetized and therefore cannot provide the charge of the emitted lepton.

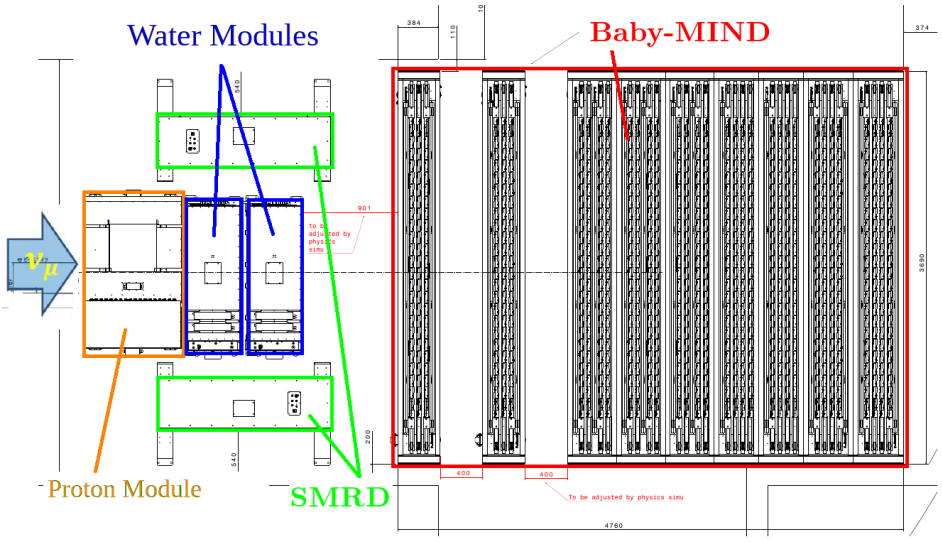

Figure 2.15 – Final configuration of the WAGASCI experiment. data taking will start at Fall 2019 and will complete all the original objectives of the detector: the high angle tracking and large target water volume.

Therefore, the WAGASCI detector provide a high angle coverage for the event detection, thanks to the combination of the grid in the Water Modules and the side-MRDs which combined allow the tracking of leptons produced at high angles. It also provides a measurement of the cross-section of neutrinos on water and carbon and the ratio of these two cross-sections at 1.5 ° off-axis.

Unfortunately, the data set I am using for this thesis was taken with an intermediate

setup:

- Only one of the two Water Module was installed
- Both side-MRDs were not installed
- Baby-MIND was not installed. Therefore the collaboration chose to use one of the INGRID module as downstream muon calorimeter. The downstream coverage is therefore done with a lesser calorimeter, non magnetized, less wide and less deep.

At the moment when these lines are written, the final setup is however operating and accumulating data. The results obtained with that set will be accordingly improved.

In the remaining part of this thesis I will focus on the intermediate setup I worked with.

2.3 The WAGASCI intermediate setup

In the intermediate setup which took data from October 2017 to April 2018, three modules are installed in line as shown on Figure 2.16 on the B2 floor of the ND280 pit. From upstream to downstream the modules are: the Proton Module, the Water Module, and an INGRID module. The blueprint of the B2 floor is depicted in Figure 2.17.

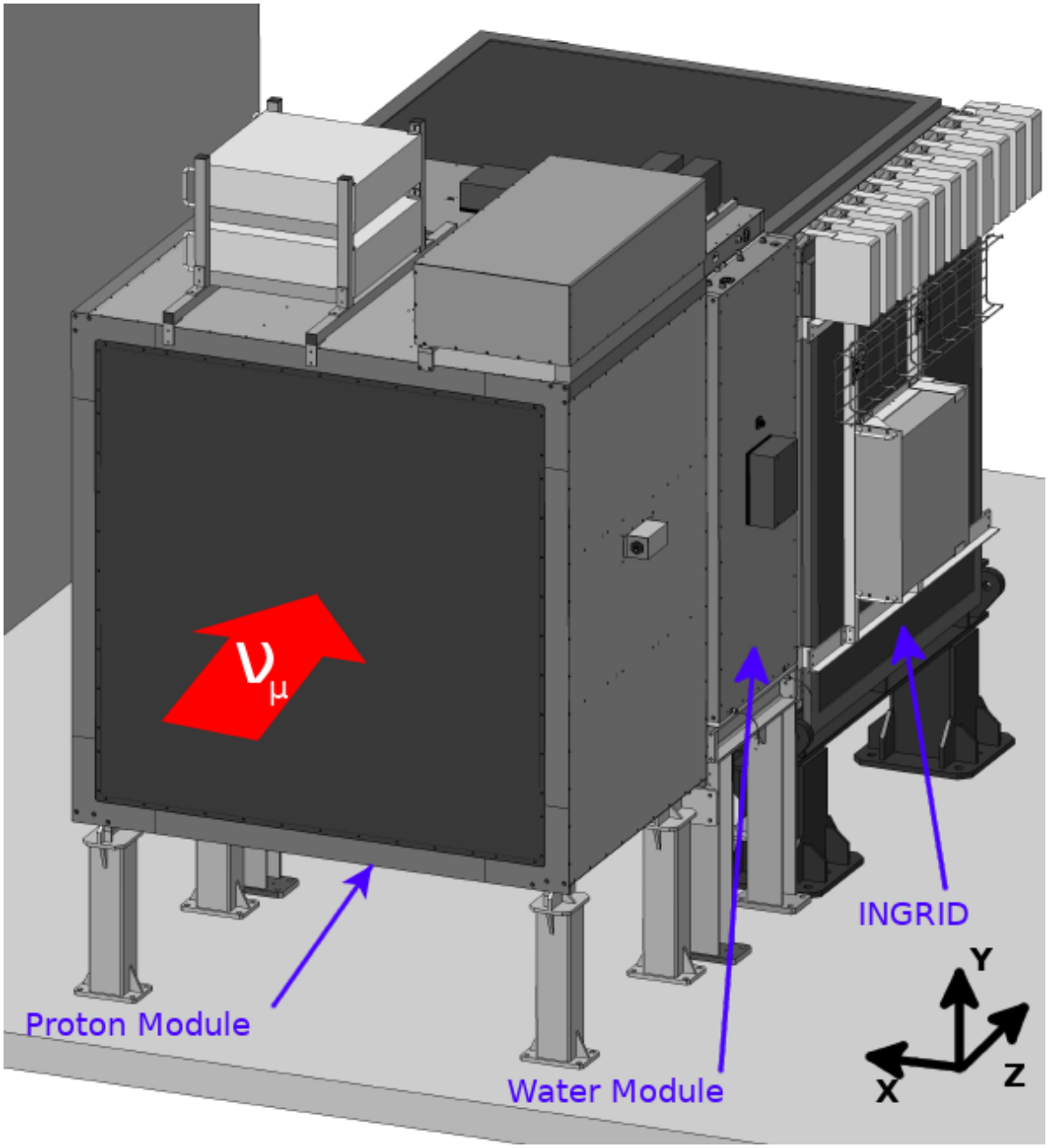

Figure 2.16 – Module arrangement for the intermediate setup. The neutrino beam first faces the Proton Module and then the Water Module. The INGRID module is the most downstream and serves as a muon calorimeter. The coordinates are the following: the z-axis is the longitudinal axis, and x and y-axis defines the transverse plane.

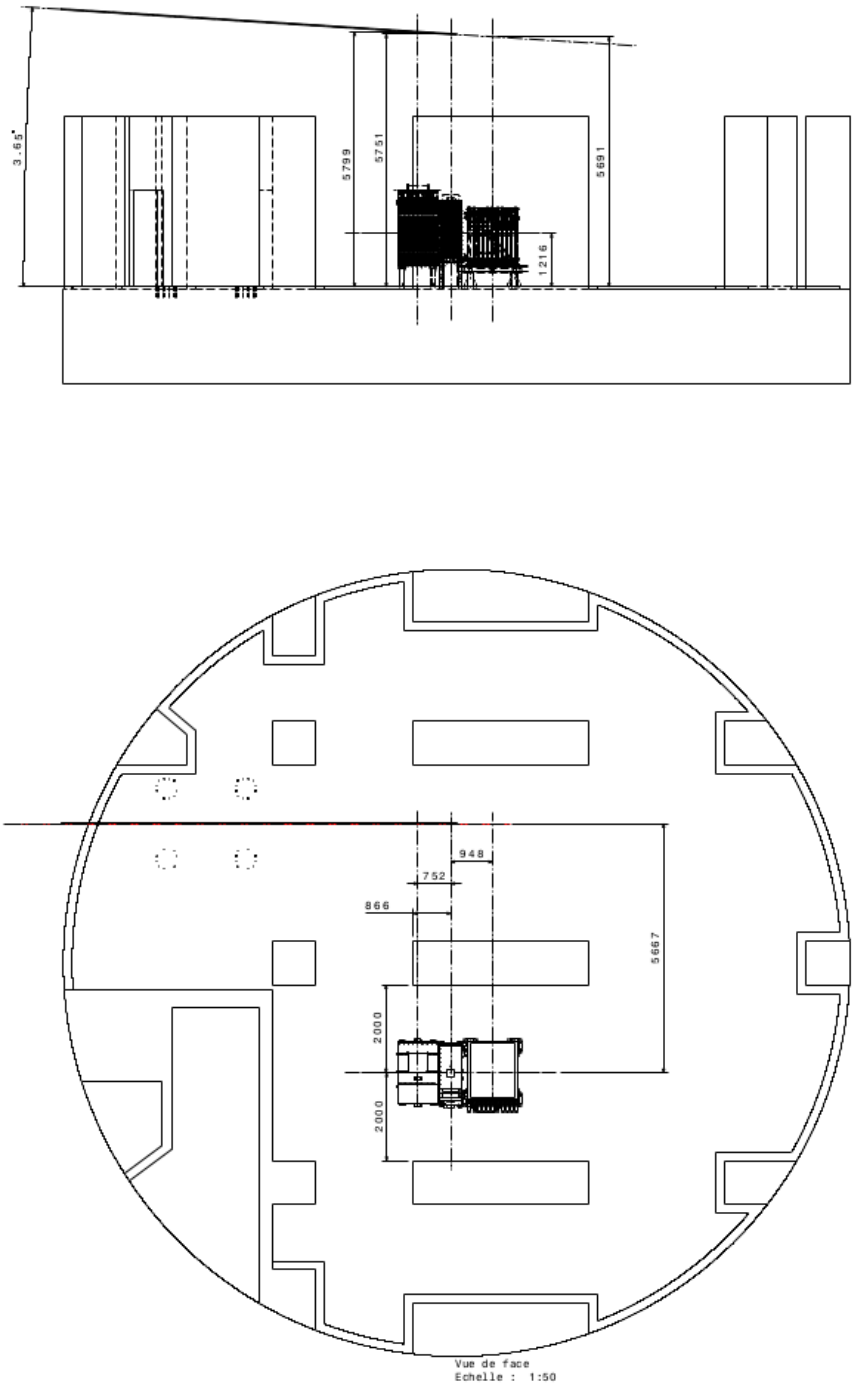

Figure 2.17 – Blueprint of the B2 floor. The 3 modules are placed in a line. They are surrounded by two concrete pillars. The beam comes from the left to the right.

2.3.1 The Water Module

The Water Module serves both as targets for the neutrino interactions and as tracking planes for the charged particles. The basic structure of this detector is a set of scintillators gathered in 8 blocks of 4 planes as depicted on Figure 2.18:

- a plane of 40 scintillators along the x-axis providing the (y,z) coordinates of an energy deposit.
- a grid of 40 scintillators: 20 along the x direction and 20 along the y direction, clipped to one another providing the (x,z) and (y,z) coordinates of an energy deposit. This grid enables the tracking to large opening angles (see Figure 2.19) as soon as the muon momentum is great enough to cross few scintillator planes ($p_\mu \geq 250$ MeV).
- a plane of 40 scintillators along the y axis providing the (x,z) coordinates of an energy deposit.
- another grid of 40 scintillators.

for a total of 1280 channels. Each scintillator is of size 2.5 cm × 0.3 cm × 102 cm. In order to be able to build the grid structure some slits are cut in the scintillators as shown in Figure 2.20

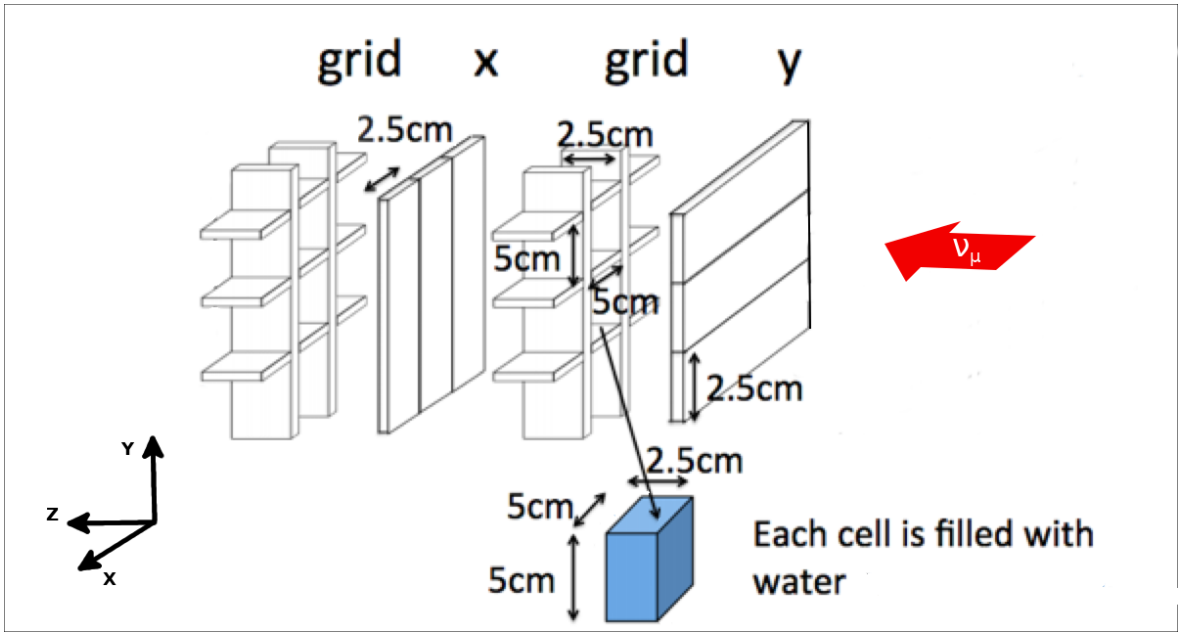

Figure 2.18 – One block of the Water module

Each scintillator is a block of polystyrene C_8H_8 with traces of diverse carbon-based materials to enhance the scintillating properties. Inside the scintillators run an optical fiber which is glued to the former with a carbon-based optical cement. The bloc is then painted with a titanium based reflecting coating whose purpose is to keep the light produced in the scintillator inside it. A black painting is then applied as a finishing touch. This step has been added after the water module prototype was proved to have significant cross-talk between the grid scintillators. The grid allows for a tracking of high angle tracks that would not be reconstructed by only a set of scintillator planes. Even though the intermediate configuration cannot make use of the high angle muons because of the lack of electric calorimeters on the side, it will be put to use in the final configuration.

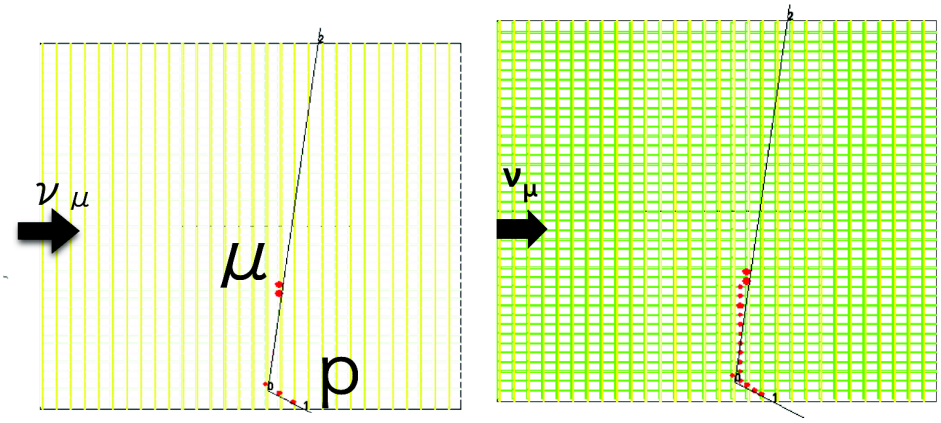

Figure 2.19 – Two dimensional tracking for a ν_μCC interaction. The muon is barely seen in (a) while it is well tracked in (b) thanks to the grid structure.

Figure 2.20 – (a) Scintillators used to build the grid structure of the Water Module. (b) Gluing of 40 scintillators to form a plane on the grid structure.

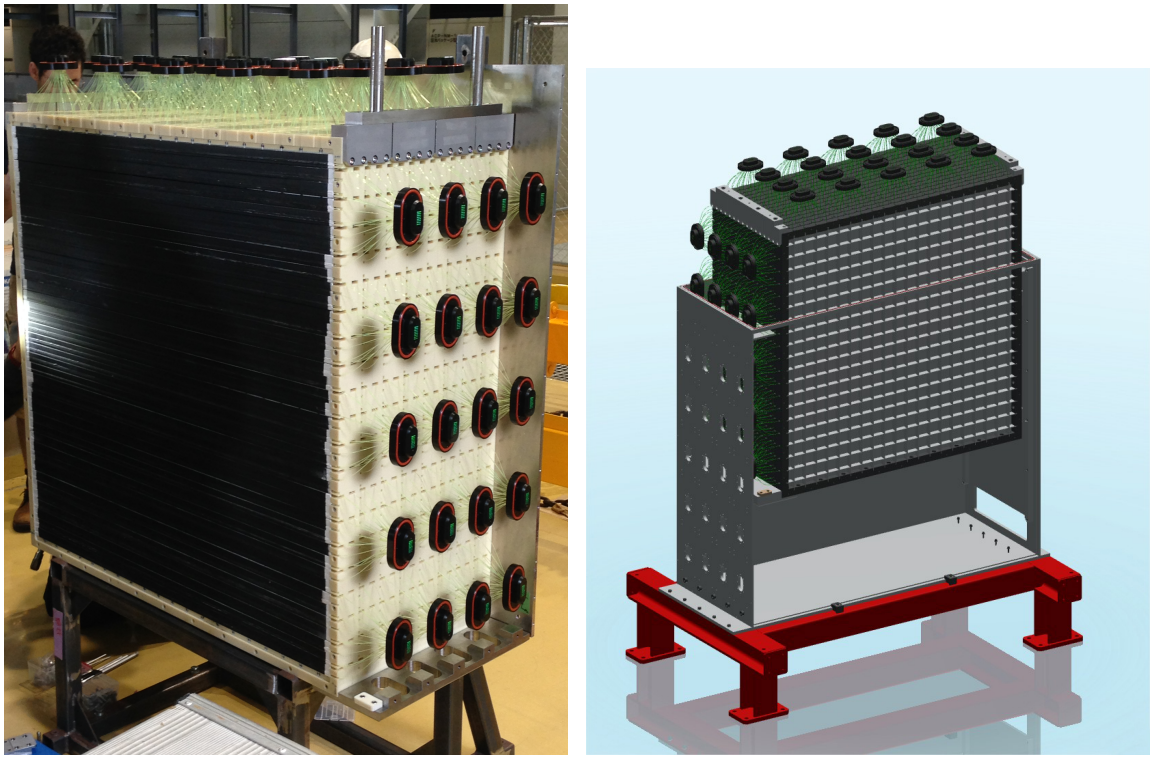

(a) Water Module scintillators (b) Water Module grid structure

Figure 2.21 – The Water Module before (left) and during (right) its installation in the stainless steel tank. The fibers of two basic structure are gathered together to be read by a ten 32 channel MPPC.

These scintillator blocks are placed inside a stainless steel tank filled with 600L of water (Figure 2.21). The relatively small thickness of the scintillator enables to have a total mass of scintillators of only 20% of the total fiducial mass. As a comparison, plastic scintillators account for about 45% of the fiducial mass of the FGD2. The water is therefore the primary target for the neutrino interactions while the scintillators track the charged particles (mainly muons) produced through neutrino interactions.

Fibers are glued inside the scintillators to collect the light created by the passage of charged particles in the material. Each fiber carries the light towards a Multi Pixel Photon Counter (MPPC): an electronic device that converts the light into an electric signal (photo-electrons, pe). These photo-electrons are then counted with an Analog to Digital Converter (ADC).

In order to properly convert the signal, we need to first calibrate the ADC so that we know how many photo-electrons correspond to a given number of ADC counts. The way to go is to disconnect the ADC from the MPPC and to record the activity of the ADC. There will be random creations of electron and holes in matter that the ADC will be able to detect. The probability to have a given number of electrons n produced by this activity is given by a thermodynamics study and has an exponential behavior $\sim \exp(-n/n_0)$. When looking at the distribution of the output electrical signal of the ADC, we will see several peaks, regularly spread and with the values of the peak decreasing. The first and highest peak is called the pedestal. The distance between the pedestal peak (no pe) and the first next peak (1 pe) is the gain of the ADC (Figure 2.22) and correspond to the electrical signal generated by the hit of one electron. We eliminate the channels whose gain deviation is larger than 10% compared

to the mean value of 40 ADC counts.

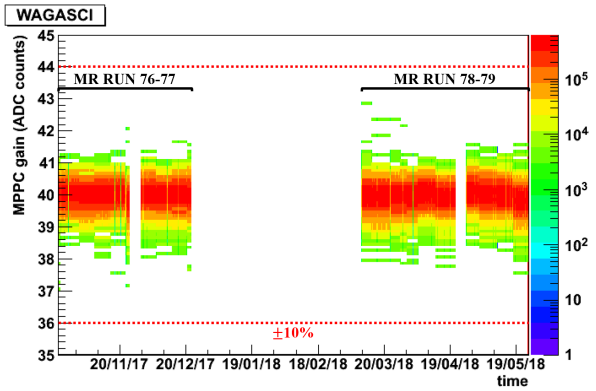

Figure 2.22 – ADC gain for the Water Module

The Water Module uses a new electronics different from the one of the on-axis prototype Water Module. However at the time when this intermediate configuration was running, the synchronization between the beam time and the electronic clock was not operational. As a result the timing of the water module events is random and this information cannot be used for the reconstruction procedure that will be described in the later sections. Fortunately this issue has been solved for the final configuration and the timing is now usable.
The light yield of a scintillator is the amount of light generated by the passage of a charged particle. It depends on the material the scintillator is made of. This light yield is estimated by detecting sand muons (muons that are produced in the B2 floor structures around the detector) and seeing how the collected photoelectrons for each event are distributed (figure 2.23). This serves later on to calibrate the MC to be as close as the data as possible. The mean light yield is of about 10 photo-electrons/3 mm which is enough to detect MIP particle.

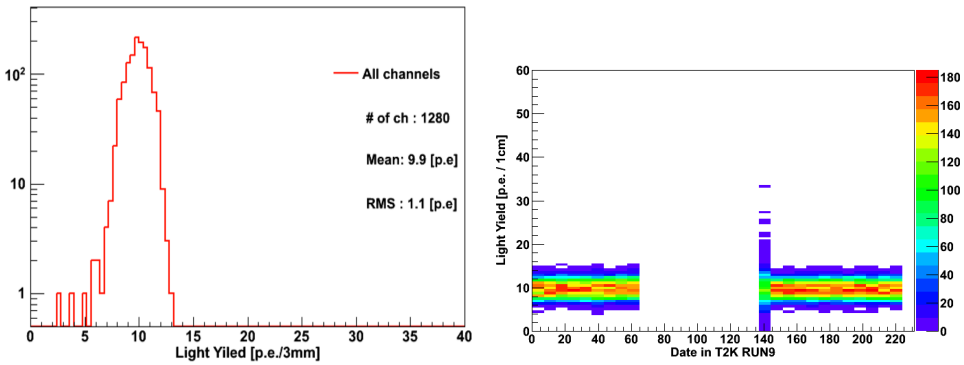

Figure 2.23 – Left: Mean Light yield of sand-muon hit in each scintillator. Right: time dependency of the light yield as a function of time. Each bin is averaged over 7 days.

5 channels are masked during the analysis:

- 3 because their ADC gain deviation is larger than 10 %
- 2 because their light yield is too low

2.3.2 The Proton Module

The Proton Module is a detector entirely made of plastic scintillators (C_8H_8) and serves as a carbon target for the neutrino interactions. A scheme of the Proton Module is displayed on Figure 2.24.

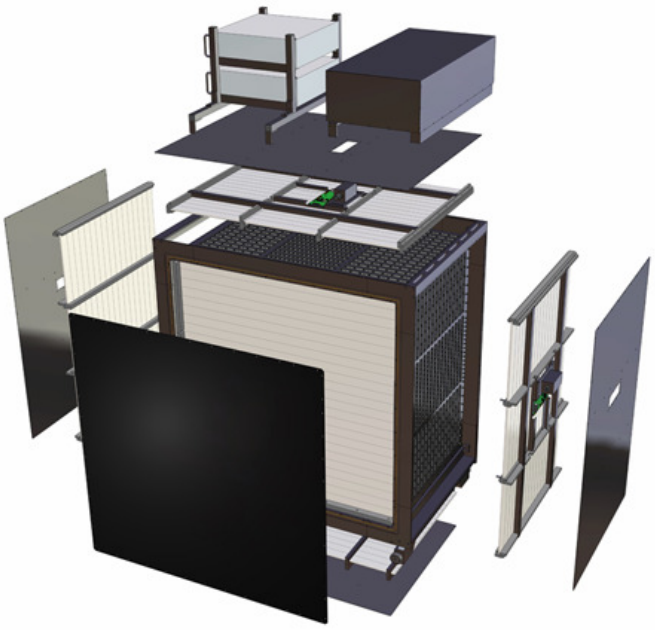

Figure 2.24 – Internal structure of the Proton Module.

It consists of 34 scintillator planes of transverse dimension 120 cm × 120 cm allowing track reconstruction in the detector and that also serve as targets for neutrino interactions with CH. Those planes are made by scintillator bars oriented along the x or y axis and give therefore the (y,z) or (x,z) coordinates of the crossing point of the charged particles in the detector. X and y-oriented tracking planes are alternatively distributed and are separated by 2.3 cm of air.

The planes are made of two different types of scintillator bars: INGRID-type of dimensions 5 cm × 1 cm × 120 cm and Scibar-type of dimensions 2.5 cm × 1.3 cm × 120 cm. The Scibar scintillators are used in the center of the detector in order to improve the granularity since they are half as large. A plane is therefore made of 8 INGRID-type scintillators (40 cm), 16 Scibar-type scintillators (40 cm) and 8 INGRID-type scintillators again. Both INGRID and Scibar-type scintillators have the same chemical composition and are made of polystyrene doped with 1% PPO and 0.03% POPOP by weight. The wavelength of the scintillation light at the emission peak is 420 nm. A thin white reflective coating, composed of Titanium dioxide (TiO2) surrounds the whole surface of each scintillator bar improving light collection efficiency by acting as an optical insolator. A hole with a diameter of about 3 mm in the center of the scintillator bar allows the insertion of a wavelength-shifting (WLS) fiber for light collection.

Two additional veto planes made only of 24 INGRID-type scintillator bars are placed upstream of the detectors. Four external veto planes of 100 cm × 75 cm × 1 cm surround the Proton Module (top, bottom, left and right sides). They are used to identifying and reject external backgrounds.

Finally, the set of scintillators, fibers and photo-sensors is contained in a light-tight dark box. Trip-T front-end electronics boards (TFBs) serve as readout. The mean light yield of each channel has been measured to be larger than ten photon-electrons per 1 cm of MIP tracks and the timing resolution of about 3.2 ns.

Similarly, as what is done for the Water Module, we record the light yield and the MPPC gain for the Proton Module. The MPPC gain is of about 10 ADC counts. The light yield is checked with the sand muons and is of about 25 (35) photo-electrons / 3 mm for INGRID-type (Scibar-type) scintillators. Figure 2.25 shows the evolution of the two quantities with time. Only one channel is masked and excluded from the analysis because its MPPC gain is too low.

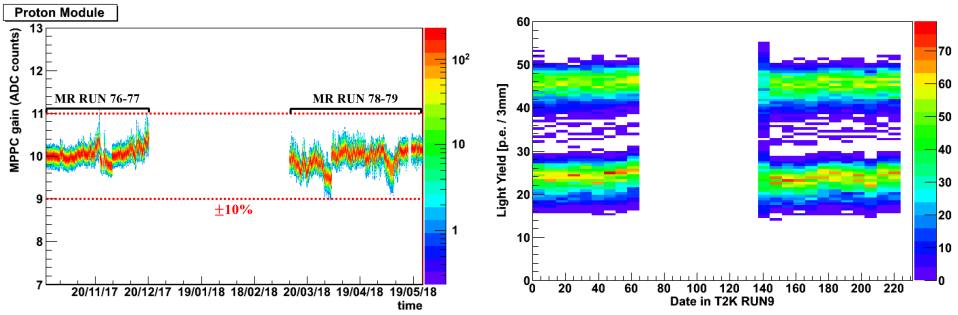

Figure 2.25 – MPPC gain (left) and light yield (right) for the Proton module

2.3.3 The INGRID Module

The INGRID module serves as a downstream muon calorimeter. It consists in a structure of 9 iron plates interleaved by 11 pairs of tracking scintillator planes as shown in Figure 2.26.

The scintillator planes are of transverse dimensions 120 × 120 cm^2. They are made of 24 INGRID-type scintillators (5 cm × 1 cm × 120 cm). Planes along the x and y direction are glued together providing for each of them either the (x,z) or the (y,z) coordinates. The iron plates are of dimensions 120 cm × 120 cm × 6.4 cm. This corresponds to about 7.1 tons of iron. The 9 iron plates are placed in the first 9 intervals between the pair of scintillator planes. No iron plate was placed between the 10th and 11th tracking planes due to weight restrictions.

The internal module is surrounded by veto scintillator planes. Each plane consists of 22 scintillator bars segmented in the beam direction.

The chemical composition of the INGRID-type scintillators has been described above. The electronic is the same than the one used for the Proton Module.

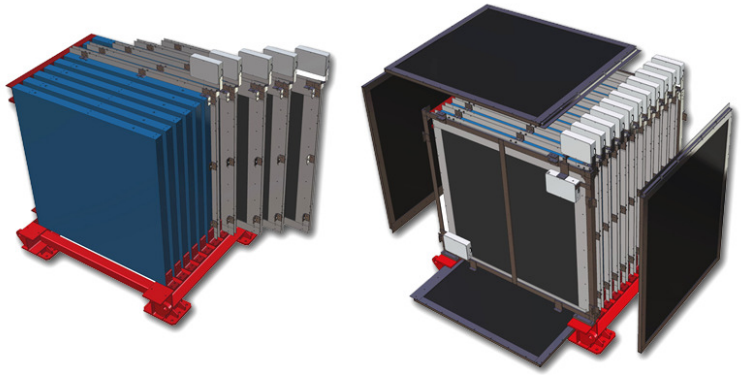

Figure 2.26 – Left: internal structure of the INGRID module with the scintillator planes (blue) and the iron plates. Right: Position of the four veto planes around the internal structure (top, bottom, left and right).

2.4 Impact of the WAGASCI measurement on the T2K experiment

Both the absolute cross-section measurement on water and carbon as well as their ratio will be used by the T2K collaboration to predict the muon neutrino interaction rate at Super-Kamiokande. The absolute measurements will be used as external constraints in the ND280 global fit especially because they give information on the cross-section :

- on a different target nucleus (water),
- at higher muon angles,
- at a different integrated neutrino energy.

The ratio in itself will be used to derive the cross-section on water from the fitted cross-section parameters on carbon.

Chapter 3

Monte-Carlo simulation and CC0π event selection

3.1 Monte-Carlo simulation

The Monte-Carlo simulation allows us to make the best selection cuts during our analysis in order to have the best compromise between purity and efficiency. During the analysis we do our best to remain as model independent as possible. We use the following software for our simulation:

- JNUBEAM 13a [48] to predict the $\overline{\nu}_\mu$, ν_μ, $\overline{\nu}_e$, ν_e fluxes.
- NEUT 5.3.3 [49] to simulate the interactions of the four neutrino flavours with different materials: H_2O, CH, O and Fe
- GEANT 4 (v9r2p01n00) [50] to simulate the propagation of particles through matter and the detector response.
- T2KReWeight [51] for the uncertainties related to the cross-section models.

3.1.1 The Flux

At 1.5°, the anti-neutrino beam has a mean energy of 0.86 GeV. The neutrino flavour breakdown of the flux is shown in Figure 3.1. The $\bar{\nu}_\mu$ makes for 90.8 % of the total flux while ν_μ makes for 8.4% of the total flux. The neutrinos enter the WM (PM) with mean angles of

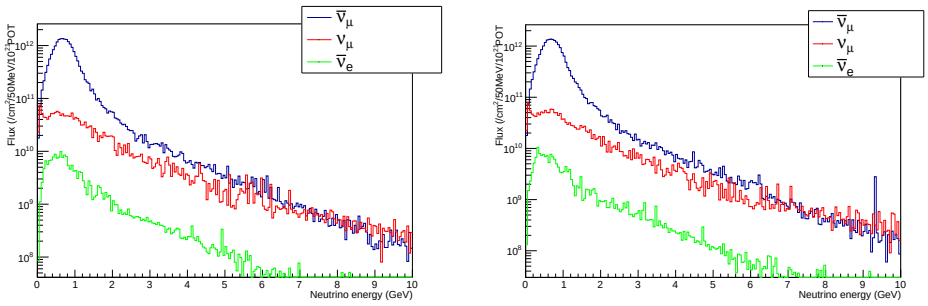

Figure 3.1 – anti-neutrino flux at WAGASCI 1.5° off-axis predicted by JNuBeam ; in the fiducial volume of the WM (left) and in the fiducial volume of the PM (right)

$-1.29°$ ($-1.30°$) in the ZX plane and $-4.70°$ ($-4.71°$) as shown in Figure 3.2 (Water Module) and Figure 3.3 (Proton Module).

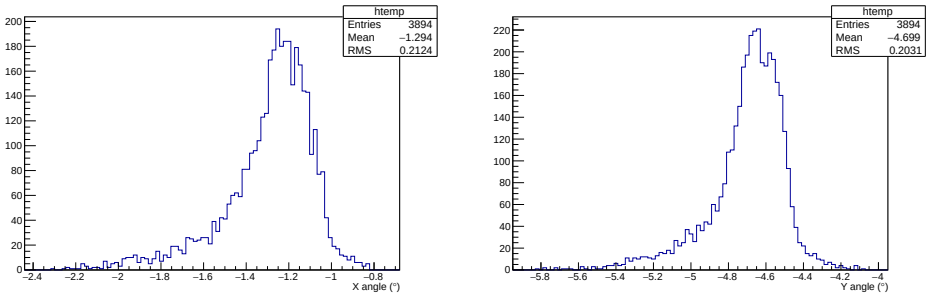

(a) Angle in the ZX plane (b) Angle in the ZY plane

Figure 3.2 – Angles of the neutrinos going through the Water Module

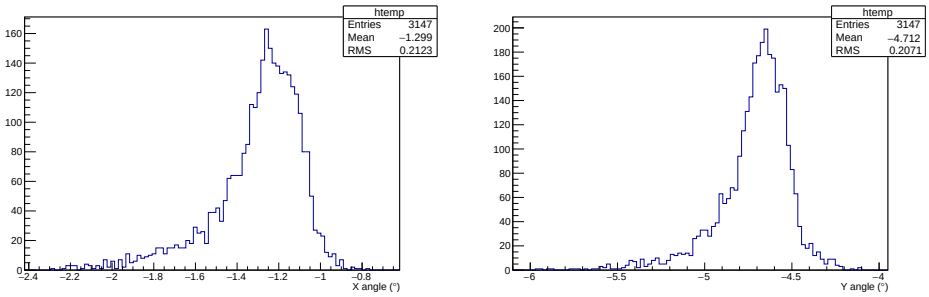

(a) Angle in the ZX plane (b) Angle in the ZY plane

Figure 3.3 – Angles of the neutrinos going through the Proton Module

3.1.2 The active detectors: scintillators

We model all three modules:

- The aluminum tank of the Water Module, the scintillators within and the water filling the tank .
- The scintillators of the Proton Module.
- The scintillators and the iron plates of INGRID
- The concrete surroundings of the detector: walls, floor, ceiling, pillars.

The dimensions of all these parts are summarized in Table 3.1. We model the scintillators by GEANT4 extruded solids, and we subtract tubes for the fiber hole for the WM scintillators (Figure 3.4), the INGRID scintillators (Figure 3.5) as well as the PM scintillators (Figure 3.6). We also subtract the dents in the grid scintillators of WAGASCI. The reason for such care in the modelization is that the scintillators are targets and also the tracking devices. We want them to be as faithfully represented as possible.

We tune the different parameters of the simulated detector by using the information collected with sand muons samples (muons that are produced in the B2 floor structures around the detector). The following quantities are calibrated:

- The number of photo-electrons (pe) created by units of energy of the particle.
- The quenching factors of the scintillators: when the energy deposit is too important, the light production cannot keep up and saturates.

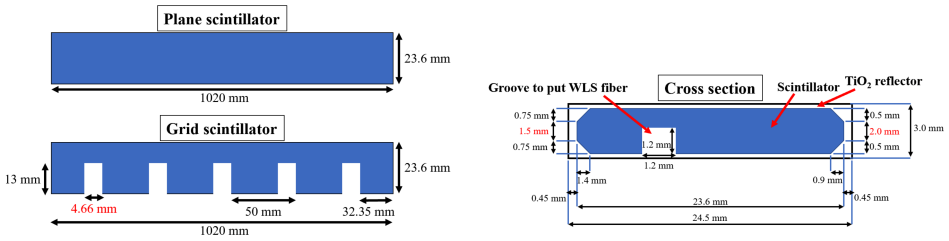

Figure 3.4 – Geometry of the WAGASCI scintillators in the Monte-Carlo

Figure 3.5 – Geometry of the INGRID scintillators in the Monte-Carlo

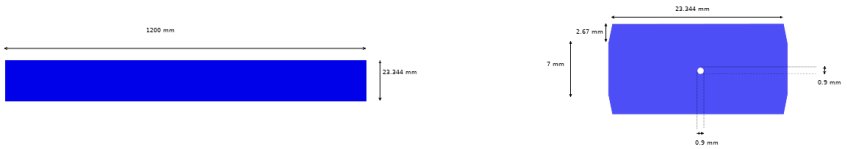

Figure 3.6 – Geometry of the Proton module scintillators in the Monte-Carlo

Table 3.1 – Dimensions of the detector

Dimension	width (cm)	height (cm)	length (cm)
Aluminium tank Inner volume	125.2	118.0	50.2
Aluminium tank Outer volume	127.6	120.4	51.0
scintillator WM	3.0	2.45	102.0
scintillator ING	1.0	4.72	120.0
scintillator PM Sci	1.23	2.33	120.0

- The conversion pe ↦ numerical signal of the ADC.
- The photon attenuation length in fiber.

The tuning of the light yield for the Water Module scintillators is shown in Figure 3.7.

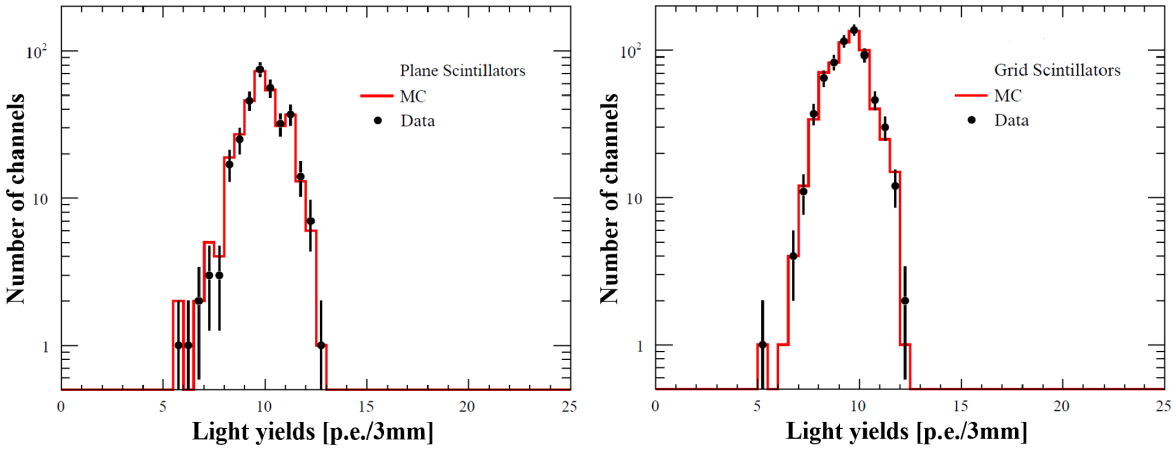

(a) Plane scintillators (b) Grid scintillators

Figure 3.7 – Mean light-yield distributions for all the plane scintillators (left) and grid scintillators (right) in the Water Module

We then store the information in a standard format for reconstruction.

3.1.3 The neutrino interactions

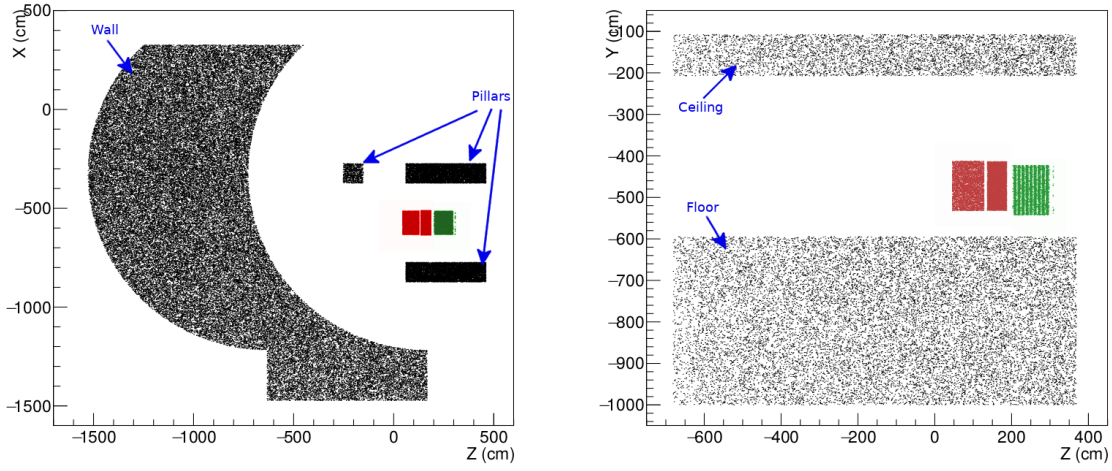

(a) ZX view (b) ZY view

Figure 3.8 – position of the simulated interaction vertices in the B2 floor. Water Module and Proton Module (red), INGRID module (green), beam background (black)

We simulate the ν_μ, $\overline{\nu_\mu}$ and $\overline{\nu_e}$ interactions in:

- The Water tank (contains the Water Module).
- The Proton Module.

- The INGRID Module.
- The Wall.
- The Floor.
- The Ceiling.
- The Pillars.

The energies and angle are the one predicted by JNUBEAM. We did not simulate the ν_e interactions because their contribution were negligible in Reverse Horn Current (RHC) mode. We use an amount of 10^{23} POT in the simulation that we normalize down to the amount of POT of the data set that we want to model, which is 7.908×10^{20} POT as we will see later in Section 7.1.

The propagation and secondary interactions are all processed with GEANT4. The cross-sections of neutrinos interactions with the target nucleons is predicted by NEUT.

We have the prediction for the kinematic distribution of the simulated particles in the two modules. The muons (Figure 3.9), the pions (Figure 3.10) and the protons (Figure 3.11).

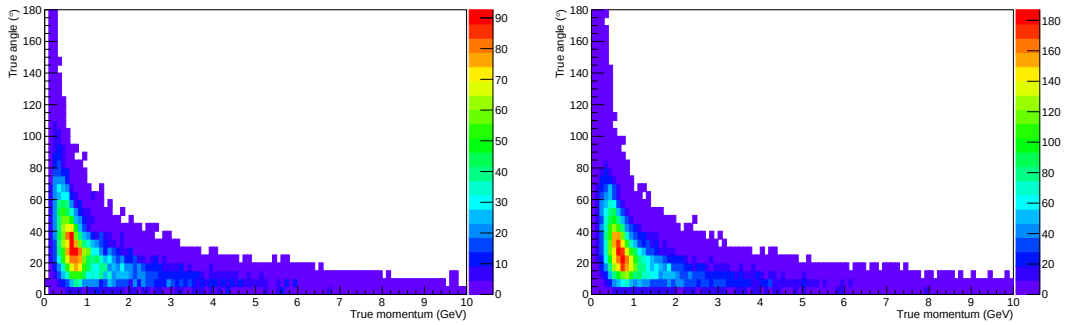

(a) in the WM (b) in the PM

Figure 3.9 – Kinematic distribution of the simulated muons

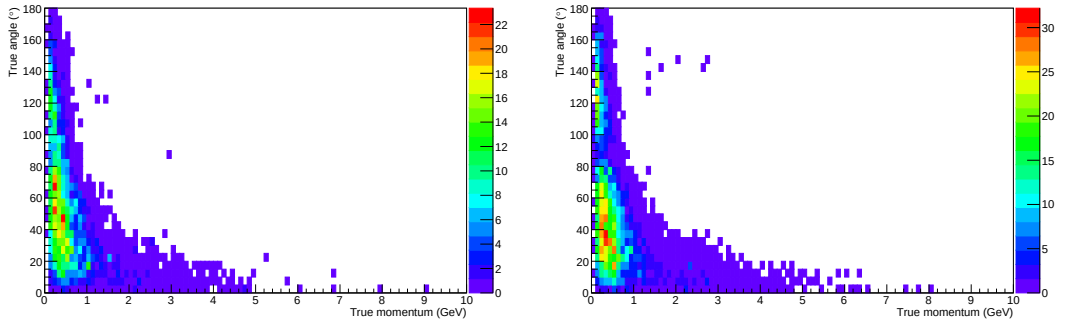

(a) in the WM (b) in the PM

Figure 3.10 – Kinematic distribution of the simulated pions

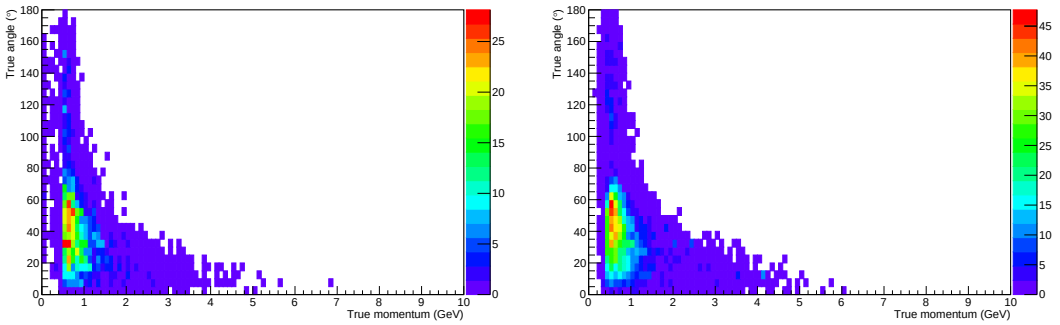

(a) in the WM (b) in the PM

Figure 3.11 – Kinematic distribution of the simulated protons

3.2 Signal definition

Because of the limited acceptance of the detectors and of the kin we define the signal as the $\overline{\nu}_\mu$ CC0π events with a muon of momentum p_μ and of angle θ_μ:

- 0.4 GeV $\leq p_\mu <$ 30 GeV.
- $\theta_\mu < 30°$.

The external background is all the interactions with a vertex located out of the fiducial volumes.

- WM fiducial volume for the WM selection
- PM fiducial volume for the PM selection

3.3 Tracking of the particle

Whether we analyze the data or the MC we have the same process to reconstruct the tracks and identify the interaction. We start from a collection of hits. Each hit contains information about the channel, the timing, the Analog to Digital Converter (ADC) count.

Thanks to the calibration of the gain with the dark noise collection (Figure 2.22), we can estimate the pe number in each hit. We put a threshold on the number of pe to eliminate some dark noise. This threshold is at 2.5 pe for the WM, at 3.5 pe for the PM and INGRID.

3.3.1 Hits clustering

An aquisition window has 23 cycles. Each cycle has a time width of 580 ns. The acquisition windows are started by the spill trigger (every 2.48 s). For the Proton Module and for INGRID, the acquisition windows are synchronized with the beam spill timing. The 8 bunches of a neutrino spill arrive in the cycles #4 to #11 (Figure 3.12). The Water Module (WM) electronics is not synchronized with the beam timing (cf Appendix B).

For each module, we create a hit cluster every time 3 hits are gathered in a 100ns time interval. We then try, for each view (ZX or ZY), to reconstruct tracks with all the hits present in that cluster, namely the hits at less than 50ns of the mean time in the cluster.

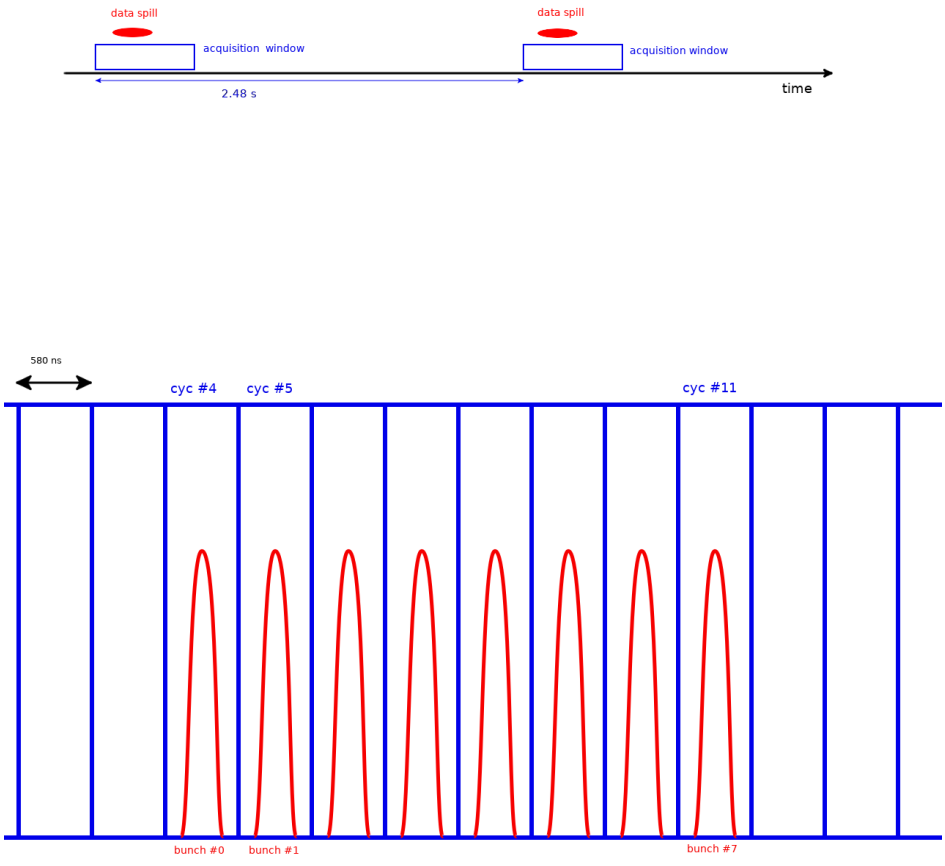

Figure 3.12 – Data acquisition. Superposition of the neutrino spill and of the acquisition window (top). Synchronization of the 8 bunches of the spill with the 23 cycles of the acquisition window (bottom)

.

3.3.2 2D track reconstruction

For the Proton Module and INGRID we take the hits within 100 ns of the beam time predicted. For WAGASCI we don't have that cut since the electronics doesn't allow the synchronization of the time. For INGRID, we make sure at least 3 planes contain hits in both views before attempting a reconstruction. If not we discard the event. The purpose is to get rid of some noise
We then start a cellular automaton algorithm [52] to reconstruct the 2D tracks from the hit collection, in the two views ZX and ZY.
For the Water Module reconstruction, we can also reconstruct large angle tracks by using the grid of the Water Module.

3.3.3 Track matching between the different modules

We have three criteria (Figure 3.13) that must be fulfilled in order to match two tracks from two different modules:

- The angle between the tracks must be smaller than 35 °.
- The difference in their transverse position in between the modules must be smaller than 15 cm.
- These two differences must be minimized among all the other tracks combinations.

We first try to match WM tracks with INGRID tracks. Then we try to match PM tracks with WM tracks (regardless of whether the latter are matched with an INGRID track already). Then finally we try to match the PM tracks (non matched yet) with the INGRID tracks.

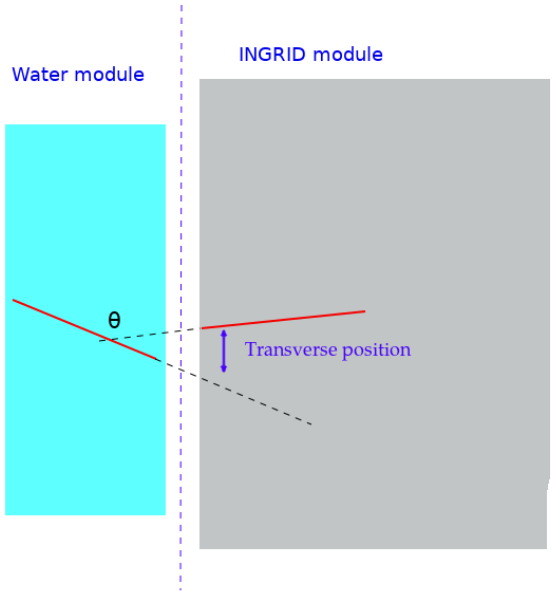

Figure 3.13 – 2D track matching between the WM and the INGRID Module

3.3.4 3D track matching

The 2D reconstruction and 2D matching produced tracks in the ZY view and ZX view. Some of them only spread in one module, some of them in two, and some of them in all three. We

now try to build 3D tracks by matching together one ZY track and one ZX track. We ask that the tracks start with less than 3 planes of difference. When this condition is verified we prioritize the track pairs that have the minimal starting plane difference, and then the minimal stopping plane difference.

1. We first try to match the tracks starting in the PM and stopping in INGRID.

2. Then we try to match the tracks starting in the PM and stopping in the WM.

3. Then we try to match the tracks starting and stopping in the PM.

4. Then we try to match the tracks starting in the WM and stopping in INGRID.

5. Then we try to match the tracks starting and stopping in the WM.

After each step we tag the tracks used in the subsequent modules that were also used in the 3D matching. For instance if a 2D WM track was matched with a 2D PM track, when the latter is successfully 3D-matched with another track starting in the PM, the former (WM track) will not be considered for 3D matching of tracks starting in the WM.

During this matching we also demand that the clustering time of the PM component of the horizontal track and the clustering time of the PM component of the vertical track be equal. We cannot have that condition applied to WAGASCI since the neutrino bunch could arrive on top of the boundary between two different cycles.

3.3.5 3D tracks vertexing

We are interested in CC0π events so we need to detect a muon and to be able to estimate its momentum. With that idea in mind, we ask that a vertex be created only if it contains at least one track with an INGRID component.
Once we have matched the 2D INGRID-matched tracks into 3D tracks, we try to see if they can be vertexed together. That is possible only if:

- Their starting planes have less than 3 planes of difference in the beam direction.
- They start with a transverse difference $|x_{track1} - x_{track2}| + |y_{track1} - y_{track2}| < 15cm$

We then try to match 2D non INGRID-matched tracks together if they are close enough to the vertex and satisfy the conditions to be matched.

3.4 Selection cuts

We are interested in CC0π events. In order to eliminate the background, we keep events that fulfill the following conditions:

- Reconstructed events where at least one of the reconstructed tracks is detected in INGRID.

- Events with a vertex in the fiducial volume of the WM for the WM selection (PM for the PM selection).
- Events where the Particle IDentification (PID) identifies one and only one "muon-like" track and identifies all the remaining ones as "proton-like" (these terms will be defined later in the PID section).
- We ask that the longest track either stops in INGRID or goes through all of it (no side-escaping particle).

We make a similar sequence of cuts in order to create a control region: a CC1π sideband. Instead of asking for one and only "muon-like" track, we ask for exactly two of them.

3.4.1 Veto cut and Fiducial Volumes (FV)

In order to filter out the particles produced out of the targets we ask that the reconstructed vertices are inside a volume that rules out the outer channels of our detector. We take the 80 cm $\times$ 80 cm central transverse section for both the WM and the PM.
We also have taken off two pairs {X plane + Y plane} from the front of the PM and use them as veto planes. We take three blocks plus one plane (Y plane + grid + X plane + grid + Y plane + grid + X plane) as VETO planes for the WM. The purpose is to make sure a particle has to cross two scintillator planes in each view before reaching the fiducial volume. That way we can decrease the chances of the particle coming from outside the WM being counted as originated from the FV.
In addition, we take out the last three pairs {X plane + Y plane} of planes off the PM target volume and the last two blocks plus one grid (grid + Y plane + grid + X plane + grid) off the WM target volume. The fiducial volumes are shown in Figure 3.14 (PM) and Figure 3.15 (WM).

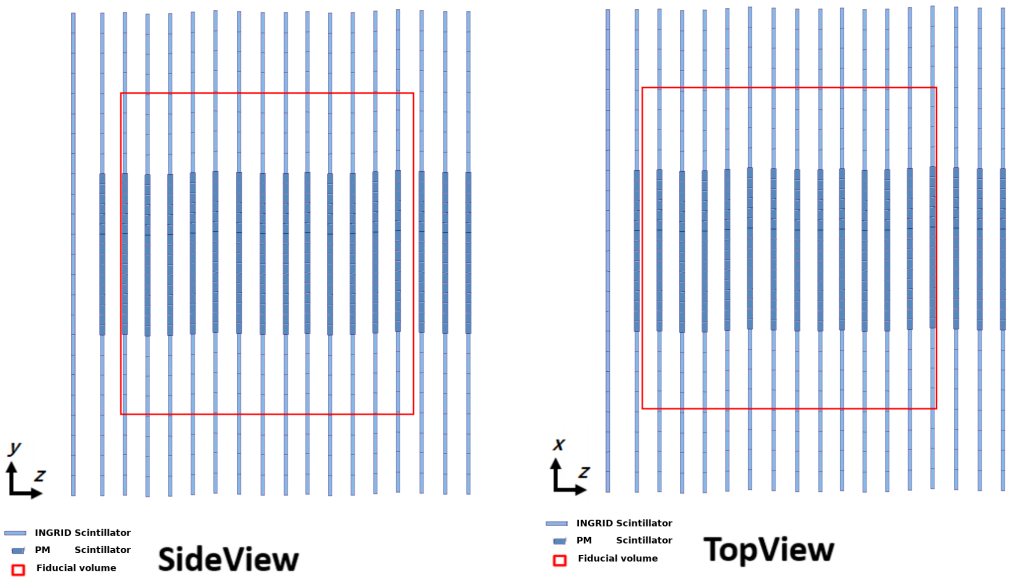

Figure 3.14 – Fiducial volume for the Proton module. For side view (left) and top view (right).

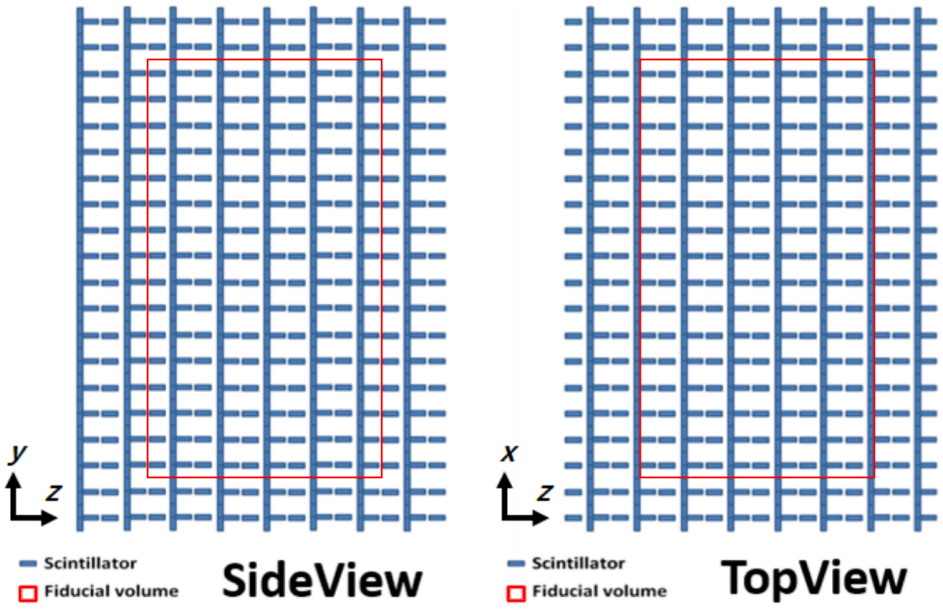

Figure 3.15 – Fiducial volume for the Water module. For side view (left) and top view (right).

3.4.2 Beam timing

For the data, we have the beam timing information available to further constraint the time window of our vertices. We only accept the PM events and the WM events whose cluster time are within 100 ns of the beam timing. For the WM events, we take the clustering time of the INGRID component of the INGRID-matched track of the event as time reference since the timing of the WM components of the tracks are random.

3.4.3 Particle IDentification (PID)

When given a track and the energy deposits of each hit of the track in the scintillators, we want to be able to tell which type of particle left that track.
Since we are interested in CC0π (and CC1π possibly), we only need to tell muons from other particles. However, muons and pions have similar masses and thus leave very similar energy deposits in matter (Figure 3.16), so we have little hope to tell them apart. For that reason, during this analysis we will talk about muons and pions at the same time. Unless specified, what we say about muons will be also valid for pions.

Since the MC simulation allows us to identify the true particle who left a track we will use this information to implement a PID that will estimate the probability that any given track is a muon/pion or another type of particle:
For each track we take:

- The total length of plastic crossed L_{CH}
- The total length of water crossed L_{H_2O}
- The total length of iron crossed L_{Fe}

We define the total equivalent iron length as:

$$L_{eq} = L_{CH} \times \frac{\rho_{CH}}{\rho_{Fe}} + L_{H_2O} \times \frac{\rho_{H_2O}}{\rho_{Fe}} + L_{Fe} \tag{3.1}$$

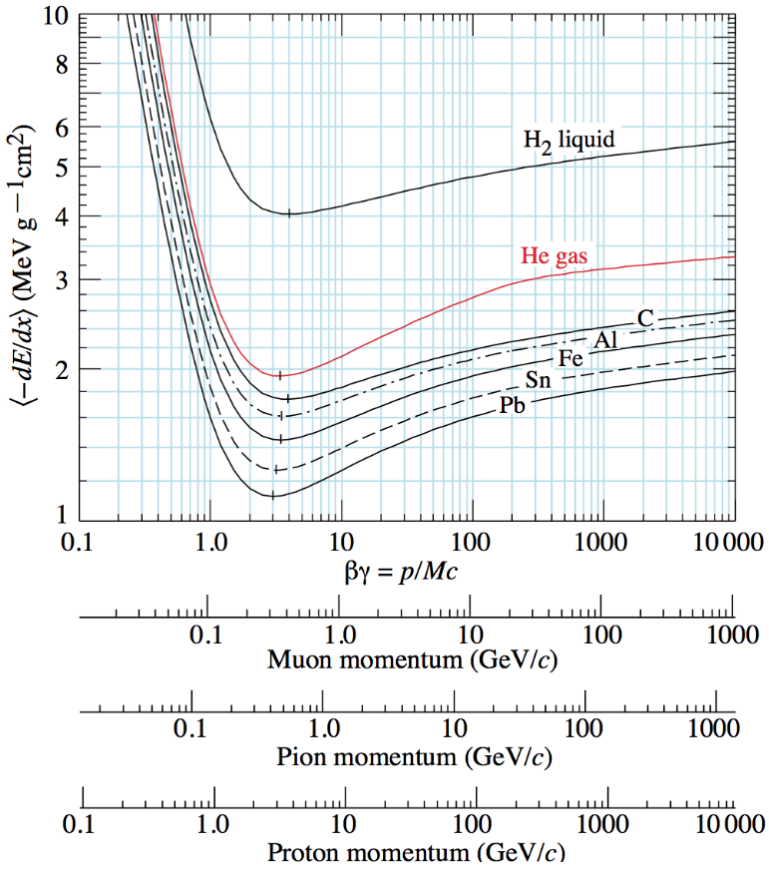

Figure 3.16 – Energy lost in matter by muons, pions and protons. Taken from [53]

Then for each hit in the track, we define the equivalent iron distance for this hit as:

$$d_{eq} = d_{CH} \times \frac{\rho_{CH}}{\rho_{Fe}} + d_{H_20} \times \frac{\rho_{H_2O}}{\rho_{Fe}} + d_{Fe} \tag{3.2}$$

where d_{CH}, d_{H_2O}, d_{Fe} are the distance crossed by the particle in plastic, water and in iron from the start of the track up to the current hit.
We then define the relative equivalent iron distance for each hit of the track as:

$$d'_{eq} = \frac{d_{eq}}{L_{eq}} \tag{3.3}$$

d'_{eq} is a quantity between 0 and 1. Then for each module (PM, WM, INGRID), for each type of track (muon or other particles) we fill two histograms:

- one for stopping tracks
- one for through-going tracks, the tracks of particles that don't clearly stop inside the INGRID Module but leave it through the downstream face of the module.

These histograms are 2D histograms that take in the relative equivalent iron distance in the first dimension and the charge deposit renormalized by the track normal slope and the thickness of the scintillator in the second dimension. The purpose is to use the evolution of the energy deposit with the propagation of the particle. The first dimension (distance) has 11 bins.

We store these histograms (Figure 3.17) and we use them whenever we need to identify a track.

We also count the number of {muons and charged pions} N_μ and of {all the other particles} $N_{\overline{\mu}}$.

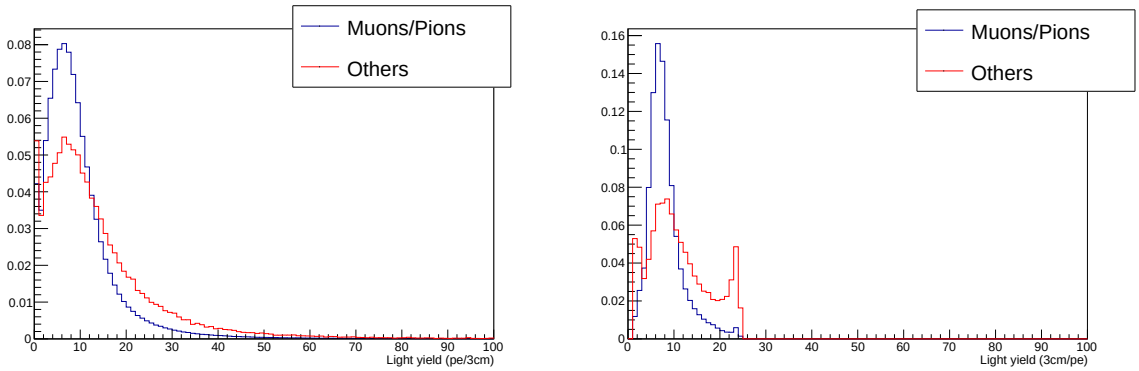

Figure 3.17 – Distributions of the light yield of the hits in the WM(left) and in INGRID (right) in the first relative equivalent iron distance bin. The peak at the end of the INGRID distribution is due to the saturation of the scintillating plastic.

Whenever we need to identify a track Tra, we take the collection of hits {hit} where hit contains the relative equivalent iron distance d'_{eq} as well as the charge deposit:

- We determine the probability that a muon or a charged pion leaved the track Tra: $P(Tra|\mu) = \prod_{hit} P(hit|\mu)$

- We determine the probability that a non-muon and non-charged pion particle leaved the track Tra: $P(Tra|\overline{\mu}) = \prod_{hit} P(hit|\overline{\mu})$

We use the distributions of charge deposit corresponding to whether or not the track stops.

We then use the Bayes formula (3.4) to deduce the probability $\mu_{CL}(Tra)$ that the particle associated to the track Tra is a muon:

$$\mu_{CL}(Tra) \equiv P(\mu|Tra) = \frac{N_\mu P(Tra|\mu)}{N_\mu P(Tra|\mu) + N_{\overline{\mu}} P(Tra|\overline{\mu})} \tag{3.4}$$

We can then put a cut on the distribution $\mu_{CL}(Tra), Tra \in \{\text{track set}\}$ (cf Figure 3.18) so that: the tracks with a high enough $\mu_{CL}(Tra)$ are identified "muon-like" while the other tracks are identified "not muon-like". We choose to put the cut at $\mu_{CL} = 0.7$.

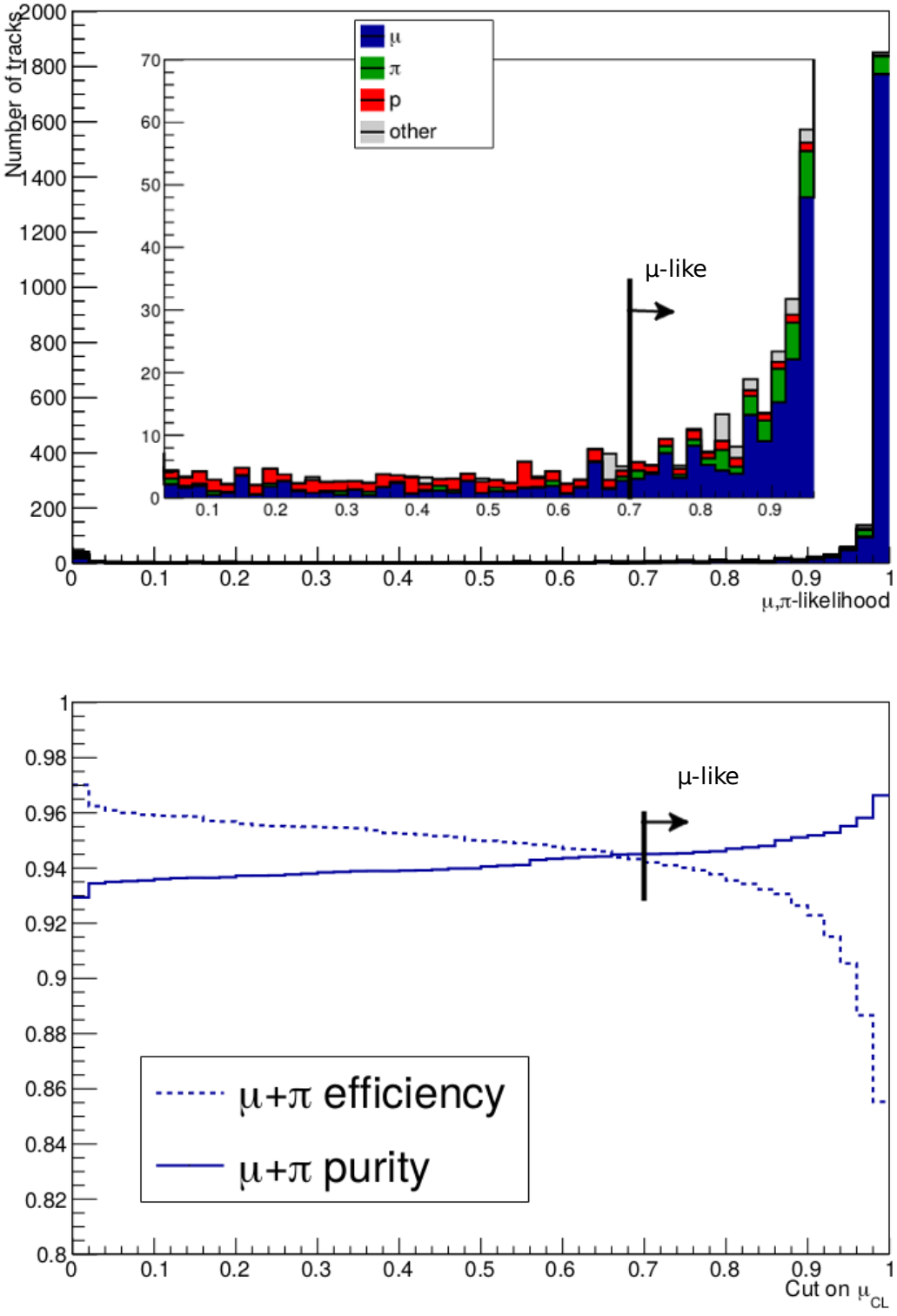

Figure 3.18 – (Top)The distribution of the μ, π-likelihood μ_{CL} and the breakdown by particle-type. "μ" contains the charged muons μ^+ and μ^-. "π" contains the charged pions π^+ and π^-. "other" contains all the particles that are not muons, pions or protons. (Bottom)The evolution of the efficiency and the purity of the PID with the cut on the value of the μ, π-likelihood μ_{CL}.

3.5 Results

3.5.1 Selection on the Monte-Carlo

Thanks to the simulation, we can take a look at which true events are selected by the cuts we apply. We can then predict the number of selected events in each bin as well as the purity and efficiency of the selection.

The reconstructed WM vertices after the fiducial volume/upstream veto cut are shown in Figure 3.19.

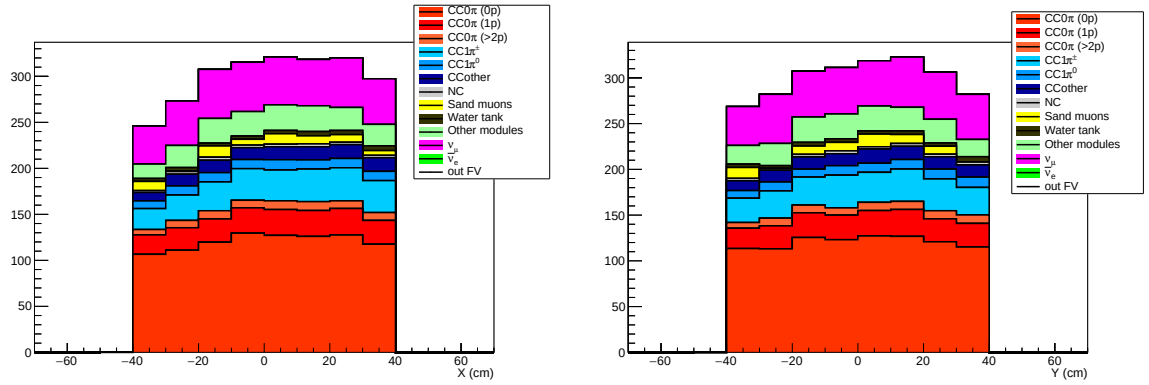

Figure 3.19 – True interaction type of the events with a reconstructed vertex in the WM after the two first cuts: 1)An INGRID-matched cut 2)VETO and Fiducial Volume cut

.

The Water Module events selection results summary is displayed in Table 3.2. The main background source are the interactions in the Water tank volume outside of the fiducial volume. The second next are the interactions in the PM. This is consistent with expectations since it is unlikely to have sand muons go through the veto cuts.

Similarly, the Proton Module events selection results are summarized in Table 3.3.
The reconstructed PM vertices after the fiducial volume/upstream veto cut are shown in Figure 3.20.

The events selected after the second-to-last cut (stopping in INGRID or going through it) all have an INGRID-matched track that has been identified as the muon of the CC0π interaction. We take the equivalent iron distance and the angle of this track as the reconstructed kinematic variables of the event. Hence, the reconstructed phase space is $\{(d_\mu, \theta^{rec})\}$. d_μ taking a finite value if the track stops or taking a special value if the track goes through. θ^{rec} goes from 0 to 90.
The true phase space is $\{(p_\mu, \theta_\mu)\}$ where p_μ is the muon momentum and θ_μ is the muon angle. θ^{rec} goes from 0 to 90.

The reconstructed WM vertices after the "MuTrk is INGRID stop/through" cut are shown in Figure 3.21.
The reconstructed PM vertices after the "MuTrk is INGRID stop/through" cut are shown in Figure 3.22.

True vertex position	In the FV	Out of the FV	Other Modules	sand muons
• Generated	7215	12751	26530	$>3\times10^8$
• Reconstructed + one INGRID track	2596	1876	911	484
• FCFV	2372	257	201	62
• PID	2084	231	175	56
• MuTrk is INGRID stop/through	1859	213	163	9
• MuTrk is INGRID stop	1080	122	85	5

	Total	Pur.	Eff.	CC0π	CC1$\pi^\pm$	CCπ^0	CCoth	NC	Wrong sign
• Generated	$> 3 \times 10^8$	0%	100%	3701	847	261	317	2089	1360
• Reconstructed + one INGRID track	5867	20%	32%	1177	268	74	127	23	409
• FCFV	2372	45%	29%	1058	212	67	101	21	353
• PID	2084	50%	28%	1043	163	51	51	11	264
• MuTrk is INGRID stop/through	1859	51%	26%	944	155	46	41	10	241
• MuTrk is INGRID stop	1080	59%	17%	634	93	22	18	10	75

Table 3.2 – WM events selection: position of the true vertices of the selected events (top) and true composition of the selected events in the true Fiducial Volume (bottom). It should be noted that the total in the first column of the bottom table counts all the selected events, event those not in the fiducial volume. The last line is a sub-sample of stopping tracks but it is the second-to-last that will be used for the cross-section extraction. The wrong sign column contains the ν_μ events and the $\bar{\nu}_e$ events.

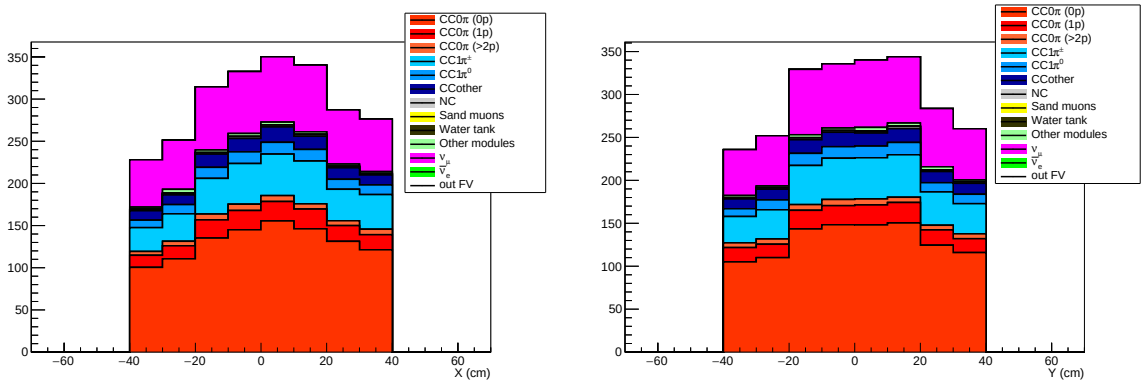

Figure 3.20 – True interaction type of the events with a reconstructed vertex in the PM after VETO and Fiducial Volume cut

.

True vertex position	In the FV	Out of the FV	Other Modules	sand muons
• Generated	6822	18419	21327	$>3\times10^8$
• Reconstructed + one INGRID track	2507	3337	58	285121
• FCFV	2367	68	20	0
• PID	2003	57	14	0
• MuTrk is INGRID stop/through	1752	51	12	0
• MuTrk is INGRID stop	870	25	7	0

	Total	Pur.	Eff.	CC0π	CC1$\pi^{\pm}$	CCπ^0	CCoth	NC	Wrong sign
• Generated	$> 3 \times 10^8$	0%	100%	3373	893	248	304	2004	1289
• Reconstructed + one INGRID track	291023	0%	39%	1300	362	104	132	18	571
• FCFV	2367	51%	36%	1213	321	96	109	16	515
• PID	2003	59%	35%	1172	218	81	51	6	399
• MuTrk is INGRID stop/through	1752	58%	30%	1022	200	71	43	4	344
• MuTrk is INGRID stop	870	69%	18%	600	97	32	10	4	91

Table 3.3 – PM events selection: position of the true vertices of the selected events (top) and true composition of the selected events in the true Fiducial Volume (bottom) It should be noted that the total in the first column of the bottom table counts all the selected events, event those not in the fiducial volume. The last line is a sub-sample of stopping tracks but it is the second-to-last that will be used for the cross-section extraction. The wrong sign column contains the ν_μ events and the $\bar{\nu}_e$ events.

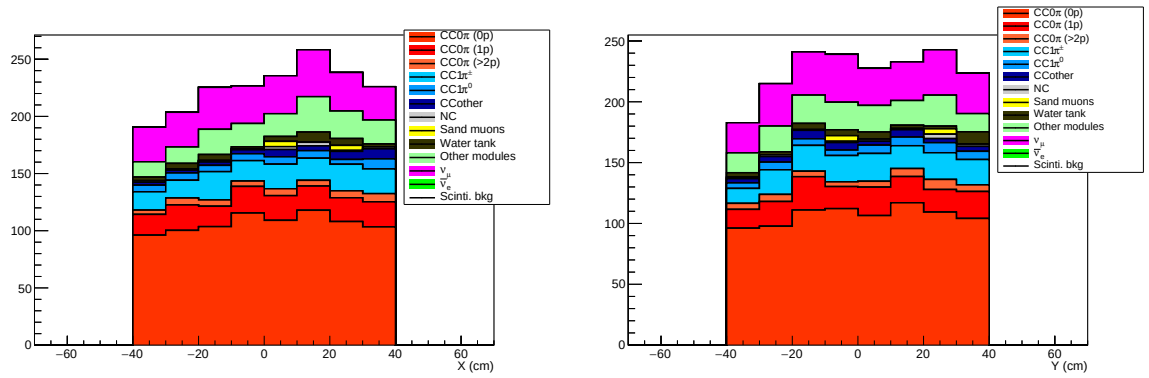

Figure 3.21 – True interaction type of the events with a reconstructed vertex in the WM after the second-to-last cut

.

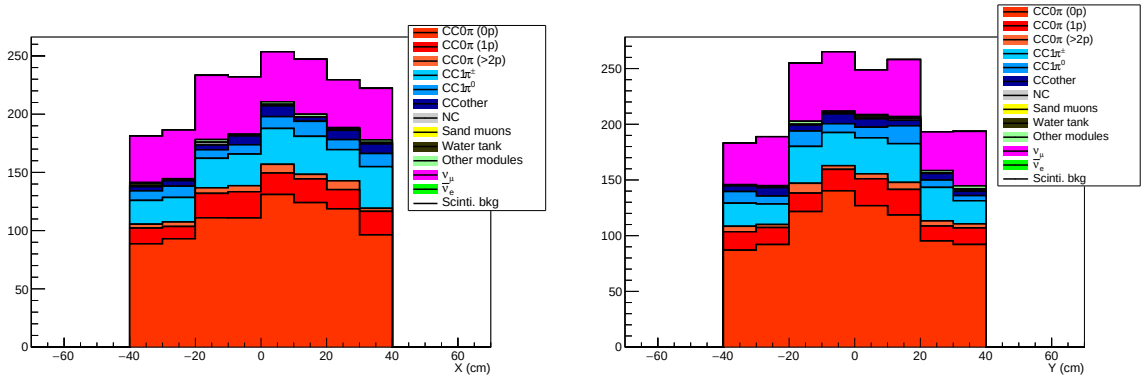

Figure 3.22 – True interaction type of the events with a reconstructed vertex in the PM after the second-to-last cut

.

The distribution of the reconstructed variables is given in Figure 3.23 for the WM sample and in Figure 3.24 for the PM sample.

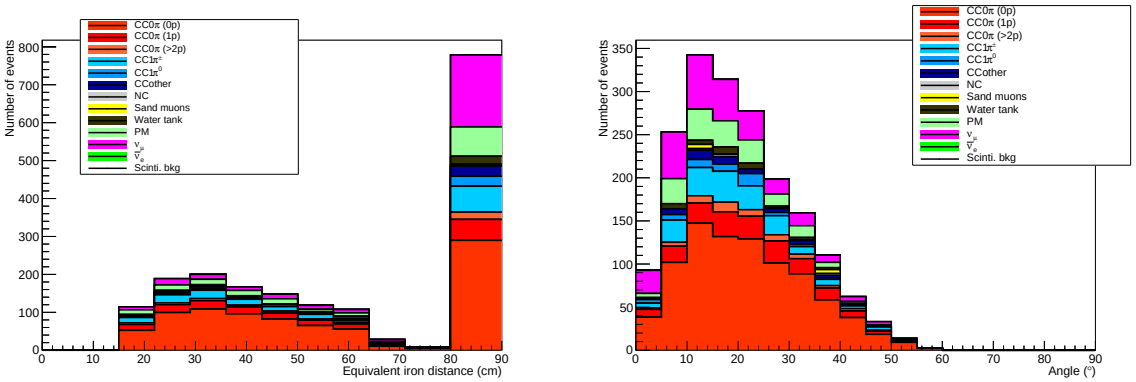

(a) Equivalent iron distance

(b) Reconstructed angle

Figure 3.23 – Distribution of the reconstructed kinematic variables of the selected events for the WM analysis. On the left is the equivalent iron distance of the muon-like track. The last bin represent the through-going events while all the bins before contains stopping events. On the right is the reconstructed angle of the muon-like track.

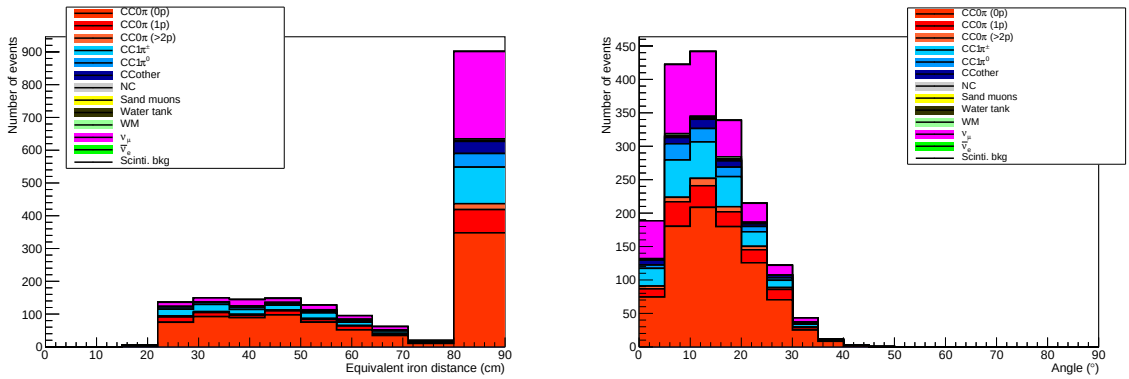

(a) Equivalent iron distance

(b) Reconstructed angle

Figure 3.24 – Distribution of the reconstructed kinematic variables of the selected events for the PM analysis. On the left is the equivalent iron distance of the muon-like track. The last bin represent the through-going events while all the bins before contains stopping events. On the right is the reconstructed angle of the muon-like track.

3.5.2 Efficiency of the selection

For both selections, we estimate the efficiency of the selection

$$\frac{\text{number of selected } \overline{\nu}_\mu - CC0\pi \text{ events}}{\text{total number of generated } \overline{\nu}_\mu - CC0\pi \text{ events}} \tag{3.5}$$

The efficiency of both selections are summarized in Figure 3.25.
For the differential cross-sections in momentum and the differential cross-section in angle, we sum the cross-sections bins of the double differential analysis, so we don't have to compute the efficiencies for the angle and momentum differential analysis.

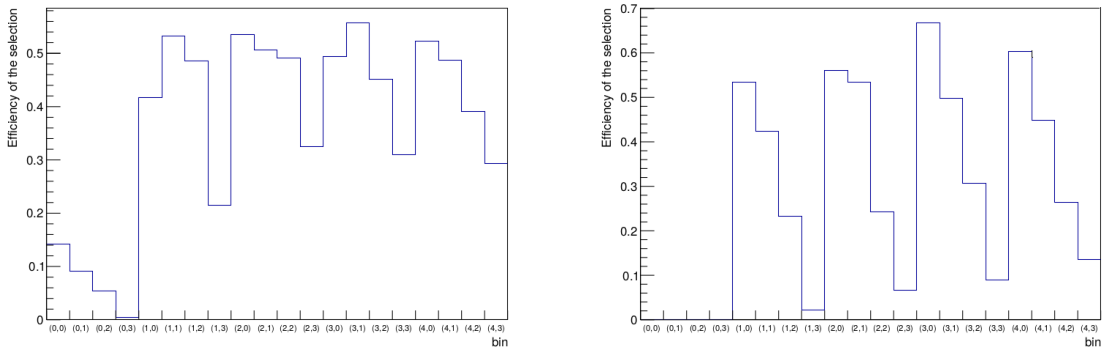

(a) WM selection (b) PM selection

Figure 3.25 – Efficiency of the selection of events. We use the true kinematic variable binning that will be defined later on in Table 4.1. The bin (i,j) labels the 2D bin with the bin#i in momentum and the bin#j in angle.

The interaction type make-up of the selection can be found in Figure 3.26 for the double differential binning, in Figure 3.27 for the momentum binning and in Figure 3.28 for the angle binning.

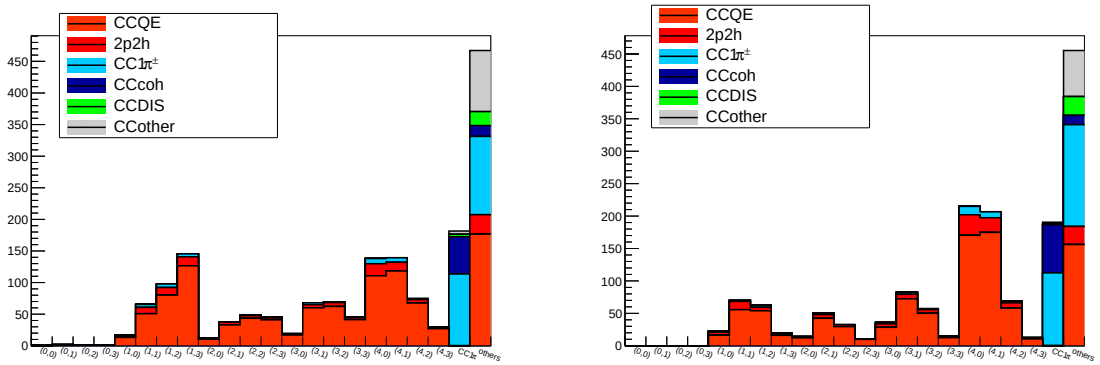

(a) WM selection (b) PM selection

Figure 3.26 – Composition of the selected events in the true phase space ; double differential binning. We use the true kinematic variable binning that will be defined later on in Table 4.1. The bin (i,j) labels the 2D bin with the bin#i in momentum and the bin#j in angle.

3.5.3 Detection efficiency of various particles

As for detection efficiency of the different particles, we are mainly interested in the muon detection efficiency (Figure 3.29), the pion detection efficiency (Figure 3.30) and the proton

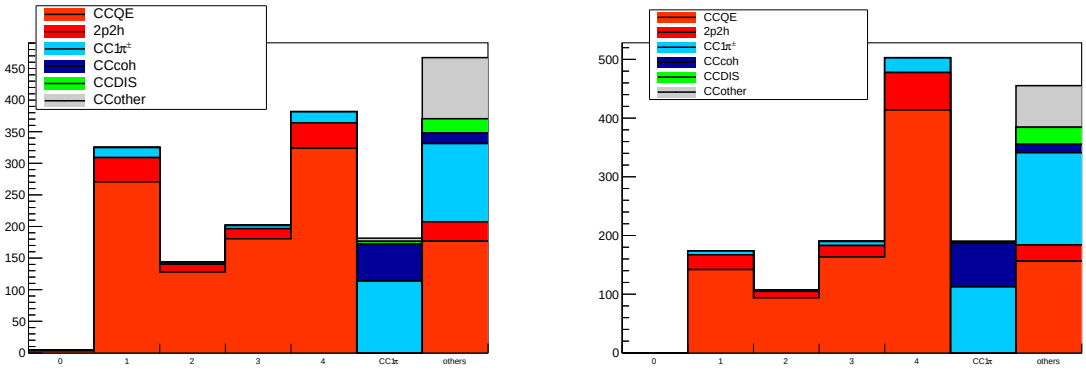

(a) WM selection (b) PM selection

Figure 3.27 – Composition of the selected events in the true phase space ; momentum binning. We use the true muon momentum binning that will be defined later on in Table 4.1.

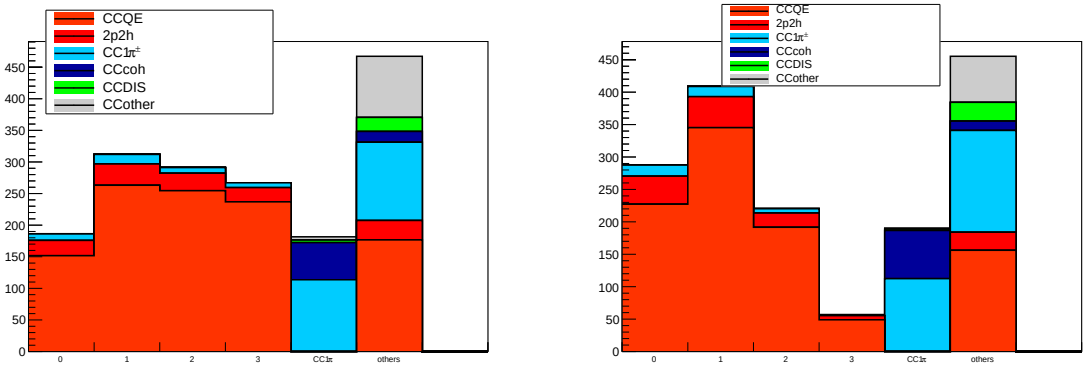

(a) WM selection (b) PM selection

Figure 3.28 – Composition of the selected events in the true phase space ; angle binning. We use the true muon angle binning that will be defined later on in Table 4.1.

detection efficiency (Figure 3.31). The detection efficiency of muons is around 90%. The detection efficiency of pions is more around 50%. The detection efficiency of protons is around 40%-50%. This can be a source of CC1π contamination as we realize that almost half the pions can go undetected while the muon is detected, effectively appearing as a CC0π at the detection.

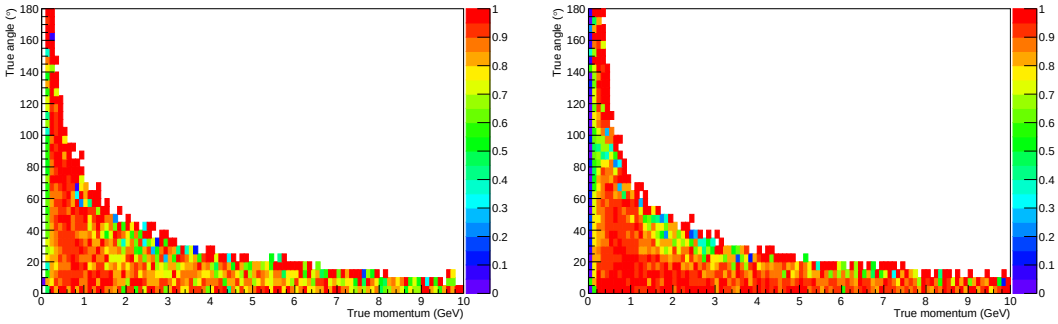

(a) in the WM (b) in the PM

Figure 3.29 – Efficiency of the muon detection

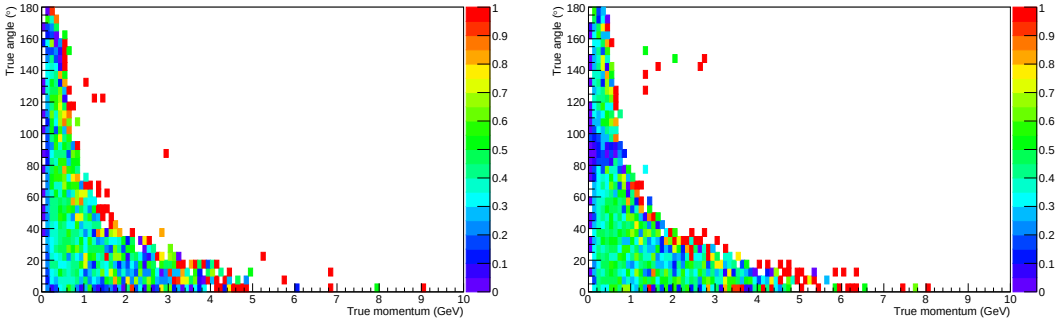

(a) in the WM (b) in the PM

Figure 3.30 – Efficiency of the pion detection

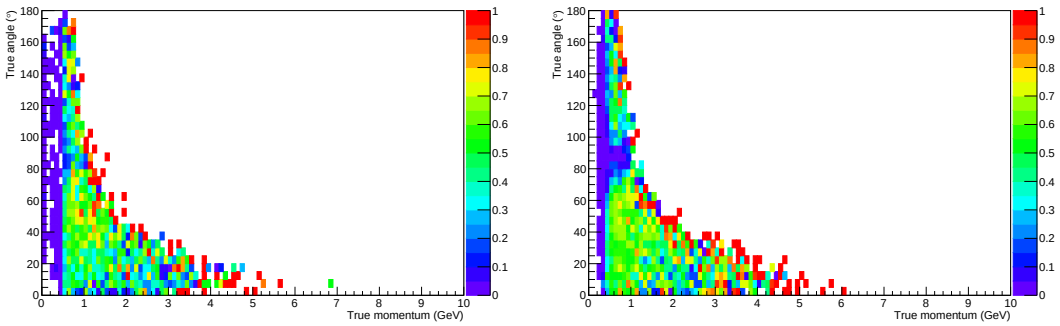

(a) in the WM (b) in the PM

Figure 3.31 – Efficiency of the proton detection

Chapter 4

Cross-section extraction

In this analysis we want to compute a differential cross-section in both momentum and angle. This means that for each bin (true momentum,true angle)

$$bin_{i,j}^{true} = \{(p_\mu, \theta_\mu) \in [p_i, p_{i+1}] \times [\theta_j, \theta_{j+1}]\}$$

we will estimate the integrated cross-section of a muon antineutrino of the beam interacting with a nucleus X of the target to give a $CC0\pi$ Final State, where μ^+ is the lepton ad X' is a sum of hadrons who are not pions. We have to choose a binning in the true phase space. The integration is on the kinematic variables of the muon μ^+ in the final state, and the integration domain is the bin $\text{bin}_{i,j}^{true}$.

$$\sigma_{i,j} = \int_{\text{bin}_{i,j}^{true}} \sigma(\bar{\nu}_\mu X \overset{CC0\pi}{\longrightarrow} \mu^+(p,\theta)X')dpd\theta \tag{4.1}$$

We will keep in mind that the differential cross section $\sigma(\bar{\nu}_\mu X \overset{CC0\pi}{\longrightarrow} \mu^+(p,\theta)X')$ is implicitly convoluted by the distribution of muon antineutrinos $\bar{\nu}_\mu$ in the kinematic true phase space and by the elemental composition of the target nuclei X.

After carefully selecting a sample of events with a succession of cuts, we now need to use it to compute the cross-sections we are interested in. For each bin we have the formula

$$\sigma_{i,j} = \frac{N_{i,j}^{CC0\pi}}{\phi_{\bar{\nu}_\mu} \times T} \tag{4.2}$$

where

- $N_{i,j}^{CC0\pi}$ is the total number of CC0π interactions with a product muon whose kinematic variables are in bin_{ij}^{true} that took place during the data acquisition.
- $\phi_{\bar{\nu}_\mu}$ is the integrated incident $\bar{\nu}_\mu$ flux.
- T is the number of target nucleus.

The question is now how to obtain the $N_{ij}^{CC0\pi}$ from the selected sample s_{kl}^{rec} we have from the selection process. The answer is to first obtain the number of CC0π events s^{true} detected and selected by the cuts. Then we take s_{ij}^{true} the number of detected and selected CC0π events in the bin_{ij}^{true} and we obtain $N_{i,j}^{CC0\pi}$ with the formula

$$s_{ij}^{true} = \epsilon_{ij} \times N_{i,j}^{CC0\pi} \tag{4.3}$$

where ϵ_{ij} is the CC0π events detection efficiency of the detector for the true phase space bin bin_{ij}^{true}

In the end we measure our cross-sections with the formula

$$\sigma_{i,j} = \frac{s_{ij}^{true}}{\phi_{\bar{\nu}_\mu} \times T \times \epsilon_{ij}} \tag{4.4}$$

What is left to do as this point is to choose a way to estimate s^{true} from the selected sample s^{rec}. For the analysis we chose the unfolding method, an iterative procedure which subtract the predicted background events from the selected sample and then bring the CC0π selected signal from the reconstructed phase space to the true phase space.
The method will be fully explained further down. But before that we need to choose a binning in the true phase space as well as in the reconstructed phase space. There are a few constraints for this choice. The true bins must be wider than the detector resolution.

The detector resolution is our ability to get back to the true kinematic variables from the reconstructed kinematic variables. So for a given value of the equivalent iron distance d_μ (reconstructed angle θ_μ^{rec}) we look at the distribution of the muon momentum p_μ (true muon angle θ_μ) and we fit it with a Gaussian function. The standard deviation gives us the resolution for this value of the reconstructed kinematic variable. The resolutions for the detector can be found in Figure 4.1. The resolution in momentum is 54 MeV and the resolution in angle is 3.5 °.

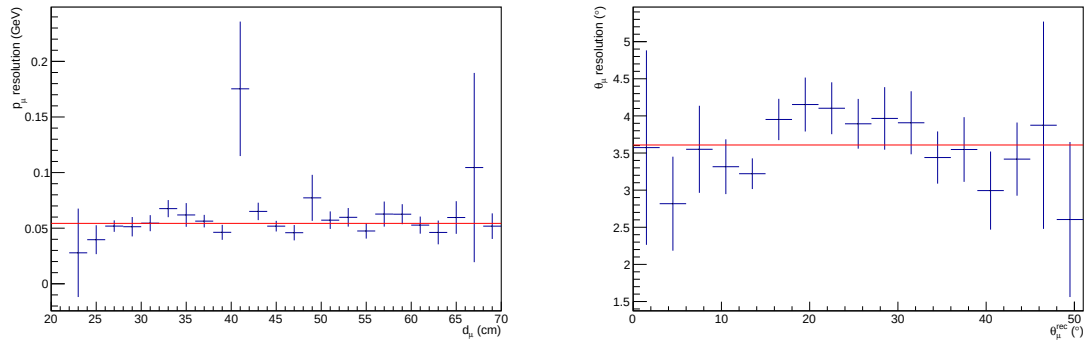

(a) Momentum resolution

(b) Angle resolution

Figure 4.1 – The resolution of the detector is taken by taking the standard deviation of the Gaussian fit of the distribution of the true kinematic variables and by averaging this standard deviation over the values of the reconstructed kinematic variables. On the left we have the resolution in momentum at around 54 MeV while on the right we have the resolution in angle at around 3.5 °

4.1 The binning choice

We consider the efficiency (figure 4.2) and number of selected events (figure 4.3) in both the WM and PM samples.
It should be noted that the efficiencies presented here are the efficiency of the CC0π events selection, after the selection cuts are applied. The efficiency plots presented in the last chapter were the efficiency of detection of the various particles, meant to describe the detector performance.

We then choose a true phase space binning so that the efficiency doesn't vary too much inside a bin (for both selections) and we make sure our bins have enough events in them (for

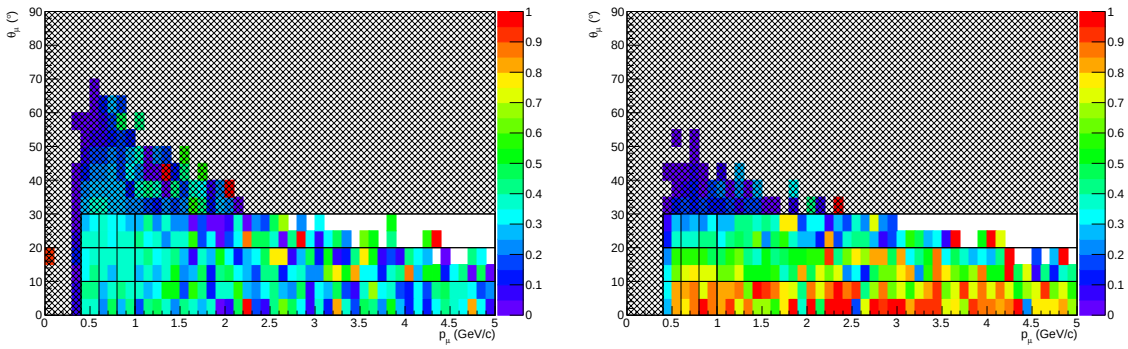

(a) For the WM (b) For the PM

Figure 4.2 – Efficiency of the selection. The last momentum bin goes from 1 GeV to 30 GeV but was truncated for display purpose. The gray areas are the bins that will not be used for the cross-section interaction, even though they will be used for the unfolding procedure. The efficiency is around 40% everywhere except for the low angular bins of the PM sample which are around 80%. This higher efficiency can be explained by the fact that these events have more matter to go through and are thus more likely to be detected.

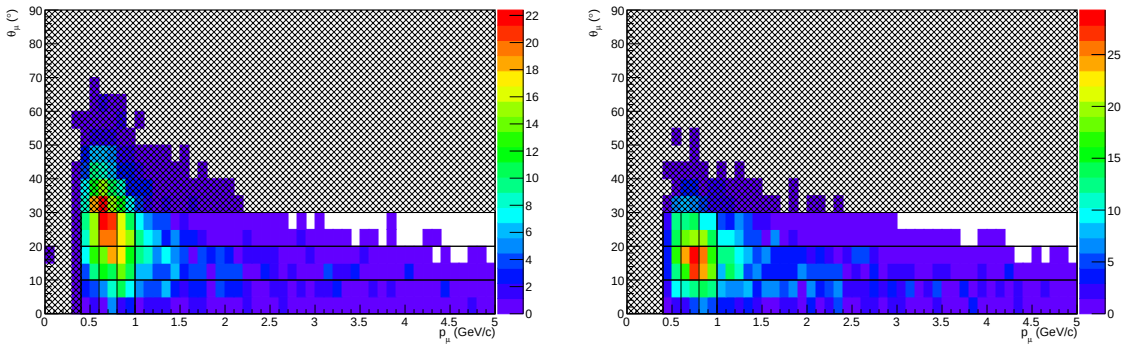

(a) For the WM (b) For the PM

Figure 4.3 – Number of selected events. The last momentum bin goes from 1 GeV to 30 GeV but was truncated for display purpose. The gray areas are the bins that will not be used for the cross-section interaction, even though they will be used for the unfolding procedure. In all the bins used for the analysis, there are at least a few dozens of events.

both samples). This is to ensure that the statistical uncertainties will not be too important and make the measurement useless. We also must ensure that the detector resolution (3.5 ° in muon angle and 54 MeV in muon momentum) is thinner than the bins width.
In the end we have the binnings given in Table 4.1 and Table 4.2.

Table 4.1 – Coordinates of the muon in the true phase space.

True phase space	# of bins	bins limits
p_μ (GeV): True momentum	5	0 , 0.4 , 0.6 , 0.8 , 1.0 , 30.0
θ_μ (°): True angle	4	0 , 10 , 20 , 30 , 180
CC1π bin	1	all CC1π interactions
other interactions bins	1	all other interactions

Table 4.2 – Coordinates of the muon in the reconstructed phase space. The last reconstructed momentum bin is for through-going particles.

Distance range	Number of bins	Distance width per bin
From 0 cm to 15 cm	1	15 cm
From 15 cm to 80 cm	9	65/9 cm
through-going tracks	1	–

Reconstructed angle	Number of bins	Angle width per bin
From 0 to 90 °	18	5 °

In the true phase space we have 20 CC0π bins (5 momentum bins × 4 angle bins)+ 1 CC1π bin + 1 other interactions bin.
In the reconstructed phase space we have 198 bins (11 momentum bins × 18 angle bins).

4.2 The unfolding method

As explained earlier the selected sample s^{rec} has its kinematic variables in the reconstructed phase space $(d_\mu, \theta_\mu^{rec})$ and also has a contamination by background events. We want to first isolate the CC0π events $s^{rec,CC0\pi}$ in the sample s^{rec}, and then transform the distribution of the CC0π events in the reconstructed phase space $s^{rec,CC0\pi}$ into a distribution of the CC0π events in the true phase space s^{true}.
For this purpose we need to predict the contamination of our sample $s^{rec,bkg}$ as well as the way our detector transform the reconstructed kinematics variables into true kinematic variables. The MC study meet both these needs, provided that we know how to use it.
One of the various methods used is the unfolding method which we will now present.

4.2.1 The original D'Agostini formulation

Based on the Monte-Carlo (MC) study, we construct a detector response matrix $\mathcal{L}$, also called smearing matrix which goes from the true phase space of the muon to the reconstructed phase space of the muon.

$$\mathcal{L}_{p_\mu,\theta_\mu}^{d_\mu,\theta_{rec}} = P(d_\mu, \theta_{rec} | p_\mu, \theta_\mu) \tag{4.5}$$

where (p_μ, θ_μ) is the true phase space bin and $(d_\mu, \theta_\mu^{rec})$ the reconstructed phase space bin for which we compute the matrix coefficient.

When a muon is detected and tracked in the detector, we obtain its coordinates in the reconstructed phase space (this is the smearing effect of the detection). Ideally, we would like to invert the smearing matrix $\mathcal{L}$ in order to obtain the coordinates in the true phase space $s^{true} = \mathcal{L}^{-1} \times s^{rec,CC0\pi}$.
But the smearing matrix is not necessarily invertible, so we have to proceed otherwise.
We are given a selected signal $s^{rec} = s^{rec,CC0\pi} + s^{rec,bkg}$ and a smearing matrix $\mathcal{L}$.
We first assume a distribution for the muons in the true phase space that we call the initial prior $P_0(p_\mu, \theta_\mu)$. That distribution can be taken from a neutrino interaction generator (NEUT, GENIE) or can be just designed by the user to decrease the bias.
We use the prior P_0 and the smearing matrix to build the unfolding matrix

$$\mathcal{U}^{p_\mu,\theta_\mu}_{d_\mu,\theta_{rec}}(0) = P(p_\mu, \theta_\mu | d_\mu, \theta_{rec}) = \frac{P(d_\mu, \theta_{rec} | p_\mu, \theta_\mu) \times P_0(p_\mu, \theta_\mu)}{\sum_{p'_\mu,\theta'_\mu} P(d_\mu, \theta_{rec} | p'_\mu, \theta'_\mu) \times P_0(p'_\mu, \theta'_\mu)} \tag{4.6}$$

where (p_μ, θ_μ) is the true phase space bin and $(d_\mu, \theta^{rec}_\mu)$ the reconstructed phase space bin for which we compute the matrix coefficient. $\sum_{p'_\mu,\theta'_\mu}$ in the denominator is a sum on all the true phase space bins. Or again:

$$\mathcal{U}^{p_\mu,\theta_\mu}_{d_\mu,\theta_{rec}}(0) = \frac{\mathcal{L}^{d_\mu,\theta_{rec}}_{p_\mu,\theta_\mu} \times P_0(p_\mu, \theta_\mu)}{\sum_{p'_\mu,\theta'_\mu} \mathcal{L}^{d_\mu,\theta_{rec}}_{p'_\mu,\theta'_\mu} \times P_0(p'_\mu, \theta'_\mu)} \tag{4.7}$$

We can then get a first estimation of the true phase space signal $s^{true}_1 = \mathcal{U}(0) \times s^{rec,CC0\pi}$
We then take a new prior P_1 from the true signal estimation s^{true}_1. We can compute a new unfolding matrix $\mathcal{U}(1)$ from the (unchanged) smearing matrix $\mathcal{L}$ and the new prior P_1.
And so on, we take the successive $\mathcal{U}(n)$ (Equation 4.8) and $s^{true}_n = \mathcal{U}(n-1) \times s^{rec,CC0\pi}$ until s^{true}_n is close enough to $\overline{s^{true}}$ the true signal in the true phase space.

$$\mathcal{U}^{p_\mu,\theta_\mu}_{d_\mu,\theta_{rec}}(n) = \frac{\mathcal{L}^{d_\mu,\theta_{rec}}_{p_\mu,\theta_\mu} \times P_n(p_\mu, \theta_\mu)}{\sum_{p'_\mu,\theta'_\mu} \mathcal{L}^{d_\mu,\theta_{rec}}_{p'_\mu,\theta'_\mu} \times P_n(p'_\mu, \theta'_\mu)} \tag{4.8}$$

The "close enough" criterion will be discussed in the Chapter 6. We will devise a criteria independent of the true distribution but tried by applying our unfolding to various simulations.

4.2.2 The modified procedure

In the original formulation, we would get $s^{rec,CC0pi}$ by subtracting the predicted background $s^{rec,bkg}$ from the selected events s^{rec}. Here we will include the background subtraction in the unfolding procedure by adding additional bins in the true phase space: a CC1π bin and a bin for non CC0π non CC1π events.
In order to constrain the evolution of the trash bins CC1π and others, we select a CC1π side band. We add 2 bins to the reconstructed phase space: the stopping CC1π selected events and the non stopping CC1π selected events.
Now in the the equation 4.7, (d_μ, θ^{rec}) can take two more values: the stopping CC1π selected events and the non stopping CC1π selected events. The rest of the process is identical to what we described earlier saved for the fact that we now have $s^{true}_n = \mathcal{U}(n-1) \times s^{rec}$ instead of $s^{true}_n = \mathcal{U}(n-1) \times (s^{rec} - s^{rec,bkg})$.

This method has the advantage of renormalizing the background contamination and to keep it consistent with the CC0π signal. Furthermore, we can now add a CC1π side-band to our sample that will also work with the CC1π bin in the true phase space to improve the unfolding procedure.

4.3 The smearing matrix

The simulation allows us to produce the detector response matrix. This matrix gives us the probability that an event in a given true phase bin is sent by the detector into a given reconstructed phase bin.
In other words our smearing matrix is:

$$L^{d_\mu,\theta_\mu^{rec}}_{p_\mu,\theta_\mu} = P(d_\mu, \theta_\mu^{rec} | p_\mu, \theta_\mu) \tag{4.9}$$

The smearing matrix for the WM analysis is given in Figure 4.4 while the smearing matrix for the PM analysis is given in Figure 4.5

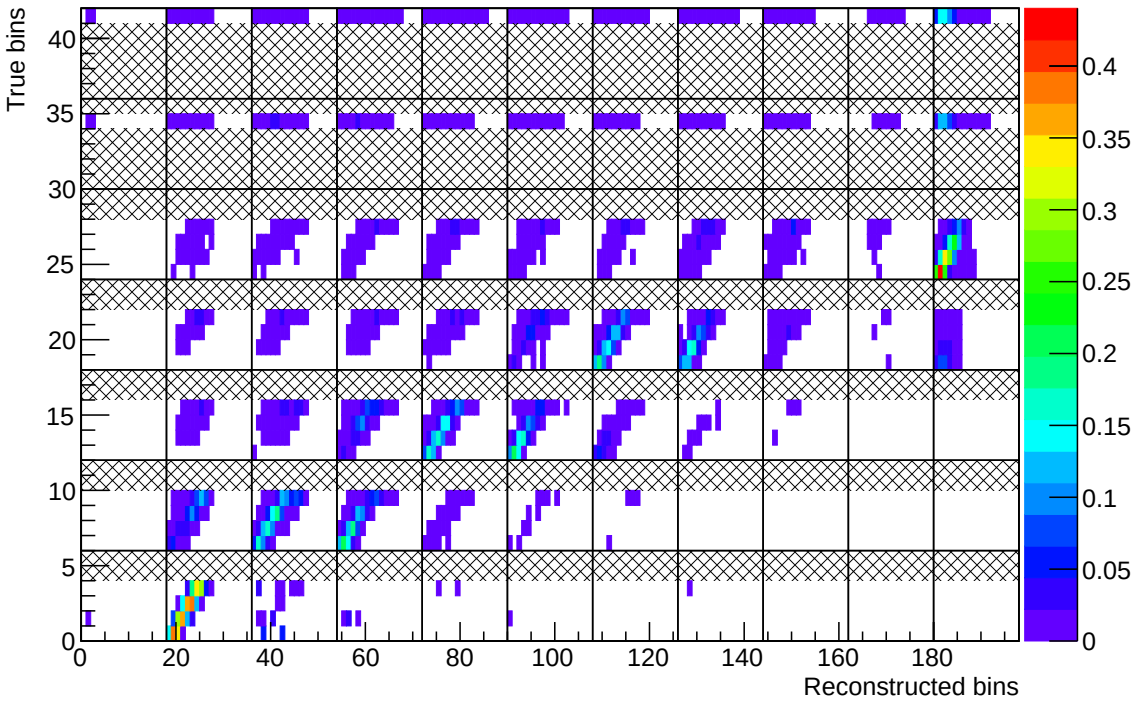

Figure 4.4 – Smearing matrix for the WM.
The horizontal axis represent the 198 reconstructed phase space bins, gathered by 11 blocks of 18 bins. In a block the equivalent iron distance d_μ is fixed and there are 18 reconstructed angle bins θ_μ^{rec}. The vertical axis represent the 22 true phase space bins for CC0π events, gathered by 5 blocks of 4 bins. In a block the muon momentum p_μ is fixed and there are 4 muon angle bins θ_μ. There are also additional bins for CC1π events and one last trash bin that takes all the non-CC0π non-CC1π interactions.

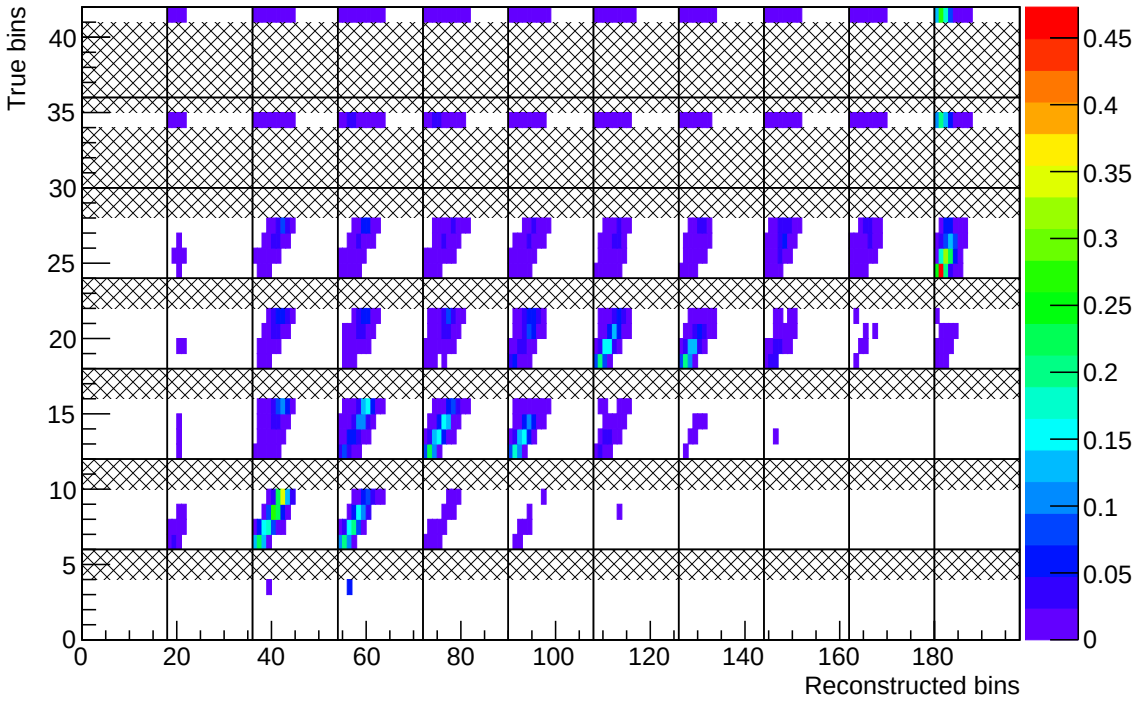

Figure 4.5 – Smearing matrix for the PM.
The horizontal axis represent the 198 reconstructed phase space bins, gathered by 11 blocks of 18 bins. In a block the equivalent iron distance d_μ is fixed and there are 18 reconstructed angle bins θ_μ^{rec}. The vertical axis represent the 22 true phase space bins for CC0π events, gathered by 5 blocks of 4 bins. In a block the muon momentum p_μ is fixed and there are 4 muon angle bins θ_μ. There are also additional bins for CC1π events and one last trash bin that takes all the non-CC0π non-CC1π interactions.

4.4 The cross-section extraction

Now that the unfolding brought us from the reconstructed phase space to the true phase space with a satisfactory precision, we want to transform the detected events into a cross-section measurement.
For each bin, the MC predicts an efficiency $\epsilon_{i,j}$ and we have a flux prediction Φ from our models. The number of nucleons in the target is T.
The formula 4.10 gives us the unfolded cross-section values for the WM (mix of plastic and water) and for the PM(plastic) after the n-th iteration:

$$\sigma_{i,j}(n) = \frac{(\mathcal{U}(n) \times s^{rec})_{ij}}{\Phi \times T \times \epsilon} \tag{4.10}$$

where $(\mathcal{U}(n) \times s^{rec})_{ij}$ the number of unfolded events in the bin (i,j).

4.5 Determination of the Flux

JNUBEAM predicts neutrino fluxes in the fiducial volumes of both the WM and the PM. These fluxes are displayed Figure 4.6 for 10^{21} POT.
Table 4.3 gives the expected flux for 7.908$\times$ 10^{20} POT, the fluxes we use for our cross-section computation.

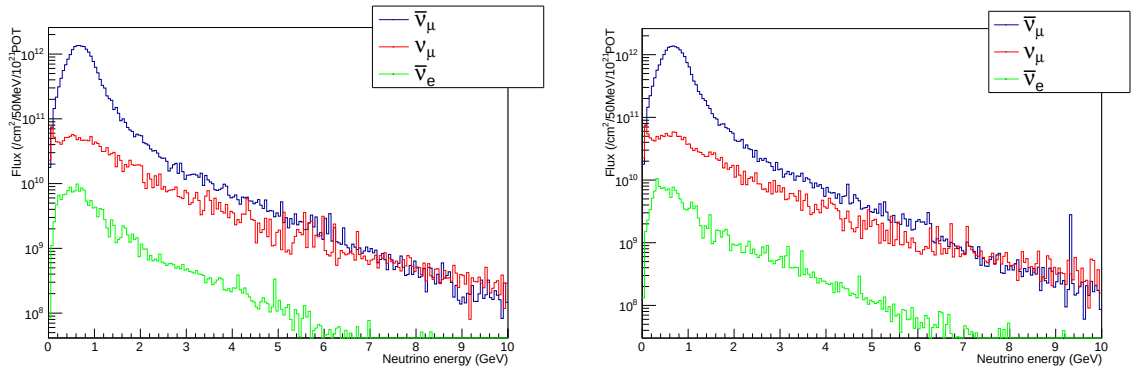

Figure 4.6 – Flux in the fiducial volumes of WAGASCI for 10^{21} POT ; In the Water Module (left) and in the Proton Module (right)

Table 4.3 – Energy integrated flux in the Water Module for 7.908 $\times$ 10^{20} POT (number of neutrinos per cm^2). We neglect the ν_e flux that is too small.

Element	Water Module	Proton Module
$\overline{\nu}_\mu$	1.645×10^{13}	1.647×10^{13}
ν_μ	1.518×10^{12}	1.492×10^{12}
$\overline{\nu}_e$	1.503×10^{11}	1.407×10^{11}

4.6 Number of nucleons of the targets

In this part, we will estimate the number of nucleon targets in the fiducial volumes of both the WM and the PM.

4.6.1 Water Module

In the fiducial volume of the WM we have water, the scintillators, the fibers. During the WM construction, we joined the fibers to the scintillators with an optical cement.
We made sure less than 50g of cement was used for each scintillator/fiber pair. We also measured the mass of the scintillators which are listed in Table 4.4 and shown in Figure 4.7.

The CH component

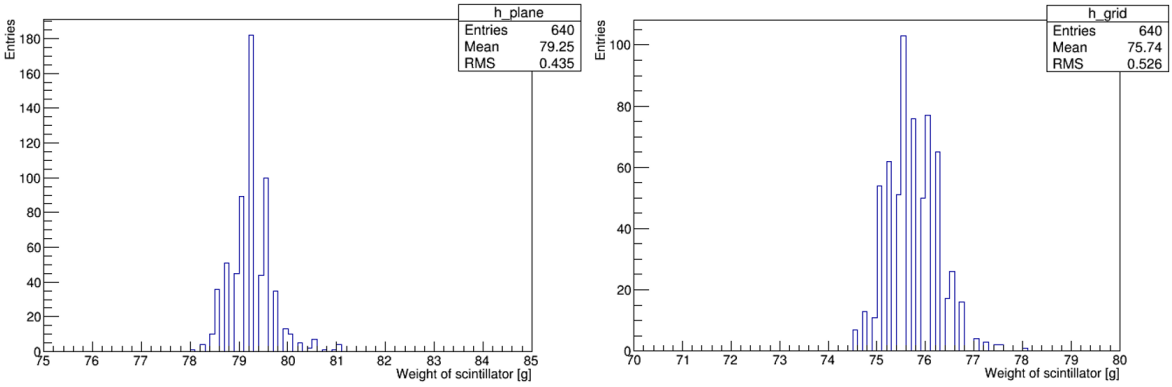

Figure 4.7 – Mass distribution of the WM scintillators ; plane scintillators (left) and grid scintillators (right). The grid scintillators are lighter becuse of the slits for the grid arrangement.

Table 4.4 – Average mass of the scintillators of the WAGASCI frame

Scintillator type	Average Mass (g)
Plane	79.25
grid	75.74

We have a fiducial volume with a transverse section of 80 cm × 80 cm. The volume also contains 10 block of 32 parallel scintillators as well as 32 grid scintillators.

Each scintillator has a mass fraction $\frac{80\,\text{cm}}{102\,\text{cm}}$ contained inside the fiducial volume.

Hence the weight of the scintillator frame in the fiducial volume is:

$$m_{WM}^{Scinti} = 79.25\,\text{g} \times \frac{80\,\text{cm}}{102\,\text{cm}} \times 10 \times 32 + 75.74 \times \frac{80\,\text{cm}}{102\,\text{cm}} \times 10 \times 32 = 38.90\,\text{kg} \qquad (4.11)$$

We now have to estimate the composition of a scintillator volume in order to compute the number of nucleon targets.

- Scintillating materials: polystyrene C_8H_8 with traces of PPO 2,5-Diphenyloxazole $C_{15}H_{11}NO$ and POPOP $C_{24}H_{16}N_2O_2$ represents 82.4 % of the total mass.
- Optical fiber: CH represent 1.1% of the total weight.
- Optical cement which glues the fiber to the scintillator: $C_4H_4O_2$ represents 2.5 % of the total weight
- Reflective coating: TiO_2 with traces of polystyrene C_8H_8 represents 12.8 % of the total weight

- Black painting $SiO_2C_5O_2H_8$ represents 1.2 % of the total weight

Using the elemental composition of each component (cf Appendix A) we can then compute the composition of the scintillators (cf Table 4.5) and see that the fractional mass of CH in the scintillator is 95.5%.

Table 4.5 – Mass fraction of the elements in the WM scintillators

Element	C	H	O	Ti	N	Si
Mass composition (%)	88.7	7.4	2.8	1.1	0.4	0.2

So the mass of CH contained in the fiducial volume is:

$$m_{WM}^{CH} = m_{WM}^{Scinti} \times 0.955 \tag{4.12}$$

Hence the number of nucleons for CH target in the fiducial volume is:

$$T_{WM}^{CH} = \frac{m_{WM}^{CH} \times (A_C + A_H)}{M_C + M_H} \times \mathcal{N}_A \tag{4.13}$$

where A_X is the number of mass of the element X, M_X is the molar mass of the element X, $\mathcal{N}_A$ is the Avogadro number. These numbers can be found in table 4.6.

Table 4.6 – Molar masses of the WM scintillators

Element	C	H	O	Ti	N	Si
Number of protons	6	1	8			
Number of neutrons	6.011	0.0001	8.00			
Molar mass ($g.mol^{-1}$)	12.011	1.008	16.00			

In the end we have:

$$T_{WM}^{CH} = 2.24 \times 10^{28} \text{ nucleons} \tag{4.14}$$

The water

The density of the scintillators of the WM frame was measured at: $\rho_{scinti} = 1.075\,g/cm^3$. The water is a mix of pure water H_2O (99.75 %) and of preservative (60 % of H_2O and 40 % of $C_8H_{14}N_4O_7$) (0.25%). The composition of the water can be found in Table 4.7. We can then estimate that the H_2O mass fraction is 99.95 %. Moreover, the density of the water is $\rho_{water} = 0.999\,g/cm^3$.

Table 4.7 – Elemental composition of the WM water

Element	H_2O	C	N
Mass composition (%)	99.75	0.03	0.02

The mass of water contained in the fiducial volume is

$$m_{water} = (V_{fiducial} - \frac{m_{WM}^{scinti}}{\rho_{scinti}}) \times \rho_{water} \tag{4.15}$$

where $V_{fiducial} = \underbrace{80\,cm \times 80\,cm}_{\text{transverse section}} \times \underbrace{29.56\,cm}_{\text{depth}}$

so we have:

$$m_{WM}^{H_2O} = 0.9995 \times m_{water} = 0.9995 \times 152.72\,\text{kg} = 152.64\,\text{kg} \tag{4.16}$$

By looking at Table 4.6, we can estimate the number of H_2O nucleons:

$$T_{WM}^{H_2O} = \frac{m_{WM}^{H_2O} \times (2 \times A_H + A_O)}{2 \times M_H + M_O} \times \mathcal{N}_A = 9.19 \times 10^{28}\ \text{nucleons} \tag{4.17}$$

4.6.2 Proton Module

We can find in [54], the mass distribution of the PM scintillators (Figure 4.8)as well as the fiber density ($1.03\,\text{g.cm}^{-3}$) and dimensions (radius $0.5\,\text{cm}^2$) We use this to compute the mass

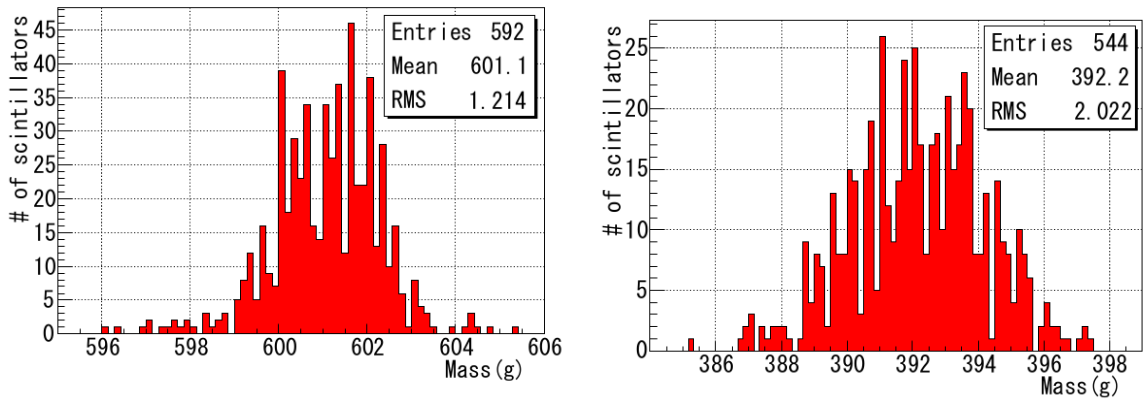

Figure 4.8 – Mass distribution of the PM scintillators ; INGRID-type (left) and Scibar-type (right). the two types don't have the same dimensions so their masses are different.

of scintillators in the fiducial volume:

$$m_{PM}^{scinti} = (392.2\,\text{g} \times 16 + 601.1\,\text{g} \times 8) \times \frac{80\,\text{cm}}{120.3\,\text{cm}} \times 13 \times 2 = 191.64\,\text{kg} \tag{4.18}$$

As well as the fiber mass in the fiducial volume which is not included in the scintillator mass:

$$m_{PM}^{fiber} = 24 \times 26 \times 80\,\text{cm} \times \pi \times 0.05\,\text{cm}^2 \times 1.03\,\text{g.cm}^{-2} = 0.404\,\text{kg} \tag{4.19}$$

Table 4.8 – Elemental composition of the PM scintillators (mass fraction)

Element	C	H	Ti	O	N
Mass composition (%)	90.96	7.61	0.76	0.59	0.07

So the mass fraction of CH in the scintillators of the fiducial volume is 98.57 %
The number of nucleon targets is:

$$T_{PM}^{CH} = 0.9857 \times \frac{(m_{PM}^{scinti} + m_{PM}^{fiber}) \times (A_C + A_H)}{M_C + M_H} \times \mathcal{N}_A = 189.30\,\text{kg} \times \frac{(A_C + A_H)}{M_C + M_H} \times \mathcal{N}_A \tag{4.20}$$

$$T_{PM}^{CH} = 1.14 \times 10^{29}\ \text{nucleons} \tag{4.21}$$

4.6.3 Dependency of the WM cross-section on the H_2O and CH cross-sections

The summary of the number of target nucleons is in Table 4.9

Table 4.9 – Number of nucleon targets in the fiducial volumes of both WAGASCI and the Proton Module

Target	number of nucleons ($\times 10^{28}$)
$T_{WM}^{H_2O}$	9.19
T_{WM}^{CH}	2.24
T_{PM}^{CH}	11.39

We can express the water module cross-section as a function of the cross-section on water and carbon in first approximation. We will validate that approximation when studying the systematics on the number of nucleon targets.

$$\sigma_{WM} = \alpha \times \sigma_{H_2O} + (1 - \alpha) \times \sigma_{CH} \tag{4.22}$$

with $\alpha = 80.4$ %

4.7 The convergence of the unfolding

If we launch an unfolding with the reconstructed sample predicted by the nominal Monte-Carlo simulation, we converge towards the predicted NEUT cross-section in a couple of iterations. However this is not enough to assert that our algorithm will always converge in so few iterations. For instance if we change the initial prior and take a flat prior instead of the prior predicted by NEUT, we converge in much more iterations (Figure 4.9).

In order to have a more comprehensive study of the closure criteria, we will use three sets of fake data. This study will be detailed in Chapter 6. For each set we will look at how the χ^2 of the difference between the unfolded signal and the true signal behaves when we increase the unfolding step.

$$\chi^2(n) = \sum_{(p_\mu,\theta_\mu),(p'_\mu,\theta'_\mu)} (\sigma_n(p_\mu,\theta_\mu) - \overline{\sigma}(p_\mu,\theta_\mu)) \times (Cov(n)^{-1})^{p_\mu,\theta_\mu}_{p'_\mu,\theta'_\mu} \times (\sigma_n(p'_\mu,\theta'_\mu) - \overline{\sigma}(p'_\mu,\theta'_\mu)) \tag{4.23}$$

where σ_n is the unfolded cross-section after the n-th step and $\overline{\sigma}$ is the true cross-section and $Cov(n)$ is the covariance matrix giving the uncertainties at the n-th step of the unfolding. The computations of the uncertainties is discussed in Chapter 5.

The cross-sections predictions used in the MC simulation are presented in table 4.10

Table 4.10 – Cross-sections predictions used in the NEUT simulation

Target	CC0π cross-section NEUT prediction
σ_{H_2O}	$1.145 \times 10^{-39} cm^2$
σ_{CH}	$1.032 \times 10^{-39} cm^2$
$\sigma_{H_2O}/\sigma_{CH}$	1.109

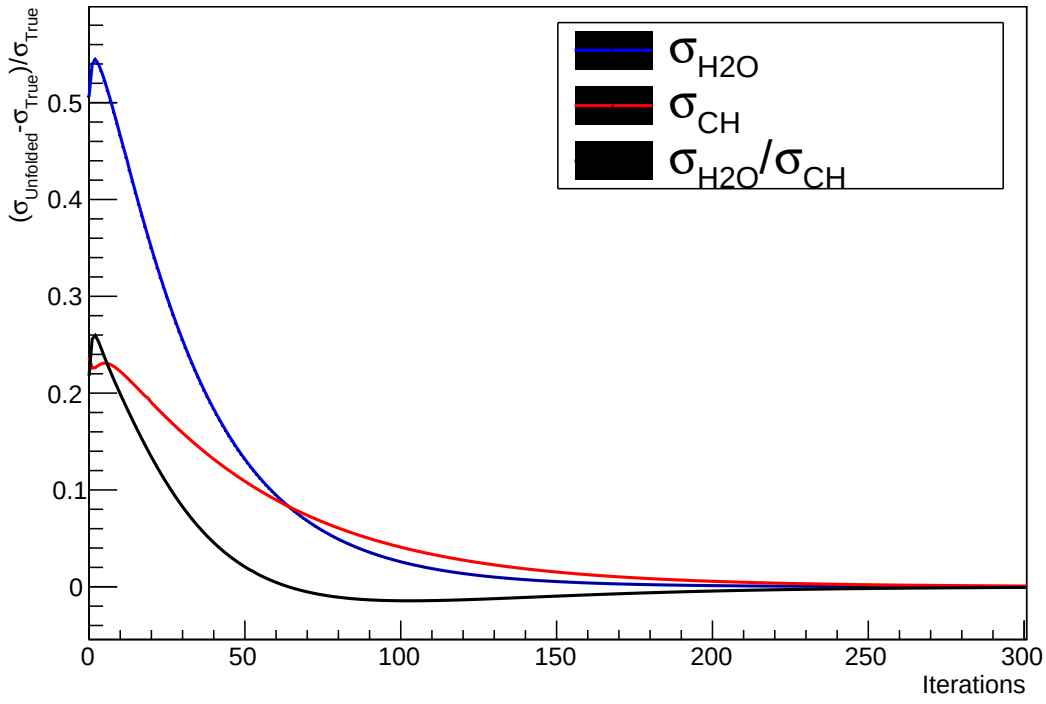

Figure 4.9 – Convergence of the unfolding procedure when we use a flat initial prior

Chapter 5

Uncertainties on the measurement

When measuring a physical quantity we have to provide the precision of our measurement. That precision depends on three main types of uncertainties:

- The statistical uncertainty: When we repeat an experiment we will most of the time obtain a distribution of values around a mean value. The central limit theorem tells us that the more we repeat an experiment the more our estimate will be precise. Here our event distribution follows a Poisson law. We use it to randomly modify the reconstructed bins of our selected events and we see how the unfolding affects that tempering. We obtain by that method a statistical uncertainty for each bin of our true phase space.
- The systematic errors of our detector response. This includes the tuning of our MC simulation as well as the track reconstruction.
- The systematic errors of our models: this includes the flux prediction (JNUBEAM) as well as the cross-section prediction by our interaction generator (NEUT).

We remind the reader that we will now consider the water cross-section σ_{H_2O}, which is a combination of the Water Module cross-section σ_{WM} and of the Proton Module cross-section σ_{PM}. We also consider the carbon cross-section which can be identified to the Proton Module cross-section σ_{PM}.

5.1 Statistical uncertainty

As described earlier, we change the content of the reconstructed signal bins following a Poisson law (uncertainty on the event count during a fixed period of time). Each of these pseudo-experiments is then unfolded to see how the true phase space bins are affected. This method allows us to compute the statistical uncertainty for the for H_2O and the for CH. For the σ_{H2O}/σ_{CH} ratio measurement, the statistical error will be computed as a derivative of the errors on the σ_{H2O} measurement and the σ_{CH} measurement:

$$\delta(\frac{\sigma_{H2O}}{\sigma_{CH}}) = \frac{1}{\sigma_{CH}} \times \delta(\sigma_{H2O}) + \frac{\sigma_{H2O}}{\sigma_{CH}^2} \times \delta(\sigma_{CH}) \tag{5.1}$$

We use that method to compute the statistical covariance matrices and the correlation matrices. The axis give the bin number, with the binning shown in Table 5.1. For the double differential analysis, the label (i, j) represents the bin for the i-th momentum bin and the j-th angle bin.

The correlation matrices are displayed on Figure 5.1 for the double differential analysis, on Figure 5.2 for the momentum analysis, on Figure 5.3 for the angle analysis. In these plots,

Table 5.1 – Coordinates of the muon in the true phase space.

True phase space	# of bins	bins limits
p_μ (GeV): True momentum	5	0 , 0.4 , 0.6 , 0.8 , 1.0 , 30.0
θ_μ (°): True angle	4	0 , 10 , 20 , 30 , 180
CC1π bin	1	all CC1π interactions
other interactions bins	1	all other interactions

the first momentum bin and first four double differential bins are empty for the CH analysis because our simulation predicts no events in these bins. Therefore, the uncertainty computed is zero for a zero number of events. They are not displayed in order to avoid confusion at the reading of the values. Besides, the relevance of these bins is moot since we do not extract cross-section measurement for these values of the true kinematic variables.

The statistical uncertainties are displayed on Figure 5.4 for the double differential analysis, on Figure 5.5 for the momentum analysis, on Figure 5.6 for the angle analysis.

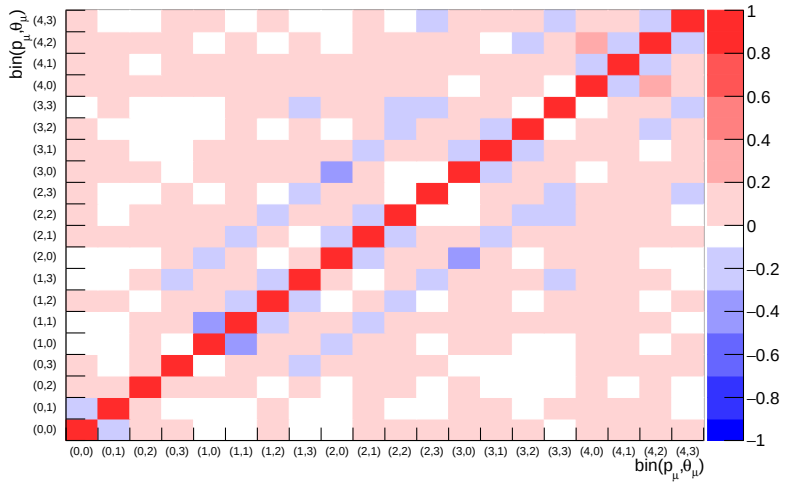

(a) σ_{H_2O}

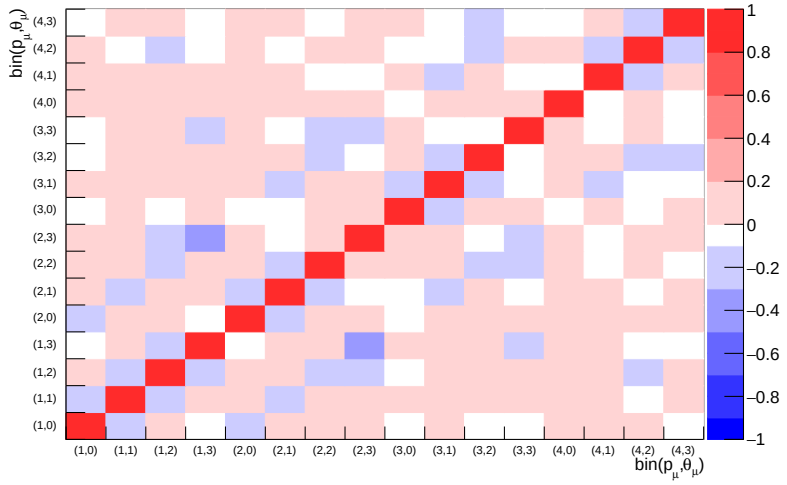

(b) σ_{CH}

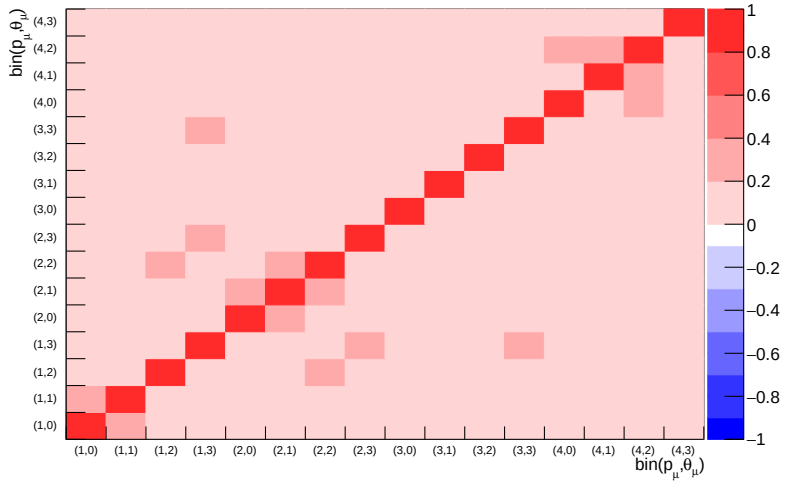

(c) $\sigma_{H_2O}/\sigma_{CH}$

Figure 5.1 – Correlation matrix for the errors on the cross-section related to the statistical error. Binning in momentum and angle. for H_2O (Top) ; for CH (Middle) ; ratio of the cross-section (Bottom). The binning is shown in Table 5.1

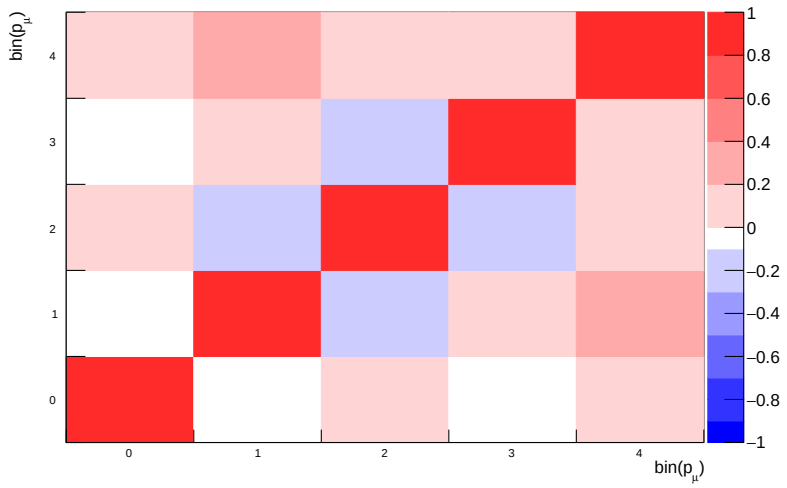

(a) σ_{H_2O}

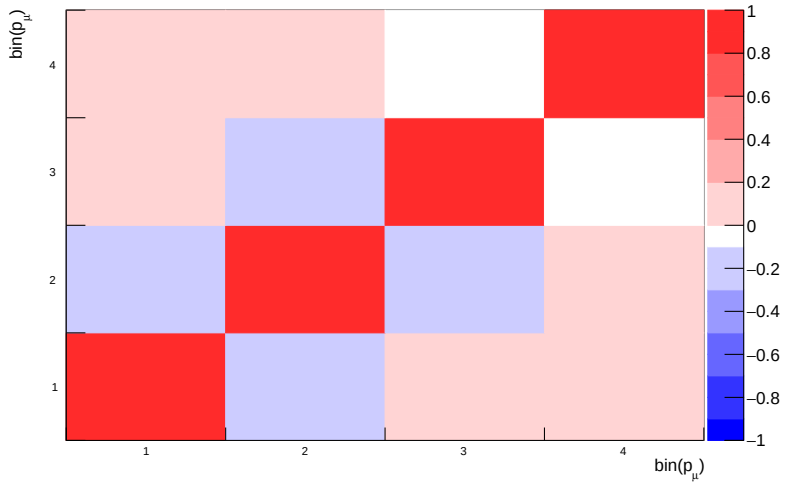

(b) σ_{CH}

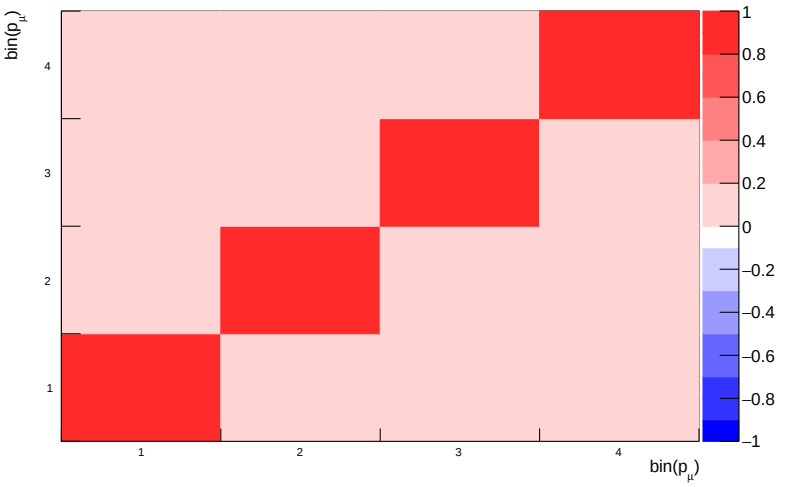

(c) $\sigma_{H_2O}/\sigma_{CH}$

Figure 5.2 – Correlation matrix for the errors on the cross-section related to the statistical error. Binning in momentum. for H_2O (Top) ; for CH (Middle) ; ratio of the cross-section (Bottom). The binning is shown in Table 5.1

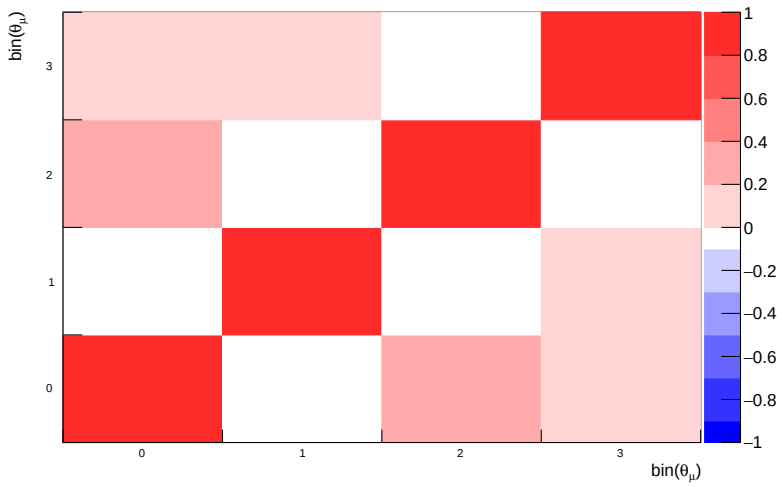

(a) σ_{H_2O}

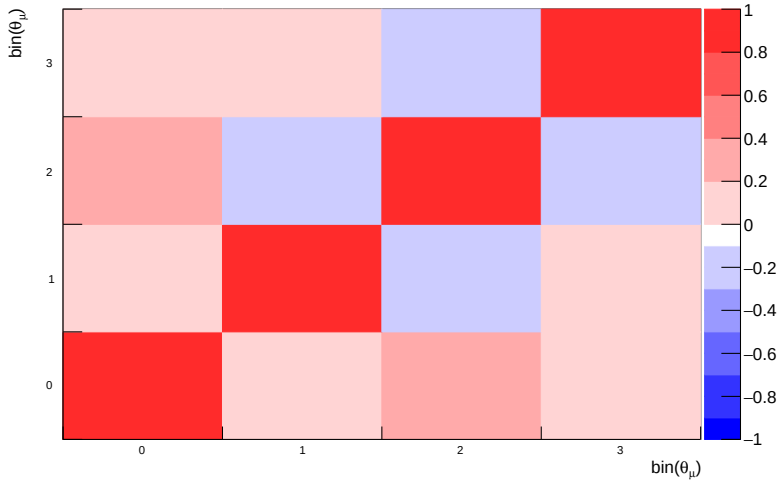

(b) σ_{CH}

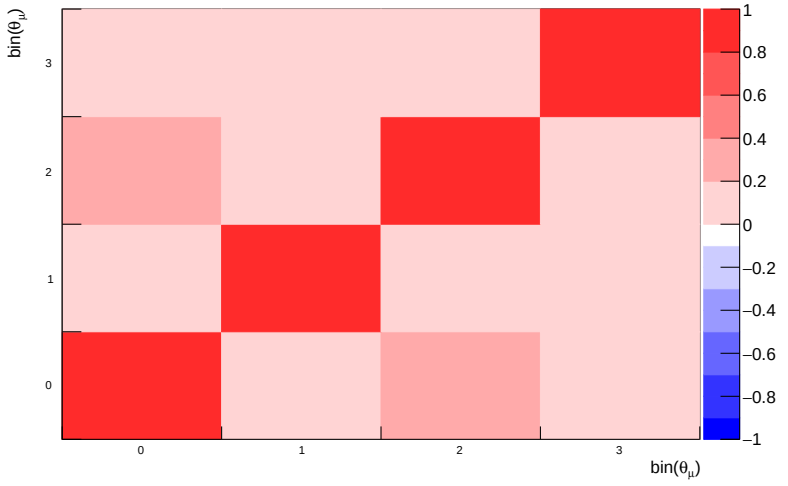

(c) $\sigma_{H_2O}/\sigma_{CH}$

Figure 5.3 – Correlation matrix for the errors on the cross-section related to the statistical error. Binning in angle. for H_2O (Top) ; for CH (Middle) ; ratio of the cross-section (Bottom). The binning is shown in Table 5.1

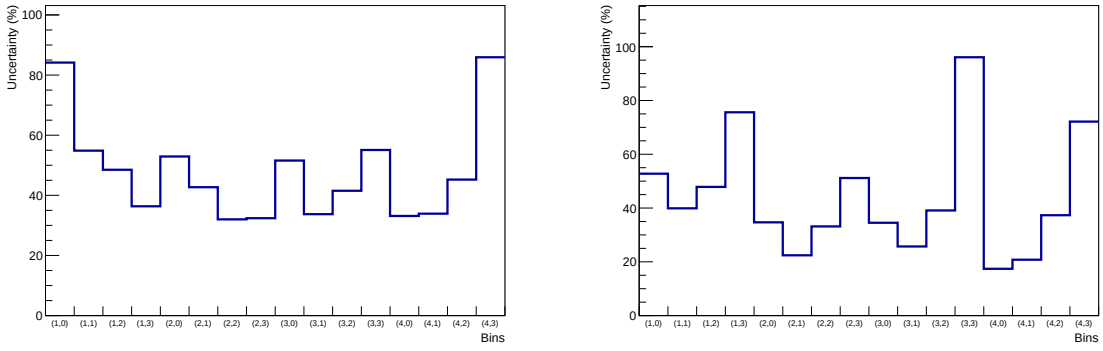

(a) for H_2O (b) for CH

Figure 5.4 – Statistical error on the cross-section for the binning in momentum and angle. The binning is shown in Table 5.1

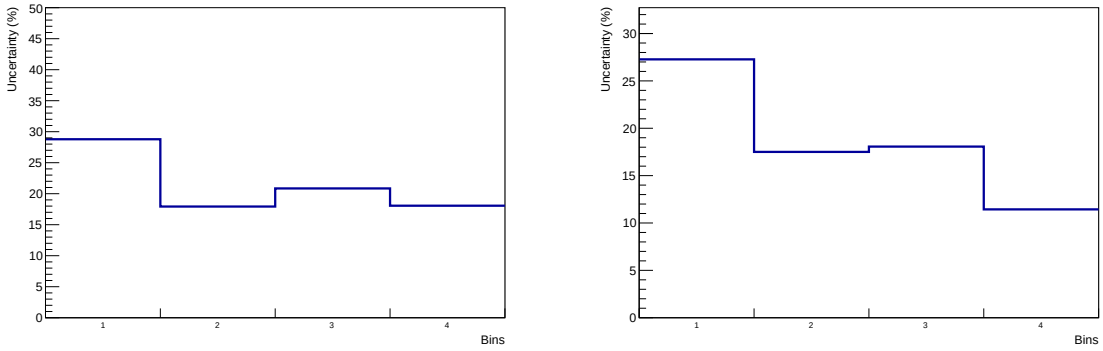

(a) for H_2O (b) for CH

Figure 5.5 – Statistical error on the cross-section for the binning in momentum. The binning is shown in Table 5.1

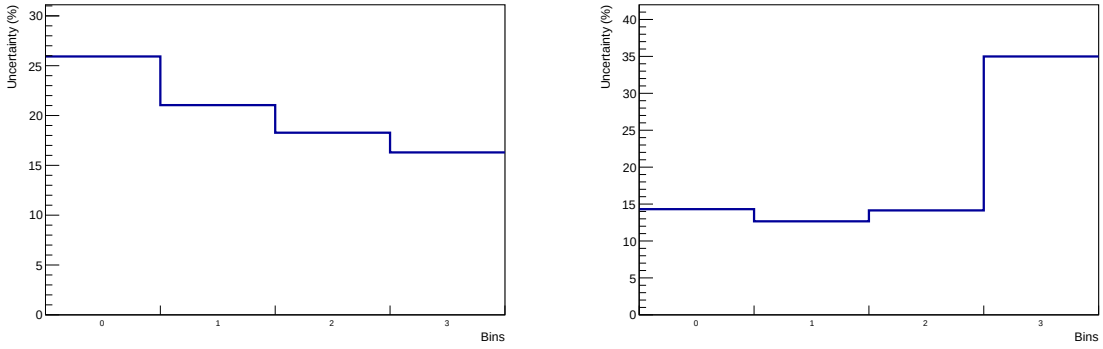

(a) for H_2O (b) for CH

Figure 5.6 – Statistical error on the cross-section for the binning in angle. The binning is shown in Table 5.1

5.2 Systematic errors

5.2.1 Flux uncertainties

By taking into account the uncertainties on all the parameters for the flux production, we have generated a covariance matrix for the $\overline{\nu}_\mu$ flux in both the WM and the PM (Figure 5.9). We take into account the uncertainties from the hadron interaction models such as the interaction length, the secondary interaction and so on (Figure 5.7) and also from the non-hadron interaction models such as the material modeling, the orientation of the target, the proton beam kinematics and so on (Figure 5.8).

We are then able to randomly change the number of background events as well as the norm of the flux predicted by the JNUBEAM simulation of the flux.

The binning used for the neutrino energy binning is the given in Table 5.2

Energy range	Number of bins	Energy width per bin
0.0 GeV to 3.0 Gev	15	0.2 GeV
3.0 GeV to 4.0 Gev	1	1.0 GeV
4.0 GeV to 10.0 Gev	3	2.0 GeV
10.0 GeV to 30.0 Gev	1	20.0 GeV

Table 5.2 – Binning for the neutrino energy

We take 1000 toy models by constructing 1000 random instances of neutrino energy spectrum. For each of these toy models, we then reweight the flux as well as the background events and the efficiency. We perform an unfolding with the toy model as the MC and the nominal MC as fake data. This allows us to build a covariance matrix depending on the flux uncertainties.

The matrix for the 2D dimension binning (momentum and angle) is presented in Figure 5.10. We notice that while the cross-sections have strongly correlated bins due to the fact that the flux uncertainties are mainly positively correlated, the ratio is much more loosely correlated. The reason is that if the flux vary similarly in the WM and in the PM, so the cross-sections are similarly renormalized.

In the same way, we compute the correlation matrix of the errors on the cross-section due to the flux uncertainty, binned in momentum. The matrix can be found in Figure 5.11.

Finally, the correlation matrix of the errors on the cross-section due to the flux uncertainty, binned in angle can be found in Figure 5.12.

The uncertainty on the cross-section related to the flux uncertainty is given in Figure 5.13. We can read values around 8%. Similarly, we have the uncertainty related to the flux for the binning in momentum displayed at Figure 5.14 is at 8 to 12 % in uncertainty. Finally, the uncertainty related to the flux for the binning in angle at Figure 5.15: 8 to 10 %.

It is worth mentioning that the systematic uncertainty on the ratio $\sigma_{H_2O}/\sigma_{CH}$ related to the flux uncertainty is much smaller than the uncertainty on the cross-sections σ_{H_2O} and σ_{CH} as we can see in the Table 5.3.

5.2.2 Cross-section model uncertainties

Our Monte-Carlo simulation is produced with the NEUT 5.3.3 interaction model.
We use T2KReWeight v1r27p3 to alter the different parameters of the cross-section model. We

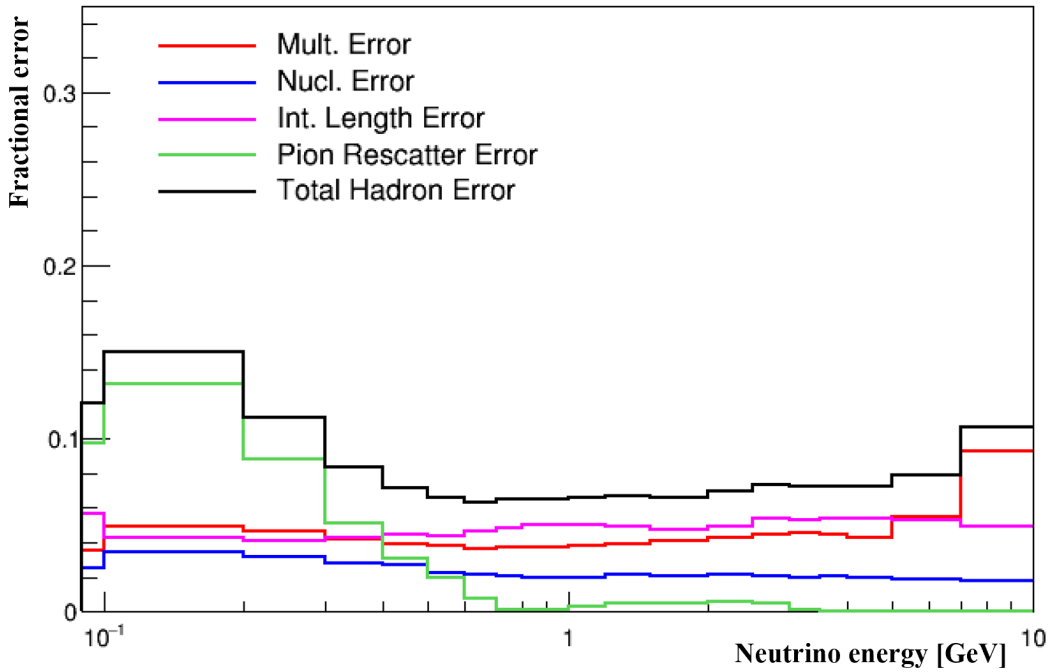

(a) for H_2O

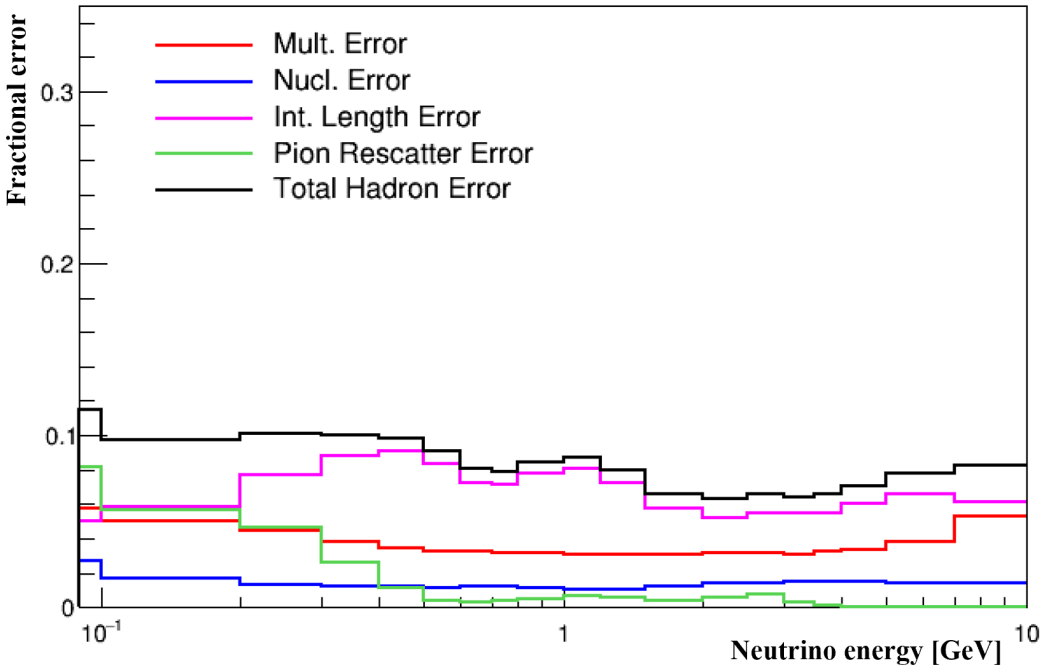

(b) for CH

Figure 5.7 – The hadron interaction model uncertainties evaluated on the WM flux prediction for ν_μ (top) and $\bar{\nu}_\mu$ (bottom). Taken from [55]

Table 5.3 – Flux systematic error on the single bin cross-section

cross-section	error (%)
σ_{H_2O}	11.60
σ_{CH}	11.23
$\sigma_{H_2O}/\sigma_{CH}$	0.40

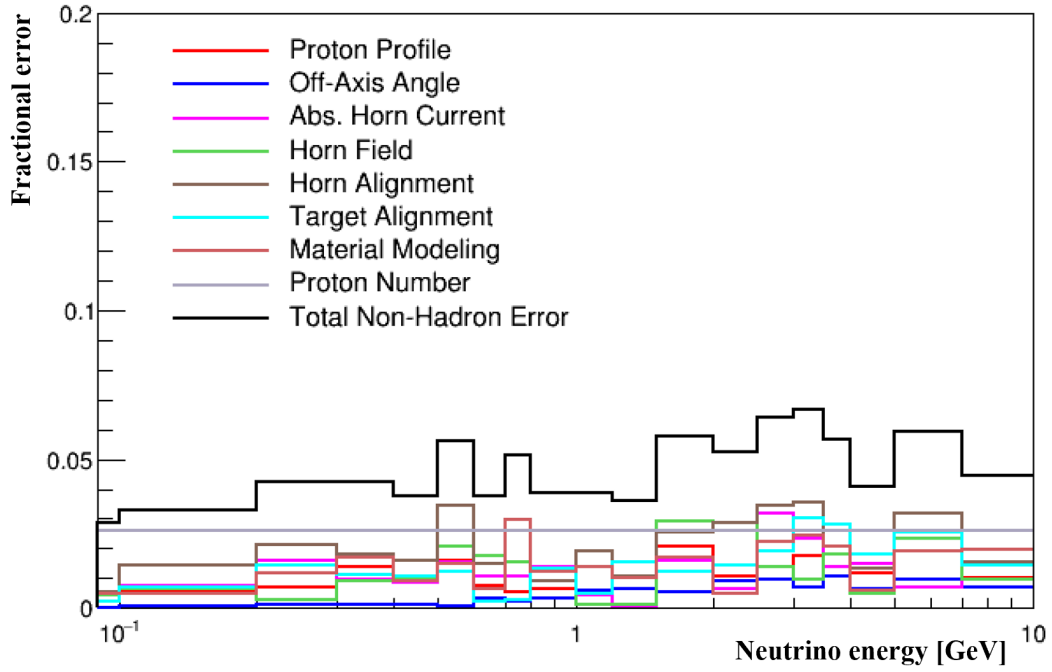

(a) for H_2O

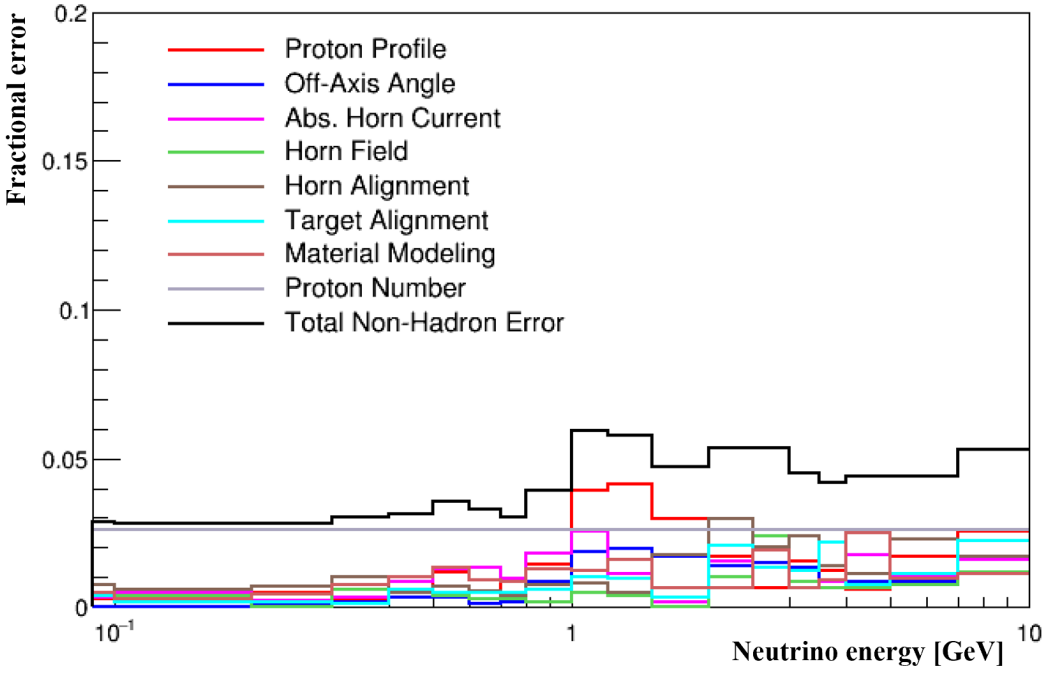

(b) for CH

Figure 5.8 – The non-hadron interaction model uncertainties evaluated on the WM flux prediction for ν_μ (top) and $\bar{\nu}_\mu$ (bottom). Taken from [55]

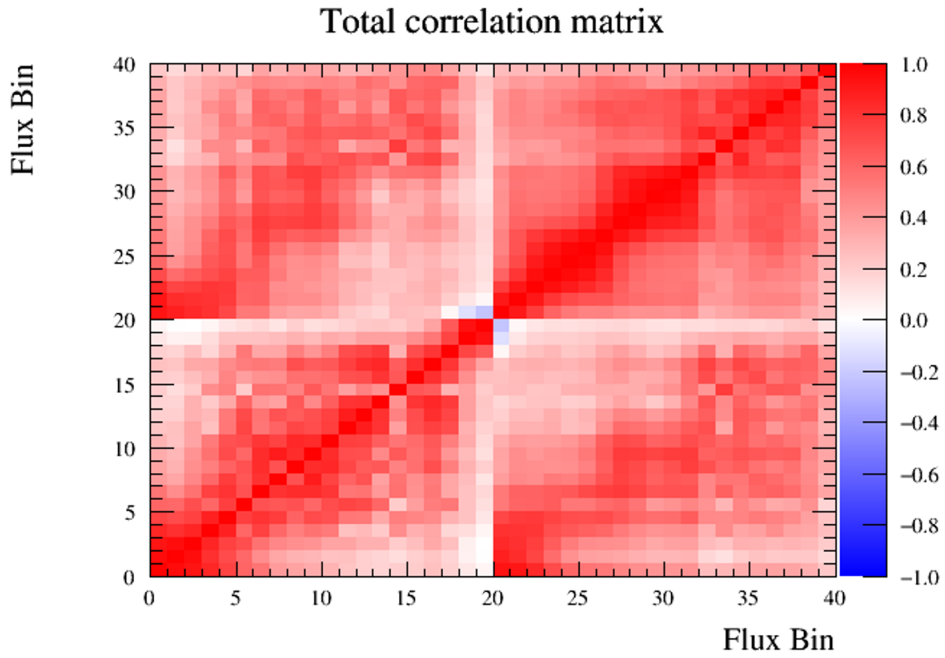

Figure 5.9 – Flux correlation matrix. The first 20 bins are the ν_μ component of the total flux while the last 20 bins correspond to the $\overline{\nu}_\mu$ component of the flux.

consider a total of 20 parameters (Table 5.4) which are needed to describe the CCQE, CCRes, CC/NC-other, the CC/NC-coherent, the FSI. We modify them and look at the impact on the efficiency, on our smearing matrix (detector response) and on the unfolding matrix. We obtain a new estimation of our cross-section and the uncertainty associated to this parameter.

For each parameter we look at the values of the modified cross-section when varying the parameter at -3σ, -2σ, $-\sigma$, the nominal value, $+1\sigma$, $+2\sigma$, $+3\sigma$. We call these 7 cross-sections the "dials"
This "modified cross-section" is the extracted cross-section when we unfold the nominal MC by the modified MC.

We then extrapolate the 7 points graph we obtain with 3 degree polynomial segments in order to have an estimation of the dependency of the cross-section on the parameter. An example is shown in Figure 5.16 for the axial mass parameter M_A^{QE}.
We then build 5000 toy-models as follow:
For each toy model, we shoot a random value for the parameter, of Gaussian random law $\mathcal{N}(0,1)$ (mean 0 and covariance 1). We then use the cross-section dependencies on the parameter extrapolated earlier on to deduce the values of the cross-sections in each bin.

This allows us to build a covariance matrix for the parameter by averaging on the collection of toy-models.
The values of the errors are summarized in Table 5.5. We can notice that the water cross-section depends on the carbon and oxygen parameter, which is expected since it is a combination of the Water Module cross-section and of the Proton Module cross-section.

The same breakdown can be established for the 2 dimension case, where we differentiate the cross-section in both momentum and angle. The results are presented in Figure 5.17. We can see that at that level; it is the FSI uncertainties that dominate the source of errors on

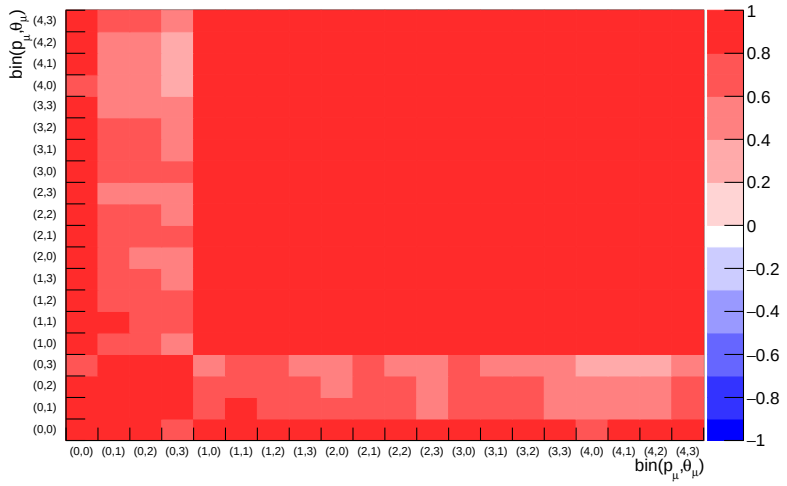

(a) σ_{H_2O}

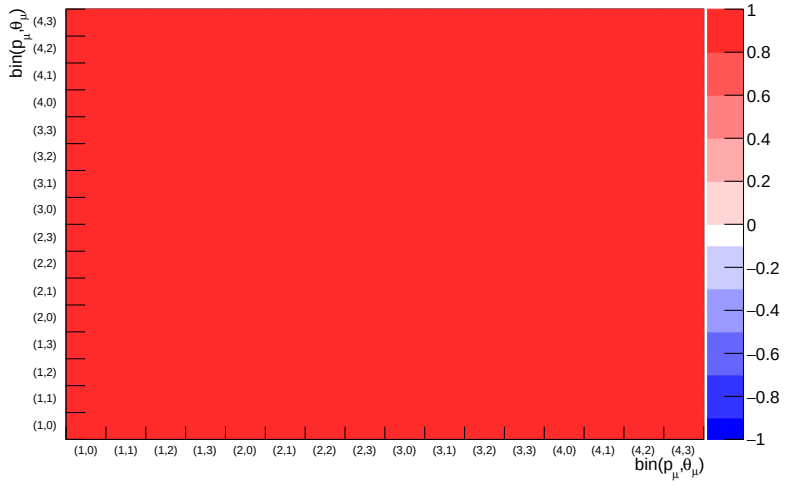

(b) σ_{CH}

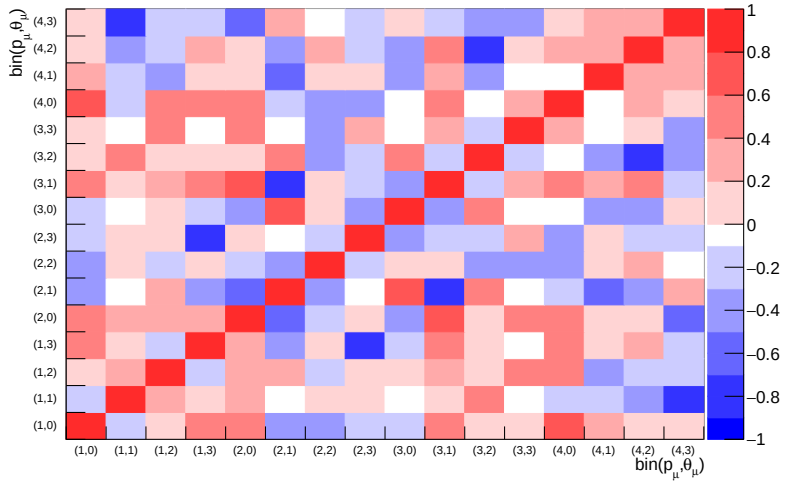

(c) $\sigma_{H_2O}/\sigma_{CH}$

Figure 5.10 – Correlation matrix for the errors on the cross-section related to the flux uncertainty. Binning in momentum and angle. for H_2O (Top) ; for CH (Middle) ; ratio of the cross-section (Bottom). The binning is shown in Table 5.1

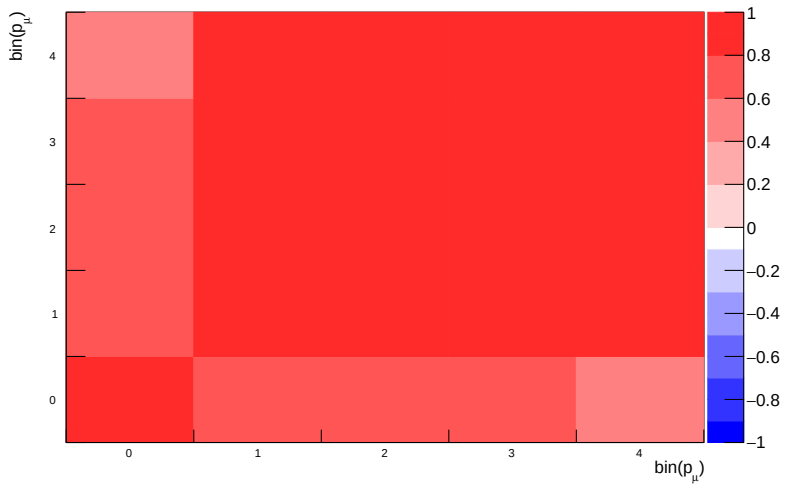

(a) σ_{H_2O}

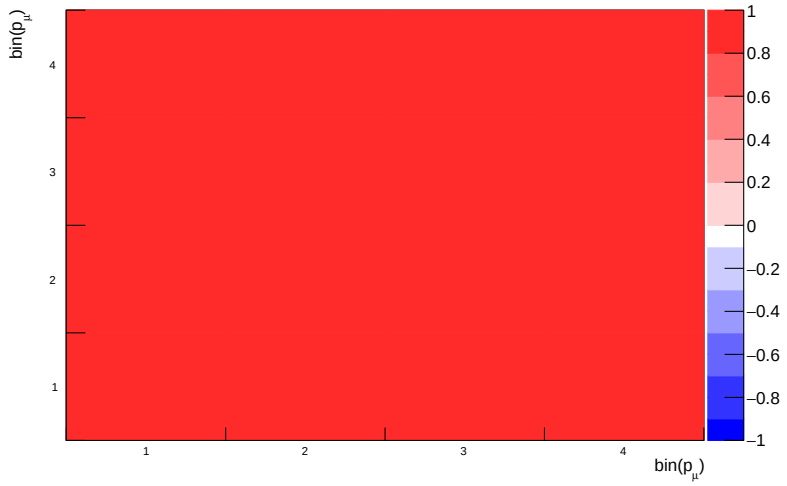

(b) σ_{CH}

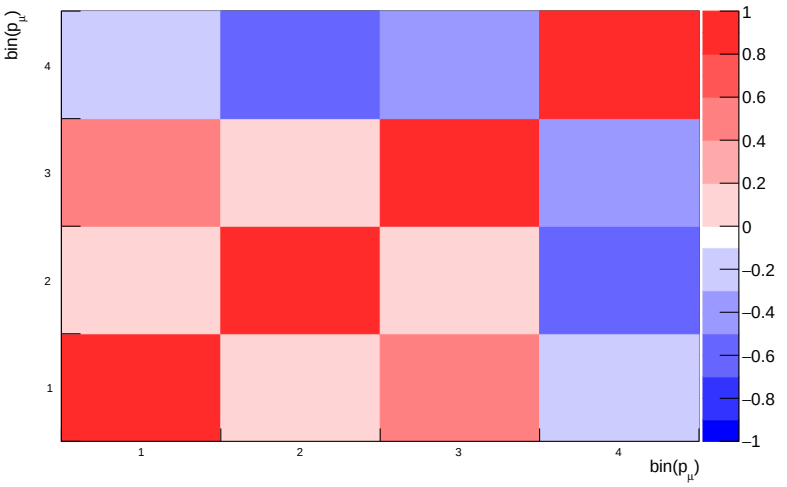

(c) $\sigma_{H_2O}/\sigma_{CH}$

Figure 5.11 – Correlation matrix for the errors on the cross-section related to the flux uncertainty. Binning in momentum. for H_2O (Top) ; for CH (Middle) ; ratio of the cross-section (Bottom). The binning is shown in Table 5.1

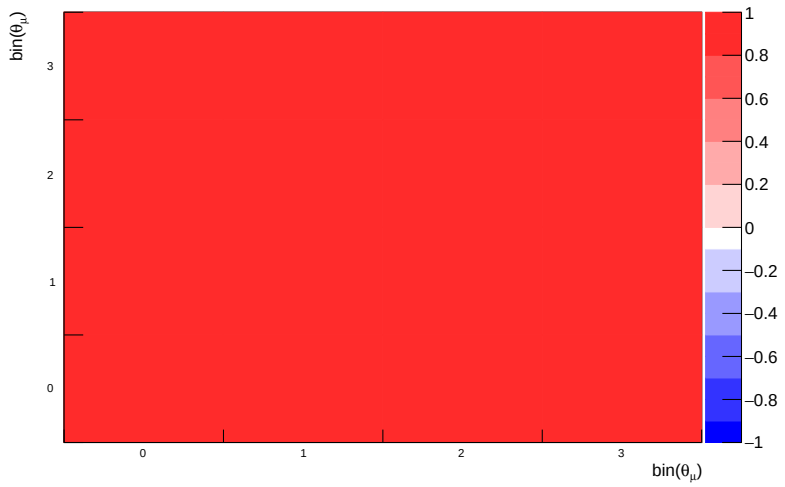

(a) σ_{H_2O}

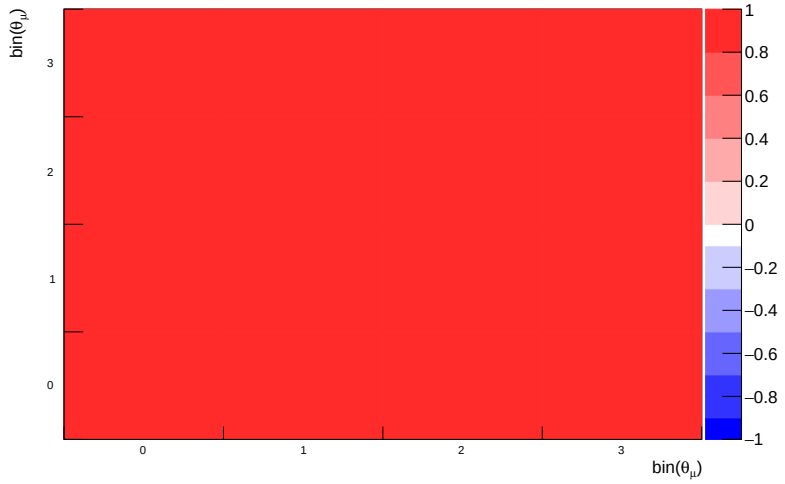

(b) σ_{CH}

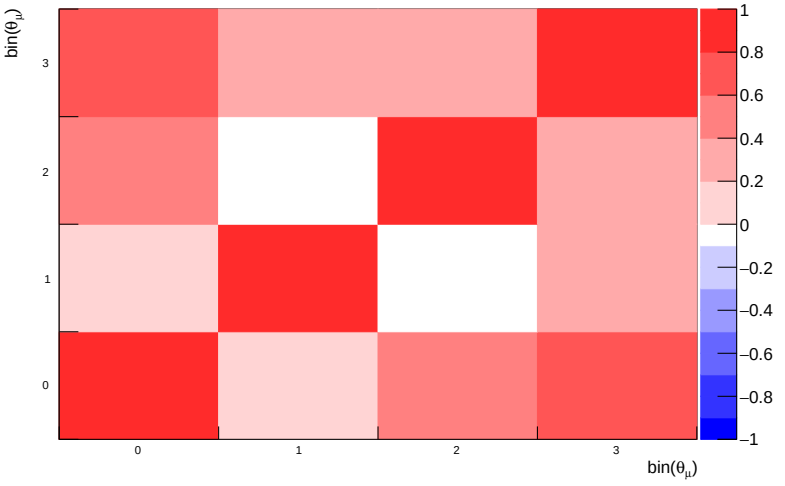

(c) $\sigma_{H_2O}/\sigma_{CH}$

Figure 5.12 – Correlation matrix for the errors on the cross-section related to the flux uncertainty. Binning in angle. for H_2O (Top) ; for CH (Middle) ; ratio of the cross-section (Bottom). The binning is shown in Table 5.1

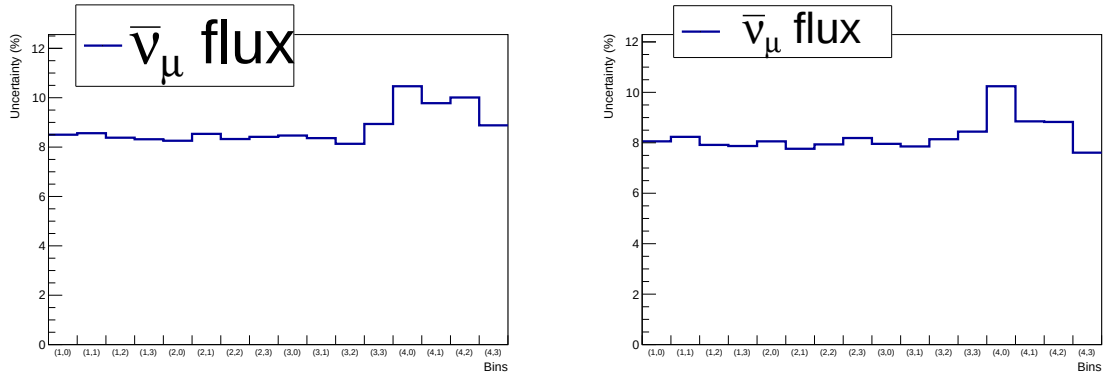

(a) for H_2O (b) for CH

Figure 5.13 – Flux related error on the cross-section for the binning in momentum and angle. The binning is shown in Table 5.1

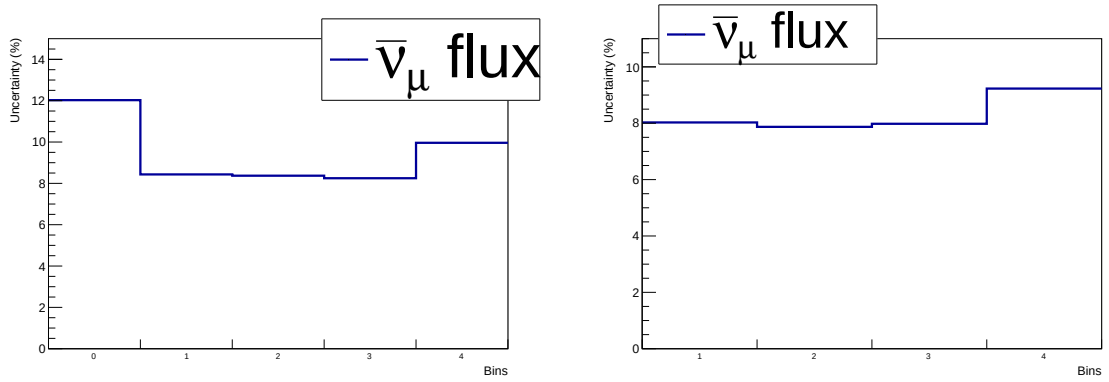

(a) for H_2O (b) for CH

Figure 5.14 – Flux related error on the cross-section for the binning in momentum. The binning is shown in Table 5.1

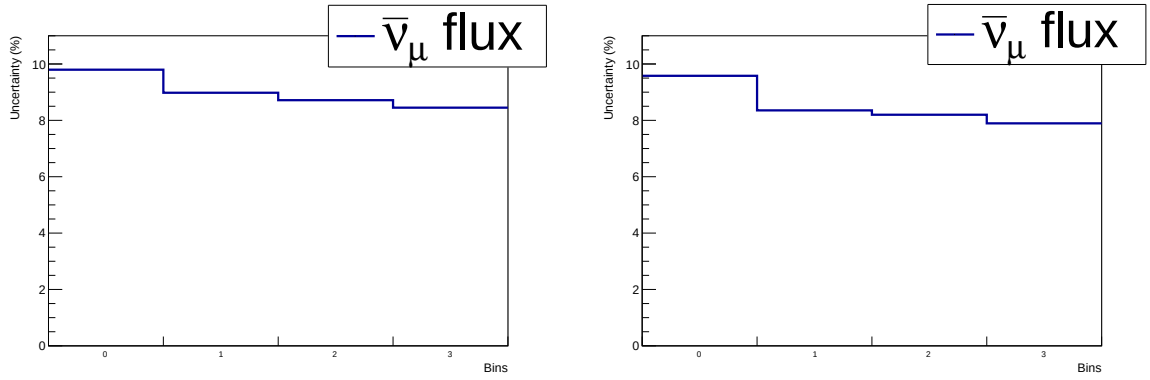

(a) for H_2O (b) for CH

Figure 5.15 – Flux related error on the cross-section for the binning in angle. The binning is shown in Table 5.1

Table 5.4 – Parameters of the cross-section model used in NEUT 5.3.3

Index	Parameter	Nominal value	Uncertainty (1σ)
19	Axial mass CCQE M_A^{QE}	1.15 GeV/c^2	0.18 GeV/c^2
20	Axial mass RES M_A^{RES}	0.95 GeV/c^2	0.15 GeV/c^2
21	C_A^5	1.01	0.12
22	Isospin $\frac{1}{2}$ background	1.3	0.2
23	CC-other shape	0.0	0.4
24	NC-other norm	1.0	0.30
32	CC-coherent ^{12}C,^{16}O,Fe (norm)	1.0	0.30
25	NC-coherent ^{12}C,^{16}O,Fe (norm)	1.0	0.30
26	p_F ^{12}C	223 MeV/c	31 MeV/c
27	p_F ^{16}O	225 MeV/c	31 MeV/c
28	E_b ^{12}C	25 MeV	9 MeV
29	E_b ^{16}O	27 MeV	9 MeV
30	2p-2h ^{12}C (norm)	100%	100%
31	2p-2h ^{16}O (norm)	100%	100%
33	FSI - π absorption	1.1	50%
34	FSI - π Charge exchange (low Energy)	1.0	50%
35	FSI - π QE scattering (low Energy)	1.0	50%
36	FSI - π Charge exchange (High Energy)	1.8	30%
37	FSI - π QE scattering (High Energy)	1.8	30%
38	FSI - π inelastic production	1.0	50%

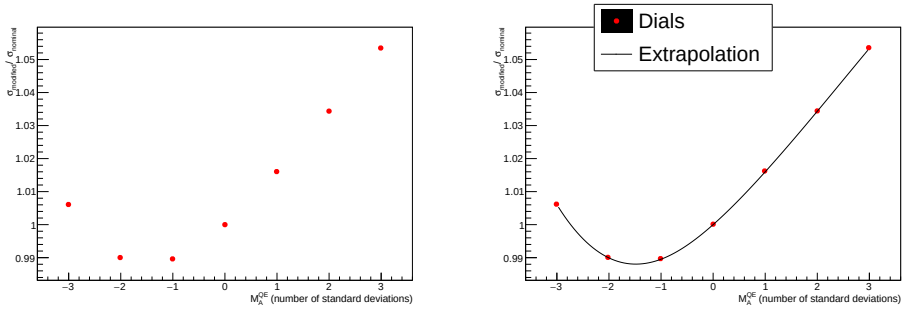

(a) Value for the 7 dials

(b) Values extrapolated by degree 3 polynomial segments

Figure 5.16 – Extrapolation of the cross-section dependance from the 7 dials for the CCQE axial mass

Table 5.5 – Uncertainties on the cross-section at one standard deviation from the nominal value of each parameter

Index	Parameter	σ_{H_2O} (%)	σ_{CH} (%)	$\sigma_{H_2O}/\sigma_{CH}$ (%)
19	Axial mass CCQE M_A^{QE}	± 1.691	± 1.269	± 0.434
20	Axial mass RES M_A^{RES}	± 0.524	± 0.548	± 0.321
21	C_A^5	± 1.288	± 0.672	± 0.605
22	Isospin $\frac{1}{2}$ background	± 0.674	± 0.266	± 0.407
23	CC-other shape	± 0.452	± 0.122	± 0.556
24	NC-other norm	± 0.348	± 0.057	± 0.410
32	CC-coherent ^{12}C,^{16}O,Fe (norm)	± 4.800	± 4.735	± 0.655
25	NC-coherent ^{12}C,^{16}O,Fe (norm)	± 0.015	± 0.198	± 0.216
26	p_F ^{12}C	± 0.170	± 0.208	± 0.388
27	p_F ^{16}O	± 0.311	<0.001	± 0.323
28	E_b ^{12}C	± 0.006	± 0.030	± 0.033
29	E_b ^{16}O	± 0.035	<0.001	± 0.035
30	2p-2h ^{12}C (norm)	± 1.243	± 1.503	± 2.844
31	2p-2h ^{16}O (norm)	± 1.045	<0.001	± 1.071
33	FSI - π absorption	± 2.528	± 0.444	± 2.078
34	FSI - π Charge exchange (low Energy)	± 0.528	± 0.371	± 0.164
35	FSI - π QE scattering (low Energy)	± 0.428	± 0.516	± 0.215
36	FSI - π Charge exchange (High Energy)	± 0.547	± 0.109	± 0.636
37	FSI - π QE scattering (High Energy)	± 0.589	± 0.449	± 1.067
38	FSI - π inelastic production	± 0.205	± 0.031	± 0.237
	Total	± 5.777	± 5.294	± 4.168

the cross-section extraction.

We also have the break down for the binning in momentum at Figure 5.18.

We also have the break down for the binning in angle at Figure 5.19.

The covariance matrix for the systematic uncertainty associated to the cross-section model is given by the sum of the covariance matrices for the errors associated to every parameters of the model. We obtain the total correlation matrices for the errors on the cross-section model in Figure 5.20. Once again, the bins for low momentum are empty for the for CH which explains why the correlation matrix doesn't take them into account. The correlation matrix for the same uncertainty binned in momentum can be found in Figure 5.21. Similarly, the matrix the uncertainty binned in angle can be found in Figure 5.22.

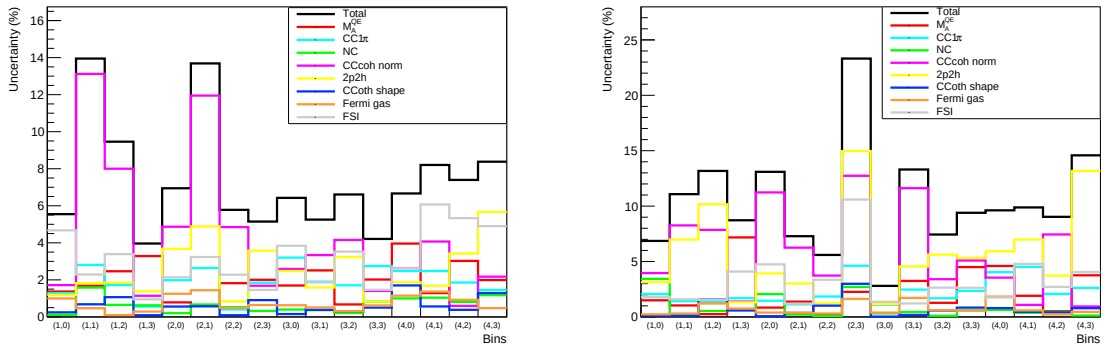

(a) for H_2O (b) for CH

Figure 5.17 – Breakdown of the source of the error from the cross-section model. Double differential binning. We take the bins where the muon momentum $p_\mu > 0.4\,\text{GeV}$

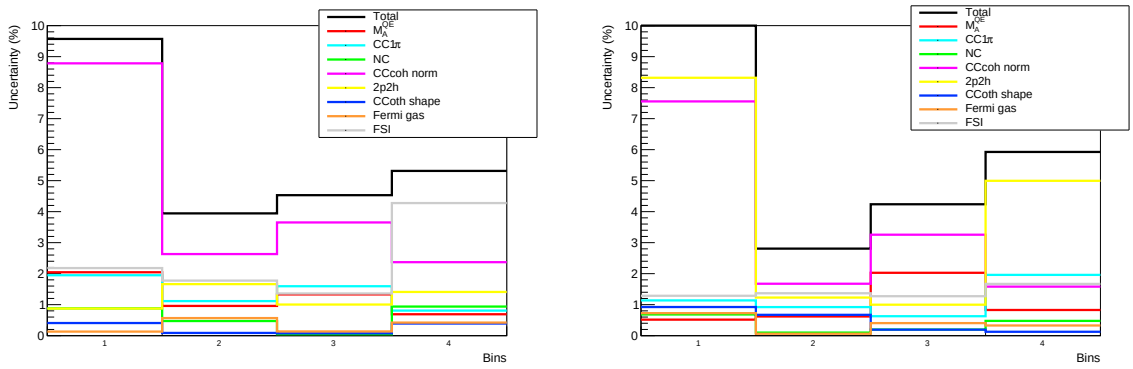

(a) for H_2O (b) for CH

Figure 5.18 – Breakdown of the source of the error from the cross-section model. Momentum binning. We take the bins where the muon momentum $p_\mu > 0.4\,\text{GeV}$

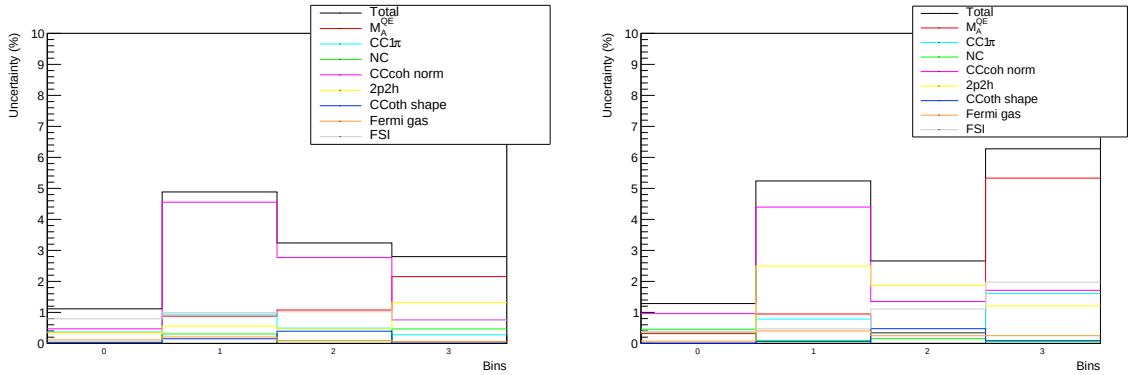

(a) for H_2O (b) for CH

Figure 5.19 – Breakdown of the source of the error from the cross-section model. Angle binning.

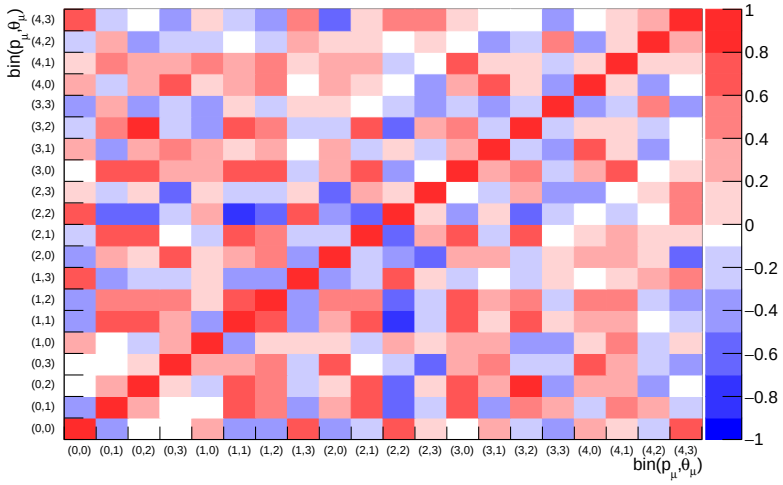

(a) σ_{H_2O}

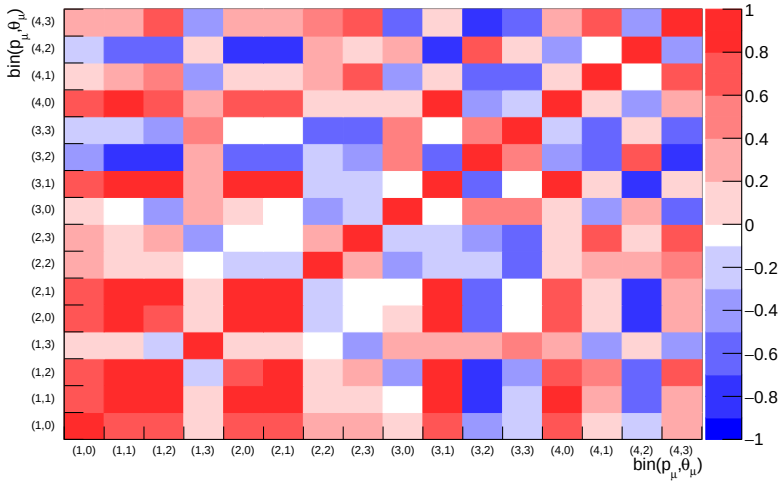

(b) σ_{CH}

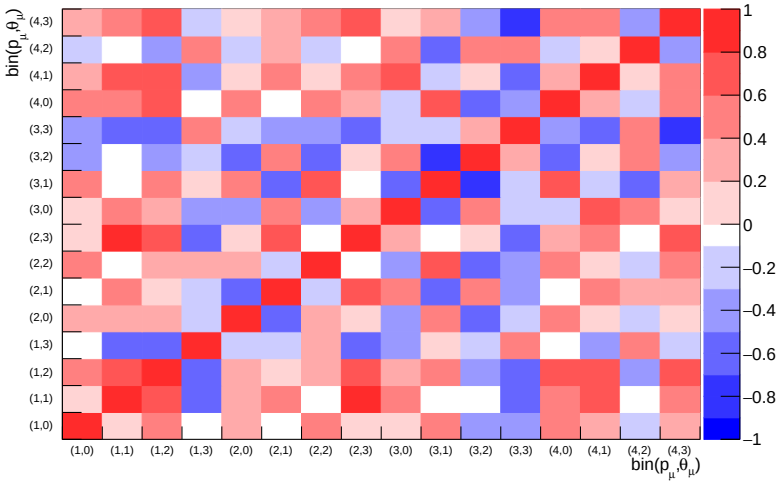

(c) $\sigma_{H_2O}/\sigma_{CH}$

Figure 5.20 – Correlation matrix of the errors on the cross-section from the uncertainty on the cross-section model. Binning in momentum and angle. for H_2O (Top) ; for CH (Middle) ; ratio of the cross-section (Bottom)

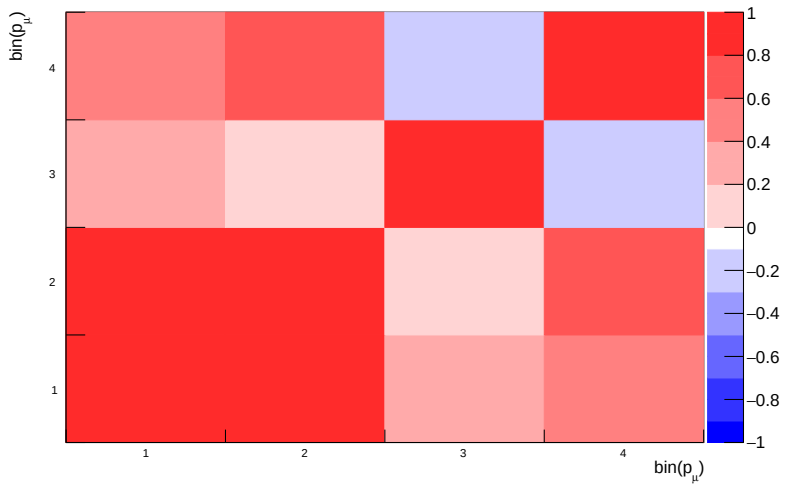

(a) σ_{H_2O}

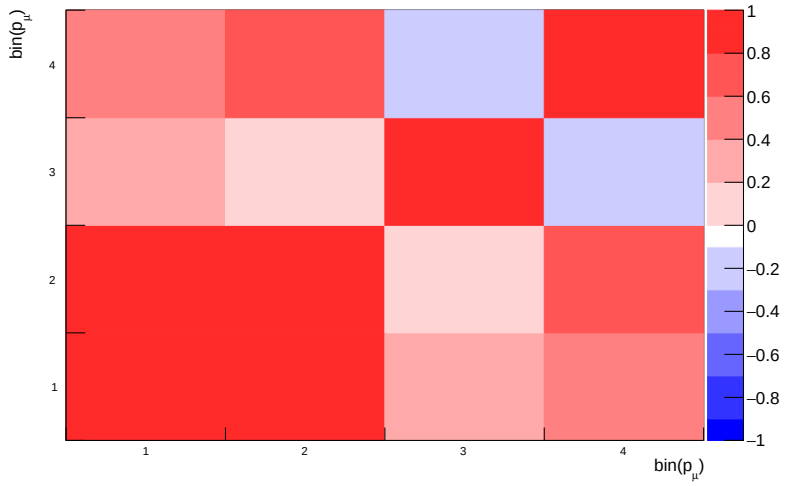

(b) σ_{CH}

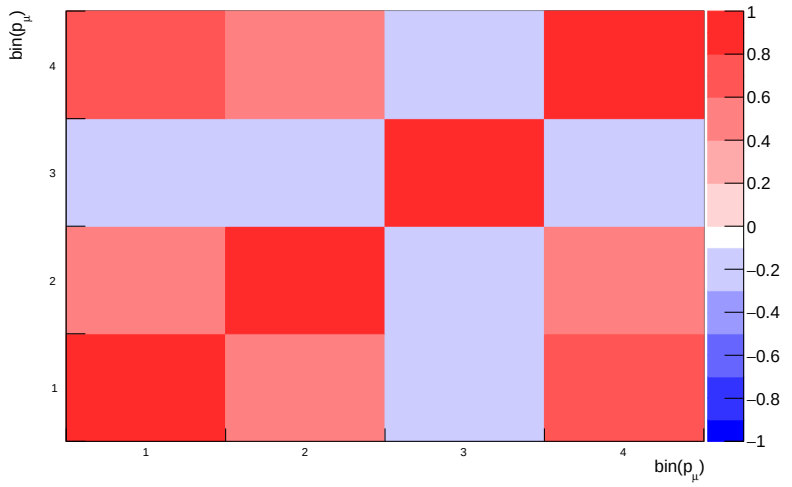

(c) $\sigma_{H_2O}/\sigma_{CH}$

Figure 5.21 – Correlation matrix of the errors on the cross-section from the uncertainty on the cross-section model. Binning in momentum. for H_2O (Top) ; for CH (Middle) ; ratio of the cross-section (Bottom)

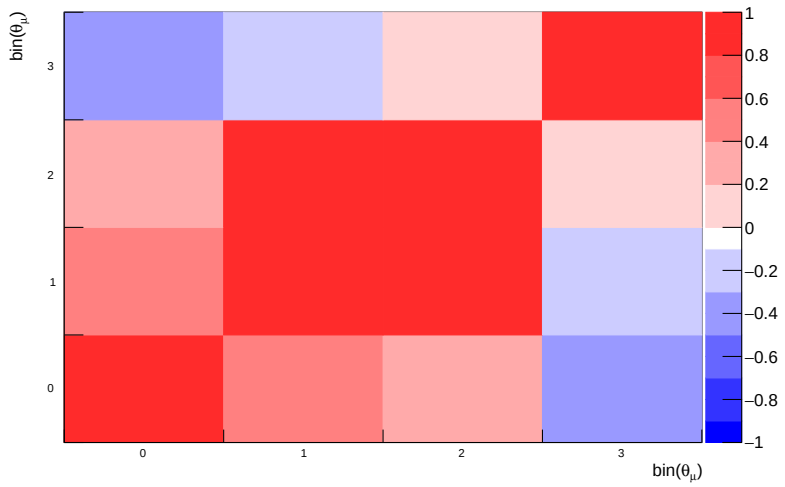

(a) σ_{H_2O}

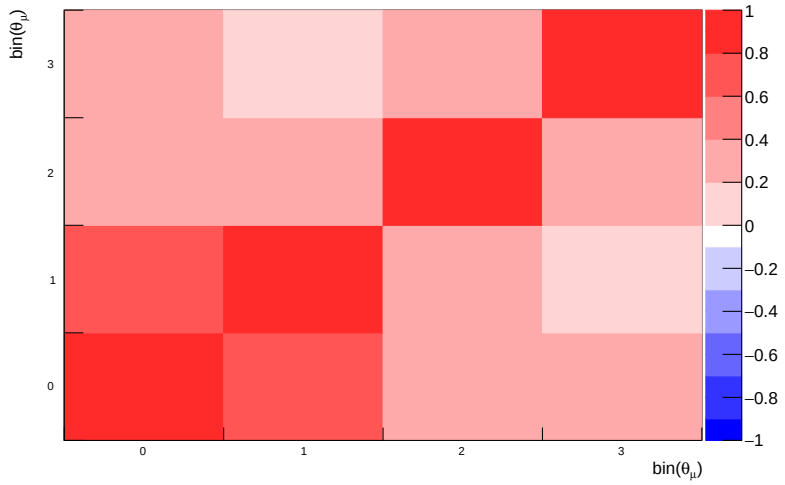

(b) σ_{CH}

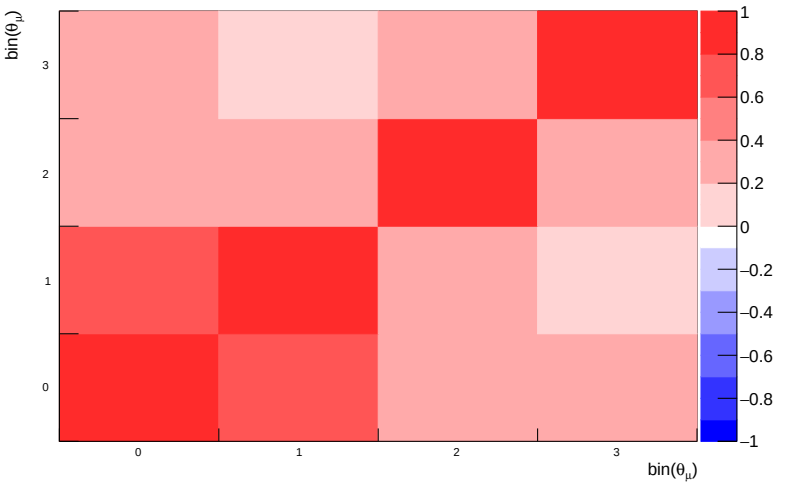

(c) $\sigma_{H_2O}/\sigma_{CH}$

Figure 5.22 – Correlation matrix of the errors on the cross-section from the uncertainty on the cross-section model. Binning in angle. for H_2O (Top) ; for CH (Middle) ; ratio of the cross-section (Bottom)

5.2.3 Detector response

The list of the systematic errors we considered is shown in Table 5.6. The total uncertainty covariance matrix is obtained as the quadratic sum of all the covariance matrices. We assumed that they are not correlated.
The errors labeled from 1 to 6 are tuning errors where we verify how well our MC simulation simulates our detector performance.
The errors labeled from 7 to 15 estimate the errors from the reconstruction algorithm between the data and the MC inputs.

Index	Parameter
1	Number of nucleons in the target
2	Dark noise
3	Hit efficiency
4	Light yield
5	Birks constant
6	Beam background
7	Number of actives planes required
8	Number of VETO planes
10	Fiducial volume
11	Vertexing plane tolerance
12	Vertexing transverse tolerance
13	3D track matching plane tolerance
14	WM/ING, PM/WM and PM/ING track matching angle
15	WM/ING, PM/WM and PM/ING track matching transverse

Table 5.6 – List of detector systematic errors

Number of nucleons

The number of nucleons in the two targets, H_2O and CH has been estimated earlier in the cross-section extraction study. However, the different parameters we used (mass of the scintillators, volume of the scintillators, density of the water, stability, presence of bubbles in the water) are known with an uncertainty. We proceed exactly. The reader interested in these uncertainties can look up [55]. We inject these uncertainties in the formulas for the number of nucleons (Equations 4.13, 4.17, 4.20) and see how the errors propagate. The results are summarized in Table 5.7

MPPC Dark noise

We take different values for the hit frequency in the water module and in the proton module and we have it vary to see how it impacts the reconstruction, the sample selection and the unfolded cross-section. The noise of the WM being so small, we only take one variation to 1 hit/cyc. For the PM noise, however, we take more variations since the nominal noise is that much higher. The values taken are summarized in Table 5.8. The effect of these variations is summarized in Table 5.10.

Hit efficiency

For a sample of 2D tracks we look at {the number of scintillators actually hit} divided by {the number of scintillators that should be hit by the track according to the fitted parameters

Source	Uncertainty	Effect on T^{CH}	Effect on T^{H_2O}
Scintillator mass measurement	0.2 %	0.2 %	0.04 %
Scintillator volume measurement	1%	0	0.20 %
Water density measurement	0.2 %	0	0.2 %
Water density stability	0.12 %	0	0.12 %
Scintillator position	1.5 mm	0	0.74 %
Air bubble	59.6 cm^3	0	0.05 %
Fraction of reflective coating area	10 %	0.24 %	0
Mass element of optical cement	50 %	0.74 %	0
Mass element of black paint	50 %	0.59 %	0
Mass element of hand painted reflector	50 %	0.45 %	0
Total		1.09 %	0.80 %

Table 5.7 – Error on the target mass. In the second column are the uncertainties on the parameters used to compute the number of target nucleons while in the third and fourth column are the results on said number of target nucleons.

module	recorded value (# hits/cyc)	variations
B2 Water module	0.025	1
B2 Proton module	12.48	5 , 10 , 15 , 20
B2 INGRID module	5.05	–

Table 5.8 – Dark noise variations. We do not vary the noise of INGRID. We only do it for the target modules: WM and PM

of said track}. We define this number for both the MC sand muons and the data set sand muons. We then reconstruct once more the MC masking the hits of reconstructed tracks with a probability determined by the ratio of these frequencies.
The hit efficiency values are determined for each type of scintillator:

- plane scintillators and grid scintillators for the Water Module (5.23)
- INGRID-type scintillators and Scibar type scintillators for the Proton Module

The efficiency is very different between MC and data because the grid scintillators are bent by their weight and the curvature creates a large position difference.

We only use the sand muons (data and MC simulation) for this systematics in order to minimize the bias. The effect of these variations is summarized in Table 5.10.

Light yield variation

The MC has been tuned to simulate the detector response as faithfully as possible but there will inevitably be some discrepancy between the responses.
So we vary the light yield of all the hits involved in the reconstruction process of the MC towards those of the data set, according to the angle of the tracks they belong to. in order to see how the difference in light yield affect the analysis.

We only use the sand muons (data and MC simulation) for this systematics in order to minimize the bias. While the tuning for the WM is very good we notice that the tuning for the PM scintillators is off by around 10 %. However, this is what this systematic error is accounting for.

The effect of these variations is summarized in Table 5.10.

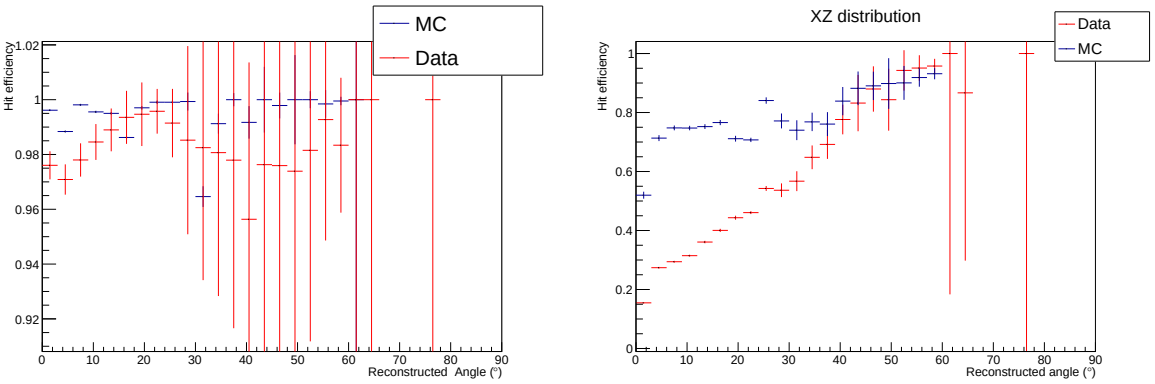

(a) Plane scintillators

(b) Grid scintillators

Figure 5.23 – Hit efficiency for the two types of layer in the WM structure: planes and grid.

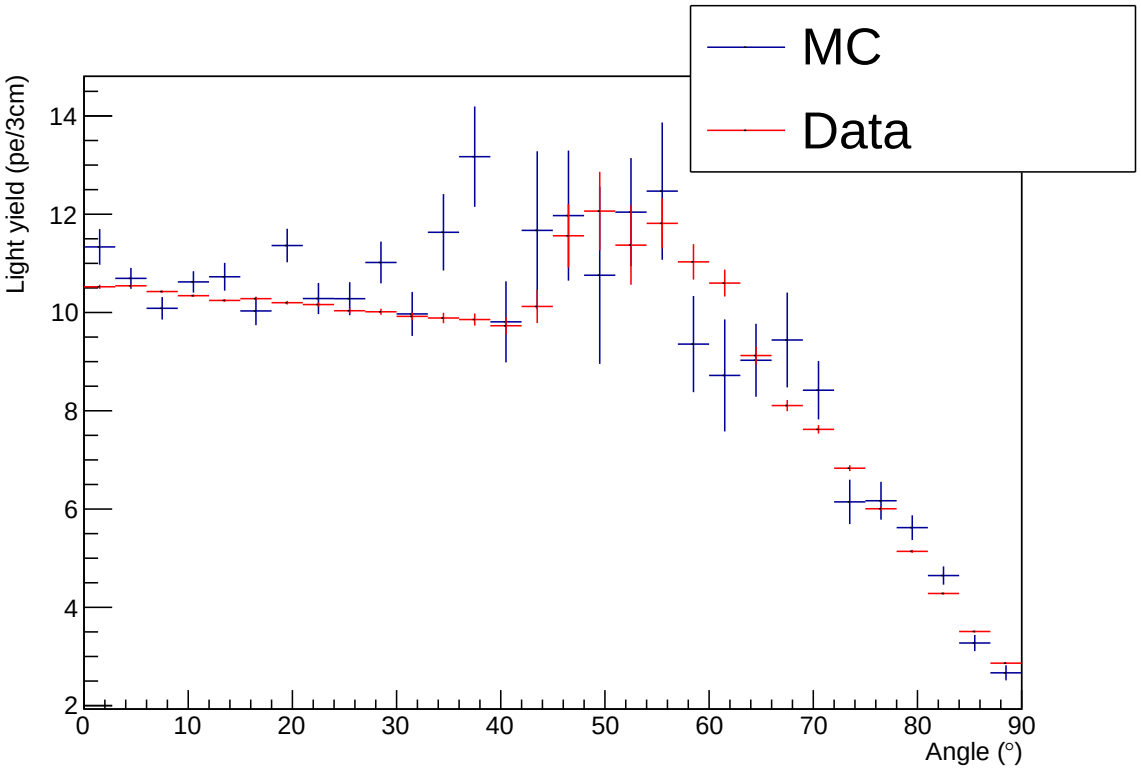

Figure 5.24 – Light yield for the WM. The two types of scintillators (planes and grid) are included in this plot.

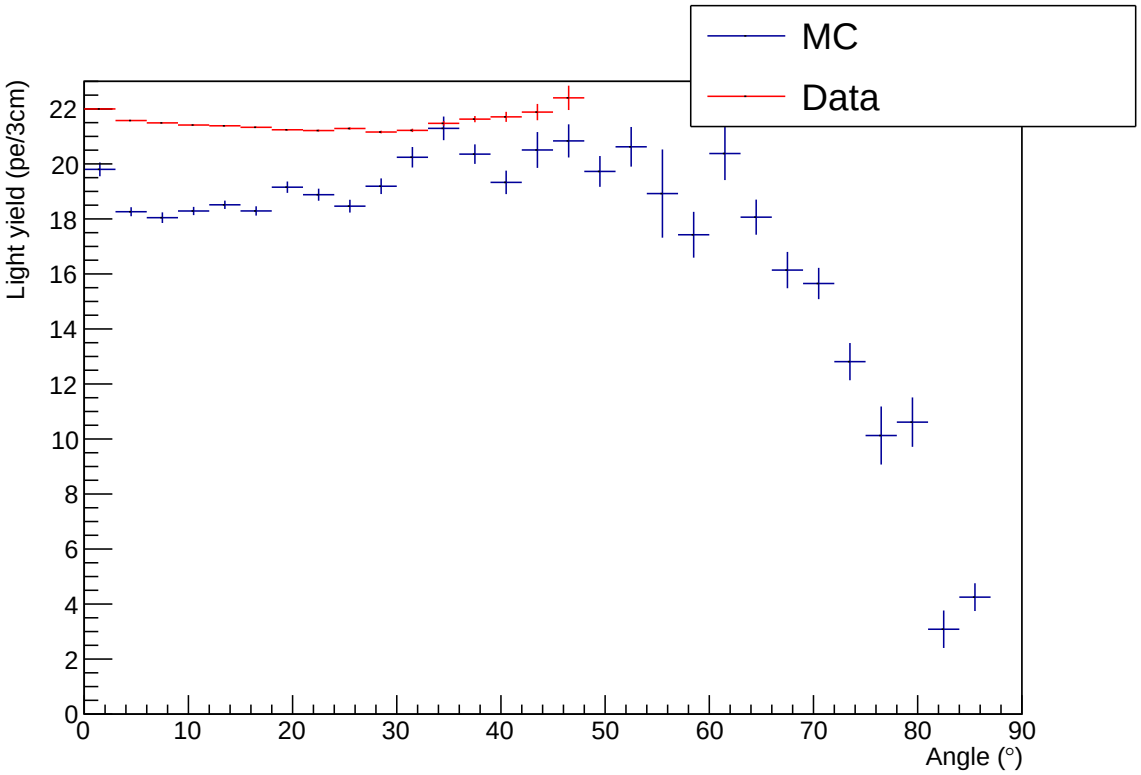

(a) INGRID type

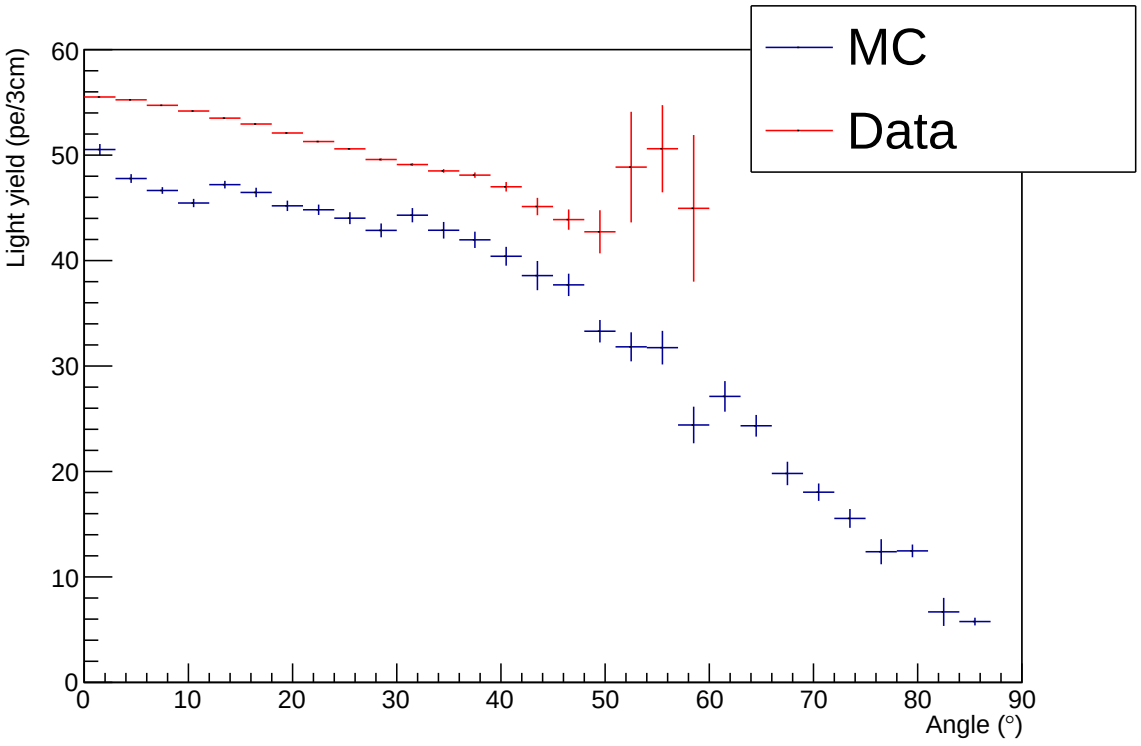

(b) Scibar type

Figure 5.25 – Light yield for the two scintillator types of the PM.

Birks' Constant

When too much energy is deposited in the scintillators by a crossing particle, a saturating effect appears. The Birks' law predicts the number of photoelectrons created by the particle:

$$pe = \frac{pe}{1 + b\frac{dE}{dz}} \tag{5.2}$$

where pe is the number of photoelectrons and b is the Birks' constant which regulates the quenching effect we discussed earlier.

The value of the Birks' constant in the polystyrene of the scintillators is $b = 0.0208\,\text{cm/MeV} \pm 0.0023\,\text{cm/MeV}$ as measured in [56]
We take the value at $-\sigma$ and at $+1\sigma$ (Table 5.9) and perform the selection and unfolding on the modified MC .

Standard deviation	Birks' constant value
-σ	0.0185 cm/MeV
nominal	0.0208 cm/MeV
+σ	0.0231 cm/MeV

Table 5.9 – Birks' constant variation

Modifying the Birks' constant creates a different number of produced photoelectrons. That impacts the PID and thus the selection of our events.

However, it needs to be said that the Birks' constant modification is applied during the analysis, right before applying the PID. The optimal method would be to apply this correction during the simulation. However, because the we have to randomly decide on the Z component of the vertices during the simulation, proceeding in this manner would add and additional statistical uncertainty to this systematic study.

Because of this, we are forced to apply our correction later on, and that suppress certain effects, the tracking for instance where the number of photoelectrons plays a role. The effect of these variations is summarized in Table 5.10.

Normalization of beam background

We change the weights of the background events, the sand muons that arrive in the detector. The data shows that the number of sand muons received is different from what we would expect from the MC, by about 0.2 % (30%) for the WM (PM). Indeed, the MC predicts 5867 (291023) reconstructed tracks for the WM (PM) while the number of events detected in the data is 5888 (211318) for the WM (PM).
Taking the value of the unfolded cross-section when reweighting our sand muons $\sigma_{modified}$, we take $|\sigma_{modified} - \sigma|$ as our error.

Summary of the MC tuning detector errors

All of the MC tuning related errors can be found in Table 5.10. for the cross-sections and the cross-section ratio.

Parameter	σ_{H_2O}	σ_{CH}	$\sigma_{H_2O}/\sigma_{CH}$
Number of nucleons	0.8 %	1.09 %	1.35 %
Dark noise	1.18 %	0.56 %	1.14 %
Hit efficiency	<0.001 %	< 0.001%	<0.001%
PE calibration	<0.001 %	<0.001 %	<0.001%
Birks constant	0.27 %	0.06 %	0.20 %
Beam background	0.20 %	<0.001 %	0.16 %
Total	1.46 %	1.23 %	1.78 %

Table 5.10 – List of tuning systematic errors

Detector systematic errors: reconstruction

When given a collection of hit, we run a 2D track reconstruction algorithm in each module for each view (ZX plane and ZY plane), then we try to match the tracks of the three modules together. Then we make a 3D matching between the 2D tracks. Finally we try to gather the tracks with a common vertex. The complete process is described in Chapter 3. All these matching are made based on comparisons with parameters. We vary these different parameters in errors #7 to error #15.
For each variation of the parameter, we compute a cross-section for the MC simulation σ_{MC} with the new reconstruction and a cross-section for the data σ_{Data} with the new reconstruction. We look at the distribution of $(\sigma_{MC} - \sigma_{Data})/\sigma_{MC}$ on the variations of the parameter, and we take the standard deviation as the relative error on the cross-section σ associated to this parameter. The variations on each parameter are shown in Table 5.11 and the values of the errors are shown in Table 5.12.

Unlike the previous systematic errors which used sand muons, we need here to use the selected sample.

	Parameter	Nominal			Variations		
7	Number of active planes in INGRID	3			2, 4, 5		
8	Number of VETO planes in PM | WM	3	7		2, 4	5, 9	
10	Fiducial Volume cut (cm) PM | WM	20	10		18, 19, 21	8, 9, 11	
11	Vert. plane PM | WM	3	12		2, 4	8, 16	
12	vert. transverse PM | WM (cm)	15	15		12.5, 17.5	12.5, 17.5	
13	3D matching plane PM| WM	3	12		2, 4	8, 16	
14	Angular module matching (°) WM/INGRID | PM/WM | PM/INGRID	35	35	35	30, 45	30, 45	30, 45
15	Tansverse module matching (cm) WM/INGRID | PM/WM | PM/INGRID	15	15	15	14, 16	14, 16	14, 16

Table 5.11 – Variation of the reconstruction parameters. The parameters #8, #11 and #13 are expressed in number of planes of the same view (XZ or YZ) for the PM. For the WM they are expressed in number of planes of all types: XZ, YZ and grid.

Summary of the detector systematic errors

The MC tuning and the track reconstruction uncertainty are all regrouped as detector systematic errors. The correlation matrices are displayed on Figure 5.26 for the double differential analysis, on Figure 5.27 for the momentum analysis and on Figure 5.27 for the angle analysis.

Parameter	σ_{H_2O}	σ_{CH}	$\sigma_{H_2O}/\sigma_{CH}$
Act. planes	± 2.41 %	± 0.62 %	± 3.32 %
VETO planes	± 2.20 %	± 1.80 %	± 3.0 %
FV	± 0.69 %	± 1.54 %	± 1.15 %
Vert. plane	± 0.83 %	± 0.57 %	± 1.12 %
Vert. transverse	± 0.25 %	± 0.25 %	± 0.25 %
3D matching plane	± 1.64 %	± 0.69 %	± 2.21 %
mod angle matching	± 0.40 %	± 0.4 %	± 0.59 %
mod matching transverse	± 0.43 %	± 0.31 %	± 0.61 %
Total	± 3.95 %	± 2.65 %	± 5.46 %

Table 5.12 – List of reconstruction systematic errors. The relative errors on the cross-sections are estimated by taking the standard deviation of the distribution of $(\sigma_{Data} - \sigma_{MC})/\sigma_{MC}$. σ_{H_2O} and $\sigma_{H_2O}/\sigma_{CH}$ have higher errors than σ_{CH} because the formers are combinations of two module cross-sections (σ_{WM} and σ_{PM}) while the latter only depends on one module cross-section (σ_{PM}).

The detector uncertainties are displayed on Figure 5.4 for the double differential analysis, on Figure 5.5 for the momentum analysis, on Figure 5.6 for the angle analysis.

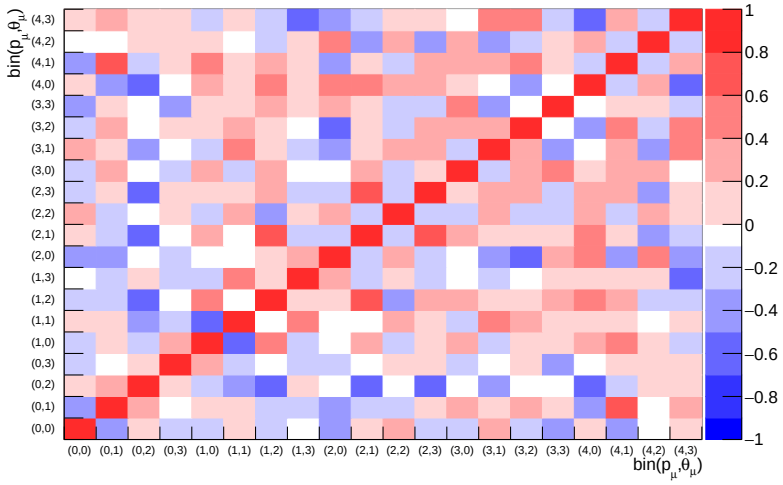

(a) σ_{H_2O}

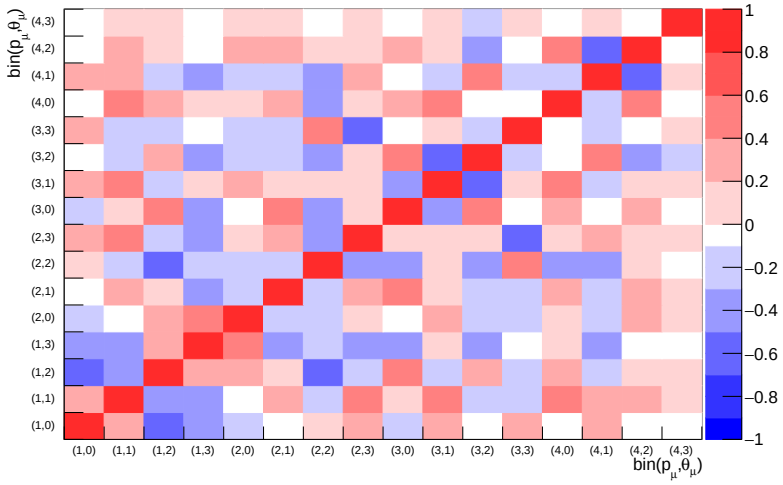

(b) σ_{CH}

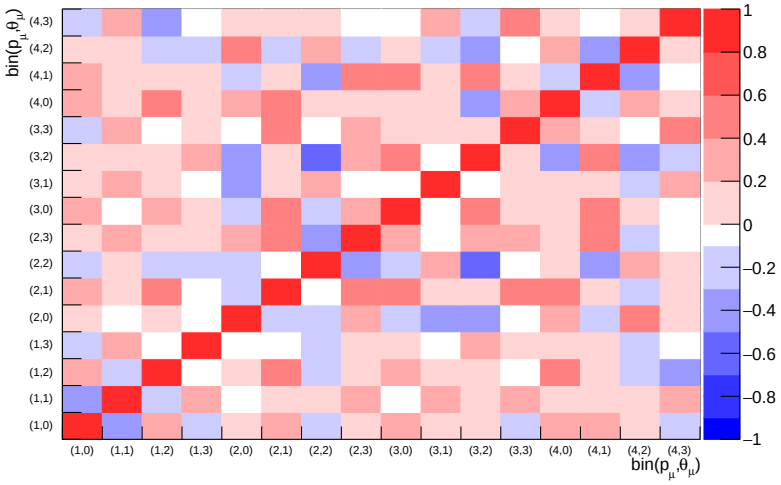

(c) $\sigma_{H_2O}/\sigma_{CH}$

Figure 5.26 – Correlation matrix for the errors on the cross-section related to the detector response. Binning in momentum and angle

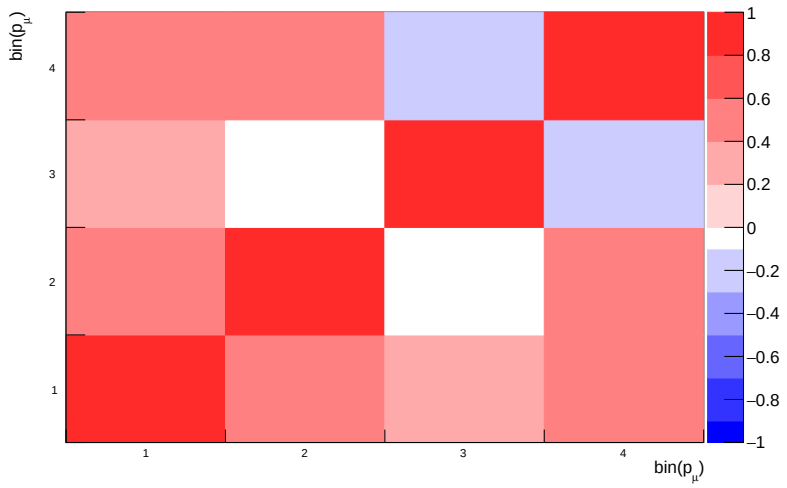

(a) σ_{H_2O}

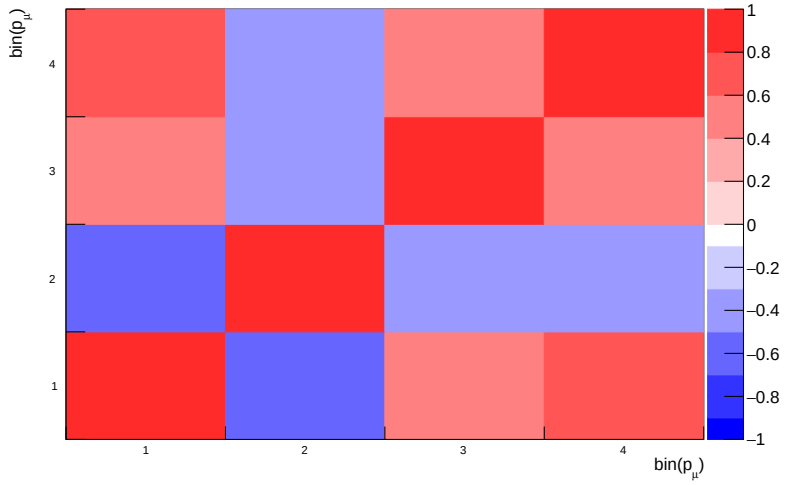

(b) σ_{CH}

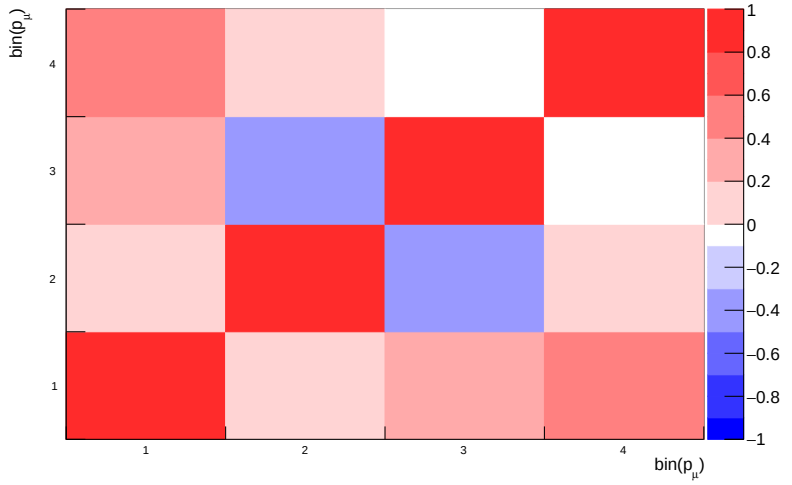

(c) $\sigma_{H_2O}/\sigma_{CH}$

Figure 5.27 – Correlation matrix for the errors on the cross-section related to the detector response. Binning in momentum

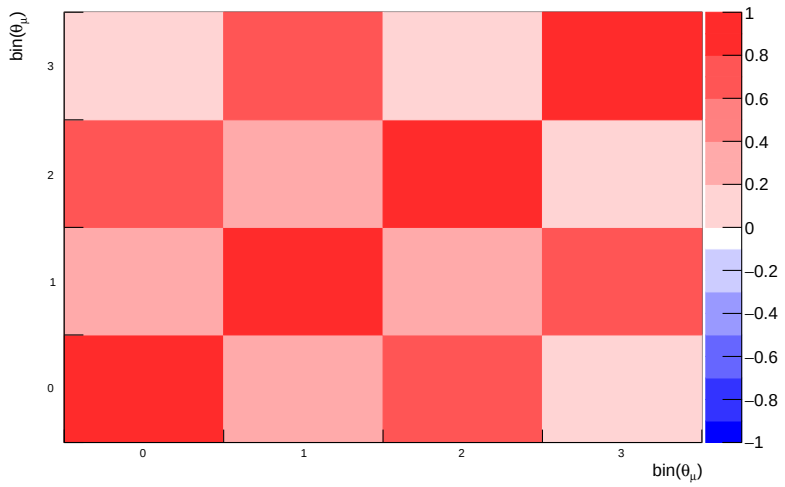

(a) σ_{H_2O}

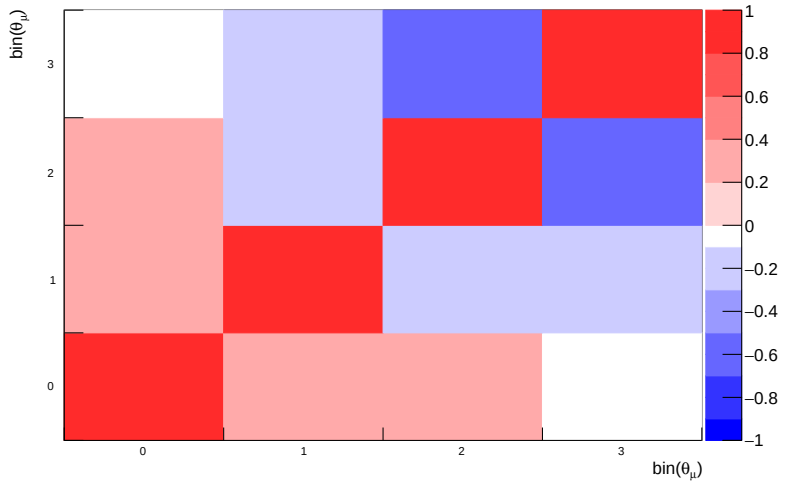

(b) σ_{CH}

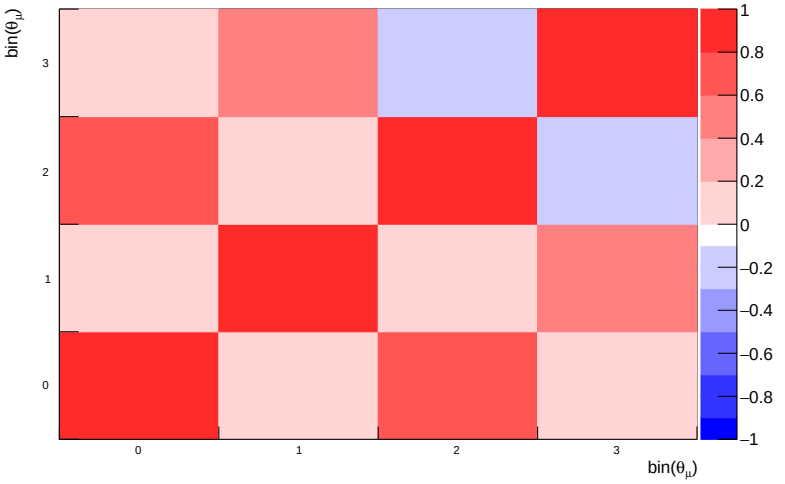

(c) $\sigma_{H_2O}/\sigma_{CH}$

Figure 5.28 – Correlation matrix for the errors on the cross-section related to the detector response. Binning in angle. The binning is shown in Table 5.1

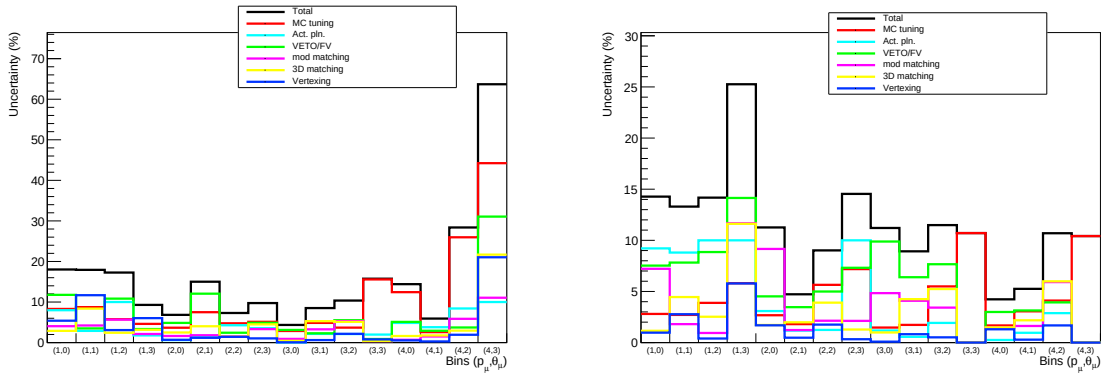

(a) for H_2O (b) for CH

Figure 5.29 – Detector error on the cross-section for the binning in momentum and angle. The binning is shown in Table 5.1

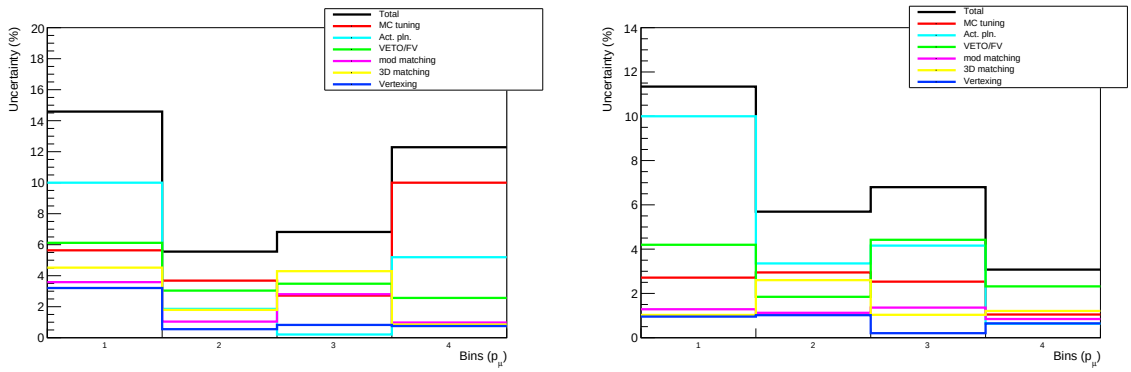

(a) for H_2O (b) for CH

Figure 5.30 – Detector error on the cross-section for the binning in momentum. The binning is shown in Table 5.1

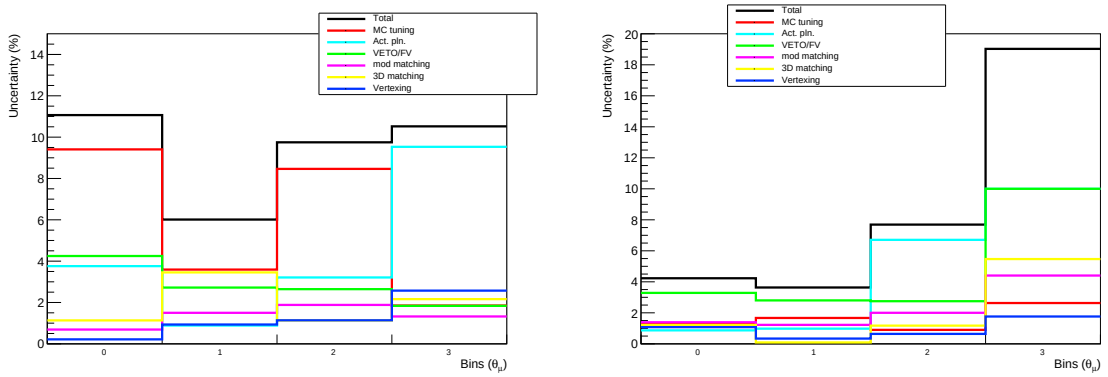

(a) for H_2O (b) for CH

Figure 5.31 – Detector error on the cross-section for the binning in angle. The binning is shown in Table 5.1

5.2.4 Summary of the systematic errors (Flux+cross-section+detector)

We computed all the systematic errors listed earlier (flux, cross-section model, detector response) and will now use these relative systematic errors for our analysis on data sets: fake data sets in Chapter 6 and the real data set in Chapter 7. As for the statistical analysis, we computed the uncertainty matrix associated to our nominal MC simulation in htis chapter. However, for each (fake) data set, we need to compute a statistical matrix associated to this particular set. Indeed, the statistical matrix represent the uncertainty on the number of detected events and thus need to be computed with the particular statistics of the set.

The summary of the systematic errors can be found in Table 5.13

Source	Relative error		
	σ_{H_2O}	σ_{CH}	$\sigma_{H_2O}/\sigma_{CH}$
Flux uncertainty	± 11.6 %	± 11.23 %	± 0.40 %
Cross-section model	± 5.78 %	± 5.29 %	± 4.17 %
Detector response	± 4.22 %	± 2.93 %	± 5.74 %
Total	± 13.62 %	± 12.75 %	± 7.10 %

Table 5.13 – Values of the systematic errors of our measurements. The low flux systematic error of the measurement on $\sigma_{H_2O}/\sigma_{CH}$ allows a total systematic error lower than on the measurement of the cross-section, as expected. The error on our measurement will be dominated by the statistical uncertainties.

We can see correlation patterns appear when looking more closely at some of the error matrices presented in this chapter. We would need more work in order to find an explanation to this patterns.

Chapter 6

Fake data studies

The choice of the number of iterations of our unfolding is non-trivial. However, the errors computed in Chapter 5 depend on the step of the unfolding. Indeed, the error is the standard deviation of the distribution of the unfolded cross-section at the n-th in regard of the variation of the parameter we consider. While the systematic errors converge, the statistical error actually increase with the number of steps. This is shown by Figure 6.1.

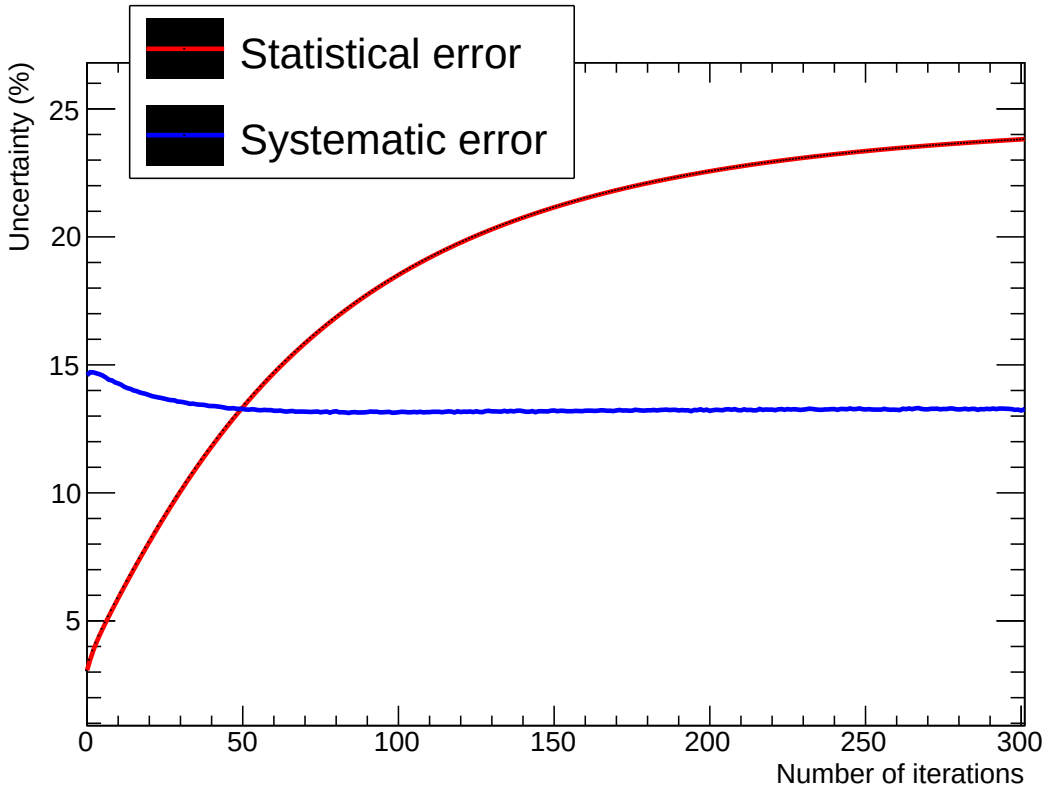

Figure 6.1 – The evolution of the systematic and statistical errors on the total water cross-section σ_{H_20} with the unfolding step. The systematic error converges while the statistical error increases. The systematic error regroups the errors from the cross-section model, flux and detector response uncertainties.

This compels us to make a choice that allow a good balance between the convergence of our procedure and reasonable uncertainties. It is not possible to make this choice based on the data since we don't have access to the true cross-section. Similarly, we cannot base our

criterion on the MC only because the criterion could be too biased.

In order to choose our criterion we will use three sets of fake data. Three simulations different from our nominal MC simulation that will allow us to observe the behaviour of the unfolding and the convergence speed towards the true value of the cross-section.

- fake data set # 1: NEUT 5.3.3 cross-section interactions with a GENIE 2.12.8 [57] reweight. We use the cross-section predicted by the GENIE neutrino interaction generator instead of the one predicted by NEUT.
- fake data set # 2: NEUT 5.3.3 without 2p2h interactions and with M_A^{QE} reweighted at $+3\sigma$. 2p-2h are an important part of the CC0π while M_A^{QE} is on of the parameters describing the CCQE which are a major part of CC0π. $+3\sigma$ represents an increase of almost 50 %.
- fake data set # 3: NEUT 5.3.3 with an arbitrary reweight on the $\overline{\nu}_\mu$ flux.

.

6.1 Fake data sets

For the first and second sets, we change the neutrino interaction model of the simulations in regard to the nominal MC simulation.
The third set has a different muon antineutrino flux, renormalized by a reweighting function visualized in Figure 6.2.

The CC interactions in the WM and in the PM for the three interactions are compared in:

- Figure 6.3 for the distribution in muon momentum. The distribution fluctuations are at around 20 %, except for the set # 1 at low momentum where we fluctuate at up to 100 %.
- Figure 6.4 for the distribution in muon angle. About 10 % of fluctuations within the statistically significant region.

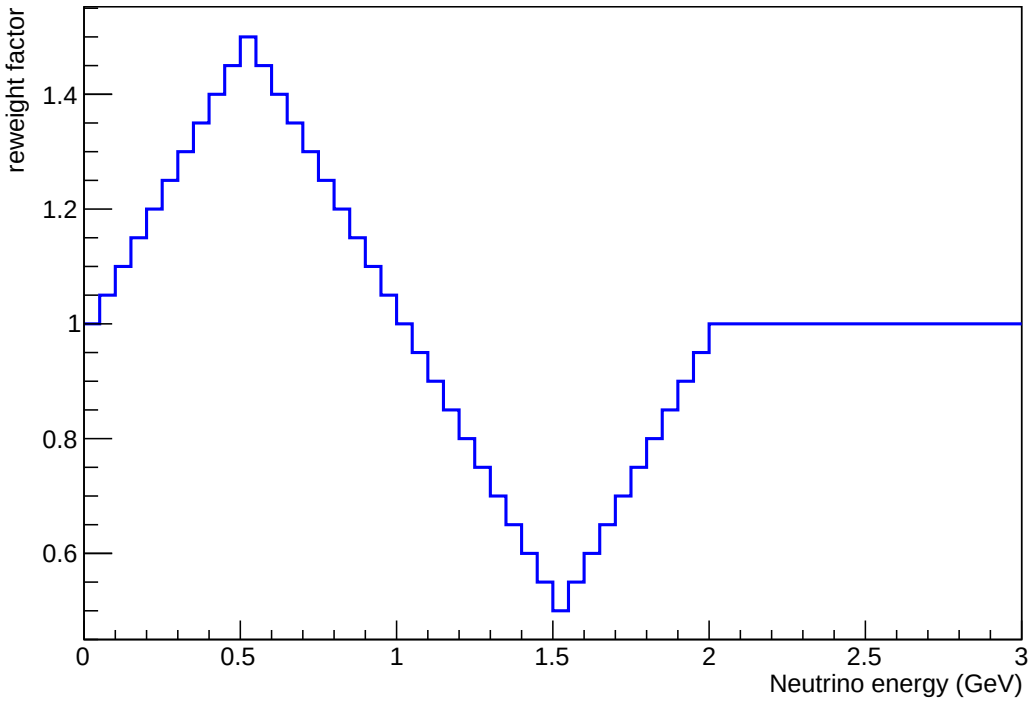

Figure 6.2 – Reweighting zigzag function for the fake data set # 2

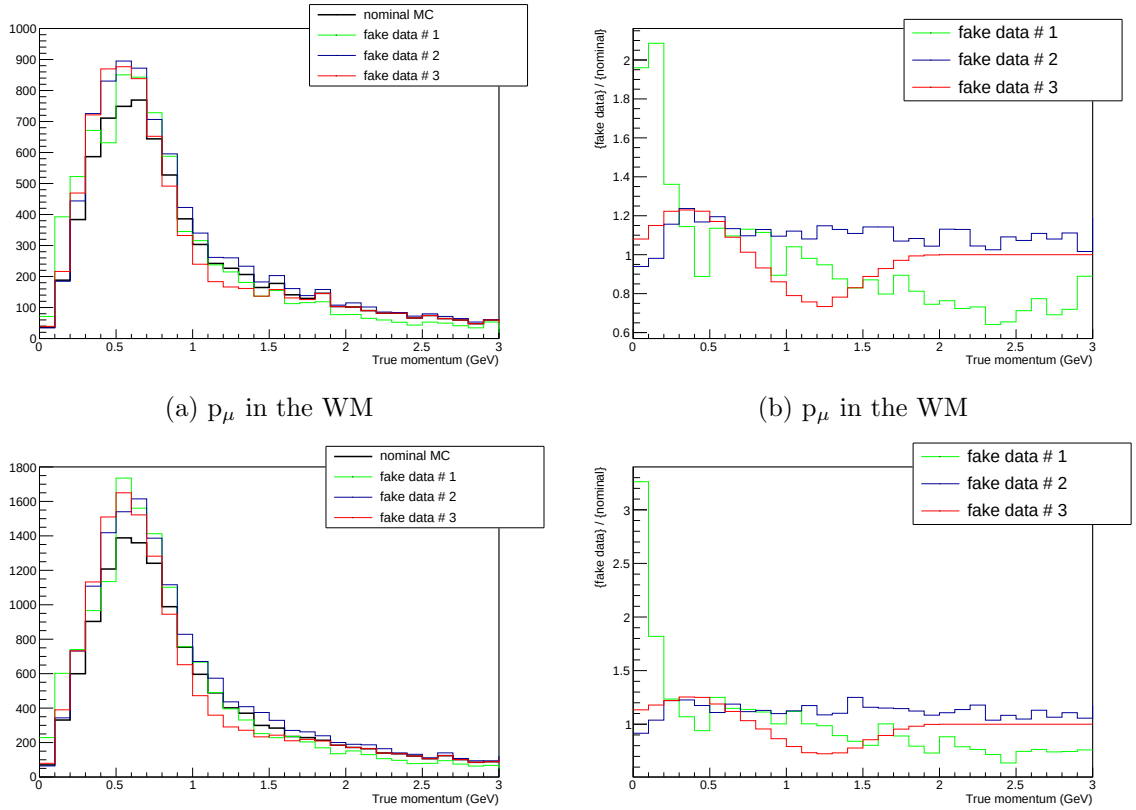

(a) p_μ in the WM

(b) p_μ in the WM

(c) p_μ in the PM

(d) p_μ in the PM

Figure 6.3 – Momentum distribution of the CC interactions: in the WM fiducial volume (Top) and in the PM fiducial volume (Bottom). The right panels show the ratio of the fake data simulation and of the nominal simulation.

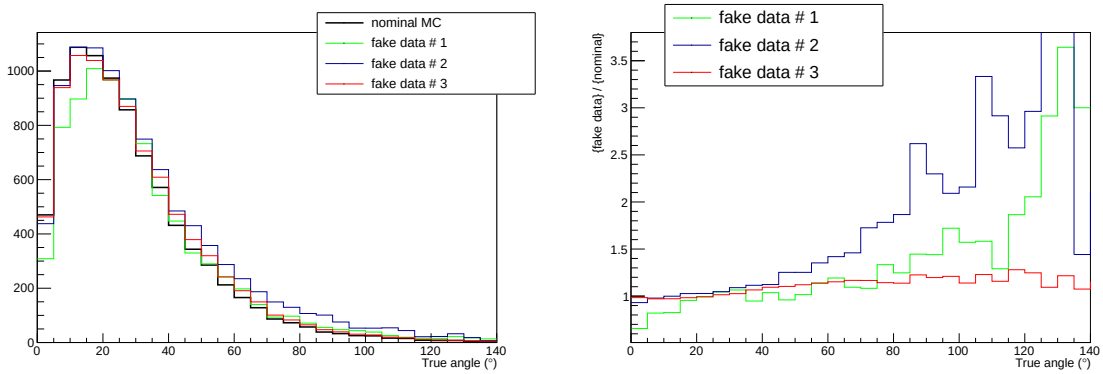

(a) θ_μ in the WM

(b) θ_μ in the WM

(c) θ_μ in the PM

(d) θ_μ in the PM

Figure 6.4 – Angular distribution of the CC interactions: in the WM fiducial volume (Top) and in the PM fiducial volume (Bottom). The right panels show the ratio of the fake data simulation and of the nominal simulation.

6.2 Convergence on fake data sets

For each of the three sets, we define the following quantities.

- $\mathbf{Cov}_{Det}(n)$ the detector uncertainties matrix at the n-th step
- $\mathbf{Cov}_{Xsec}(n)$ the cross-section model uncertainties matrix at the n-th step
- $\mathbf{Cov}_{Flux}(n)$ the flux uncertainties matrix at the n-th step
- $\mathbf{Cov}_{Stat}(n)$ the statistical uncertainties matrix at the n-th step for the set (there is one such matrix for each set)
- $\mathbf{Cov}(n) = \mathbf{Cov}_{Det}(n) + \mathbf{Cov}_{Xsec}(n) + \mathbf{Cov}_{Flux}(n) + \mathbf{Cov}^{k}_{Stat}(n)$ the total uncertainties matrix at the n-th step for the set. The detector, cross-section model and flux relative uncertainties matrices are common to all data/fake data sets and have been evaluated in Chapter 5). The statistical uncertainty matrix, however, is unique to each fake-data set.
- s^n the unfolded signal of the fake data at the n-th step
- $\overline{s}$ the true signal of the fake data simulation
- s^∞ the unfolded signal of the fake data simulation after a high number of iterations

.

The number of degrees of freedom of this system is equal to the number of bins in the true phase space. Here our unfolding has $d_m = 5$ true momentum bins and $d_a = 4$ true angle bins in the true CC0π phase space. Therefore, the number of degrees of freedom is $d = d_m \times d_a = 20$ and we then define the covariance χ^2 per degree of freedom as follow:

$$\chi^2_{Cov}(n)/d = \frac{1}{d} \sum_{0\leq i,k<d_m, 0\leq j,l<d_a} (s^n_{i,j} - \overline{s}_{i,j}) \times \left(\mathbf{Cov}^{-1}(n)\right)^{k,l}_{i,j} \times (s^n_{k,l} - \overline{s}_{k,l}) \tag{6.1}$$

The covariance matrices have all been estimated in Chapter 5.

This χ^2 estimates the distance of the unfolded cross-section from the true cross-section of the fake-data model relatively to the error on each bin $\sigma_{i,j} = \sqrt{\mathbf{Cov}(n)^{i,j}_{i,j}}$ as well as the bin to bin errors given by the non diagonal coefficient of the matrix.

If we can find a criterion guaranteeing the convergence of all three sets, we can then apply the same criterion to the data unfolding later on.

We proceed as in [58] where define a data-oriented χ^2:

$$\chi^2_{data}(n)/d = \frac{1}{d} \sum_{0\leq i,k<d_m, 0\leq j,l<d_a} (s^n_{i,j} - s^\infty_{i,j}) \times (\mathbf{Cov}^{-1}(n))^{k,l}_{i,j} \times (s^n_{k,l} - s^\infty_{k,l}) \tag{6.2}$$

The reason for this definition is that when unfolding real data we cannot access the true distribution. We then compare the current unfolded signal to the limit we tend to after a high number of iterations. We will choose here 1000 iterations as the limit signal s^∞.

We also define

$$\chi^2_{model}(n)/d = \frac{1}{d} \sum_{0\leq i,k<d_m, 0\leq j,l<d_a} (s^{n,NEUT}_{i,j} - s^{n,GENIE}_{i,j}) \times (\mathbf{Cov}^{-1}(n))^{k,l}_{i,j} \times (s^{n,NEUT}_{k,l} - s^{n,GENIE}_{k,l}) \tag{6.3}$$

where $s^{n,NEUT}$ is the signal unfolded with a NEUT initial prior after n iterations and $s^{n,GENIE}$ the signal unfolded with a GENIE initial prior.
This χ^2 is meant to check that the choice of the initial prior has no bearing on the value of the limit unfolded signal s^{∞}.

For the first fake data set, Figure 6.5 shows χ^2_{Cov}/d and χ^2_{data}/d as functions of the number of iterations. We can see on the figure the convergence of the unfolding on the H_2O sample within the error given by the total covariance matrix (χ^2_{Cov}) after $\sim$ 40 iterations.
We also have the convergence of the χ^2_{data} towards 0.

Same study is shown in Figure 6.6 for the convergence of the unfolding of the CH sample, we converge towards a value within the total error after $\sim$ 40 iterations.

The same study has been done for the two other fake data simulation samples:

- Figure 6.7 (Figure 6.8) shows the results for the H_2O sample (CH sample) of the fake data simulation # 2.
- Figure 6.9 (Figure 6.10) shows the results for the H_2O sample (CH sample) of the fake data simulation # 3.

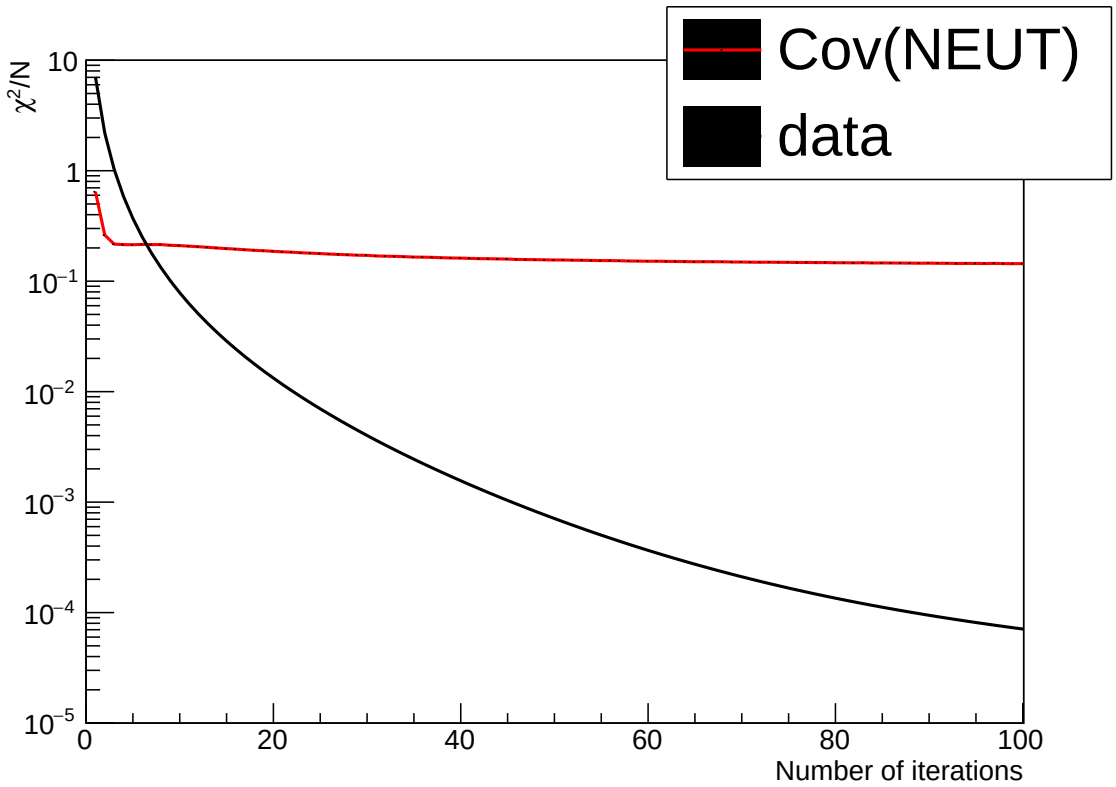

Figure 6.5 – Convergence of the unfolding of the H_2O selection for fake data#1

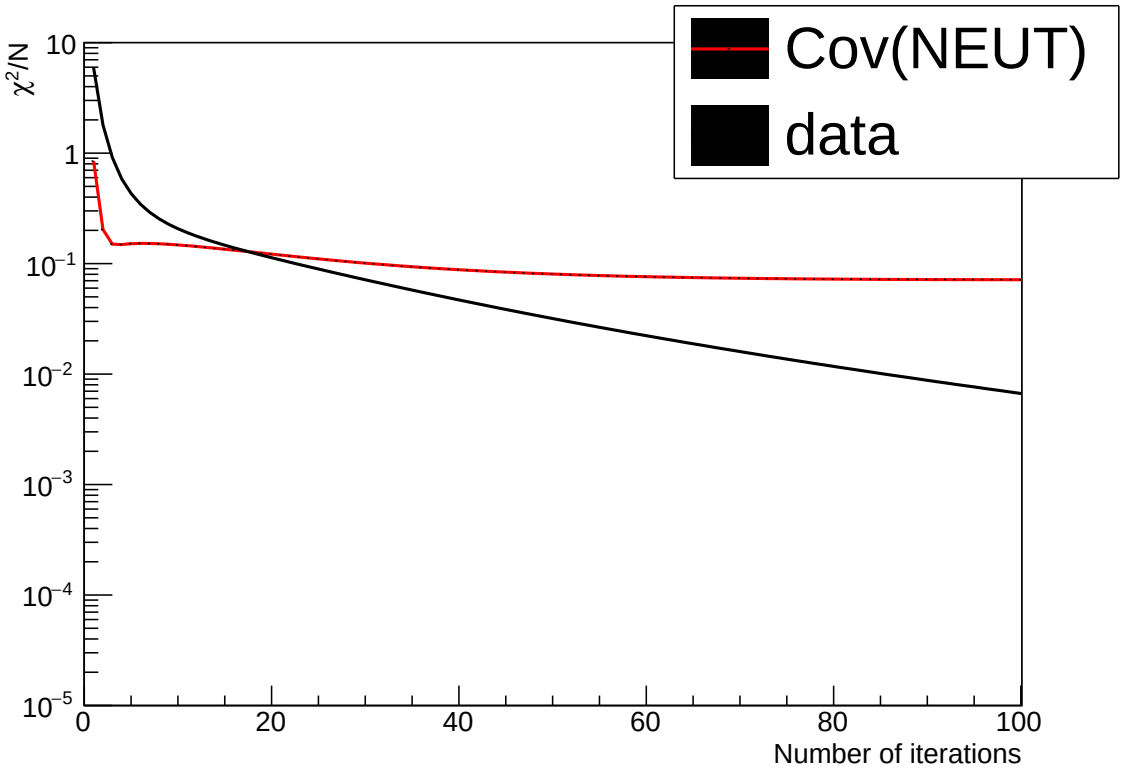

Figure 6.6 – Convergence of the unfolding of the CH selection for fake data#1

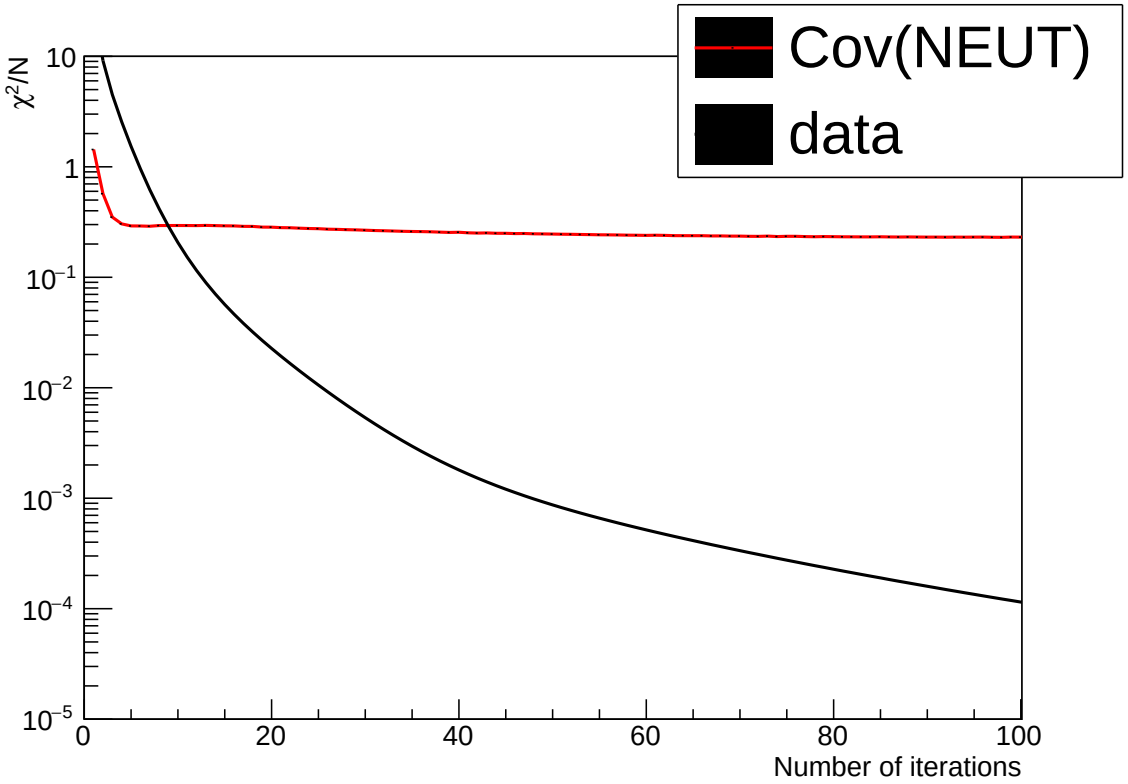

Figure 6.7 – Convergence of the unfolding of the H_2O selection for fake data#2

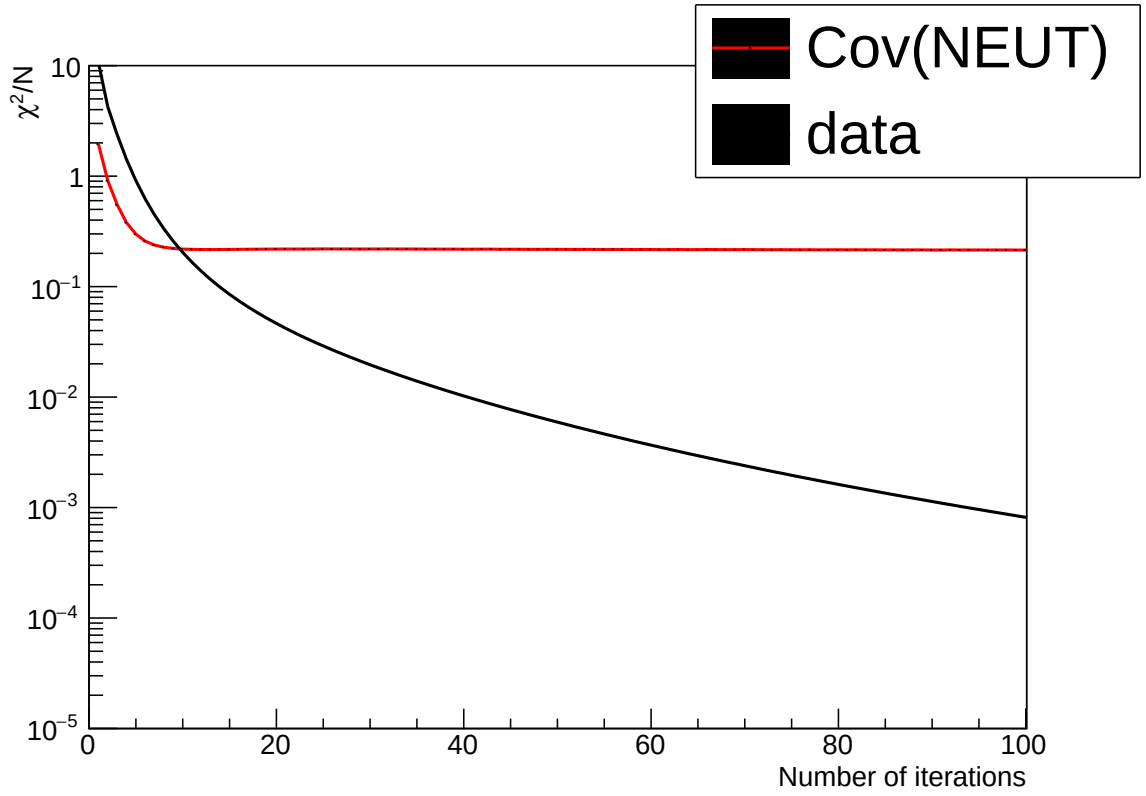

Figure 6.8 – Convergence of the unfolding of the CH selection for fake data#2

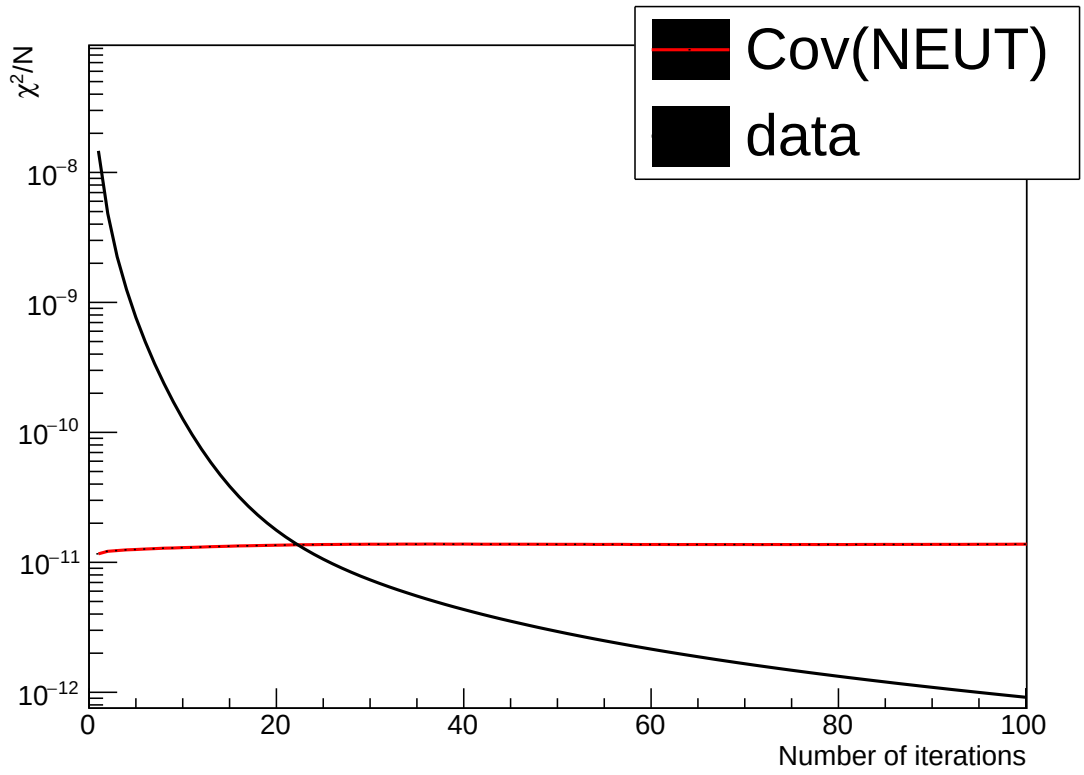

Figure 6.9 – Convergence of the unfolding of the H_2O selection for fake data#3

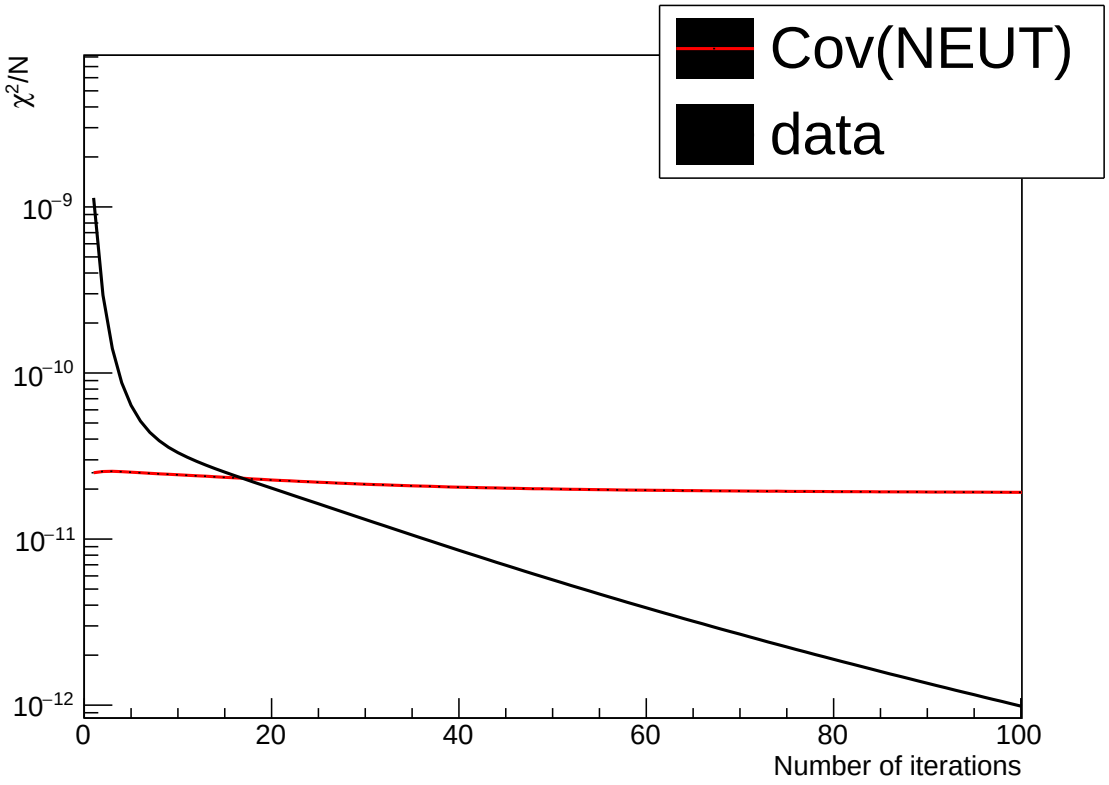

Figure 6.10 – Convergence of the unfolding of the CH selection for fake data#3

6.3 A criterion independent of the model

As said earlier, when we unfold the data, we won't be able to rely on χ^2_{Cov} because we do not have access to the true cross-section in the data analysis. We need to base our number of iterations on χ^2_{data}.

We first determine the limit of the various χ^2,

$$l_{Cov} = \lim_{n \mapsto \infty} \chi^2_{Cov}(n)/d \tag{6.4}$$

Similarly we define

$$l_{data} = \lim_{n \mapsto \infty} \chi^2_{data}(n)/d \tag{6.5}$$

In this study we take the "limit" values at $n = 1500$, step big enough to estimate an unregularized unfolded signal. So

$$\begin{aligned} l_{Cov} &= \chi^2_{Cov}(1500)/d \\ l_{data} &= \chi^2_{data}(1500)/d \end{aligned} \tag{6.6}$$

The criterion on the fake data simulation

Then we choose a number ϵ such that we stop the algorithm when

$$|\chi^2_{Cov}(n)/d - l_{Cov}| < \epsilon^2 \tag{6.7}$$

When we stop the algorithm at the step $\bar{n}$, we compute the χ^2 with an uncertainty matrix computed using the unfolded signal at the final step $s^{n,NEUT}$. We want the uncertainty matrix around the unfolded signal $s^{n,NEUT}$ to be close to the uncertainty matrix around the limit

signal $s^{\infty,NEUT}$.
The one dimension case can help formulate the criterion. we define $\Delta s^n = s^{n,NEUT} - s^{\infty,NEUT}$ and σ^{tot} the total uncertainty. The condition $|\chi^2_{Cov}(n)/d - l_{Cov}| < \epsilon^2$ becomes $\left|\frac{\Delta s^n}{\sigma^{tot}}\right| < \epsilon$

After stopping the algorithm the total uncertainty is increased by the bias from the early stopping

$$(\sigma^{tot})^2 \mapsto (\sigma^{tot})^2 + (\epsilon \times \sigma^{tot})^2 = (1+\epsilon^2) \times (\sigma^{tot})^2 \tag{6.8}$$

We want this variation of the uncertainty $(\sigma^{tot})^2$ to be smaller than 10%, that is to say we want $1 + \epsilon^2 < 1.1$

We then choose

$$\epsilon^2 = 0.1 \tag{6.9}$$

The criterion on the data

Then we need to choose a number η such that when $|\chi^2_{data}(n)/d - l_{data}| < \eta^2$ we also have $|\chi^2_{Cov}/d - l_{Cov}| < \epsilon^2$ for all three sets. Additionally we want the χ^2_{Cov} to vary like a typical χ^2 when varying the reconstructed signal sample bins along with the statistical uncertainties at the stopping step.

Since we have d degrees of freedom the χ^2 follows a probability density function

$$P_d(\chi^2) = \frac{1}{2^{\frac{d}{2}}\Gamma(\frac{d}{2})}(\chi^2)^{\frac{d}{2}-1}e^{-\frac{\chi^2}{2}} \tag{6.10}$$

with a maximum probability attained at $d-2$ (cf Figure 6.11)

By taking 1000 toy models where we statistically fluctuate the reconstructed sample bins and unfold the sample, we look at how it compares to the theoretical χ^2 law.

The Table 6.1 summarizes the values of $|\chi^2_{Cov}/d - l_{Cov}|$ and χ^2_{data}/d at the first step $\bar{n}$ when we have $|\chi^2_{Cov}/d - l_{Cov}| < 0.1$. We notice that the fake data set# 3 is right of the bat under the convergence criterion. This is due to the fact that it is the closest to the nominal simulation as shown by Figure 6.3 and Figure 6.4.

Fake Data set	$\bar{n}$	$\lvert\chi^2_{Cov}(\bar{n})/d - l_{Cov}\rvert$	$\chi^2_{data}(\bar{n})/d$
Set # 1 H_2O	4	0.08	0.56
Set # 2 H_2O	4	0.07	2.4
Set # 3 H_2O	1	$< 10^{-5}$	$< 10^{-5}$
Set # 1 CH	4	0.06	0.48
Set # 2 CH	5	0.07	0.77
Set # 3 CH	1	$< 10^{-5}$	$< 10^{-5}$

Table 6.1

Hence, we will not consider the set # 3 in the determination of the bias η.

We can now look at the χ^2_{Cov} distribution at the stopping steps for the fake data sets. As explained, we statistically vary the number of events in each reconstructed bin and look at the distribution we obtain.

However, we compute the χ^2 only with the statistical uncertainty as well as the systematic uncertainty associated to the creation of the fake data set. More explicitly, the uncertainties used to compute the χ^2 distributions for each of the sets are

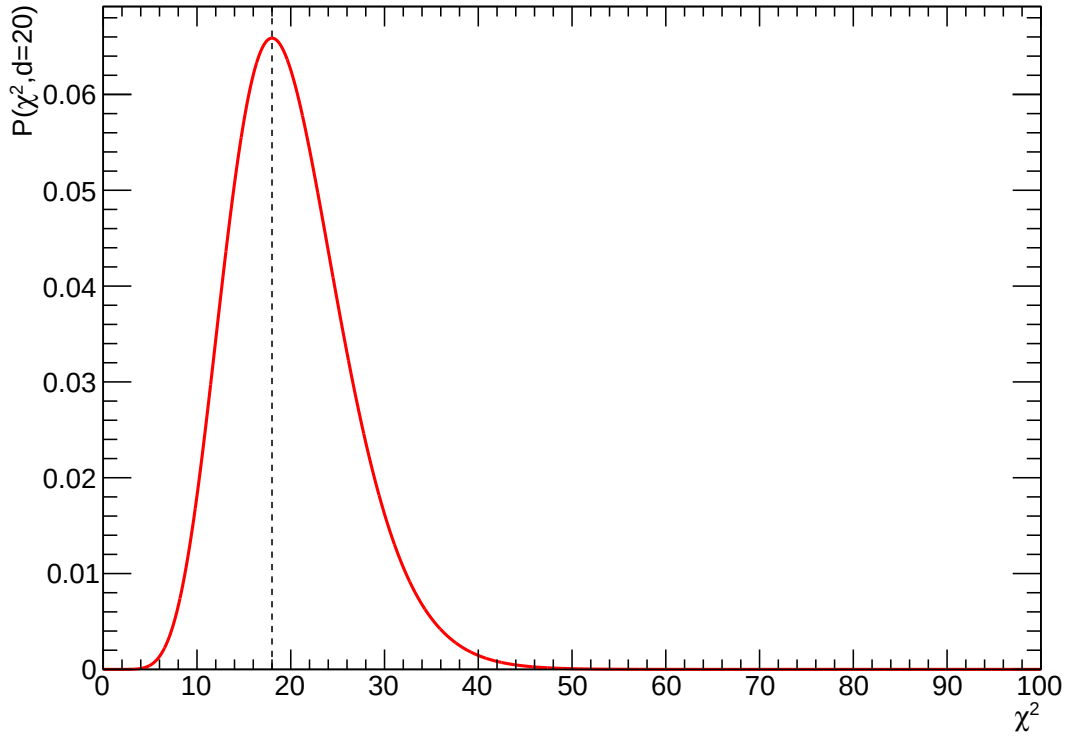

Figure 6.11 – χ^2 law probability density function for a number of degrees of freedom $d = 20$. The mean value coincides with peak value and is at $\overline{\chi^2} = d - 2 = 18$

- set # 1: $\mathbf{Cov}_{Stat} + \mathbf{Cov}_{Xsec}$: because this simulation was obtained by changing the cross-section model.
- set # 2: $\mathbf{Cov}_{Stat} + \mathbf{Cov}_{Xsec}$: because this simulation was obtained by changing the cross-section model.
- set # 3: $\mathbf{Cov}_{Stat} + \mathbf{Cov}_{Flux}$: because this simulation was obtained by changing the flux model.

We compare it to the theoretical behaviour. This is called a "coverage test". There is undercoverage (overcoverage) if the mean value is higher (lower) than the theoretical one. The results for the set # 1 is shown in Figure 6.12, the set # 2 in Figure 6.13 and the set # 3 in Figure 6.14.

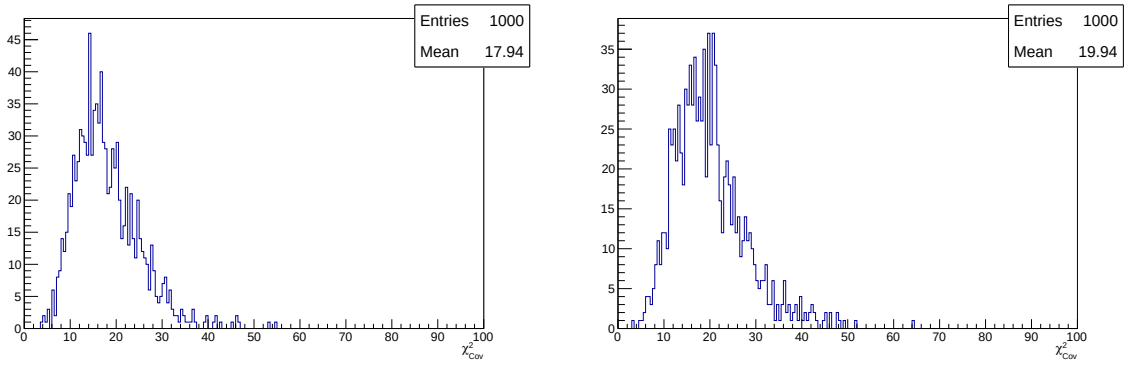

Figure 6.12 – Fake data set # 1: Coverage test for the WM (left) and PM (right). This set is well covered after the unfolding is stopped

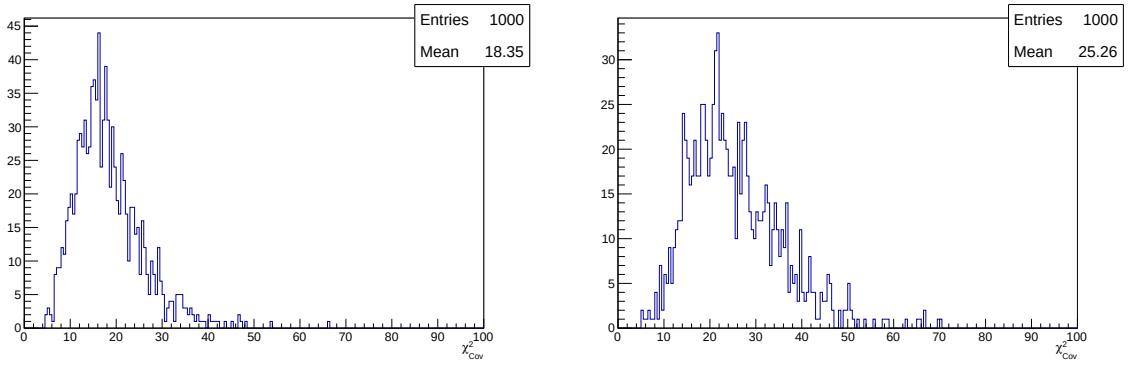

Figure 6.13 – Fake data set # 2: Coverage test for the WM (left) and PM (right). This set has the PM unfolding undercovered

Except for the CH unfolding of the fake data set # 2 which is undercovered after unfolding the other samples have behaviours close to what we would expect from a χ^2. This means that the fake data samples are regularized enough: they are close enough to the limit value.

We will stop the unfolding on the data at the first step N_s such that

$$\boxed{\chi^2_{data}(N_s) < 0.48} \tag{6.11}$$

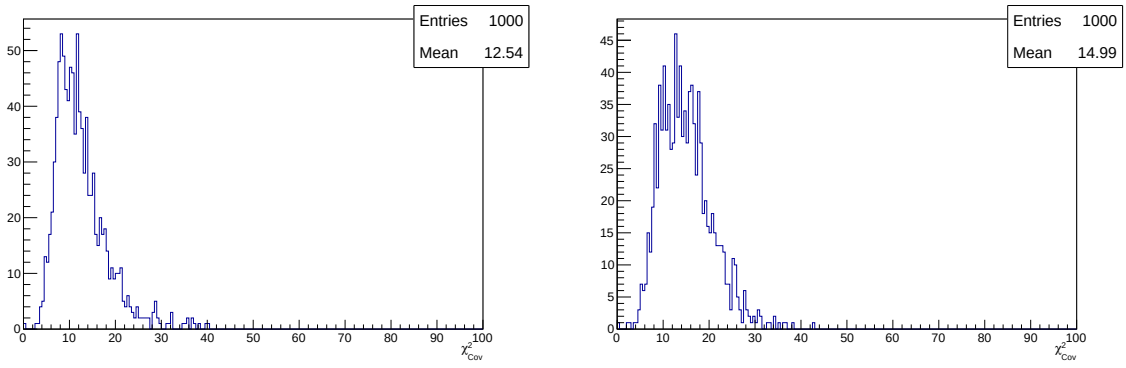

Figure 6.14 – Fake data set # 3: Coverage test for the WM (left) and PM (right). This set has both unfoldings very overcovered. This was however expected since the set is very similar to the nominal simulation and has the flux uncertainties added to the statistical uncertainties even though the latter would suffice to cover the χ^2 distribution. Furthermore, the unfolding for the fake data set # 3 is stopped after merely 1 step which means that the cross-section uncertainty dominates the statistical uncertainty

for both the H_2O unfolding and the CH unfolding. This is the criterion that we will use in Chapter 7 to stop the unfolding on real data.

Chapter 7

Experimental results

7.1 The data set

The T2K experiment has been operating since 2010. Over the years different detectors have been added to the roster or modified. Also, the power of the beam representing the number of protons in each spill, has progressively increased over the years. When talking about the accumulated data of the T2K experiment or of a special sub-experiment or analysis, we talk in Proton On Target, which are the number of accelerated protons sent to collide on the carbon target in the target station. Our models of hadron interaction then allow us to predict the number of neutrinos contained in the beam.
As said earlier the target is inside or followed by three electromagnetic horns. These horns can operate with positive or negative current and switch accordingly the direction of the magnetic field and the charge of the charged hadrons focalised in the decay tunnel. When positively charged hadrons are focalised we talk about Forward Horn Current (FHC) mode while when the hadrons are negatively charged we talk about Reverse Horn Current (RHC). The history of T2K runs and of the accumulated POT over the years can be visualized in Figure 7.1.

For this analysis, We use the RHC data of T2K Run 9 (Figure 7.2 and Table 7.1). The data was taken from October 22nd 2017 to May 24th 2018 with an efficiency of 94.1%. The efficiency here represent the percentage of spills labeled as "good spill". A spill is considered as good if the beam quality at the time it was delivered is up to the quality standards of the experiment. This totals up to 7.908×10^{20} POT and the amount of incident neutrinos we use in our cross-section measurement will be derived from this number. The WAGASCI experiment is placed on the second basement which is commonly referred to as the "B2 floor". The emplacement is at a 1.5° angle off-axis from the beam. We normalize the Monte-Carlo down to this number of POT.

Table 7.1 – The accumulated POT during T2K RUN 9

MR Run	Run period	Beam good spills	Detector good spills	POT
76	Oct. 22 - Nov. 16, 2017	663 378	653 500	1.505×10^{20}
77	Nov. 16 - Dec. 22, 2017	932 995	757 003	1.796×10^{20}
78	Mar. 9 - Apr. 2 , 2018	624 486	615 049	1.473×10^{20}
79	Apr. 4 - May. 24, 2018	1 334 452	1 276 823	3.134×10^{20}
Total	Oct. 22, 2017 - May. 24, 2018	3 555 311	3 302 375	7.908×10^{20}

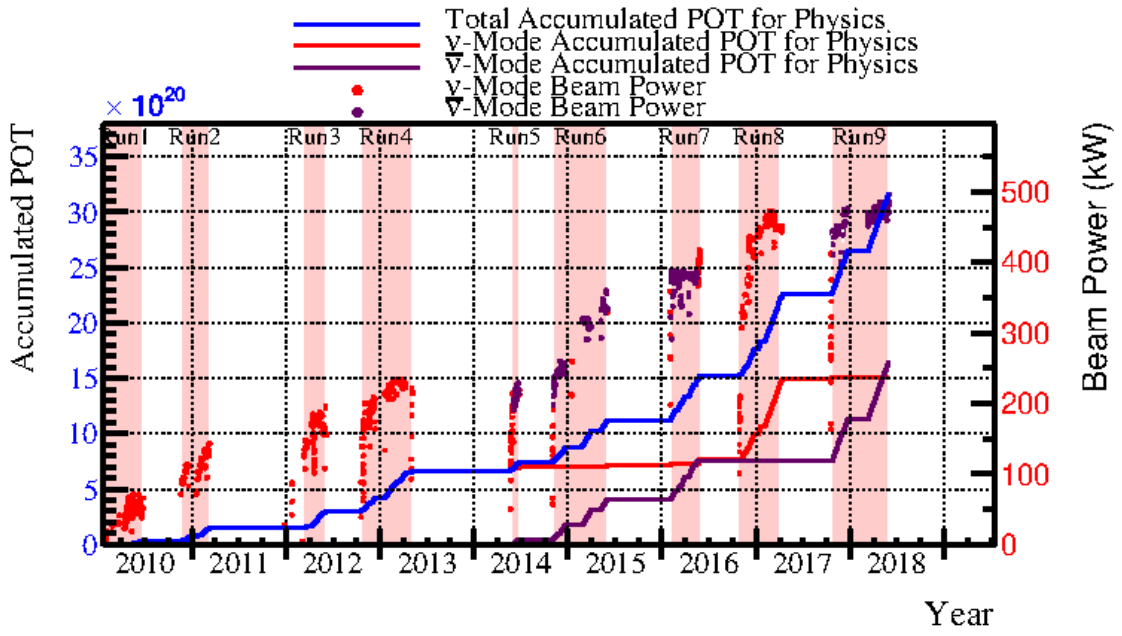

Figure 7.1 – The accumulated POT over the years in the T2K experiment from 2010 to 2018. The POT total can be read on the left vertical axis while the power of the beam can be read on the right vertical axis.

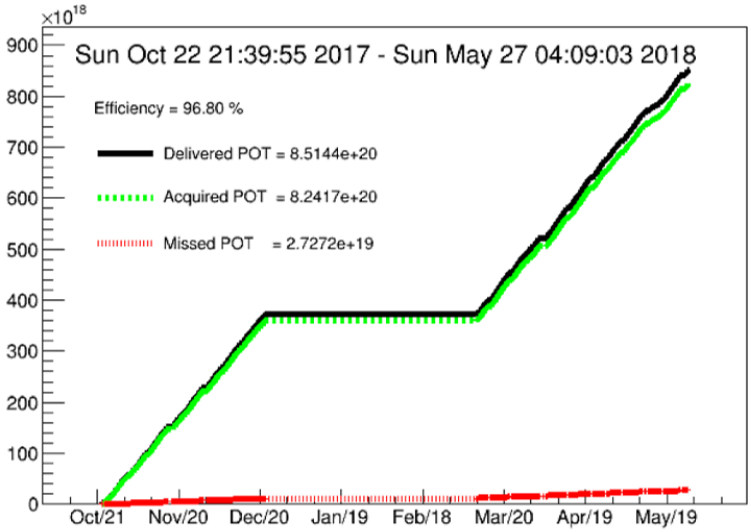

Figure 7.2 – The accumulated POT during T2K RUN 9

7.2 Selections results on data

We use the cuts presented in Section 3.4 to choose the events in the data sample. The results for the WM selection are presented in Table 7.2 while the results for the PM selection are presented in Table 7.3

Cut	Selected events
Reconstructed + one INGRID track	5888
FCFV	2252
CC0pi Selection	2143
On time	2137
MuTrk is INGRID stop/through	1876
MuTrk is INGRID stop	924

Table 7.2 – WM events selection on data

Cut	Selected events
Reconstructed + one INGRID track	211318
FCFV	2608
CC0pi Selection	2133
On time	2117
MuTrk is INGRID stop/through	1755
MuTrk is INGRID stop	940

Table 7.3 – PM events selection on data

The vertices position in the data sample for the WM selection can be compared to the predictions by the Monte-Carlo simulation (Figure 7.3) The vertices position in the data sample for the PM selection can be compared to the predictions by the Monte-Carlo simulation (Figure 7.4)

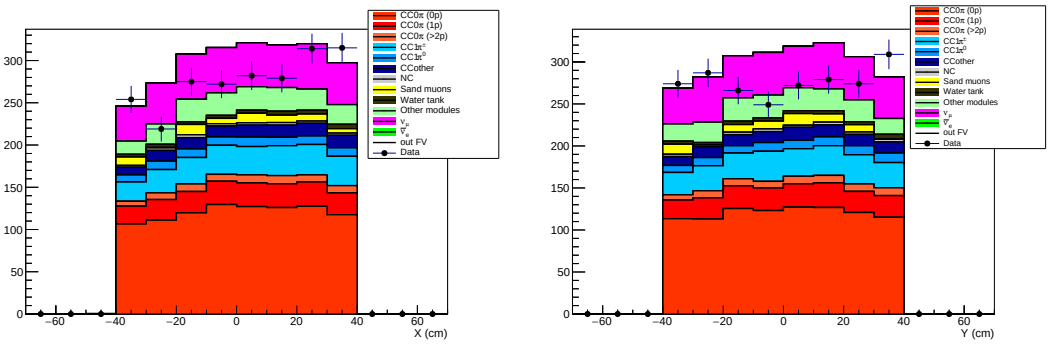

Figure 7.3 – Position of the vertices in the WM selection sample. The data points also have the statistical error associated. The simulation prediction is broken down by the different sources.

Similarly, we can compare the distributions of selected event in the reconstructed phase spaces for the WM selection (Figure 7.5) and for the PM selection (Figure 7.6)

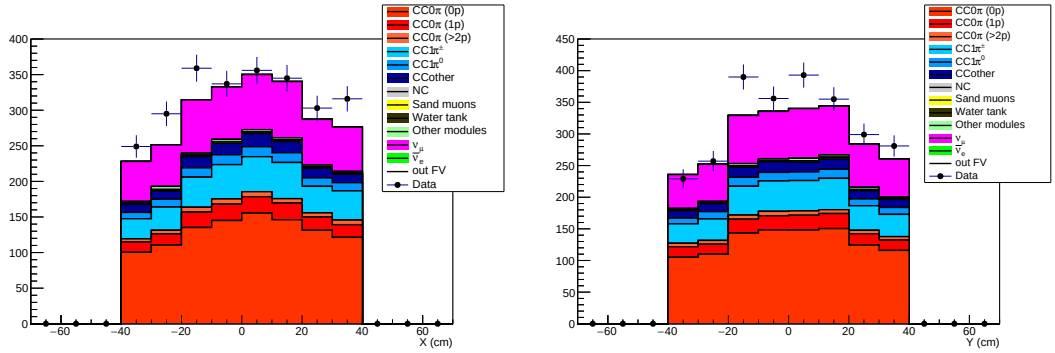

Figure 7.4 – Position of the vertices in the PM selection sample. The data points also have the statistical error associated. The simulation prediction is broken down by the different sources.

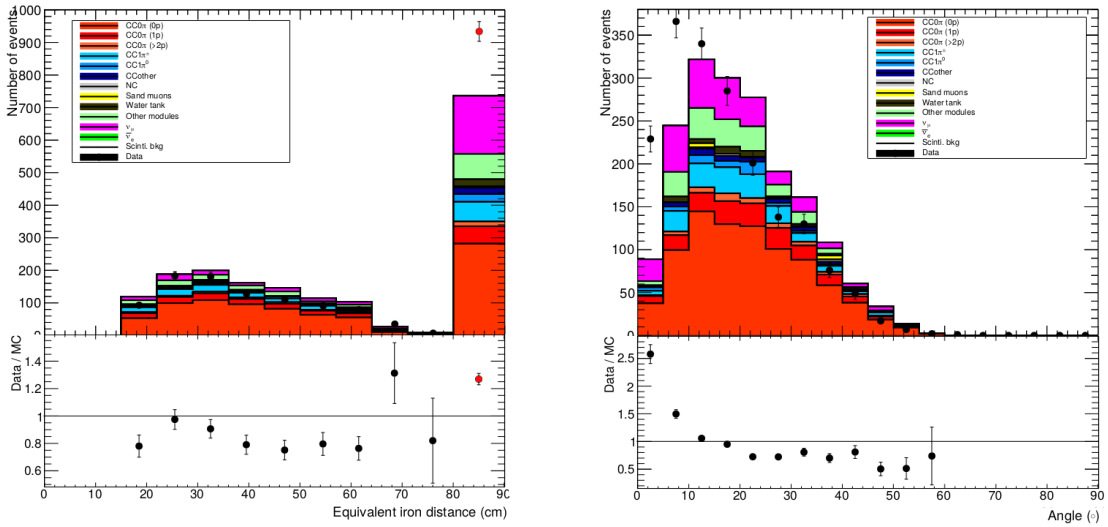

Figure 7.5 – WM selection: distributions of equivalent iron distance (left) and distributions of reconstructed angles (right). The number of events is on top while the ratio between the data sample and the MC sample is displayed at the bottom. The red dot on the reconstructed momentum distribution represents the through-going events.

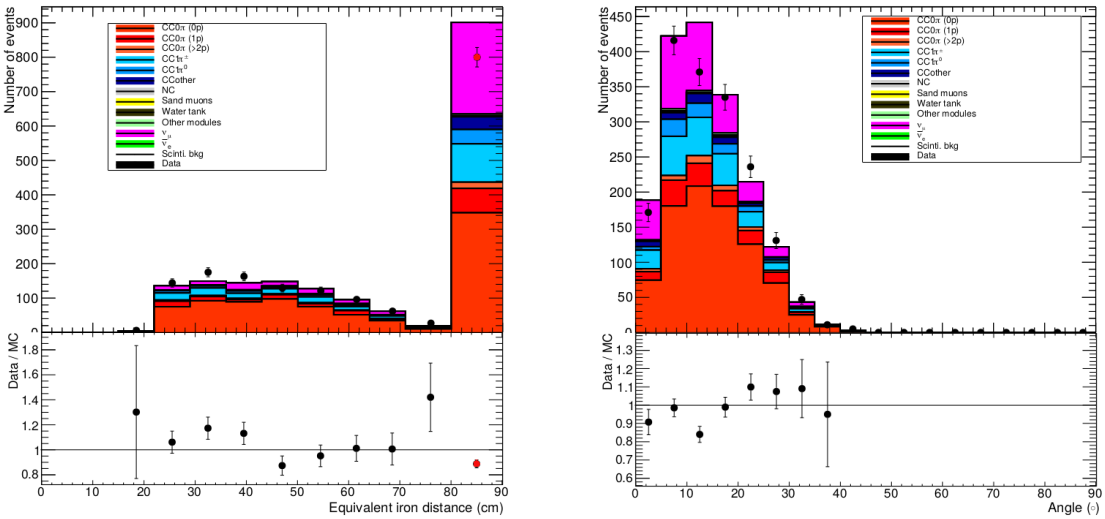

Figure 7.6 – PM selection: distributions of equivalent iron distance (left) and distributions of reconstructed angles (right). The number of events is on top while the ratio between the data sample and the MC sample is displayed at the bottom. The red dot on the reconstructed momentum distribution represents the through-going events.

7.3 Cross-sections results on data

We use the criterion shown in Equation 6.11, to stop the unfolding of the data sample. We decided to stop the procedure at the same step for both the WM unfolding and the PM unfolding. Both χ^2 go under 0.48 after 20 iterations:

$$\begin{aligned} \chi^2_{Data}(20) &= 0.477 \quad \text{for } H_2O \\ \chi^2_{Data}(20) &= 0.13 \quad \text{for CH} \end{aligned} \tag{7.1}$$

Thus we take the uncertainties given by the total uncertainty matrix at the 20-th step $\mathbf{Cov}(2)$

7.3.1 Total cross-sections

The total cross-section is the cross-section integrated for a muon energy $0.4\,\text{GeV/c} < p_\mu < 30\,\text{GeV/c}$ and a muon angle $0 < \theta_\mu < 30°$.
The results of our measurement are shown in Table 7.4. We see that for the cross-sections

	σ_{H_2O}	σ_{CH}	$\sigma_{H_2O}/\sigma_{CH}$
Measured value	$1.31 \times 10^{-39}\,\text{cm}^2$	$1.12 \times 10^{-39}\,\text{cm}^2$	1.17
Statistical uncertainty	± 8.08 %	± 5.57 %	± 10.79 %
Flux uncertainty	± 11.6 %	± 11.23 %	± 0.40 %
Cross-section model	± 5.78 %	± 5.29 %	± 4.17 %
Detector response	± 4.22 %	± 2.93 %	± 5.74 %
Total error	± 15.84 %	± 13.92 %	± 12.92 %

Table 7.4 – Unfolded cross-sections and associated uncertainties.

measurements, the dominating error comes from the flux knowledge while for the ratio measurement the dominating error is the statistical error. In this latter case the flux error was significantly reduced.

7.3.2 Differential cross-section

Differential cross-section in momentum

The differential cross-sections in momentum are measured for the muons having an angle θ_μ between 0 and 30°. The results for the two cross-sections σ_{H_2O}, σ_{CH} are shown in Figure 7.7 while the results for the ratio of the cross-sections are shown in Figure 7.8.

Differential cross-section in angle

The differential cross-sections in angle are measured for the muons having a momentum p_μ between 0.4 GeV/c and 30 GeV/c. The results for the two cross-sections σ_{H_2O}, σ_{CH} are shown in Figure 7.9 while the results for the ratio of the cross-sections are shown in Figure 7.10.

7.3.3 Double differential cross-section

The double differential cross-sections are measured for the muons with an angle $0 < \theta_\mu < 10°$ (Figure 7.11 and Figure 7.12), for the muons with an angle $10° < \theta_\mu < 20°$ (Figure 7.13 and Figure 7.14) and for the muons with an angle $20° < \theta_\mu < 30°$ (Figure 7.15 and Figure 7.16). Each figure shows the results for the two cross-sections σ_{H_2O}, σ_{CH} as well as for the ratio of the cross-sections.

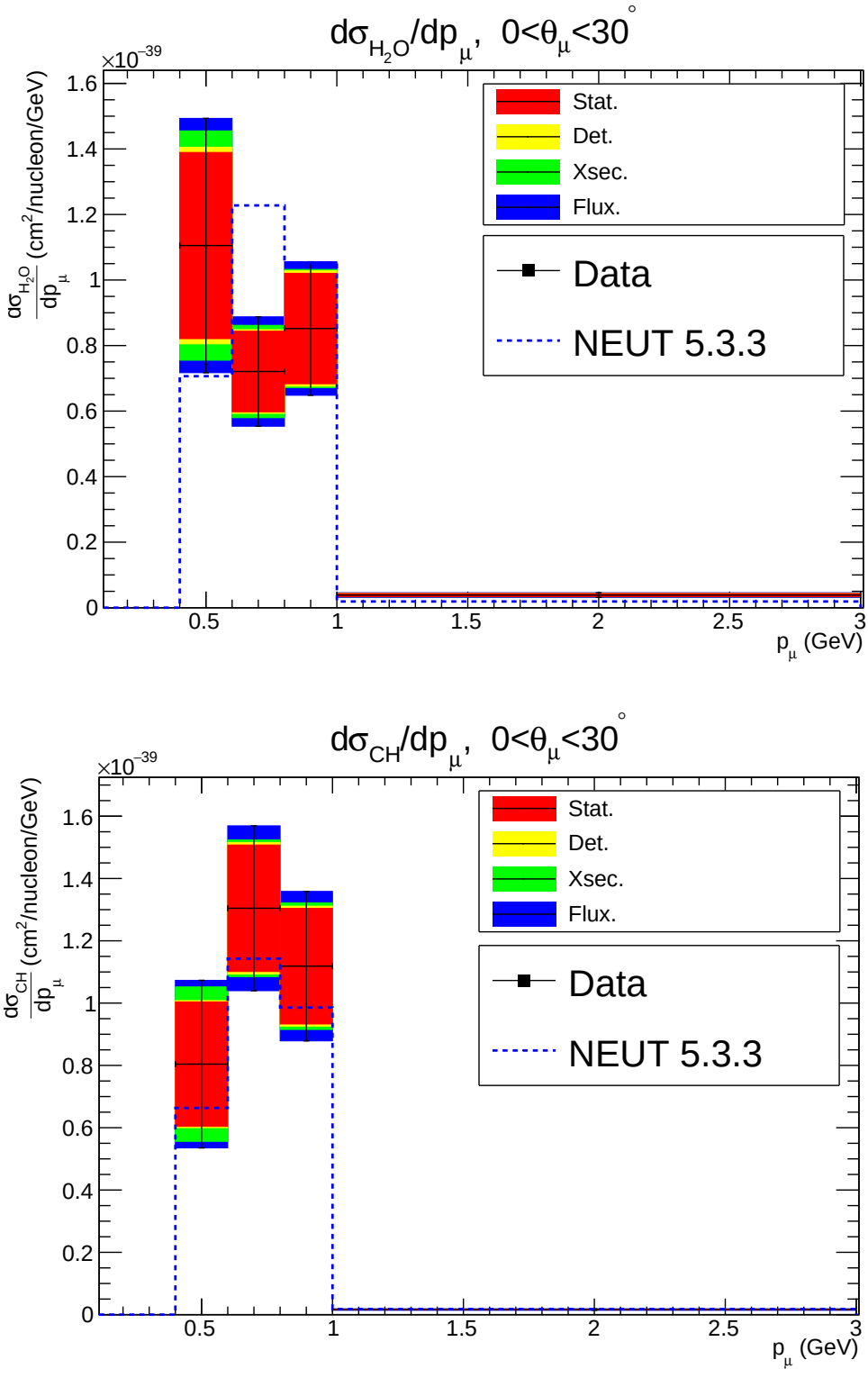

Figure 7.7 – Differential cross section in momentum measured with the data. For water (Top) and for carbon (Bottom). The dotted line gives the cross-section predicted by NEUT 5.3.3. The muon angle is constrained by $0 < \theta_\mu < 30°$.

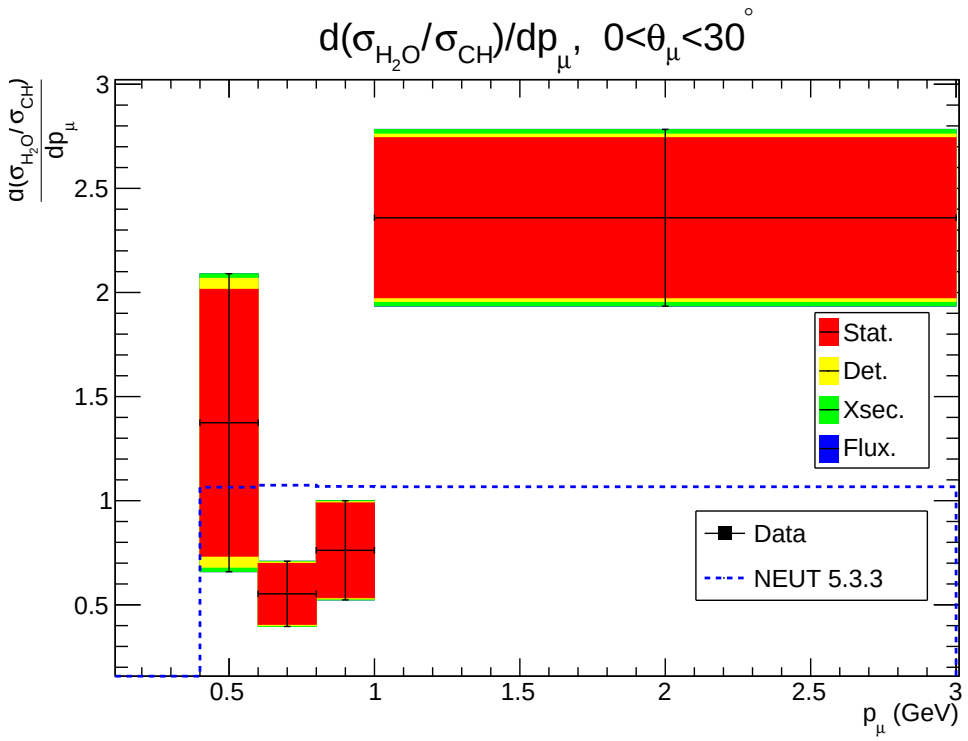

Figure 7.8 – Differential cross section in momentum measured with the data for the ratio of the two cross-sections. The dotted line gives the cross-section predicted by NEUT 5.3.3. The muon angle is constrained by $0 < \theta_\mu < 30°$.

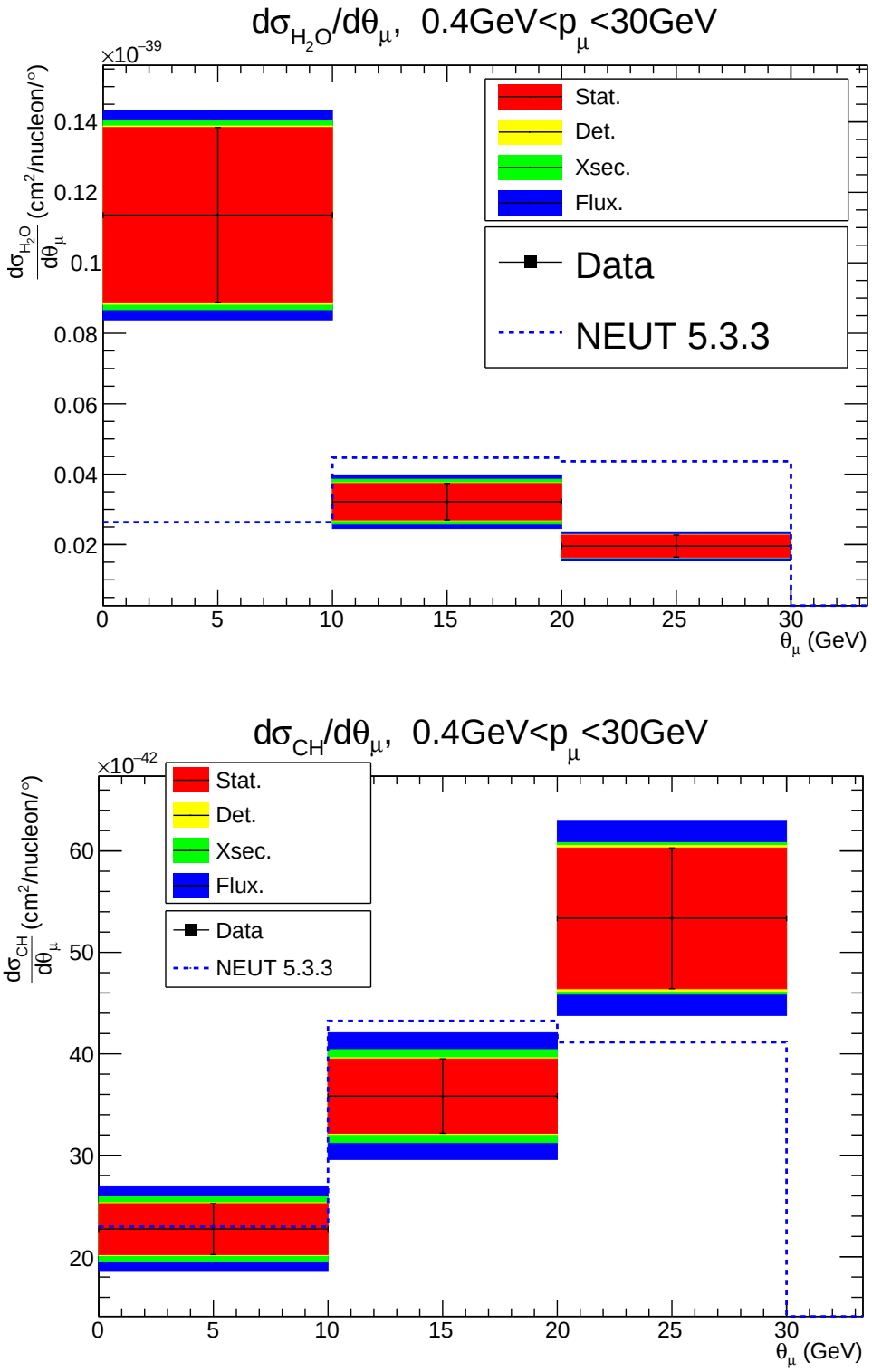

Figure 7.9 – Differential cross section in angle measured with the data. For water (Top) and for carbon (Bottom). The dotted line gives the cross-section predicted by NEUT 5.3.3. The muon momentum is constrained by $0.4\,\mathrm{GeV/c} < p_\mu < 30\,\mathrm{GeV/c}$.

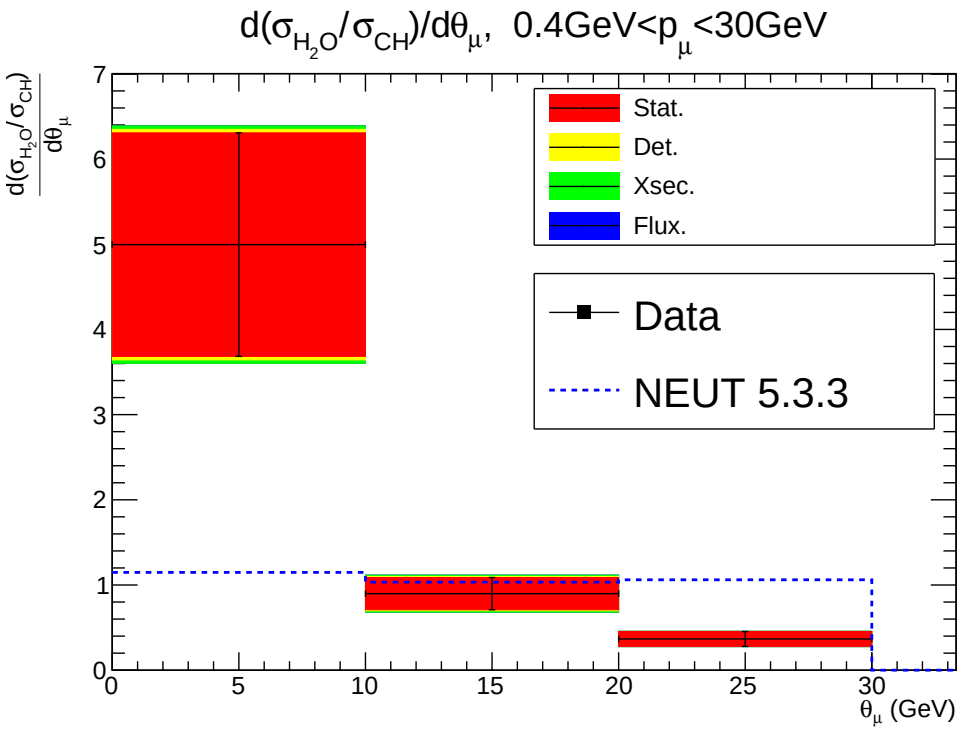

Figure 7.10 – Differential cross section in angle measured with the data for the ratio of the two cross-sections. The dotted line gives the cross-section predicted by NEUT 5.3.3. The muon momentum is constrained by $0.4\,\mathrm{GeV/c} < p_\mu < 30\,\mathrm{GeV/c}$.

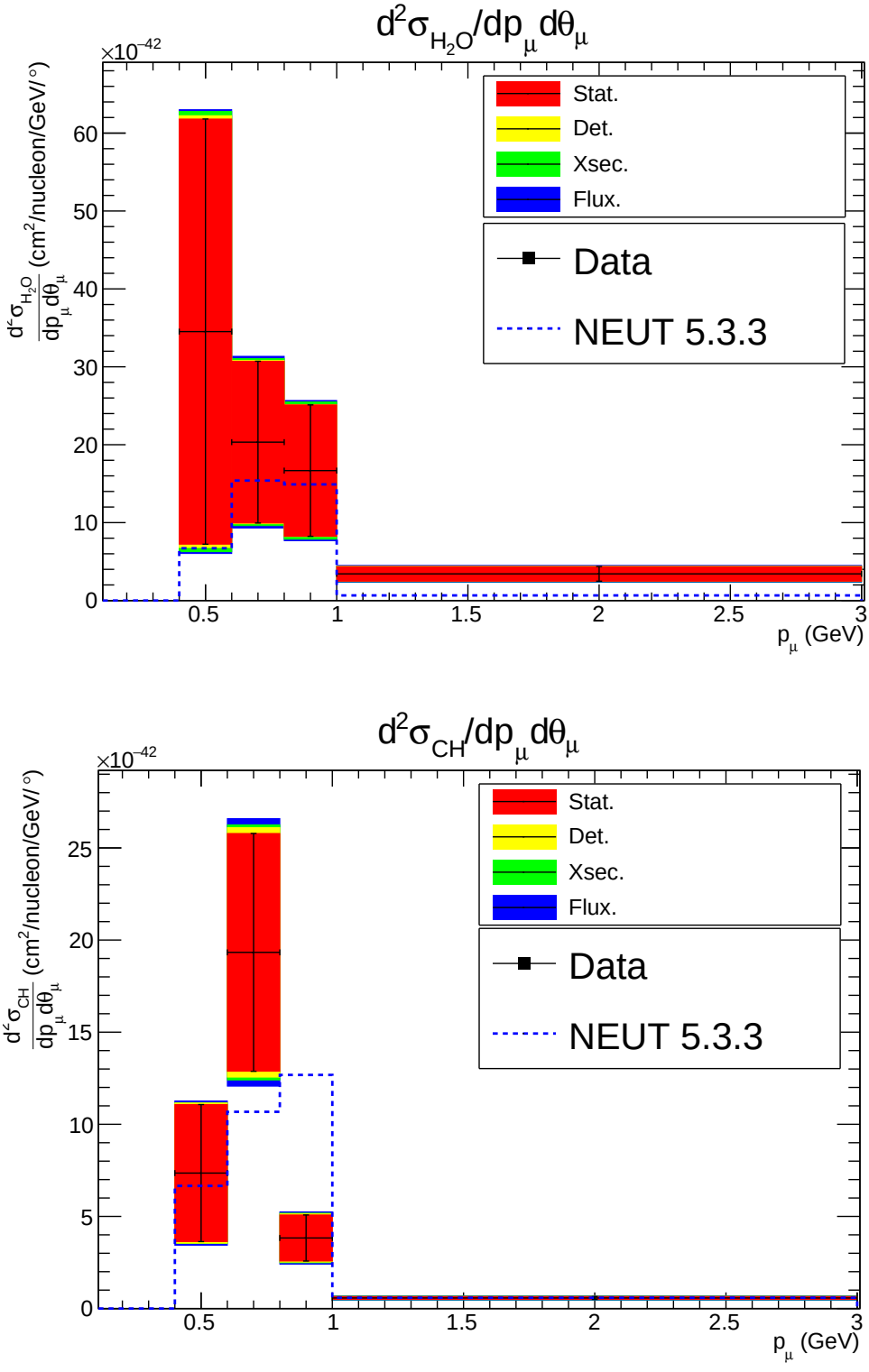

Figure 7.11 – Double differential cross section measured with the data. For water (Top) and for carbon (Bottom). The dotted line gives the cross-section predicted by NEUT 5.3.3. The plots show the momentum dependency for muons with an angle $0 < \theta_\mu < 10°$.

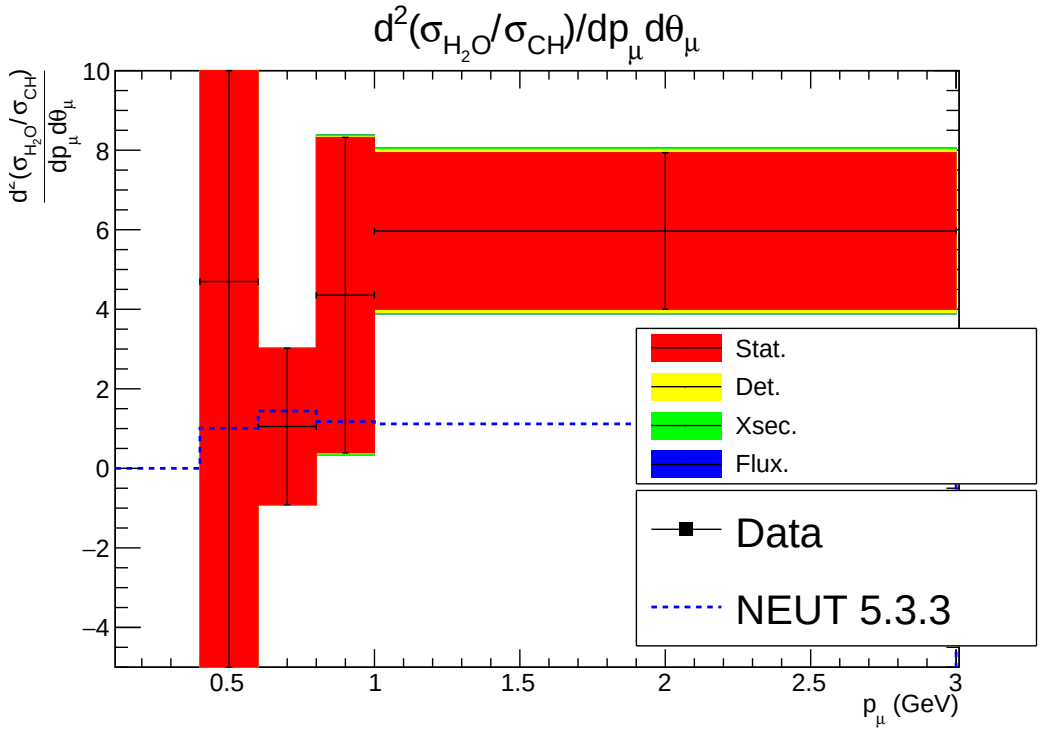

Figure 7.12 – Double differential cross section measured with the data for the ratio of the two cross-sections. The dotted line gives the cross-section predicted by NEUT 5.3.3. The plots show the momentum dependency for muons with an angle $0 < \theta_\mu < 10°$.

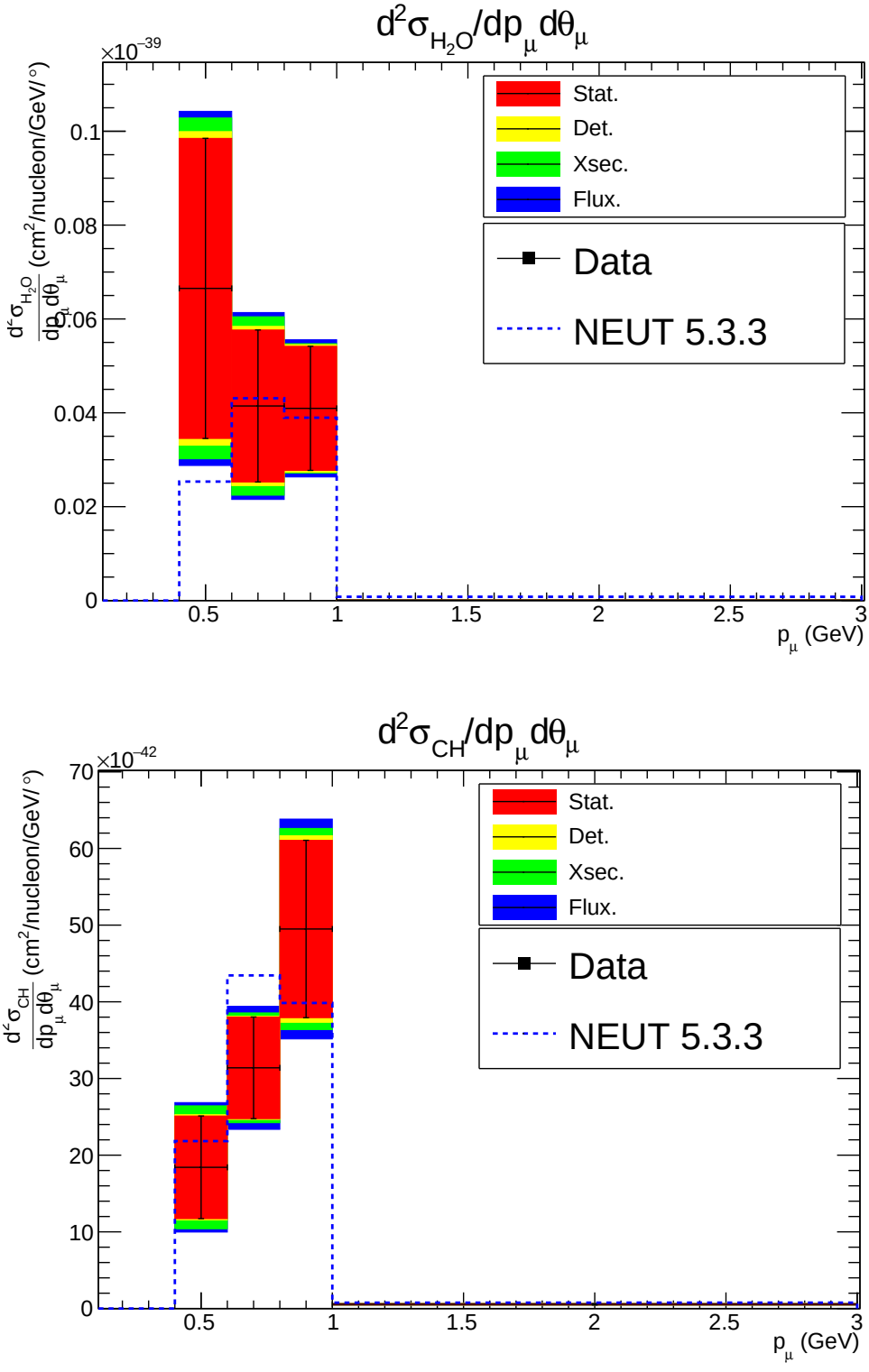

Figure 7.13 – Double differential cross section measured with the data. For water (Top) and for carbon (Bottom). The dotted line gives the cross-section predicted by NEUT 5.3.3. The plots show the momentum dependency for muons with an angle $10° < \theta_\mu < 20°$.

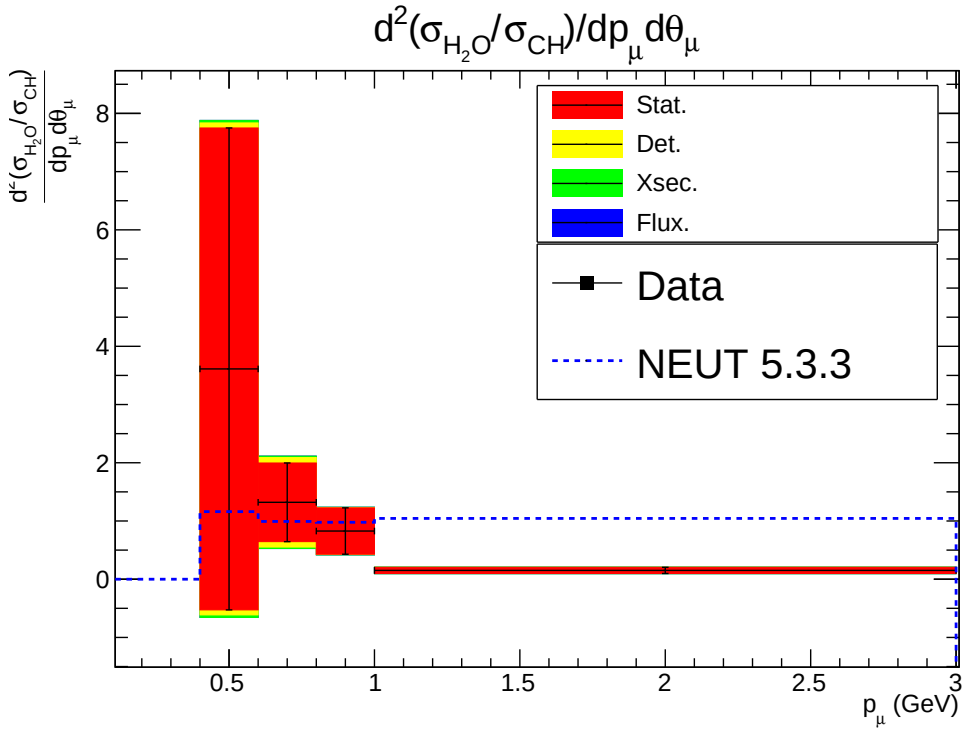

Figure 7.14 – Double differential cross section measured with the data for the ratio of the two cross-sections. The dotted line gives the cross-section predicted by NEUT 5.3.3. The plots show the momentum dependency for muons with an angle $10^\circ < \theta_\mu < 20^\circ$.

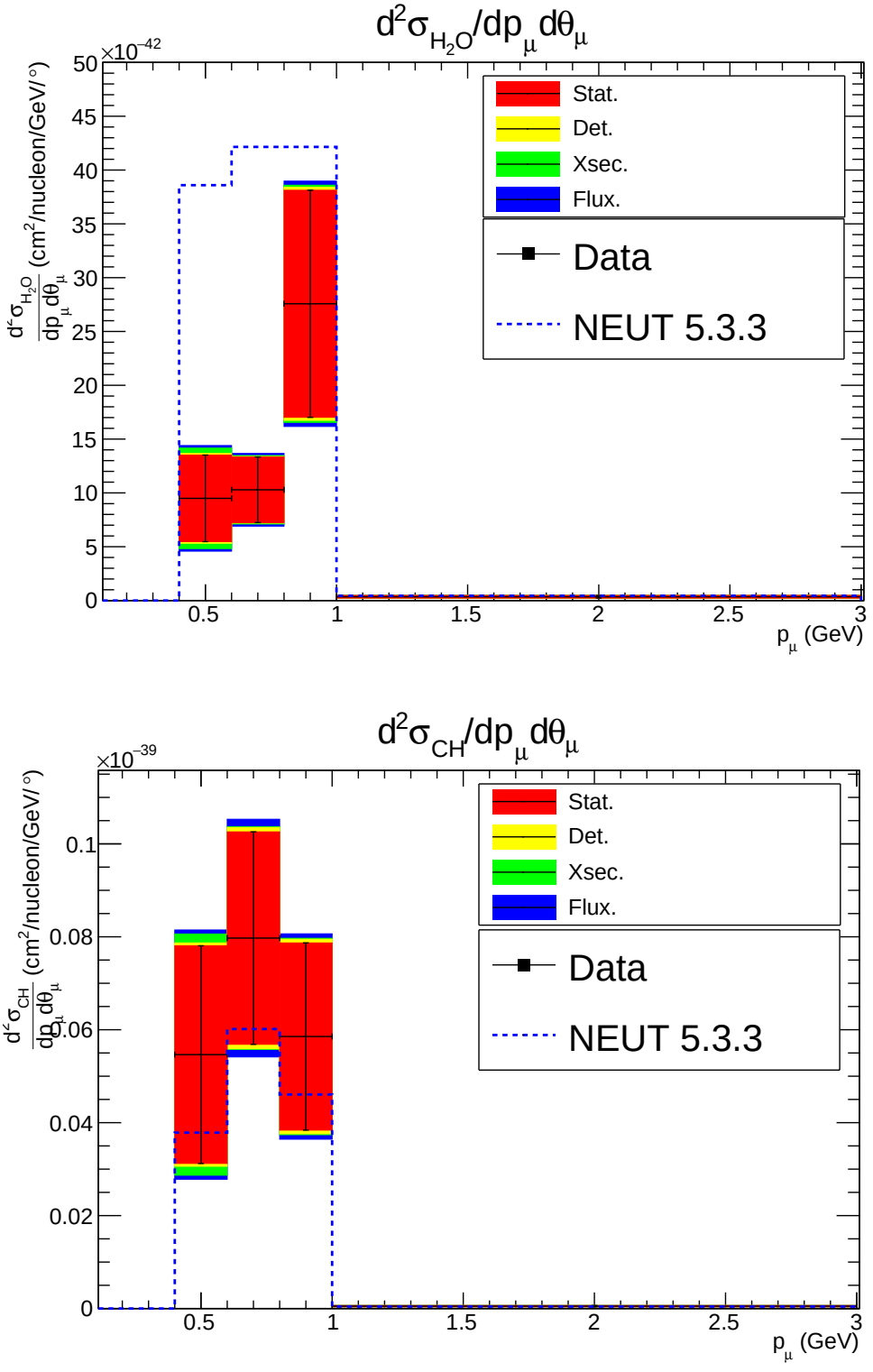

Figure 7.15 – Double differential cross section measured with the data. For water (Top) and for carbon (Bottom). The dotted line gives the cross-section predicted by NEUT 5.3.3. The plots show the momentum dependency for muons with an angle $20° < \theta_\mu < 30°$.

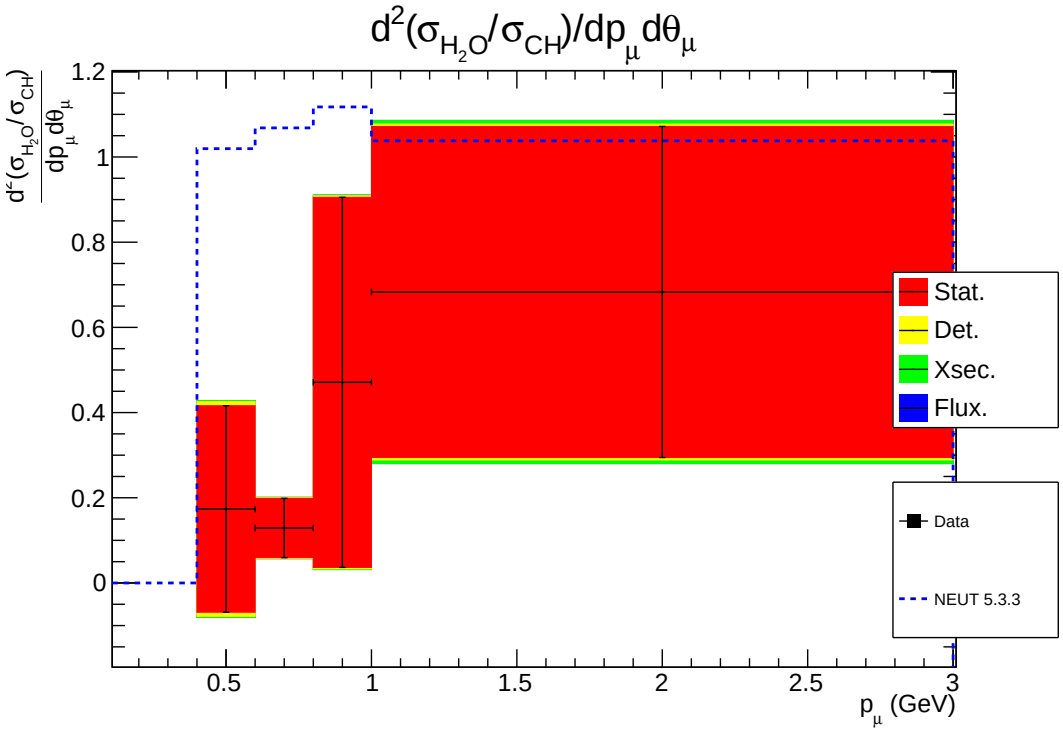

Figure 7.16 – Double differential cross section measured with the data for the ratio of the two cross-sections. The dotted line gives the cross-section predicted by NEUT 5.3.3. The plots show the momentum dependency for muons with an angle $20° < \theta_\mu < 30°$.

7.4 Comparison with the predictions of neutrino generators

The values of the cross-sections predicted by NEUT 5.3.3 are shown in Table 4.10 while the measurement on the data are in Table 7.4. The comparison between our data and NEUT is shown in Table 7.5.

Cross-section	NEUT 5.3.3	Data	Number of standard deviation
σ_{H_2O}	$1.145 \times 10^{-39}\,\mathrm{cm}^2$	$(1.31 \pm 0.21) \times 10^{-39}\,\mathrm{cm}^2$	0.78
σ_{CH}	$1.032 \times 10^{-39}\,\mathrm{cm}^2$	$(1.12 \pm 0.15) \times 10^{-39}\,\mathrm{cm}^2$	0.59
$\sigma_{H_2O}/\sigma_{CH}$	1.109	(1.16 ± 0.15)	0.41

Table 7.5 – Comparison between the predictions of NEUT 5.3.3 and the measurement from our data

For both materials, the total cross-sections are in agreement with the NEUT predictions. For the carbon, the shapes in momentum and angle for our data are in good agreement with the predictions but for the water, there is a significant discrepancy. The equivalent iron distance distribution is very different between the prediction and our data for the WM sample as shown in Figure 7.5 and this propagates to the differential cross-section in angle for the water (Figure 7.9) and in the ratio of the cross-sections in angle (Figure 7.10). Conversely, the angle distributions match in the PM and this shows in the measurement on the differential cross-section in angle for the carbon.

Two explanations can be proposed. It can be a difference between the model and real data. It could also be that there is some difficulty to properly identify the hits belonging to a same track and the algorithm includes parasite hits that negatively impact the reconstructed angle. This idea is supported by the fact that the problem arose with the Water Module which is a relatively new detector while the Proton Module, which has been operating for much longer, is better understood. It is necessary to better understand the functioning of the Water Module and the impact of the scintillators being much closer than they are in the PM. This could help to engineer a more efficient cellular automaton algorithm. The T2K collaboration will investigate these leads.

A similar comparison is done between GENIE 2.12.8 and our measurement. The comparison is shown in Table 7.6. GENIE predicts a value of the cross-section on carbon closer to

Cross-section	GENIE 2.12.8	Data	Number of standard deviation
σ_{H_2O}	$1.147 \times 10^{-39}\,\mathrm{cm}^2$	$(1.31 \pm 0.21) \times 10^{-39}\,\mathrm{cm}^2$	0.78
σ_{CH}	$1.073 \times 10^{-39}\,\mathrm{cm}^2$	$(1.12 \pm 0.15) \times 10^{-39}\,\mathrm{cm}^2$	0.31
$\sigma_{H_2O}/\sigma_{CH}$	1.069	(1.16 ± 0.15)	0.67

Table 7.6 – Comparison between the predictions of GENIE 2.12.8 and the measurement from our data

our measurement than NEUT but the difference is not significant

Conclusion

The study of neutrino oscillation is a very actual field of research and a measurement of the CP violation phase would be of major importance in order to shed the light on the origin of the matter-antimatter asymmetry of the Universe. As we have shown, a precise measurement of this phase by accelerator experiments requires a deep knowledge of the neutrino interactions with the detectors. The complexity of nuclear physics effects prevent any analytical description of these interactions. Several phenomenological models are used in order to be able to predict the neutrino rate at the far detector but all of them need parameter tuning from experimental measurement. In particular, the CC0π channel is the channel used for the T2K oscillation analyses.

The main objectives of this thesis were to properly select a sample, to use it to measure the CC0π cross-section in the allowed phase-space, and to identify and to evaluate the different error sources on our measurement

We presented the selection process and the predicted composition of our selected events sample in both target modules. We then presented the D'Agostini unfolding procedure as well as a modification to include the backgrounds (CC1π, other interactions) in the unfolding itself. This modified procedure is less model dependent. The different parameters we used it with in order to extract a CC0π cross-section measurement from our selected sample have also been presented and estimated.

Then came the estimation of the errors, coming from three main sources : the statistics of our sample, the models we used in our MC simulation (flux prediction by JNUBEAM, neutrino interactions with matter with NEUT 5.3.3), and the response of our detector. We successfully proved that the error coming from the flux uncertainties was greatly reduced by making a measurement on the ratio of the cross-sections σ_{H_2O} and σ_{CH}. Even though the error from the detector response took a jump as a result, the results were still beneficial by a large margin. As a matter of fact, this error is one of the leading ones in usual cross-section measurement in T2K.

Finally we got to the task of determining a stopping criterion for our unfolding, an iterative process. We had to deal with the fact that the errors on our measurement increase the more we iterate the process and also with the fact that not iterating it enough lead to a measurement not regularized enough. We decided to use a data-driven criterion by looking at the way our algorithm worked on fake data simulations. These simulations were different from the nominal MC simulation, but we still knew their true cross-sections which allowed us to devise the aforementioned criterion.

Thanks to all of these steps we managed to measure a cross-section within the chosen phase-space: $0.4\,\text{GeV} < p_\mu < 30\,\text{GeV}$. We compared this measurement to the values pre-

dicted by the NEUT and GENIE generators. Even though we stayed within one standard deviation when comparing the total cross-sections, we saw that the shape of the water cross-section was very different between the NEUT prediction and the data sample, especially in angle. This could be caused by the model but could also very well be due to the cellular automaton algorithm used to reconstruct the tracks. The new structure of the Water Module and the proximity and thinness of the scintillator as well as the innovative grid structure will need further work.

As we stated we have worked with an intermediate setup which did not allow to measure the cross-sections at high angle. Nonetheless, this analysis clearly shows that our objectives are attainable. The current T2K data taking will give us the desired high angle analysis. Furthermore, the magnetized downstream MRD (baby-MIND) will provide an additional identification of the particle charge which will decrease the wrong-sign contamination (ν_μ and $\bar{\nu}_e$) which is an important part of our current signal contamination.

Appendix A

Elemental composition of the scintillators

The scintillator of the WAGASCI consists of polystyrene, POP, POPOP, reflector, wavelength shifting fiber, optical cement and black painting.

The composition of the scintillator itself is 98.97 % polystyrene(C 8 H 8)n, 1 % of PPO (C 15 H 11 NO) and 0.03 % of POPOP (C 24 H 16 N 2 O 2) by weight.

The mass of the optical cement (mainly C 4 H 4 O 2) is measured as 0.93 (1.12) g for the plane (grid) scintillator. The mass of the black paint (mainly (SiO 2 C 5 O 2 H 8))is measured as 0.64 g (0.61 g) for the plane (grid) scintillator. The mass of the painted reflector (mainly C 2 HN 2 O 3) is measured as 1.77 g (1.86 g) for the plane (grid) scintillator.

The elemental composition of the plane (grid) scintillators can be found in Table A.1 (Table A.2)

Components	Mass fraction	Element					
		H	C	N	O	Ti	Si
Scintillator	81.6%	7.71%	92.12%	0.08%	0.09%	0	0
Reflective coating area	13.1%	6.58%	78.42%	0	6.01%	8.99%	0
Fiber	1.04%	7.74%	92.26%	0	0	0	0
Optical cement	1.17%	4.8 %	57.1 %	0	38.1%	0	0
Hand painted reflector	2.23%	1.0 %	23.8 %	27.7%	47.5%	0	0
Black paint	0.81%	5.0 %	37.5 %	0	40.0%	0	17.5%
Total	100 %	7.4 %	87.9 %	0.7%	2.7 %	1.2 %	0.1%

Table A.1 – Mass fraction of the elements in the plane scintillators of the Water Module

Components	Mass fraction	Element					
		H	C	N	O	Ti	Si
Scintillator	81.0%	7.71%	92.12%	0.08%	0.09%	0	0
Reflective coating area	13.1%	6.58%	78.42%	0	6.01%	8.99%	0
Fiber	1.09%	7.74%	92.26%	0	0	0	0
Optical cement	1.48%	4.8 %	57.1 %	0	38.1%	0	0
Hand painted reflector	2.46%	1.0 %	23.8 %	27.7%	47.5%	0	0
Black paint	0.81%	5.0 %	37.5 %	0	40.0%	0	17.5%
Total	100 %	7.3 %	87.7 %	0.7%	2.9 %	1.2 %	0.1%

Table A.2 – Mass fraction of the elements in the grid scintillators of the Water Module

Appendix B

Timing of the hits in the modules

The Time-to-Digital Converters (TDCs) for the Water Module were not functioning properly and could not synchronize ith the beam timing trigger. As a result the timings of the hits for the Water Module are completely random as seen in Figure B.1

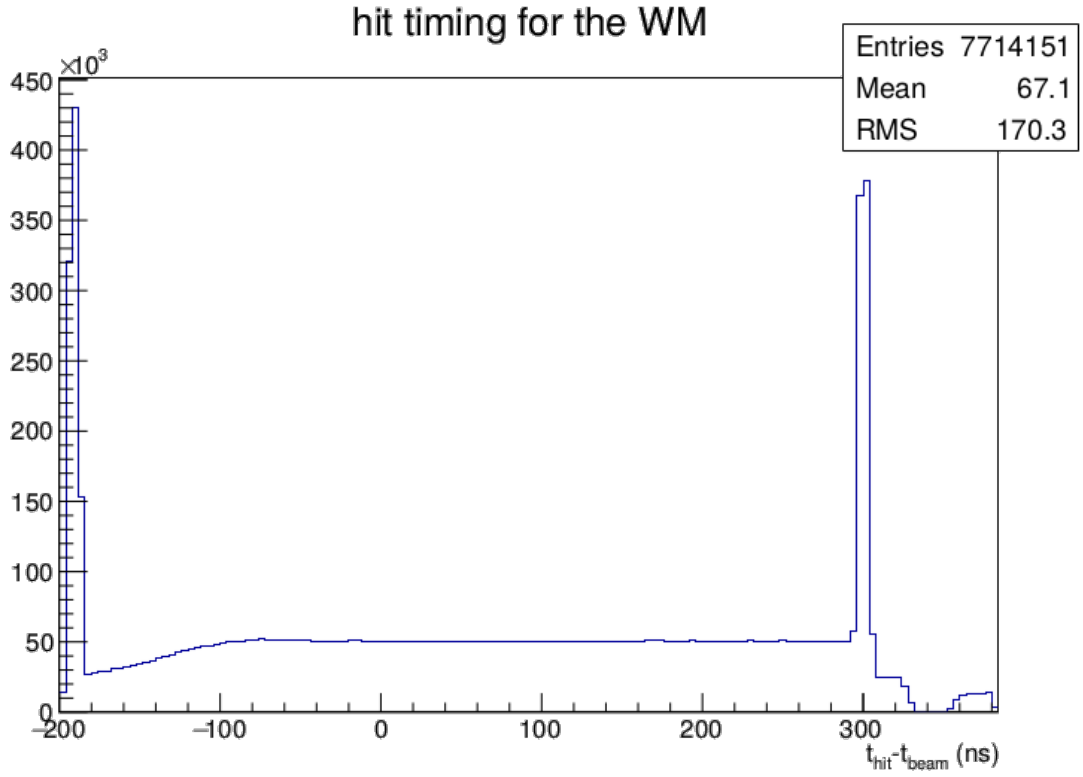

Figure B.1 – Timing of the hits for the Water Module. The distribution of the hits timing is random and spread all over the width of the acquisition window. The two peaks are due to the saturation of the TDCs.

Conversely, the timings for the Proton Module and Ingrid Module are properly synchronized with the beam timing (Figure B.2 and Figure B.3).

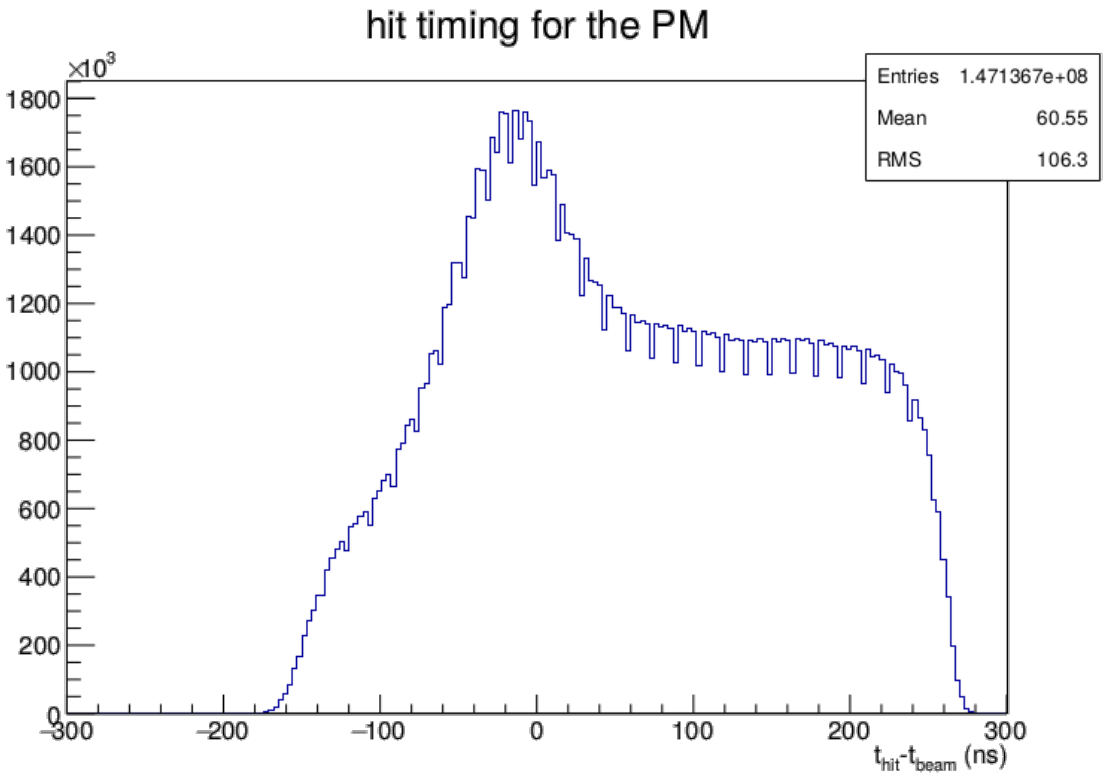

Figure B.2 – Timing of the hits for the Proton Module.

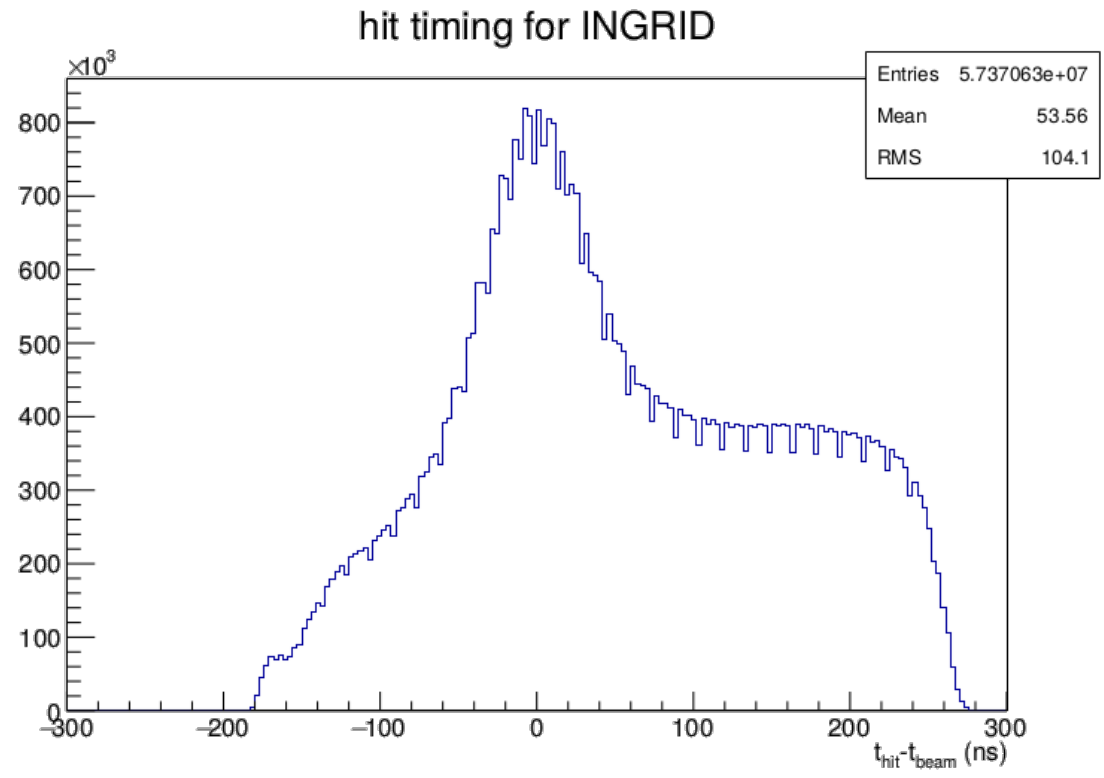

Figure B.3 – Timing of the hits for the INGRID Module.

Appendix C

Construction of the Water Module

During the first year, I participated in the construction of the Water Module. The first step was to prepare the scintillators. We used an automated gluing system (Figure C.1) to stick the fibers to the scintillators (Figure C.2). The fibers are connected to the scintillators with an optical cement dispensed with a syringe and a pump that are electronically controlled (Figure C.3). Then we measured the parameters for each of the scintillators : the mass, the volume, the light yield.

All these parameters are used for the computation of the number of target nucleons and it was thus imperative to know them as accurately as possible. The automatization of the gluing procedure was decided in order to uniformize the amount of optical cement and avoid the wide variation induced by a hand-made gluing.

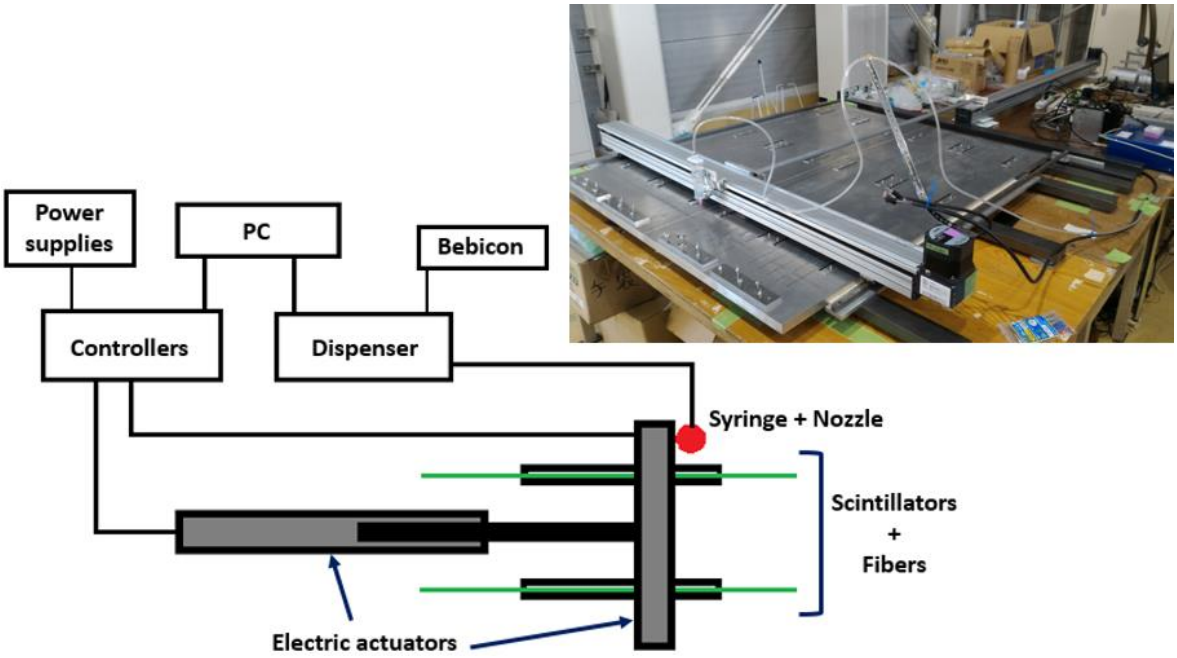

Figure C.1 – Automated gluing system. A mechanical arm directs the syringe over the scintillators setup on the surface.

Finally we assembled the scintillator frame, put it in the tank anf filled it with water.

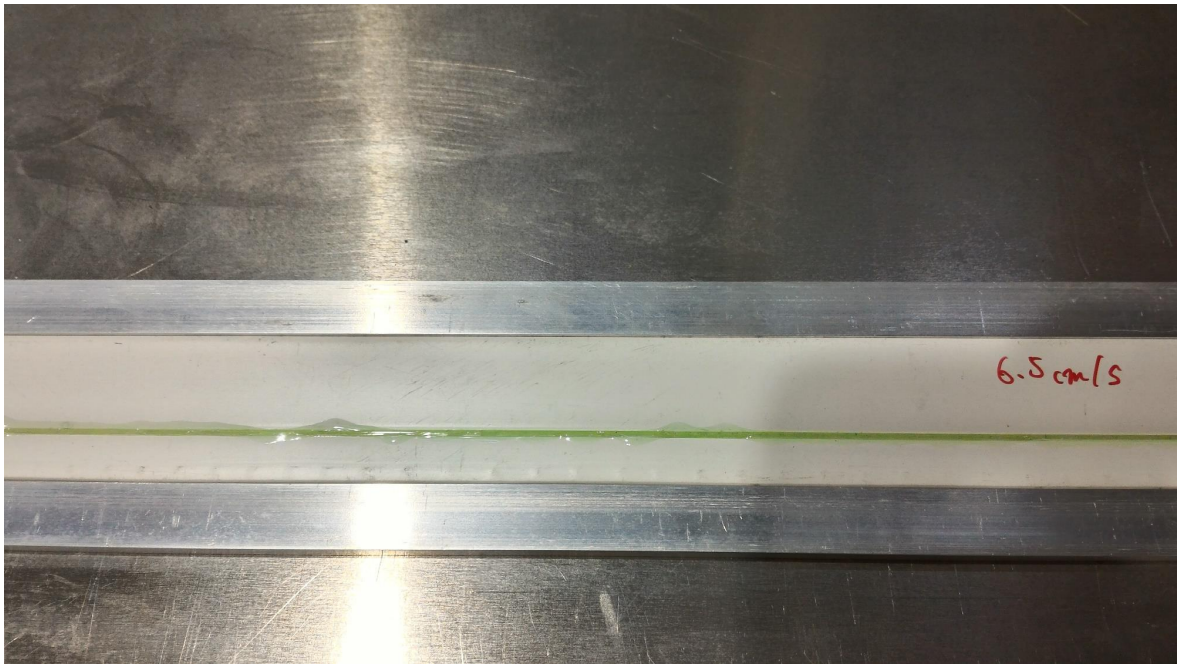

Figure C.2 – Scintillators after the gluing procedure. The amount of optical cement has been dispensed uniformly over the fiber.

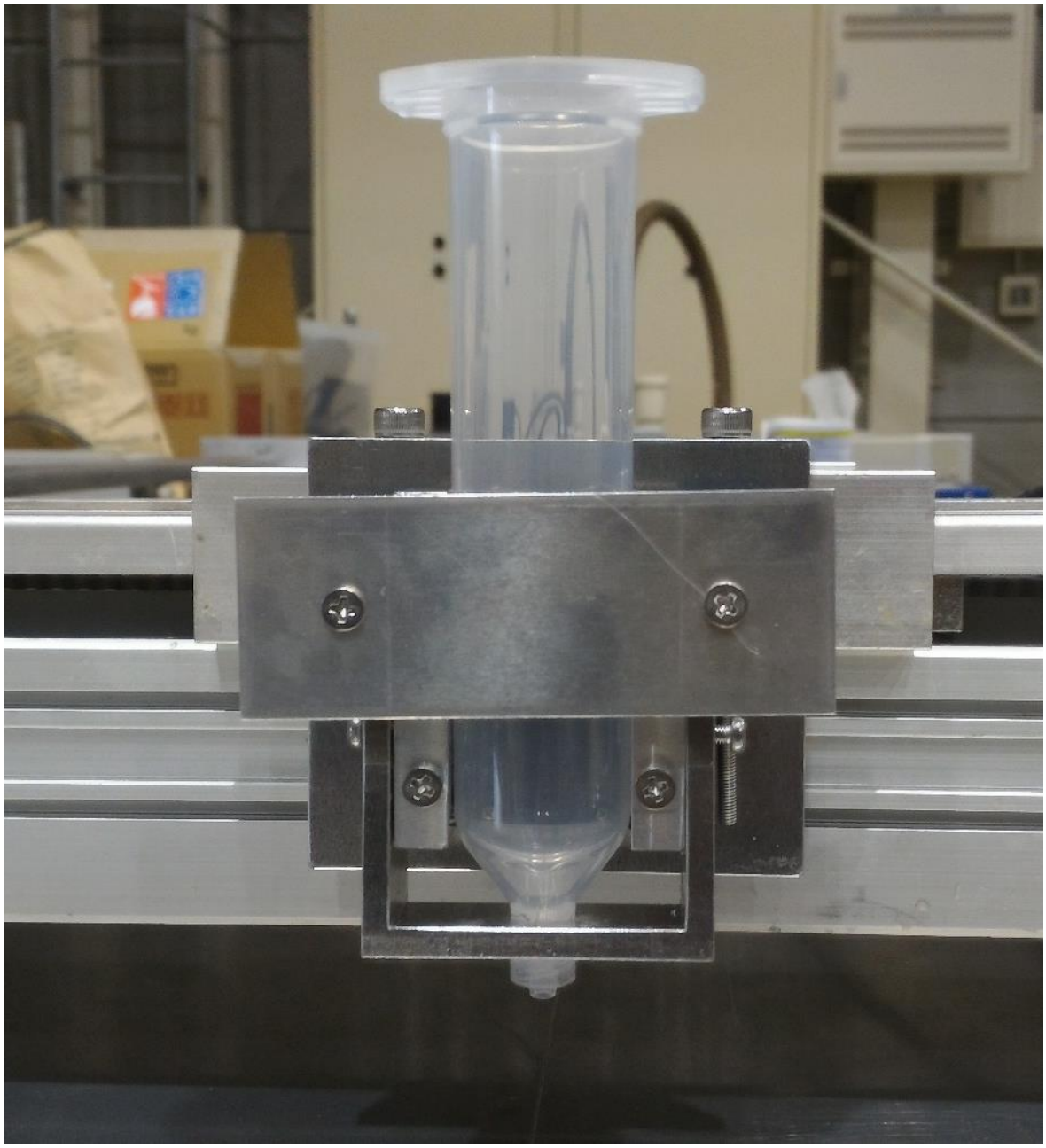

Figure C.3 – Automated gluing system. The syringe dispenses the optical cement over the fibers to stick them to the scintillators.

Appendix D

Résumé

Cette thèse porte sur la mesure des sections efficaces CC0π des antineutrinos muoniques sur l'eau, le carbone ainsi que le rapport de ces deux sections efficaces avec le détecteur WAGASCI.

Dans le Chapitre 1, nous établissons le cadre général du Modèle Standard, la théorie quantique des champs décrivant les interactions entre particule dans la physique moderne. Nous définissons les champs de matières fermioniques : quarks et leptons, ainsi que le Lagrangien libre associé à leur propagation. À partir de là, nous introduisons les trois interactions fondamentales décrites par la théorie ainsi que le principe d'invariance de jauge. Ce principe nous permet de dériver les couplages entre champs fermioniques et champs bosoniques. Nous introduisons également les matrices de mélange qui expriment les relations entres états de masse et états de saveur. Le Lagrangien établi, nous nous intéressons au phénomène d'oscillation des neutrinos créé par l'existence de ce mélange et la différence des masses des neutrinos. Les effets de matières, le moyennage dû aux incertitudes sur les caractéristiques de l'expérience. Un formalisme simplifié à deux saveurs est aussi présenté afin de mieux visualiser le mécanisme. Les résultats des mesures sur les paramètres d'oscillation sont aussi présentés. Finalement la théorie des interactions entre neutrinos et matière est présentée à la fin de cette partie. Les interactions avec quark libre, nucléon libre ou nucléon dans un noyau, ainsi que les interactions cohérentes. Les états finaux d'interactions sont alors décrits, en particulier le terme CC0π qui désigne les interactions d'un neutrino avec un noyau produisant un lepton chargé, n'importe quel nombre de nucléons et aucun pion sortant du noyau.

Nous poursuivons dans le Chapitre 2 avec une description de l'expérience T2K (Tokai To Kamioka), l'expérience de neutrinos d'accélérateurs dans le cadre de laquelle s'inscrit cette thèse. Nous abordons le processus de production du faisceau de neutrinos muoniques utilisé pour nos mesures, ainsi que des détecteurs proches et lointains utilisés pour détecter le faisceau avant et après oscillation des neutrinos. C'est en observant les caractéristiques de ces différents détecteurs que nous expliquons la nécessité d'une expérience comme WAGASCI. Nous explicitons les enjeux auxquels elle s'attaque (réduction des erreurs systématiques liés à la connaissance des sections effaces d'interaction, mesure de la phase de violation CP) et détaillons les modules composant l'expérience.

Dans le Chapitre 3, nous décrivons brièvement la simulation Monte-Carlo qui nous a permis de développer l'analyse de l'expérience. Les logiciels utilisés ainsi que la démarche sont listés en début de chapitre. Nous présentons alors l'algorithme de l'analyse. Il y a deux parties générales : la reconstruction des évènements détectés qui nous permet de partir des dépôts d'énergie des particules dans les scintillateurs et d'arriver à des évènements contenant des

traces reconstruites et arrangées en vertex. La deuxième partie est constituée des coupures de sélection des évènementsi CC0π. Nous justifions tout du long de l'évolution de la pureté et de l'efficacité de la sélection. Les prédictions de notre simulation sont présentées en fin de chapitre et seront comparées aux résultats sur les données plus tard dans le manuscrit. Après la dernière coupure nous obtenons des puretés entre 50% et 60% et des efficacités entre 25% et 30%. Les répartitions des évènements dans l'espace des variables reconstruites du détecteur sont aussi prédites et présentées.

Nous désirons alors extraire une mesure de section efficace de cet échantillon sélectionné. il nous faut pour cela inverser les effets de détecteur, une tâche non triviale. Le Chapitre 4 entre dans le détail de la procédure choisie dans cette thèse : la méthode d'unfolding Bayésien de D'Agostini et les modifications apportées à sa formulation originelle sont détaillées. En effet nous ajoutons deux bins supplémentaires aux bins CC0π : un bin qui fera office d'échantillon auxiliaire pour les CC1π, et bin contenant toute les autres interactions. Ces deux bins permettront une soustraction du bruit de fond en tenant compte de la normalisation de l'échantillon de données. On peut ainsi mieux gérer les fluctuations de statistiques par rapport à ce qui est prédit par la simulation. Les binnings choisis sont aussi présentés. Les différents paramètres intervenant dans la formule de calcul des sections efficaces sont aussi évalués dans cette partie, avec une description des méthodes d'estimation. Le chapitre se conclut avec une mention des considérations de convergence de la méthode, même si les raisons ne sont pas encore expliquées.

Cependant comme pour toute mesure, il convient d'estimer les erreurs. C'est dans le Chapitre 5 que nous rentrons dans le détail des deux catégories d'erreurs qui interviennent dans les mesures de sections efficaces. Premièrement une succinte explication succinte de la méthode de calcul des erreurs statistiques. Dans un deuxième temps les erreurs systématiques sont introduites. Trois types d'erreurs systématiques sont considérées. Les erreurs dues aux incertitudes sur le flux, d'environ 10% pour les sections efficaces absolues et réduite sous 1% pour le rapport des sections efficaces. Les erreurs dues aux incertitudes sur le modèle de section efficace à environ 4% pour les trois mesures. Et enfin les erreurs dues au fonctionnement du détecteur et à sa modélisation par notre simulation. Pour chaque type d'erreur systématique les sources d'erreurs sont à chaque fois détaillées. La méthode de calcul est toujours la même : On crée plusieurs toy-models (une dizaine pour les paramètres discrets ou un millier pour les paramètres continus) pour lesquels on fait varier la valeur du paramètre autour de sa valeur nominale en fonction de son erreur associée). La déviation standard sur la distribution des sections efficaces de ces toy-models nous fournit l'erreur générée par l'incertitude sur le paramètre associé.

En regardant l'évolution de nos erreurs avec le nombre d'itération de l'unfolding nous observons une divergence des erreurs statistiques, alors que les erreurs systématiques convergent. Le Chapitre 6 s'intéresse aux enjeux de convergence et de la nécessité d'arrêter l'algorithme d'unfolding aussi tôt que possible. Il nous faut définir un critère qui garantira que le résultat de l'unfolding sera suffisamment exact mais aussi que les erreurs statistiques resteront raisonnable. Pour ce faire, nous introduisons des jeux de pseudo-données, des simulations significativement différente de la simulation nominale sur laquelle notre analyse est basé. Ces jeux sont obtenus en faisant varier les paramètres de modèle utilisés : le modèle de section efficace ou le modèle de flux. Nous testons alors la robustesse de l'algorithme en vérifiant la convergence de l'algorithme sur chacun de ces jeux de pseudo-données et définissons un critère pour lequel la convergence est satisfaisante dès qu'un jeu de pseudo-donnée le respecte. C'est ce critère que nous utilisons pour arrêter l'unfolding sur les données.

Finalement, nous terminons avec le Chapitre 7 où nous appliquons l'intégralité de l'analyse développée jusque là aux données et où nous analysons les résultats obtenus. Le critère de convergence nous fait arrêter l'unfolding à la 20ème itération. À cause des erreurs statistiques sur les échantillons sélectionnés, les erreurs statistiques sur les sections efficaces sont entre 5% et 11%. Ce sont toujours les erreurs dues au flux qui dominent pour les sections efficaces absolues tandis que l'erreur statistique domine pour le rapport de sections efficaces totales. Nous les comparons aux prédictions des générateurs d'interactions NEUT et GENIE. Si les prédictions et les résultats sur les données s'accordent bien sur les sections efficaces totales, nous observons une différence en forme pour la section efficace sur l'eau. Cette différence provient d'un désaccord sur les angles reconstruits au niveau du Water Module entre données et prédictions. Nous tentons d'expliquer ce désaccord. Une possibilité est une vraie différence de physique. L'autre est une compréhension imparfaite du Water Module, un nouveau détecteur à la structure innovante qui pourrait nécessiter plus de travail pour être compris et pour avoir des algorithmes de reconstruction dédiés.

En conclusion, cette thèse valide l'approche choisie pour la réduction des erreurs systématiques. Il reste à mettre à jour l'analyse, afin de tenir compte de l'évolution de la configuration de WAGASCI, et possiblement d'un nouvel algorithme de reconstruction pour le Water Module de WAGASCI. L'expérience T2K pourra continuer sur cette voie prometteuse.

Bibliography

[1] J. Chadwick. The intensity distribution in the magnetic spectrum of beta particles from radium (B + C). *Verh. Phys. Gesell.*, 16:383–391, 1914. 3

[2] W. Pauli. Dear radioactive ladies and gentlemen. *Phys. Today*, 31N9:27, 1978. 3

[3] E. Fermi. An attempt of a theory of beta radiation. *Z. Phys.*, 88:161–177, 1934. 3

[4] C. L. Cowan et al. Detection of the free neutrino: A Confirmation. *Science*, 124:103–104, 1956. 3

[5] G. Danby et al. Observation of High-Energy Neutrino Reactions and the Existence of Two Kinds of Neutrinos. *Phys. Rev. Lett.*, 9:36–44, 1962. 3

[6] K. Kodama et al. Observation of tau-neutrino interactions. *Phys. Lett.*, B504:218–224, 2001. 3

[7] E. Majorana. Theory of the Symmetry of Electrons and Positrons. *Nuovo Cim.*, 14:171–184, 1937. 3

[8] B. Pontecorvo. Inverse beta processes and nonconservation of lepton charge. *Sov. Phys. JETP*, 7:172–173, 1958. [Zh. Eksp. Teor. Fiz.34,247(1957)]. 3

[9] Ziro Maki, Masami Nakagawa, and Shoichi Sakata. Remarks on the Unified Model of Elementary Particles. *Progress of Theoretical Physics*, 28(5):870–880, 11 1962. 3

[10] R. Davis. A review of the homestake solar neutrino experiment. *Prog. Part. Nucl. Phys.*, 32:13–32, 1994. 3

[11] Y. Fukuda, T. Hayakawa, E. Ichihara, K. Inoue, K. Ishihara, H. Ishino, Y. Itow, T. Kajita, J. Kameda, S. Kasuga, and et al. Evidence for oscillation of atmospheric neutrinos. *Physical Review Letters*, 81(8):1562–1567, Aug 1998. 4

[12] Q. R. Ahmad, R. C. Allen, T. C. Andersen, J. D. Anglin, G. Bühler, J. C. Barton, E. W. Beier, M. Bercovitch, J. Bigu, S. Biller, and et al. Measurement of the rate of $\nu_e + d \rightarrow p + p + e^-$ interactions produced by ^{8}b solar neutrinos at the sudbury neutrino observatory. *Physical Review Letters*, 87(7), Jul 2001. 4

[13] F. P. An, J. Z. Bai, A. B. Balantekin, H. R. Band, D. Beavis, W. Beriguete, M. Bishai, S. Blyth, K. Boddy, R. L. Brown, and et al. Observation of electron-antineutrino disappearance at daya bay. *Physical Review Letters*, 108(17), Apr 2012. 4

[14] Y. Abe et al. Indication of Reactor $\bar{\nu}_e$ Disappearance in the Double Chooz Experiment. *Phys. Rev. Lett.*, 108:131801, 2012. 4

[15] J. K. Ahn, S. Chebotaryov, J. H. Choi, S. Choi, W. Choi, Y. Choi, H. I. Jang, J. S. Jang, E. J. Jeon, I. S. Jeong, and et al. Observation of reactor electron antineutrinos disappearance in the reno experiment. *Physical Review Letters*, 108(19), May 2012. 4

[16] K. Abe, N. Abgrall, H. Aihara, T. Akiri, J. B. Albert, C. Andreopoulos, S. Aoki, A. Ariga, T. Ariga, S. Assylbekov, and et al. Evidence of electron neutrino appearance in a muon neutrino beam. *Physical Review D*, 88(3), Aug 2013. 4

[17] Carlo Giunti. Neutrino Wave Packets in Quantum Field Theory. *Journal of High Energy Physics*, 2002(11):017, Nov 2002. 24

[18] Super-Kamiokande Collaboration, :, K. Abe, and al. Solar Neutrino Measurements in Super-Kamiokande-IV. *arXiv e-prints*, page arXiv:1606.07538, Jun 2016. 31, 34

[19] B. Aharmim and al. Combined analysis of all three phases of solar neutrino data from the Sudbury Neutrino Observatory. *arXiv e-prints*, 88(2):025501, Aug 2013. 31

[20] The KamLAND Collaboration. Reactor On-Off Antineutrino Measurement with KamLAND. *arXiv e-prints*, page arXiv:1303.4667, Mar 2013. 31

[21] T2K Collaboration, K. Abe, and al. First combined analysis of neutrino and antineutrino oscillations at T2K. *arXiv e-prints*, page arXiv:1701.00432, Jan 2017. 31

[22] MINOS Collaboration, P. Adamson, and al. Combined analysis of ν_μ disappearance and $\nu_\mu \rightarrow \nu_e$ appearance in MINOS using accelerator and atmospheric neutrinos. *arXiv e-prints*, page arXiv:1403.0867, Mar 2014. 31

[23] P. Adamson and al. First measurement of muon-neutrino disappearance in NOvA. *arXiv e-prints*, 93(5):051104, Mar 2016. 31

[24] IceCube Collaboration and al. Determining neutrino oscillation parameters from atmospheric muon neutrino disappearance with three years of IceCube DeepCore data. *arXiv e-prints*, page arXiv:1410.7227, Oct 2014. 31

[25] Daya Bay Collaboration and al. New measurement of θ_{13} via neutron capture on hydrogen at Daya Bay. *arXiv e-prints*, page arXiv:1603.03549, Mar 2016. 31

[26] The Double Chooz Collaboration. First Double Chooz $\boldsymbol{\theta_{13}}$ Measurement via Total Neutron Capture Detection. *arXiv e-prints*, page arXiv:1901.09445, Jan 2019. 31

[27] S. H. Seo and al. Spectral Measurement of the Electron Antineutrino Oscillation Amplitude and Frequency using 500 Live Days of RENO Data. *arXiv e-prints*, page arXiv:1610.04326, Oct 2016. 31

[28] Website. nu-fit.org. Accessed: 2019-09-27. xi, 32

[29] Kaoru Hagiwara, Naotoshi Okamura, and Ken-Ichi Senda. The earth matter effects in neutrino oscillation experiments from Tokai to Kamioka and Korea. *Journal of High Energy Physics*, 2011:82, Sep 2011. 33

[30] K. Abe and al (T2K Collaboration). Measurement of neutrino and antineutrino oscillations by the T2K experiment including a new additional sample of ν_e interactions at the far detector. *arXiv e-prints*, 96(9):092006, Nov 2017. 35

[31] K. Abe and al (T2K Collaboration). Search for C P Violation in Neutrino and Antineutrino Oscillations by the T2K Experiment with 2.2 $\times 10^{21}$ Protons on Target. *arXiv e-prints*, 121(17):171802, Oct 2018. 35

[32] C. Giunti and C.W. Kim. *Fundamentals of Neutrino Physics and Astrophysics*. Oxford University Press, 2007. 38, 40

[33] S.M. Bilenky. *Basics of Introduction to Feynman diagrams and Electroweak Interactions Physics*. Editions Frontières, 1994. 38

[34] M. Gell-Mann. *The interpretation of the new particles as displaced charge multiplets*. Nuovo Cimento 4 Supplement 2, 848-866, 1955. 39

[35] M.L. Goldberger and S.B. Treiman. *Form Factors in β Decay and μ Capture*. Phys. Rev. 111,354, 1958. 40

[36] Omar Benhar and Noemi Rocco. Nuclear Effects in Neutrino Interactions and their Impact on the Determination of Oscillation Parameters. *arXiv e-prints*, page arXiv:1310.3869, Oct 2013. 42

[37] J. A. Formaggio and G. P. Zeller. From eV to EeV: Neutrino cross sections across energy scales. *Reviews of Modern Physics*, 84(3):1307–1341, Jul 2012. 45

[38] J. Zmuda. Construction efficient monte carlo generators. *VANISH Summer school lecture*, 2014. vii, 46

[39] K. Abe and al. T2K neutrino flux prediction. *arXiv e-prints*, 87(1):012001, Jan 2013. 51, 52

[40] N. Abgrall and al. Measurements of $\pi^{\pm}$, $K^{\pm}$ and proton double differential yields from the surface of the T2K replica target for incoming 31 GeV/ c protons with the NA61/SHINE spectrometer at the CERN SPS. *European Physical Journal C*, 79(2):100, Feb 2019. 52

[41] WebSite. http://www-sk.icrr.u-tokyo.ac.jp. Accessed: 2019-10-15. vii, 58

[42] K. Abe and al. The T2K experiment. *Nuclear Instruments and Methods in Physics Research A*, 659(1):106–135, Dec 2011. 59

[43] K. Abe and al. Updated T2K measurements of muon neutrino and antineutrino disappearance using 1.5e21 protons on target. *arXiv e-prints*, page arXiv:1704.06409, Apr 2017. 60

[44] Internal t2k communication. Accessed: 2019-10-10. 60

[45] T2K Collaboration, K. Abe, and al. Measurement of the muon neutrino inclusive charged-current cross section in the energy range of 1-3 GeV with the T2K INGRID detector. *arXiv e-prints*, page arXiv:1509.06940, Sep 2015. 61

[46] K. Abe and al. Measurement of the ν_μ charged current quasielastic cross section on carbon with the T2K on-axis neutrino beam. *arXiv e-prints*, 91(11):112002, Jun 2015. 61

[47] M. Antonova and al. Baby MIND: A magnetised spectrometer for the WAGASCI experiment. *arXiv e-prints*, page arXiv:1704.08079, Apr 2017. 61

[48] N. Abgrall et al. T2K Technical Note 38 : Neutrino flux prediction for the 2010a Analysis . 73

[49] Y. Hayato. NEUT. *Nucl. Phys. Proc. Suppl.*, 112:171–176, 2002. 73

[50] S. Agostinelli et al. GEANT4: A Simulation toolkit. *Nucl. Instrum. Meth.*, A506:250–303, 2003. 73

[51] P. Perio and al. T2K Technical Note 113 : Implementation of the NIWG cross section parameterization . 73

[52] T.Koga and al. T2K Technical Note 322 : Measurements of the flux averaged inclusive ν_μ charged current cross section on H_2O and cross section ratios between H_2O, CH and Fe at on-axis . 80

[53] C. Patrignani et al. Review of Particle Physics. Passage of particles through matter. *Chin. Phys.*, C40(10):100001, 2016. 84

[54] INGRID group. T2K Technical Note 160 : Measurement of the flux averaged inclusive ν_μ charged current cross section with INGRID and Proton Module. 107

[55] Chikuma and Kim. T2K Technical Note 366 : Measurement of CCOπ0p cross sections on H_2O and CH with WAGASCI and the Proton Module. 118, 119, 131

[56] T. Kikawa et al. T2K Technical Note 181 : Measurement of the ν_μ charged current quasi-elastic cross section with the Proton Module. 135

[57] M. Alam and al. GENIE Production Release 2.10.0. *arXiv e-prints*, page arXiv:1512.06882, Dec 2015. 144

[58] Licciardi M. and Quilain B. T2K Technical Note 352 : Differential measurement of the ν_μ-CC1π cross section on H_2O and CH and of the H_2O/CH cross-section ratio using the on-axis detectors. 148

université PARIS-SACLAY | ÉCOLE DOCTORALE PHENIICS

Titre : Mesure des sections efficaces $\overline{\nu_\mu}$-CC0π différentielles sur H_2O et CH et le rapport des sections-efficaces H_2O /CH avec le détecteur hors-axe WAGASCI

Mots clés : section efficace, neutrino, WAGASCI, T2K, violation CP, unfolding

Résumé : Alors que presque tous les paramètres d'oscillation ont été mesurés, la mesure de la phase de violation CP δ_{CP} est l'un des objectifs majeurs de la physique des neutrinos d'accélérateurs. L'expérience T2K est l'un de celles qui poursuivent cet objectif. La mesure est effectuée en détectant un faisceau de neutrinos, directement après sa production, avec des détecteurs proches, puis , après propagation, au détecteur lointain Super-Kamiokande. Il s'agit d'observer l'apparition de neutrinos électroniques dans un faisceau initialement constitué seulement de neutrinos muoniques. Le pic du spectre énergétique du faisceau est choisi de façon à maximiser l'apparition de neutrinos électroniques à la distance de propagation. Parmi les erreurs systématiques liées à cette mesure, certaines sont dues au fait que les caractéristiques des détecteurs proches et lointain sont différentes. En effet Super-Kamiokande est un détecteur Cerenkov à eau et avec une acceptance angulaire isotropique tandis que les détecteurs proches sont à base d'hydrocarbone et d'acceptance angulaire portée vers l'avant. Afin de réduire ces erreurs systématiques, nous avons besoin d'un nouveau détecteur avec des caractéristiques similaires à celles de Super-Kamiokande: c'est le concept de l'expérience WAGASCI. Le détecteur possède des cibles d'eau et de carbone, ce qui permet de mesurer les sections efficaces sur ces deux matériaux ainsi que le rapport de ces sections efficaces. Ces mesures seront combinées aux données actuelles et permettront de réduire les erreurs sur la mesure de δ_{CP}. Cette thèse traite du développement de l'analyse des données prise par WAGASCI. Nous parlons des neutrinos dans le Modèle Standard. Puis nous décrivons la simulation Monte-Carlo utilisée dans l'analyse. Enfin, nous détaillons l'analyse avant de fournir les résultats expérimentaux. À cause du fait que nous n'avons pu travailler qu'avec une configuration intermédiaire dans cette thèse nous n'avions pas accès aux évènements à grand angle. Les détecteurs de muons latéraux n'étaient pas installés et le détecteur à muon axial avait une efficacité limitée. Cependant cette configuration intermédiaire suffit à mener une analyse préliminaire complète.

Title : Differential measurement of the $\overline{\nu_\mu}$-CC0π cross section on H_2O and CH and the H_2O /CH cross-section ratio using the off-axis WAGASCI detector

Keywords : cross-section, neutrino, WAGASCI, T2K, CP-violation, unfolding

Abstract : At a time when almost all the oscillation parameters have been measured, the measurement of the CP violation phase δ_{CP} is one of the major goals of current accelerator neutrinos experiments. The T2K experiment is one of these experiments that have taken to the task. The measurement is done by detecting a neutrino beam right after its production, with a set of near detectors, and also after it has propagated, at the far detector Super-Kamiokande. We look at the appearance of electron neutrinos, in the beam that originally only contained muon neutrinos. The energy peak of the beam has been chosen in order to maximize the appearance rate at the distance of Super-Kamiokande. Among the systematic errors associated to this measurement, some of them are due to the near and far detectors having very different characteristics. Indeed, Super-Kamiokande is a water Cerenkov detector with an isotropic angular acceptance while the near detectors are mostly based on hydrocarbon and have a forward angular acceptance. In order to reduce the systematic errors, we need a new near detector with characteristics more similar to Super-Kamiokande. The WAGASCI experiment is the answer to this need. The detector has a water as well as hydrocarbon targets. This allows to measure the cross-sections on both these materials as well as the ratio of the cross-sections. These measurements will be added to the current data and allow a reduced systematic error on the measurement of the CP violation parameter. This thesis covers the development of the analysis to exploit the data taken with the WAGASCI experiment. We recall the framework of the Standard Model and the place of neutrinos in particle physics. Then we describe the Monte-Carlo simulation we used to develop our analysis, before detailing the successive steps of said analysis. We Finally discuss the experimental results.
Because the configuration used in this thesis is not the final one, we cannot yet work with high-angle events. Side-MRDs were not yet installed at the time the data were taken. Furthermore, the muon detector used could not stop high-momentum muons because of a limited depth. However, our intermediate setup will be enough to conduct a comprehensive analysis with sufficient statistics.

Université Paris-Saclay
Espace Technologique / Immeuble Discovery
Route de l'Orme aux Merisiers RD 128 / 91190 Saint-Aubin, France